Aim & Scope
The journal publishes original papers in the extensive field of Electrical-Electronics and Computer engineering. It accepts contributions which are fundamental for the development of electrical engineering, computer engineering and its applications, including overlaps to physics. Manuscripts on both theoretical and experimental work are welcome. Review articles and letters to the editors are also included.

Application areas include (but are not limited to): Electrical & Electronics Engineering, Computer Engineering, Software Engineering, Biomedical Engineering, Electrical Power Engineering, Control Engineering, Signal and Image Processing, Communications & Networking, Sensors, Actuators, Remote Sensing, Consumer Electronics, Fiber-Optics, Radar and Sonar Systems, Artificial Intelligence and its applications, Expert Systems, Medical Imaging, Biomedical Analysis and its applications, Computer Vision, Pattern Recognition, Robotics, Industrial Automation.

Balkan Journal of Electrical & Computer Engineering

BAJECE

An International Peer Reviewed, Indexed and Open Access Journal

CONTENTS

BALKAN JOURNAL OF ELECTRICAL & COMPUTER ENGINEERING

The Design and Implementation of a Semantic-Based Proactive System for Raw Sensor Data: A Case Study for Laboratory Environments

Mehmet Milli, Ozlem Varliklar, Musa Milli, Sanaz Lakestani

Abstract— In the last decade, raw sensor data from sensor-based systems, the area of use of which has increased considerably, pose a fundamentally new set of research challenges, including structuring, sharing, and management. Although many different academic studies have been conducted on the integration of sets of data emerging from different sensor-based systems until present, these studies have generally focused on the integration of data as syntax. Studies on the semantic integration of data are limited, and still, the area of the study mentioned have problems that await solutions. In this article; parameters (Carbon Dioxide (CO_2), Total Volatile Organic Compounds (TVOC), Carbon Monoxide (CO), Particulate Matter 2.5 ($PM_{2.5}$), Particulate Matter 10 (PM_{10}), Temperature, Humidity, Light), affecting laboratory analysis results and threatening the analyst's health, were measured in laboratory environments selected as "use cases", and semantic-based information management framework was created for different sensor-based systems. Classical machine learning methods, and regression approaches which are frequently used for such sensor data, have been applied to the proposed sensor ontology and it has been measured that machine learning algorithm performs better on ontological sensor data. The most efficient algorithms in terms of accuracy and time were selected, and integrated into the proposed proactive approach, in order to take the selected laboratory environment's condition under control.

Index Terms— Sensor ontology, Semantic sensor web, Machine learning, Prediction on stream data, Supervised learning.

Mehmet Milli, is with Department of Computer Engineering University of Bolu Abant İzzet Baysal University, Bolu, Turkey, (e-mail: mehmetmilli@ibu.edu.tr).

https://orcid.org/0000-0002-0759-4433

Ozlem Varliklar, is with Department of Computer Engineering University of Dokuz Eylül University, İzmir, Turkey, (e-mail: ozlem@cs.deu.edu.tr).

https://orcid.org/0000-0001-6415-0698

Musa Milli, is with Department of Computer Engineering Turkish Naval Academy University of National Defense University, Istanbul, Turkey, (e-mail: musamilli@gmail.com).

https://orcid.org/0000-0001-8323-6366

Sanaz Lakestani, is with Scientific Industrial and Technological Application and Research Center University of Bolu Abant İzzet Baysal University, Bolu, Turkey, (e-mail: sanazlakestani@ibu.edu.tr).

https://orcid.org/0000-0002-1661-7166

I. INTRODUCTION

ALTHOUGH SENSORS are defined differently in many studies, the most common definition is that it is known as devices that detect phenomena in the physical environment in which it is located [1]. In another definition, sensors are defined as devices that can convert chemical, physical, and biological values into digital values [2].

Sensors have evolved continuously since the day they emerged and reached such a capacity that it can be utilized in almost every application, presenting efficiency in size, cost and adequacy. As a result of all these developments, sensor-based systems have become the heart of many electronic systems today. The use of such systems in many areas has caused an exponential increase in raw data on the Internet. A demonstration of how the raw sensor data obtained from the sensor reaches consumers of data appears in Fig. 1.
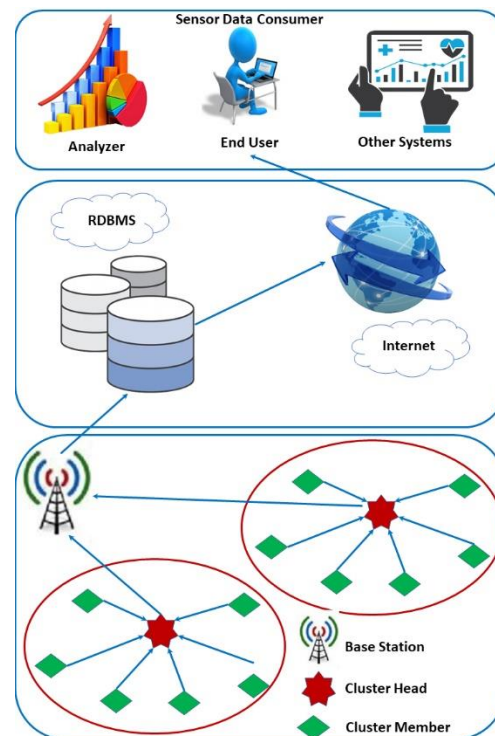
Fig. 1. The simple structure of a sensor-based system.

Most of the sensor data obtained from such systems on the Internet reach consumers without configuration. The unstructured presentation of sensor data causes a series of

problems that include sharing, interpreting, and managing data. Moreover, the sensor data is heterogeneous in nature because it bears different syntaxes, structures, and meanings in different systems [3]. The heterogeneity of the sensor data causes these data to remain application-specific, and hinders the management of independent sensor-based systems under a common infrastructure. An intermediate layer, independent of the application, enabling the sensor data semantically enriched to make it more useful is of crucial need.

In recent years, due to the reduction in size of sensors to a level suitable for use in every system, developments in the academic environment, and the continuous decrease in prices, sensor-based systems have rapidly spread to various aspects of daily life, particularly in industrial fields. The use of sensors in many fields has led to a significant increase in the raw data obtained from them. However, the lack of syntactic and semantic coherence among sensor data limits their sharing, reusability, and interpretability. The reusability, interpretability, and management of large-scale sensor data remain areas in need of effective solutions today. In the scope of this study, it is contemplated to address the mentioned issues by creating an ontology for raw sensor data.

Recently, researchers argue that semantic sensor web technologies can enrich the raw data obtained from sensors semantically and fill this intermediate layer [4-7]. Besides, a common framework is required for sensor-based information systems. Sensor data should be defined using Uniform Resource Identifiers (URIs) and delivered to sensor data consumers over HTTP [8]. In addition, sensor data should be encoded in formats that can be read by machines such as Resource Description Framework (RDF) and Web Ontology Language (OWL) so that they can be easily read and processed by machines. However, at this point, the lack of a comprehensive and understandable standard for the enrichment of sensor data around the world appears to be a major problem in the common manageability and operability of sensor systems.

The World Wide Web Consortium established the Semantic Sensor Network Incubator Group (SSN-XG) in 2011 to fill this intermediate layer and identified a set of standards for sensor data [9]. It has conducted many studies and defined certain standards for the semantic enrichment of raw sensor data obtained from SSN-XG sensor-based systems. The latest version of the Semantic Sensor Network (SSN), which is still used as a common framework in many studies today, was published in 2017 [10]. The core of SSN forms a lightweight but independent core ontology called SOSA (Sensor, Observation, Sample, and Actuator), which holds basic classes and properties. SOSA complies with the minimum interoperability limits, i.e. the sensor ontologies created with SOSA guarantees its sharing and interoperability with all other SSN and SOSA ontologies. Conceptual modules forming the infrastructure of sensor-based systems such as deployment, system, platform, procedure, and etc. are defined in the framework of SOSA and SSN. Some basic conceptual modules of SOSA/SSN are shown in Fig. 2.

The semantic sensor network is an application-independent framework that needs to be expanded with a certain concept and provides the manageability of the sensor systems on different platforms under a common infrastructure [11]. Shortly, SOSA/SSN is a model that allows the scope of the sensor ontology framework to be extended with other ontologies and concepts. For instance, in a biosensor application planned to be created in the field of medicine, a medical ontology, specific to the related field, including the technical medical terminology, classes, object properties and data properties can be employed to expand the ontological framework of SOSA-SSN.

A domain ontology that includes chemistry-related sensor measurements might import chemistry ontology, which includes chemical terminology (atomic number, orbital number, noble gas, element, etc.), classes, and object properties can be depicted as an example of the expansion of the SSN core ontology. The basic components of the SSN ontology are shown in Fig. 3.
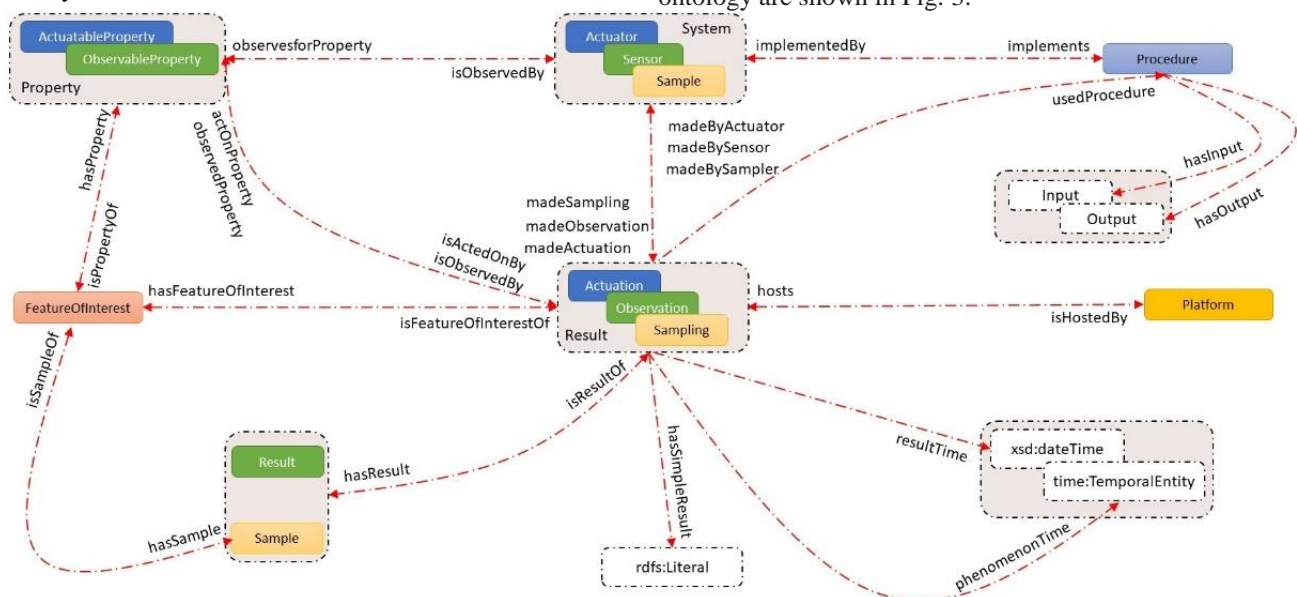

Fig. 2. Overview of the core structure of the SOSA classes, object properties, and data properties

The proposed ontology for laboratory environment parameters that affect the results of laboratory analysis and threaten the analyst's health during the analysis includes the general basic SOSA/SSN main classes. Only a few classes have been added to the basic SOSA/SSN framework. The added classes are described in detail in Section 3.2.

There is more than one purpose within the scope of the study. The main objectives of the study are listed below.

• Establishing a common infrastructure with a high capability to represent raw sensor data. Moreover, ensuring semantic integration of sensor data with each other by using ontological concepts such as Class, Object Property, Data Property. Hence, providing the capability to manage data obtained from different platforms, different systems, and different sensors under a common framework.

• To establish a system that provides real-time monitoring and control of laboratory environment parameters that negatively affect the laboratory analysis results and threaten the analyst's health.

• Determining the best algorithm for the designated laboratory environment parameters by using classical machine learning algorithms on ontological sensor data. And accordingly, detection of unforeseen environmental situations thanks to the ontological based proactive system created, and avoiding unwanted situations by executing appropriate action plans in time.

In this study, it is considered that creating an ontology of sensor data will contribute to the literature. These contributions roughly include: (i) Establishing a common framework for inherently heterogeneous sensor data, (ii) facilitating the shareability and reusability of sensor data across different platforms, hence enhancing the sustainability of sensor-based systems, (iii) ensuring machine readability of sensor data by encoding it in structural languages such as RDF and OWL, (iv) enriching sensor data semantically to make it machine-interpretable, (v) finally, in this study, an example of ontological sensor data was created, and commonly used regression models and machine learning algorithms were tested to demonstrate which ones can be applied to ontological sensor data in the literature.

The remainder of the article is organized as follows. In Section 2, previous studies in the field of sensor ontology are examined, and the differences between those and the current ongoing study are clearly revealed. Setting up systems infrastructure, creating sensor nodes, and use case are presented in Section 3. The data collection, the experiments to prepare data for the machine learning algorithm, and choosing the appropriate machine learning algorithms for the proposed sensor ontology are presented in Section 4. Section 5 describes the comparison of machine learning algorithms, determination of the most suitable algorithm in every aspect, and integration into the proposed proactive system. Finally, the results and future studies are discussed in detail in Section 6.
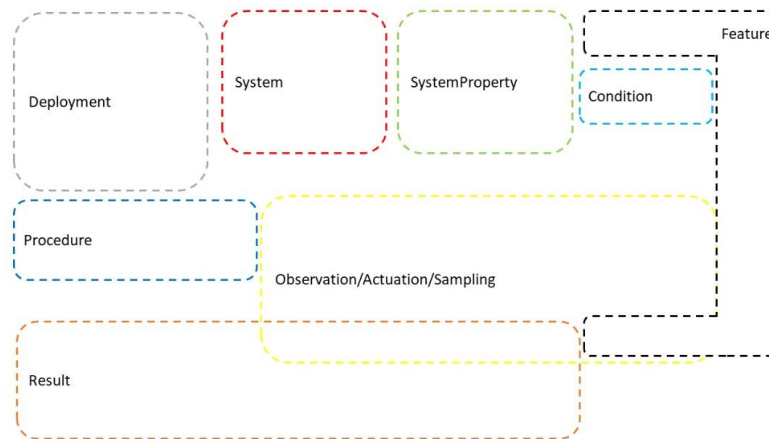
Fig. 3. Basic conceptual ontology modules of SOSA/SSN frameworks [9].

II. RELATED WORK

The concept of sensor data ontology was first introduced by Avancha et al. [12]. Since 2004, many studies have been carried out in this field, and sensor ontology has become an area of study that attracts more attention. Considering the components (machine learning, semantic web technologies, wireless sensor networks) that form the basis of the proposed study, there are many studies in the literature. Therefore, it is possible to classify the literature review under 3 headings by selecting articles that are similar to this study.

The works in the first group focus on the integration of machine learning algorithms built on data from wireless sensor networks (WSN). In this category, studies focusing on machine learning algorithms processing sensor data and excluding semantic enrichment approaches are argued. In this

context, many studies have been administered in different domains in the last 20 years. These studies cover the applications of machine learning approaches in the field of health in [13-15]. In [16, 17] there are studies in which machine learning approaches are applied in the field of environment and agriculture. In addition to these, machine learning approaches have been used in areas such as smart cities [18], security [19 -21] where WSN's are frequently utilized. Studies in this area are not assessed in detail, as they are a bit far from the proposed study. The major difference between these studies in the first group and the proposed study is that the sensor data collected is not enriched by using the ontological concepts. The best advantage of the proposed system is that it enables the management of ontologically oriented application-specific sensor-based systems before the emergence of the SOSA/SSN common framework.

In the second group, studies focusing on structuring sensor data to be managed under a common framework are considered. Although the semantic sensor web is beneficial in ensuring analytical integration between different sets raw data, the complexity of semantic techniques is often unacceptable for some end-users and data consumers due to the long processing time. The suggested system in [22] proposes IoT-Lite to reduce complexity and shorten transaction times. The IoT-Lite contains a simple example of semantic sensor ontology. The greatest feature of this sensor ontology is an approach that provides interoperability of sensor data on heterogeneous Internet of Things (IoT) platforms and includes minimum concepts and relationships that can respond to most end-user questions in a reasonable time. In the work mentioned in [23], a semantic sensor network has been used to solve interoperability problems of different platforms and devices in an e-health system. Apart from these, Kuster et al. [24], Wang et al. [25], Ali et al. [26] proposed different semantically based architectures to describe sensor information collected from different environments.

In these studies, the focus is on the management of sensor data feeding from different systems under a common infrastructure. The major difference between these studies and the proposed study is that machine learning algorithms are not operated on the sensor data of which ontology is created. In other words, these systems only perform real-time monitoring in real-world applications. In the suggested system, one of the main objectives is to find the most suitable machine learning approach for the proposed ontological sensor system.

In the third group, the studies cover the application of machine learning approaches to semantic sensor data. The studies closest to the proposed study are examined in this group. The system proposed in [27] mentions a sensor ontology which is presented using the World Wide Web Consortium's (W3C) SSN frame. Adeleke et al. developed a statistical machine learning-based prediction model using this proposed sensor ontology. In the respected study, in order to predict an unhealthy situation in the near future, their models are evaluated on $PM_{2.5}$ and PM_{10} values. 5 different classification algorithms are applied to ontological sensor data in their studies. By comparing these algorithms, they claim that the most effective algorithm on PM values is the Multilayer Perceptron.

In the work mentioned in Onal et al. [28], another semantic sensor web-based proactive system is presented. This system has been applied and evaluated for clustering and sensor anomaly detection using a public data set. In this study, the LinkedSensorData and LinkedObservationData dataset containing different weather parameters such as air temperature, wind speed, relative humidity, pressure, and visibility are used. LinkedSensorData is an RDF dataset that describes approximately 8000 air sensor information. The K-means algorithm, which is widely used for proactive systems in the literature, has been chosen as the appropriate model in this system.

The studies that are the most similar to the proposed study in terms of technology and scope are evaluated in this group. Studies under this category have also created a semantic-based

framework for the definition of sensor information, and classical machine learning approaches have been performed on ontological sensor information. The main purpose of SSN is to create a common identification frame for sensor information from different platforms, different domains, and different sensors. However, in these studies, the number of platforms, sensors, and domains are limited and the capacity of SSN to represent sensor information in different systems, platforms, and domains could not be fully utilized. In the proposed study, 3 different environments, 4 different platforms, 5 different sensors are used and 8 different parameter values are measured. In previous studies, machine learning algorithms applied to ontological sensor data are limited in number, so in this study, the number of algorithms running on sensor data is increased. Another difference is that many studies focused on either regression or binary classification. In this study, regression and binary classification approaches are evaluated together.

Apart from all these studies explained above, the study field of semantic sensor data has been expanded to include increasing scalability, aligning ontologies, and integrating them into the Internet of Things platforms. Al-Baltah et al. [29] have focused on the semantic integration of heterogeneous sensor data from different systems and sources between machines. One of the biggest hurdles in integrating heterogeneous sensor data is scalability. Therefore, the researchers propose a scalable semantic data aggregation framework that aims to improve the scalability of data integration in their models and to detect and reconcile unit of measure conflicts. In this study, to prove the feasibility of the proposed framework, real sensor data was collected and carried out as a web application. Experimental results on the use-case conducted by the researchers show that their proposed framework improves the scalability of data aggregation between heterogeneous sensors data. Another result of the proposed framework is that it is effective in detecting and resolving measurement unit conflicts.

Another area where semantic sensor technologies have been used recently is the IoT. IoT sensors continuously generate large volumes of observed stream data. Processing this data and integrating it into other systems may sometimes require going beyond classical approaches. For this reason, recently, many researchers argue that integrating semantic web technologies into IoT systems plays an active role in the instant decision-making mechanisms of the proposed studies [30-32]. These researches focus on real-time processing and interpretation of sensor flow data by integrating different semantic descriptions into the proposed frameworks. It is thought that efforts to integrate Semantic Web technologies into IoT frameworks will increase day by day due to their data integration capabilities.

The subject under study is actually closely related to smart buildings as well. Monitoring indoor air quality and ensuring actions are taken in inappropriate situations are subtopics of creating smart buildings. The success of smart building designs relies on bringing together expertise from various fields. Coordinating processes that require different fields of expertise involves integrating data and concepts obtained from

these fields in an appropriate manner. The study conducted in [33] includes a taxonomy on semantic web technologies and categorizes ontology studies for smart buildings into three main categories and several subcategories. Indoor air quality measurement with sensor data and intervention when necessary has been classified among dynamic features. Because indoor air is a spatiotemporal feature that varies over time and space. In the study, in addition to the developed taxonomy, a new ontology that integrates the static and dynamic features of smart buildings has been proposed. Our proposed study can be described as a more comprehensive and practical version of the dynamic part of the ontology created in the mentioned study.

Ontologies, which are useful tools for integrating data collected from different fields, also appear in smart city models, just like in smart buildings. Smart city concepts have been researched in order to alleviate traffic difficulties and the associated problems [34]. In the "Understanding Traffic Flows to Improve Air Quality" (TRAFAIR) project proposed by Desimony et.al, cameras recording the traffic situation and sensors measuring environmental parameters have been placed on the roadsides in Modena (Italy) and Zaragoza (Sapin). The data collected through cameras and sensors are processed and stored in the TRAFAIR database in CSV format. Semantic relationships between data in CSV format have been established using appropriate ontologies. The aim of the project is to examine the impact of traffic flow data on air pollution in cities and to predict future air pollution. The main difference between the study conducted within the TRAFAIR project and our study is that, in the TRAFAIR project, environmental parameters are collected in an open-air environment, while in our current study, environmental parameters are collected in an indoor environment.

Poor indoor air quality has long been a major concern for human health. Recently, especially with the SARS-CoV-2 pandemic, studies have been conducted to control indoor air quality and improve indoor air quality with appropriate actions when necessary [35, 36]. During the SARS-CoV-2 pandemic, 24/7 lockdown has been enforced for 45 days in Spain. Domínguez-Amarillo et.al [35] conducted indoor air parameter measurements (CO_2, $PM_{2.5}$, NO_2, TVOC) in four different types of homes in Madrid before and during the lockdown. The study reveals that, during the lockdown, while outdoor air quality improved, indoor air quality deteriorated dramatically. In the study, measures to be taken during a full or partial lockdown, especially for individuals with respiratory problems, have been evaluated. In our proposed work, measurements of a greater number of environmental parameters have been conducted. In our study, a sensor ontology concept was proposed to facilitate the integration of the obtained data. Additionally, using various machine learning algorithms, the environmental air quality was assessed to determine whether it falls within normal values for human health.

Unlike outdoor air, due to limited circulation indoors, air pollutants tend to accumulate continuously in the environment, leading to a faster penetration of disease-causing organisms. Monitoring, controlling, and taking necessary actions for air quality have become even more crucial, especially with the SARS-CoV-2 pandemic. In this context, Mumtaz et.al [36] measured indoor air quality using gas and particle sensors, and they established an indoor air quality monitoring system. The study involves measuring air quality, generating alerts if any measured parameter exceeds a threshold value, and predicting future air quality. As a result, the study contains several preventative strategies. Similar to our work, a sensor node measuring 8 different parameters affecting air quality has been created. The main difference in our study compared to this study is the use of a conceptual sensor ontology for the integration of data.

III.   MATERIALS AND METHODS

A. Sensor Nodes

In order to measure the values of parameters determined in the selected use case, 4 different nodes to perform 4 different tasks have been established. These sensor nodes are named Type A, Type B, Type C, and Type D and the purpose of installation and fundamentals components are given below. Arduino Uno is used as a microprocessor in all sensor nodes due to its ease of use and low cost. Considering transmission distance, energy consumption, and compatibility with Arduino Uno, the nrf24l0+ antenna is chosen as the communication device. In order to reduce the load on the nodes and to provide the flexibility of deployment during the distribution of the sensors in the environment, two different sensor nodes are installed, and the sensors are placed on them.

Type A Sensor Node (Gateway Node): The gateway node is the most important node in the network, as it is the one to collect the data and transmit to the base station. In cases where the Type A sensor node fails to function due to physical obstacles or any problem arising from its electronics, or if communication with other nodes is interrupted, all data communication in the network stops. Thus, the Type A sensor node is vital for the system. No sensor was placed on it as no measurement in the environment is expected from it.

Type B Sensor Node (Sensor Node 1): In the proposed project, 5 different sensors are used to measure 8 parameters. These sensors are integrated into the two nodes, measuring an equal number of parameters. The digital humidity and temperature Sensor (DHT22), which measures the temperature and humidity parameters in the environment, and the combined CO_2 and TVOC sensor (CCS811) that measures the carbon dioxide and total volatile organic compounds, are integrated on the Type B Sensor Node.

Type C Sensor Node (Sensor Node 2): Another sensor node that makes measurements in the environment is the Type C sensor node. MQ-7 sensor measuring carbon monoxide, Nova SDS011 sensor measuring $PM_{2.5}$, and PM_{10} values, and light-dependent resistance (LDR) sensor measuring light intensity in the environment are integrated into this node.

Type D Sensor Node (Repeater Node): After the nodes are installed in the measurement environment and WSN is established, a communication problem occurs due to the distance and obstacles between some nodes. In order to solve this communication problem and to ensure healthy data communication, repeater nodes are placed to strengthen the received signal and to enable the data received from the node to reach the gateway node. The sensors used, the nodes created, the technical infrastructure of this network, the characteristics, and detailed description of this system used are available in the previous study of the research team [37].

B. Sensor Ontology

The SOSA/SSN provides an application-independent common framework that needs to be expanded with specific concepts and opportunity to manage sensor data for different domains. The concepts to be added can be classes, object properties, data property, or individuals depending on the application. In the proposed project, the core SSN ontology for the ontology of laboratory environment parameters is expanded by adding some classes, object properties, and individuals. This ontology is designed with the Protege [38] ontology editor developed by Stanford University. Protege is a free open source framework that provides an interface for users to review ontologies. The Protege 5.5.0 editor has the capability to create classes and subclasses, define and visualize the relationship between classes to extend the SSN ontology.

Since this article focuses more on seeking the most appropriate machine learning approaches on ontological sensor data for proactive system design, the creation of sensor ontology is not explained in detail. Technical information on the proposed sensor ontology is available in the article previously written by the project team [37]. SSN core sensor ontology has been expanded to represent the environmental parameters that affect the analysis performed in the laboratory environment used and the indoor environment parameters that affects the health of the analyst. This extension includes appropriate classes, object properties, data properties, and instances. The following example is given in order to better understand the proposed sensor ontology. In the core SSN ontology, the most significant concept is the "sosa:Observation" class, as it represents the sensor value and measurement date and time with the data properties attached to it. Fig. 4 below shows an example of an extended sensor ontology from the point of view of the "sosa:Observation" class in the proposed sensor ontology.

"sosa:Observation" is the indicator representing the value of the property of a "sosa:FeatureOfInterest", or computing through a "sosa:Procedure". The algorithm connects to "sosa:Sensor", subclass of "ssn: System" class with "sosa: madeBySensor" object property, to understand what shapes "sosa:Observation". In the above illustration, Nova SDS011 sensor used in the project is given as an example. An individual of the class "sosa:Observation" measured by this sensor is shown in Fig. 4. Each measurement is given a unique value consisting of 32 characters and represented by it. So that, data consumers can access each sensor value they want to display with this unique id. The $PM_{2.5}$ value measured by the Nova SDS011 value is "xsd:double" 7.73. As illustrated, the measurement date and time are "xsd:dateTime" 2019-08-30T06: 00: 00 + 03: 00. Since there is a good number of units for the same or different parameters in the literature, the "MeasurementUnit" class has been added to the basic SOSA/SSN framework to avoid unit complexity. The unit of the value measured by the Nova SDS011 sensor given in the example is assigned as "PartsPerMillion", which is frequently used in the literature.
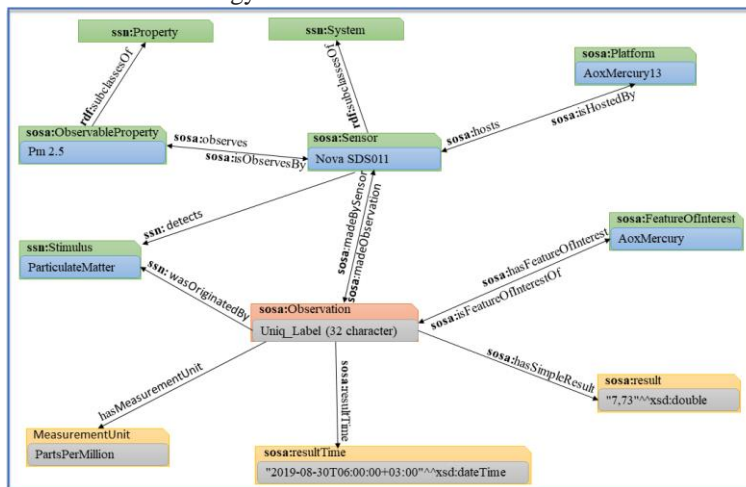
Fig. 4. Overview of some SOSA/SSN classes and properties from the sosa:Observation class perspective.

Looking at the other concepts in the given example, to explain which parameter is measured by "sosa:Sensor" class , a link is given to "sosa:ObservableProperty", which is a sub-class of "sosa:Property" class, with "sosa:observes" object property. In this example, it is seen that the parameter measured by Nova SDS011 sensor, which is a member of the "sosa: Sensor" class, is $PM_{2.5}$ "sosa:isFeatureOfInterestOf" object property is given as a link to "sosa:FeatureofInterest" classes to explain to which environment the value "sosa:Observation" is associated. "sosa:FeatureOfInterest" class is the area or environment where you want to measure. In this study, 3 laboratories that are frequently used in Scientific Industrial and Technological Application and Research Center (SITARC) have been selected as the measurement area. One of them is the AoxMercury laboratory where various analyses are carried out. To summarize the example given above, in the

AoxMercury measurement area, the value measured by the Nova SDS011 sensor on the AoxMercury13 platform at 06:00 a.m. on 30.08.2019 is 7.73 ppm.

C. Use Case

The proposed sensor ontology is created using the sensor data collected in the SITARC within the Bolu Abant Izzet Baysal University (BAIBU). Data collection has been carried out in 3 laboratories frequently used in SITARC. These laboratories are MaldiTof, AoxMercury, and Chromatography laboratories. In these laboratories selected as Use Cases, microorganism identification, proteomic analysis, bacteria count, fatty acid analysis, anion-cation determination, total halogen determination, solid-phase extraction, etc. analyses are done frequently.

During analyses, both the environmental parameters that will affect the analyst's health and the environmental parameters that will affect the analysis result must be monitored instantaneously in order to be kept under control. According to the report of the World Health Organization (WHO) [32] one of the most important causes of disease and death in the world is an unhealthy living environment. Therefore, avoiding unhealthy conditions and monitoring the working environment effectively to keep the environmental parameters under control emerges as a serious issue.

In this study, a total of 8 parameters: temperature, humidity, CO_2, TVOC, CO, $PM_{2.5}$, PM_{10}, and light intensity are measured by 5 sensors. For this, a total of 8 sensor nodes, including 1 Type A, 3 Type B, 3 Type C, and 1 Type D nodes, are established and deployed to measurement environments. 1 Type B and 1 Type C sensor nodes are placed in every 3 laboratories selected as measurement areas, one for each sensor. Type A sensor node (Gateway) is placed in AoxMercury Laboratory because it is close to the midpoint of all nodes. Once the sensor network is established, it is realized that there are communication problems between the Gateway and Type C sensor node, due to distance and physical obstacles such as walls, tables, and devices in the Chromatography laboratory from time to time. This problem is solved by placing a Type D sensor node between these nodes and strengthening the signal.

IV. EXPERIMENTS

A. Collecting Data

After placing the sensor nodes in the measurement area and sending the data properly, the data collection process is started on 29.08.2019 at 16:05. Each sensor in the installed system is programmed to measure an average per minute and send it to the gateway. The hourly average of the collected data is added to Apache Jena Fuseki, which is frequently used as a triple database (Apache Software Foundation) [39]. Jena Fuseki is a SPARQL Protocol and RDF Query Language (SPARQL) server. In addition, it has been preferred as a triple database in this project as it provides a clear user interface for server monitoring and management.

The data collection process has been terminated on 12.10.2019 due to the annual maintenance of the devices in the laboratory. A total of 45 days of uninterrupted data has been collected at the selected measurement sites. Between these dates, each sensor has made approximately 62,000 measurements, and a total of approximately 1,500,000 measurements have been made. Theoretical and practical training have been given twice in the first 10 days of September and October in the laboratories specified between the dates of measurement, and the 3 laboratories where the measurement is made have been used. This situation has been beneficial for the project results in terms of observing what kind of changes may occur in the parameters during the analysis and training in the laboratory. Daily average values of temperature and CO_2 between the measurement dates are shown in Fig. 5 and Fig. 6 respectively.

The graph in Fig. 5 is given as a box-whisker plot to clearly show the central position and spread of the mean of temperature data collected. Although the low values of some parameters such as temperature during analysis have a positive effect on analysis studies, it negatively affects the health of the personnel, especially in long-term analyses. Especially in MaldiTof and Chromatography laboratories, the ambient temperature must be below 18 °C for a proper analysis activity to be carried out. However, considering the health of the personnel, it is important to keep the temperature in these laboratories within a narrow range. Although there are air conditioners, keeping the ambient temperature at appropriate levels that do not expose a threat on human health and not negatively affect the analysis results in laboratories, is more complicated than in other environments.

The graphic in Fig. 6 shows the daily average CO_2 level in the laboratories selected for the measurement area within the specified date range. Especially during the dates of theoretical and practical training, it is seen that the amount of CO_2 in the environment exceeded the value of 1000 ppm determined by the WHO health organization as a reference value for indoor environments. It has been observed that the value of many parameters measured within the scope of this study increased during the dates of formal education. The reason for this increase is thought to be directly related to the amount of gas released as a result of the analysis performed in the experiments and increasing the human activity in the environment.
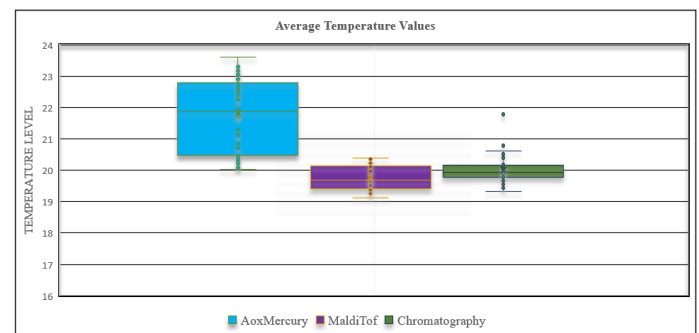

Fig. 5. Box and Dispersion (spread) graph of average temperature values between 29.08.2019 and 12.10.2019 in laboratories.
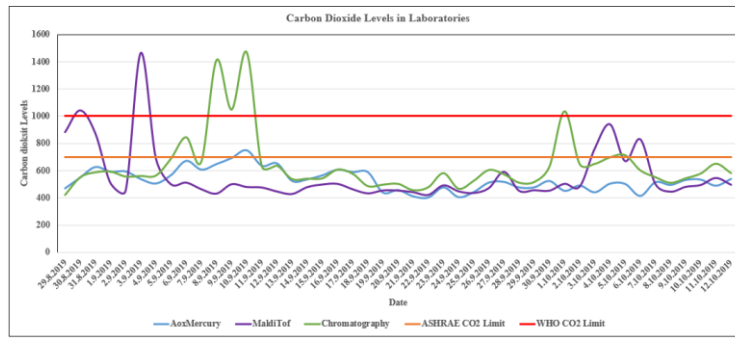
Fig. 6. The daily average CO_2 value between 29.08.2019 and 12.10.2019 in all laboratories.

B. Pre-Processing and Data Manipulation

Determination of Classes

The accepted reference values of important parameters that determine indoor air quality such as CO_2, CO, TVOC, $PM_{2.5}$, PM_{10} have been determined by the institutions that are accepted worldwide such as WHO, Environmental Protection Agency (EPA), American Society of Heating, Refrigerating and Air-Conditioning Engineers (ASHARE). In this study, these reference values are used while classifying and labelling the data. However, while determining the limit values of parameters such as temperature and humidity, the past experiences of researchers who made analyses in other research and laboratories have been used. Although the level of light, which is the last parameter measured, is effective in many laboratory processes such as bacterial growth, no data indicating its impact on indoor air quality has been recorded. Generated classes and their limit values are shown in Table 1.

TABLE I
CLASSES AND LIMIT VALUES OF ENVIRONMENTAL PARAMETERS

	Excellent (5)	Good (4)	Moderate (3)	Poor (2)	Terrible (1)
T (ºC)		18-19	17-18	16-17	<16
	19-21	21-22	22-23	23-24	>24
Humidity		30-40	20-30	10-20	<10
	40-60	60-70	70-80	80-90	>90
CO₂	<700	700-900	900-1100	1100-1300	>1300
TVOC	<40	40-70	70-100	100-150	>150
PM₂.₅	<10	10-20	20-30	30-40	>40
PM₁₀	<20	20-40	40-60	60-80	>80
CO	<25	25-50	50-75	75-100	>100
Light	Nan	Nan	Nan	Nan	Nan

In many respected studies, generally, one parameter and two different classes are used, such as "Good" and "Poor" [40]. Since the overall purpose of this study is to find a suitable prediction algorithm for ontological sensor data, the situation for the algorithms to be selected is shaped to present a more complicated state; 5 different classes are defined for 7 parameters and the limit values are determined. The class label of an instance is identified by the parameter with the worst value of class among the parameters that make up that row. Table 2 shows how the class value of the row is determined.

When the instances are classified according to the aforementioned rule, it has been seen that 65% of the total of 3168 rows of data are at the desired level for the laboratory interior environment. However, in the remaining 35%, timely preparation of necessary action plans is vital for laboratory analysis results, and employee health. The experiments reveal that laboratory air quality is monitored at ideal ranges when there is no biological analysis and no human activity in the environment. Fig. 7 shows the number of individuals in each class.

Certain pre-processes are required to make logical inferences and obtain good conclusions on the data collected. Pre-processes such as removing noisy data, conveniently filling missing data, shift all parameter values to the same range (normalization) are absolutely necessary for determining a better prediction model. Pre-process operations performed before making estimates on the data and how they are applied are explained in detail below.

Missing Value Imputation

On the specified dates, approximately 25,920 data would be expected to have been saved to the Apache Jena Fuseki RDF database, though only 23,252 data have been recorded due to the malfunction of the devices operating in the system or human error. This number corresponds to approximately 90% of the data that should be recorded. It is important to fill the missing values with a reasonable approach, especially if the algorithms in effect that are sensitive to missing values such as Decision Tree (DT) and Random Forest (RF) are to be studied. In this manner, the missing 10% has been filled with the well-known and accepted methods, and data continuity was ensured.

In data mining, it is possible to deal with the missing value issue with different approaches, such as deleting the missing values, accepting the average of that feature as the standard, or accepting them zero. Deleting or statistically filling missing values causes bias and negative effects on the results. Therefore, unlike these approaches, inputting data can significantly improve the quality of the data set [37]. Recently, many studies have shown that filling missing values with classification approaches has positive effects on the output [13, 41, 42]. In our work, missing values are filled by utilizing a hybrid approach of the K-nearest neighbor (K-NN) algorithm and Decision Tree, and the quality of the data set is increased.

TABLE II
DETERMINING THE CLASS VALUES OF PARAMETERS AND ROWS

Temperature	Humidity	CO₂	TVOC	PM₂.₅	PM₁₀	CO	Light	Nominal
22.93	54.16	534.55	20.86	10.66	12.85	27	74.63	Moderate
23.01	53.78	541.1	21.68	10.09	11.83	27	67.1	Poor
21.03	42.12	422	2.48	0.88	1.12	21.6	26	Good
20.99	42.2	417.45	1.71	1.32	1.38	21	4	Excellent
20.27	50.94	879.46	71.31	5.08	5.78	32.59	78.07	Moderate
20.31	50.94	554.24	23.08	4.67	5.73	32.8	76.56	Good
20.25	52.34	1348.59	142.37	7.58	8.96	37.28	28	Terrible
20.31	52.3	1223.55	128.47	7.79	9.22	34.65	28	Poor
19.66	52.25	1306.33	138.5	6.53	7.71	255.35	79.43	Terrible
19.59	55.33	407.04	0.28	3.42	3.73	22.57	26	Excellent
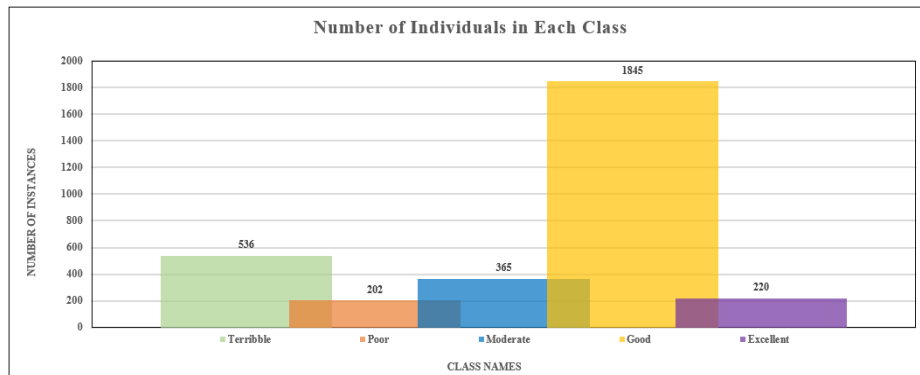
Fig. 7. Scatter graph of classes by row.

Outlier Detection

An Outlier can be defined as any observation different from other observations in the data set [43]. Outliers in the data collected by WSN can generally be caused by sensor measurement errors or some problems arising from data communication. Occasionally the outliers can be caused by human error. For example, if someone blows or touches the sensor in an environment where the temperature parameter is measured, this is a human error that causes the sensor value to deviate upwards. Both system-based and human-based errors cause the estimation to be biased and wrong. Therefore, analyzing the collected data and eliminating some inconsistent parts will increase the accuracy of the prediction.

There are some types of outlier detection approaches such as Probabilistic, Distance Based (cosine, Euclidean distance, etc.), algorithm-based (neighbor based, neural networks based, etc.). We evaluated outlier detection in two stages. First, the outlier data in each attribute has been found in itself and eliminated. During this process, the cosine distance approach, which is one of the distance-based outlier detections measures, is used, and a total of 10 observation data inconsistent with the other data have been deleted from each column. In the second step, after the class label of each instance (row) is assigned, outliers have been determined over this class label and eliminated. While determining outliers, the K-NN neighborhood approach has been used (k =10) and a total of 20 observation data eliminated.

Normalization

The measurement ranges, limit values, of each sensor used in this study are different. The measuring range is the total range that the instrument can measure under normal conditions. Table 3 shows the maximum and minimum values that can be measured by the sensors used in this study.

Absolute distance measuring methods such as Euclidean and Minkowski consider features in the same value ranges in the similarity calculation with equal importance. When using such distance measuring methods, calculating the similarity between instances without any pre-processing on the data set causes the feature with a large variance to have a high effect on the result [44]. In other words, the feature with large variance dominates the effect of other features on the result. It is called "feature domination". Moreover, the feature with high variance may not have a positive correlation with data in the same class, so it may not have the capability to parse data properly. In this case, the classification process might be misleading. To avoid feature domination; (i) all features are shifted to a certain interval. Normalization has significantly increased the performance of the classifiers used in this study. (ii) Cosine like similarity measures can be used that are not affected by the feature domination problem.

As demonstrated in Table 3, the values of some parameters can be between 0 and 100, while some parameter values may go up to 10,000. Therefore, it is certain that the prediction algorithms will decide according to the parameter with high values. In order to prevent this situation and to ensure that the parameters affect the estimation algorithm equally, all parameters have been shifted to the range of [0-1].

TABLE III
VALUE RANGES OF MEASURED PARAMETERS

Sensor	Parameter	Unit	Measurement Range
DHT22	Temperature	°C	-40 °C-125 °C (± 0.5)
DHT22	Humidity	% rh	0%-100% {± 2.5-5}
CCS-811	Carbon Dioxide	ppm	400-29,206 ppm
CCS-811	TVOC	ppb	0-32,768 ppb
Nova PM	Particular Matter 2.5	ppm	0.0-999.9 ppm
Nova PM	Particular Matter 10	ppm	0.0-999.9 ppm
MQ-7	Carbon Monoxide	ppm	10-10,000 ppm
LDR	Light Level	%	0%-100%

V. EXPERIMENTAL RESULTS

The results of classification algorithms on the aforementioned data set are presented in this section with different aspects. The results indicated in the figures and tables are the outcomes obtained for the test dataset. In order to reveal the achievements of algorithms, they have been run on the collected data set and it has been evaluated that the testbed established as a real-life case is sufficient for a fair evaluation of the classifiers. The algorithm performance tests have been performed on a computer with windows 10 operating system and equipped with Intel I7 7700HQ 2.8 GHz processor, 16 Gb DDR4 Memory, Nvidia Geforce Gtx 1050 video card.

When algorithm performance tests have been enforced on ontological sensor data, 70% percent of the data has been divided into the training set, and 30% percent test set. Indoor environmental parameters do not change rapidly at a dramatic pace. The deployed sensors tend to measure similar values in recent times and locations, meaning they are generally records of the same class. Therefore, it is crucial to be extremely careful when partitioning the dataset to minimize potential biases resulting from dataset partitioning. The dataset used is imbalanced. Working with k-fold on imbalanced datasets can lead to some challenges. If the records that make up the dataset are not randomly shuffled before applying k-fold, the test data may consist solely of records from a single class. The dataset includes temporal records, and if the dataset is randomly shuffled before applying k-fold, the temporality of the dataset may be affected, leading to an unfair evaluation. Due to the mentioned reasons, when creating the test data, records are selected randomly from different time periods, different classes, and different locations. The aim is to achieve a homogeneous distribution. 6 out of 9 machine learning algorithms evaluated are used with default parameter values. However, depths and the maximum number of tree parameters of RF, GBT, and DT algorithms negatively affect the time performances at their default values. Therefore, these parameters have been optimized for these algorithms, without much compromise on accuracy. The Maximal Depth and Number of Trees parameters are set to 10 in order to compete with other algorithms in terms of time.

All of the algorithms obtained acceptable accuracy values except Naive Bayes (NB) and Logistic Regression (LR). But the most successful algorithms in terms of accuracy among them are RF, Deep Learning (DL), and DT with the value 90%, 89%, 88% respectively. Therefore, it has been observed that these three algorithms are equally suited for this case. Generally, complexity and accuracy performance specify a trade-off in many cases, for this scenario the performance/complexity ratio of DT is better than others. The comparison of the accuracy percentages of the algorithms used in the case study is shown in Fig. 8.

The results obtained in terms of time comparison of the algorithms can be seen in Fig. 9. According to the results, we see that the most effective algorithms at the total time aspect are DT and Generalized Linear Model (GLM) methods, respectively. The biggest reason underlying the high speed of DT is the fast decision-making mechanism thanks to its tree structure. Also, DT doesn't need a large training set to get good results. GLM is a regression-based method and it is obvious and known that regression-based methods are effective especially in terms of running time. So it is not surprising that DT and GLM achieve the fastest scores. However, DT, NB, and RF algorithms have shown a tendency to learn faster. For this reason, the training time of these algorithms is the lowest. In addition, the duration of time spent in a training set with 1000 records are observed in the time graph in Fig. 9. According to this statistic, DT again gets the lowest score while DL gets the second place. This graphic demonstrates that the DL method has good scalability.

Fig. 10 shows the average correlations calculated by all models between labels and attributes. According to these correlations, the most important parameters affecting the result is PM_{10}, $PM_{2.5}$, and Temperature. While it is predictable that PM_{10} and $PM_{2.5}$ are active attributes, it is a surprise that the temperature is effective. However, the lectures in labs have increased the human presence and activity and the linear relationship of the temperature attribute with CO_2 has been caused by this situation.

The results in Fig. 10 revealed that the parameter of light does not have much effect on the results obtained however, it is an expected result. While setting the label value of each row in advance, it has been thought that the parameter of light would not affect the result and it is stated that it is not used in defining the line label.

In addition to the run time and accuracy comparisons of the selected algorithms, the amount of gain and loss is also an important parameter in the selection of the algorithm, especially in multi-class labelling. In a multi-class dataset, more acceptable it is for a predicted value to be in a class close to the real value than if in a class far from the true value is. The benefits and costs of the wrong and correct estimates are given in Table 4. Losses are represented as negative numbers while benefits or gains are represented as positive numbers.
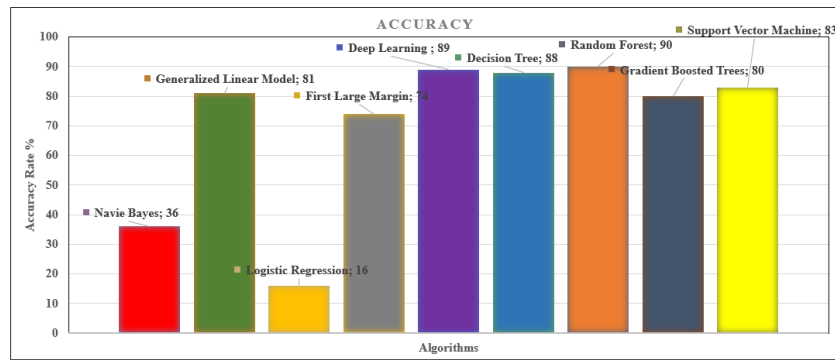
Fig. 8. Comparison of accuracy percentages of algorithms used in the case study.
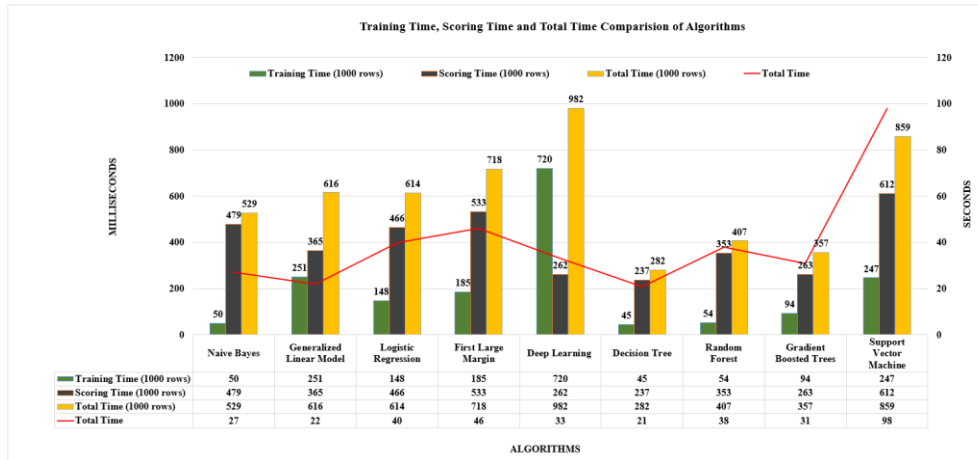
Fig. 9. Comparison of the training time, the scoring time, and the total time of algorithms used in the case study.
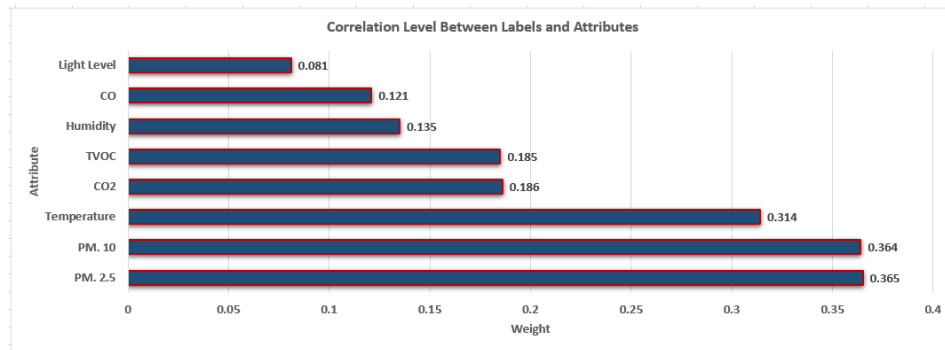
Fig. 10. The average correlations calculated by all models used between labels and attributes are seen.

For example, if the label value of an instance with an actual label value of Excellent is estimated as Excellent with any classifier, the prediction is correct and takes 1 as the gain point. On the other hand, if the classifier labelled the same Excellent instance as a Good, Moderate, Poor, or Terrible the classifier takes -1, -2, -3, -4 loss point respectively and this prediction becomes wrong. These loss points give the value of the wrong prediction. In some cases, it may be more beneficial to choose the best performing algorithm by looking at gain rather than accuracy.

When the performances of the algorithms are compared in terms of gain, it is seen that the sum of the costs of NB and LR algorithms is negative, while the remaining algorithms are positive. When the performances of algorithms are assessed via gain metric, it is seen that the algorithms that give the best results in parallel with their accuracy rates are RF, DL, and DT. A comparison of algorithm performances in terms of gain is given in Fig. 11.
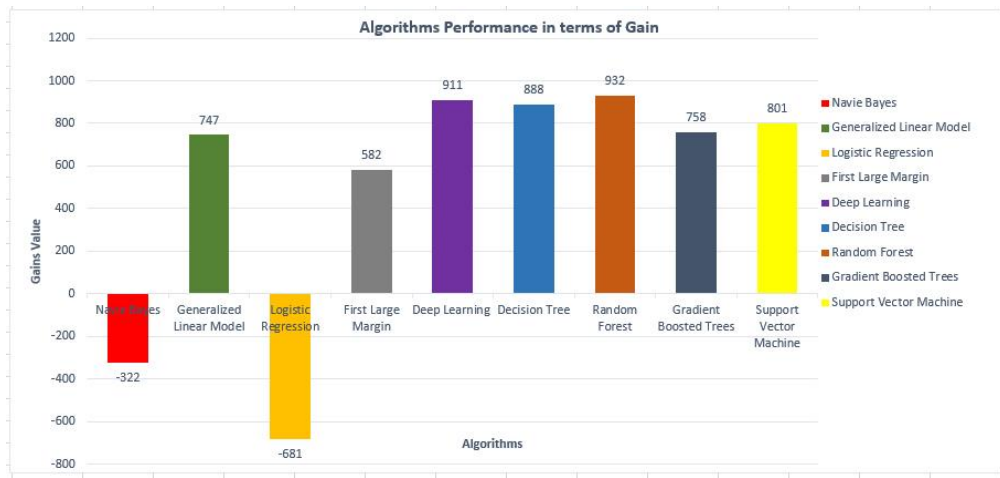
Fig. 11. Comparison of algorithms used in the proposed system from the perspective of gain.

TABLE IV
COST MATRIX REFERENCED WHEN COMPAIRING THE GAIN
PERFORMANCE OF ALGORITHM USED

Cost Matrix	True Terrible	True Poor	True Moderate	True Good	True Excellent
Predicted Terrible	1	-1	-2	-3	-4
Predicted Poor	-1	1	-1	-2	-3
Predicted Moderate	-2	-1	1	-1	-2
Predicted Good	-3	-2	-1	1	-1
Predicted Excellent	-4	-3	-2	-1	1

VI. CONCLUSION AND FUTURE WORK

In recent years, sensor-based systems have rapidly spread to all areas of daily life as a result of the physical minimization of sensors in size, enabling the use in every field, the developments in the academic community, and the decrease in their prices. The intensive use of sensor and sensor based systems in every field has caused an exponential increase in sensor data in the internet environment. However, the heterogeneous nature of the sensor data makes it difficult to manage them under a single infrastructure. In addition, the absence of a common framework for the representation of sensor data makes it difficult for the machines to be understood and interpreted. Although a syntactic relationship has been established between sensor data in studies conducted so far, this is insufficient to make meaningful inferences from sensor data.

Semantic Sensor Web technology has been suggested and used by many researchers to address all these problems. Creating semantic relationships instead of establishing syntactic relationships between sensor data will provide more meaningful inferences. In addition, sensor data must be encoded in languages that machines can understand and interpret, such as RDF and OWL. Each sensor data should be represented by URIs and it should be easier for data consumers to reach it. In the first step of this study, a different model has been created by using the SSN framework to manage the data collected from different platforms, different environments, and different sensors under the same infrastructure. In the second step of the proposed study, in order to establish a proactive system design, some traditional and state-of-art prediction algorithms on ontological sensor data are tested and compared by using data from this model. When the values obtained by running the algorithms on the collected sensor data are compared, it is seen that the most effective algorithms are RF and DT in terms of run time, accuracy and gain.

The proposed model can be combined with different domains, different platforms, and different systems to expand its scope in future studies. With this extended model, sensor data can be used to make a common inference. Although the proposed sensor ontology associates the data semantically, the complexity of the semantic techniques often causes an increase in processing times. A new model that includes minimum concepts to ensure that the proposed semantic systems respond in a reasonable acceptable time to data consumers can be created. Object properties and data properties can be used within the scope of the minimum concept. Thus, the triple number in the RDF database is reduced and the system can be more efficient.

The ontological sensor data framework developed within the scope of the study, while providing a range of advantages such as semantic enrichment of data and reusability, is also considered to have some weaknesses. Undoubtedly, the major disadvantage of ontological datasets is low coverage and high complexity. Creating ontological datasets can be a complex process, and developing a comprehensive ontology for a subject may take time. The ontological dataset created for any subject for the first time must adapt to the changes occurring in that field. This situation necessitates making additional updates to the ontological dataset over time. In addition to all these problems, excessively enriching the dataset semantically will lead to unnecessary overloading of the dataset. Therefore, the decision on the extent to which raw sensor data should be enriched needs to be made considering the cost-benefit ratio.

Data availability

All data of 8 measurements collected over 45 days using 5 different sensors from 3 different laboratories are in the links:

link1: https://doi.org/10.4121/14805960.v1

link2: https://figshare.com/articles/dataset/Labs_Sensor_Data/14742858

REFERENCES

[1] L. Bermudez, E. Delory, T. O'Reilly and J. Del Rio Fernandez, "Ocean observing systems demystified", *MTS/IEEE Biloxi - Mar. Technol. Our Futur. Glob. Local Challenges, Ocean.* 2009, pp. 1–7.

[2] S. Abd Hakim, K. Tarigan, M. Situmorang, and T. Sembiring, "Synthesis of Urea Sensors using Potentiometric Methods with Modification of Electrode Membranes Indicators of ISE from PVA-Enzymes Coating PVC-KT p ClPB", *J. Phys. Conf. Ser.*, vol. 1120, no. 1, 2018.

[3] A. Sheth, "Interoperating Geographic Information Systems", *Interoperating Geogr. Inf. Syst.*, pp. 5–30, 1999.

[4] F. Wang, L. Hu, J. Zhou, J. Hu and K. Zhao, "A semantics-based approach to multi-source heterogeneous information fusion in the internet of things", *Soft Comput.*, vol. 21, no. 8, pp. 2005–2013, 2017.

[5] M. Arooj, M. Asif and S. Zeeshan, "Modeling Smart Agriculture using SensorML", *Int. J. Adv. Comput. Sci. Appl.*, vol. 8, no. 5, pp. 0–6, 2017.

[6] A. Haller *et al.*, "The modular SSN ontology: A joint W3C and OGC standard specifying the semantics of sensors, observations, sampling, and actuation", *Semant. Web*, vol. 10, no. 1, pp. 9–32, 2018.

[7] J. Liu, Y. Li, X. Tian, A. K. Sangaiah and J. Wang, "Towards semantic sensor data: An ontology approach", *Sensors (Switzerland)*, vol. 19, no. 5, 2019, pp. 1–21.

[8] H. K. Patni and C. A. Henson, "Linked Sensor Data", 2010, pp. 362–370.

[9] A. N. U. Armin Haller, S. B. Krzysztof Janowicz, University of California, C. Simon Cox, T. U. of B. Danh Le Phuoc, A. N. U. Kerry Taylor, and É. N. S. des M. de S.-É. Maxime Lefrançois, "Semantic Sensor Network Ontology—W3C," 2011. [Online]. Available: https://www.w3.org/TR/2017/REC-vocab-ssn-20171019/. [Accessed: 20-May-2021].

[10] P. Barnaghi *et al.*, "Semantic Sensor Network XG Final Report", 2017.

[11] J. P. Calbimonte, H. Jeung, O. Corcho and K. Aberer, "Enabling query technologies for the semantic sensor web", *Int. J. Semant. Web Inf. Syst.*, vol. 8, no. 1, 2012, pp. 43–63.

[12] S. Avancha, C. Patel and A. Joshi, "Ontology-driven adaptive sensor networks", *Proc. MOBIQUITOUS 2004 - 1st Annu. Int. Conf. Mob. Ubiquitous Syst. Netw. Serv.*, 204, pp. 194–202.

[13] M. Chen, J. Zhou, G. Tao, J. Yang and L. Hu, "Wearable affective robot", *IEEE Access*, vol. 6, 2018, pp. 64766–64776.

[14] L. Hu, J. Yang, M. Chen, Y. Qian and J. J. P. C. Rodrigues, "SCAI-SVSC: Smart clothing for effective interaction with a sustainable vital sign collection", *Futur. Gener. Comput. Syst.*, vol. 86, 2018, pp. 329–338.

[15] H. Rathore, A. Al-Ali, A. Mohamed, X. Du and M. Guizani, "DLRT: Deep learning approach for reliable diabetic treatment", *IEEE Glob. Commun. Conf. GLOBECOM 2017 - Proc.*, vol. 2018, 2017, pp. 1–6.

[16] A. A. Sarangdhar, P. V. R. Pawar and A. B. Blight, "Machine Learning Regression Technique for using IoT", *Int. Conf. Electron. Commun. Aerosp. Technol. ICECA 2017*, pp. 449–454.

[17] S. S. Patil and S. A. Thorat, "Early detection of grapes diseases using machine learning and IoT", *Proc. - 2016 2nd Int. Conf. Cogn. Comput. Inf. Process. CCIP 2016*, pp. 7–11.

[18] I. U. Din, M. Guizani, J. J. P. C. Rodrigues, S. Hassan and V. V. Korotaev, "Machine learning in the Internet of Things: Designed techniques for smart cities", *Futur. Gener. Comput. Syst.*, vol. 100, 2019, pp. 826–843.

[19] N. J.Patel and R. H. Jhaveri, "Detecting Packet Dropping Misbehaving Nodes using Support Vector Machine (SVM) in MANET", *Int. J. Comput. Appl.*, vol. 122, no. 4, 2015, pp. 26–32.

[20] J. Canedo and A. Skjellum, "Using machine learning to secure IoT systems", *2016 14th Annu. Conf. Privacy, Secur. Trust. PST 2016*, pp. 219–222.

[21] I. Kotenko, I. Saenko, F. Skorik and S. Bushuev, "Neural network approach to forecast the state of the Internet of Things elements", *Proc. Int. Conf. Soft Comput. Meas. SCM 2015*, pp. 133–135.

[22] M. Bermudez-Edo, T. Elsaleh, P. Barnaghi and K. Taylor, "IoT-Lite: a lightweight semantic model for the internet of things and its use with dynamic semantics", *Pers. Ubiquitous Comput.*, vol. 21, no. 3, 2017, pp. 475–487.

[23] I. Yang, "Design and Implementation of e-Health System Based on Semantic Sensor Network Using", 2018.

[24] C. Kuster, J. L. Hippolyte and Y. Rezgui, "The UDSA ontology: An ontology to support real time urban sustainability assessment", *Adv. Eng. Softw.*, vol. 140, 2020, pp. 102731.

[25] C. Wang, Z. Chen, N. Chen and W. Wang, "A hydrological sensor web ontology based on the SSN ontology: A case study for a flood", *ISPRS Int. J. Geo-Information*, vol. 7, no. 1, 2018.

[26] S. Ali, S. Khusro, I. Ullah, A. Khan and I. Khan, "SmartOntoSensor : Ontology for Semantic Interpretation of Smartphone Sensors Data for Context-Aware Applications", vol. 2017, 2017.

[27] J. Adeleke, D. Moodley, G. Rens and A. Adewumi, "Integrating Statistical Machine Learning in a Semantic Sensor Web for Proactive Monitoring and Control", *Sensors*, vol. 17, no. 4, 2017, pp. 807.

[28] A. C. Onal, O. Berat Sezer, M. Ozbayoglu and E. Dogdu, "Weather data analysis and sensor fault detection using an extended IoT framework with semantics, big data, and machine learning", *Proc. - 2017 IEEE Int. Conf. Big Data*, 2017 pp. 2037–2046.

[29] I.A. Al-Baltah, A.A.A. Ghani, G. M. Al-Gomaei, F. A. Abdulrazzak and A. A. A. Kharusi, "A scalable semantic data fusion framework for heterogeneous sensors data", *Journal of Ambient Intelligence and Humanized Computing*, 2020, pp. 1-20.

[30] C. Kuster, J. L. Hippolyte and Y. Rezgui, "The UDSA ontology: An ontology to support real time urban sustainability assessment", *Advances in Engineering Software*, vol. *140*, 2020, 102731.

[31] A. A. Sarangdhar and V. R. Pawar, "Machine learning regression technique for cotton leaf disease detection and controlling using IoT", In *2017 International conference of Electronics, Communication and Aerospace Technology (ICECA)* vol. 2, 2017, pp. 449-454.

[32] World Health Organization, "Global status report on noncommunicable diseases 2014", (No. WHO/NMH/NVI/15.1), World Health Organization, 2014.

[33] A. Donkers, D. Yang, B. de Vries and N. Baken, "Semantic web technologies for indoor environmental quality: A review and ontology design", *Buildings*, vol. 12, no. 10, 2022.

[34] F. Desimoni, S. Ilarri, L. Po, F. Rollo and R. Trillo-Lado, "Semantic traffic sensor data: The TRAFAIR experience", *Applied Sciences*, vol. 10, no. 17, 2020.

[35] S. Domínguez-Amarillo, J. Fernández-Agüera, S. Cesteros-García and R. A. González-Lezcano, "Bad air can also kill: residential indoor air quality and pollutant exposure risk during the COVID-19 crisis", *International Journal of Environmental Research and Public Health*, vol. 17, no. 19, 2020.

[36] R. Mumtaz et al., "Internet of things (Iot) based indoor air quality sensing and predictive analytic—A COVID-19 perspective", *Electronics*, vol. 10, no. 2, 2021.

[37] Ö. Aktaş, M. Milli, S. Lakestani and M. Milli, "Modelling sensor ontology with the SOSA/SSN frameworks: a case study for laboratory parameters", *Turkish Journal Of Electrical Engineering And Computer Sciences*, vol. 28, no. 5, 2020, pp. 2566-2585.

[38] M. A. Musen, "The protégé project: a look back and a look forward", AI matters, vol. 1, no. 4, 2015, pp. 4-12.

[39] Apache Software Foundation, "'Apache Jena' A free and open source Java framework for building Semantic Web and Linked Data applications", [Online]. Accessed on September 11, 2021. https://jena.apache.org/documentation/fuseki2/index.html.

[40] J. A. Adeleke, D. Moodley, G. Rens and A. O. Adewumi, "Integrating statistical machine learning in a semantic sensor web for proactive monitoring and control", *Sensors*, vol. 17, no. 4, 2017, 807.

[41] N. Z. Abidin, A. R. Ismail and N. A. Emran, "Performance analysis of machine learning algorithms for missing value imputation", *International Journal of Advanced Computer Science and Applications*, vol. *9, no.* 6, 2018.

[42] N. D. Darryl and M.M. Rahman, "Missing value imputation using stratified supervised learning for cardiovascular data", *J Inform Data Min*, vol. *1*, no. 13, 2016.

[43] V. Barnett and T. Lewis, "Outliers in statistical data", John Wiley & Sons, Chichester, 1994.

[44] A. K. Jain, M. N. Murty and P. J. Flynn, "Data clustering: a review", *ACM computing surveys (CSUR)*, vol. *31, no.* 3, 1999, pp. 264-323.

BIOGRAPHIES

MEHMET MİLLİ Karşıyaka, İZMİR in 1984. He graduated from the Computer Engineering Department of Mersin University. He received M.Sc. and Ph.D. degrees in Computer Engineering from the University of Dokuz Eylül in 2016 and 2021 respectively. His research interests include embedded systems, artificial intelligence, data mining and sensor networks.

ÖZLEM VARLIKLAR Adana, in 1981. She received the B.Sc., M.Sc., and Ph.D. degrees in computer engineering from the University of Dokuz Eylül, Izmir, Turkey, in 2003, 2005, and 2010, respectively. Since 2004, she has been with the Department of Computer Engineering, University of Dokuz Eylül, where she is currently assistant professor. Her research interests include artificial intelligence, computer software, decision support systems and natural language processing.

MUSA MİLLİ Karşıyaka, İZMİR in 1984. He graduated from the Computer Engineering Department of Sakarya University. He received M.Sc. and Ph.D. degrees in Computer Engineering from the University of Ege, İzmir, Turkey in 2013 and 2019 respectively. He has been with the Department of Computer Engineering of Turkish Naval Academy, National Defense University, Tuzla, İSTANBUL. His research interests include artificial intelligence, data mining, machine learning, information retrieval, big data and network security.

SANAZ LAKESTANI Abadan, IRAN in 1975. She graduated from Sehit Behesti University in 1997. She received the M.Sc. from the University of Islami Azad in 2001 and Ph.D in Environmental Engineering Department of Hacettepe University in 2015. Her research interests include air pollution and control, environmental impact assessment and risk management.

Research Article

Detection of Preterm Labor from Electrohysterogram (EHG) Data Using Empirical Wavelet Transform-Based Machine Learning Methods

Erdem Tuncer

Abstract— **Accurate early prediction of preterm labor can significantly reduce birth complications for both mother and baby. This situation increases the need for an effective technique in early diagnosis. Therefore, machine learning methods and techniques used on Electrohysterogram data are increasing day by day. The aim of this study is to evaluate the effectiveness of the Empirical Wavelet Transform approach on Electrohysterogram data and to propose an algorithm for early prediction of preterm labor using single Electrohysterogram signal. The data used in the study were taken from Physionet's Term-Preterm Electrohysterogram Database and scored in one-minute windows. The feature matrix was obtained by calculating the sample entropy value from each of the discretized Electrohysterogram modes obtained as a result of this method, which was used for the first time on Electrohysterogram data, and the average energy value from the signal obtained by recombining the modes. The obtained features were applied to Random Forest, Support Vector Machine, Long Short-Term Memory algorithms to predict preterm birth. Among the classifier algorithms, the Random Forest algorithm achieved the best result with a success rate of 98.20%.**

Index Terms— **Classification, Electrohysterogram, Empirical Wavelet Transform, Preterm Birth.**

I. INTRODUCTION

THE AVERAGE gestation period in humans is between 37-42 weeks. Births occurring between these weeks are called term births. Births after 42 weeks are called late births. Births ending between 24-37 weeks are called Preterm births. Preterm birth is one of the leading causes of infant mortality and can have long-term negative consequences. Therefore, accurate and early diagnosis is very important [1-3]. Accurate diagnosis of preterm labor is one of the most important problems faced by obstetricians [4]. Many methods have been researched and tried to detect preterm birth. Commonly used methods;

Erdem TUNCER, is with Department of Biomedical Engineering University of Kocaeli University, Kocaeli, Turkey,(e-mail: erdemtuncerr@gmail.com).

https://orcid.org/0000-0003-1234-7055

tocodynamometer device, Transvaginal Cervix Length measurement, Bishop Score and Electrohysterogram (EHG) signal. Tocodynamometer is the recording of uterine contractions and baby movements. It measures the contractions that occur on the uterine surface. Transvaginal Cervix length can be measured with the help of ultrasound. The shorter the length, the higher the risk of preterm delivery. The Bishop score is calculated from many values such as the amount of expansion of the pelvis, the rate of shortening of the uterus, its location and condition. The higher the Bishop Score, the higher the probability of normal delivery. All these methods have been used for preterm birth detection [5]. The other method is to examine the EHG signals recorded with the electrodes on the outer surface of the uterus. EHG signals for preterm birth detection give more applicable and reliable results compared to other methods applied. These signals are one of the most important sources of information for the prediction of preterm labor. Electrodes are placed at specific points on the uterine surface to record the signals. Electromyogram (EMG) signals are recorded from the uterus at different times of pregnancy or at the time of delivery [6]. EMG signals are not stationary signals, so the signals are difficult to distinguish visually. Due to such complex feature of EMG signals, it is possible to distinguish between preterm birth or term birth by determining various features with machine learning methods 7].

Many studies in the literature have used EHG signals to distinguish between term and preterm birth. From studies using the Term-Preterm EHG Database, Shahrdad et al. [8] presented a new approach to estimating the risk of preterm labor by analyzing EHG signals and classifying term/preterm signal recordings. EHG signals are divided into windows and linear predictive coding technique is applied to extract features from each window. The data were analyzed in 5 different clusters, and term and preterm deliveries detected before the twenty-sixth gestational week were classified with the highest accuracy (100%). Fergus et al. [9] used radial basis function neural network and random neural network classifiers in their study. As a result of the filtered and single channel (0.34–1 Hz filter on Channel 3) study, they reached 91% sensitivity. In the study by Vinothini et al. [10], EHG signals recorded before the twenty-sixth week of pregnancy were analyzed using topology-based shape features to distinguish between term and preterm states during early pregnancy. The signals were passed through

the discrete Fourier transform. As a result of classification using Naive Bayes (NB), Decision Tree (DT) and Random Forest (RF) algorithms, a success rate of 98.6% was achieved with the RF algorithm. Far SM et al. In the study by [11], a single channel EHG signal was divided into two modes using Empirical Mode Decomposition (EMD) and sample entropy, Root Mean Square (RMS) and mean teager–kaiser energy values were calculated. In total, six features were extracted from each channel. Data were scored in one minute windows and 0.08-4 Hz. passed through a band pass filter. Three classifier performances were evaluated; K-Nearest Neighbor (KNN), Support Vector Machine (SVM) and DT. As a result of the term and preterm classification, they reached a success rate of 99,7% with the SVM algorithm. In the study by Lou et al. [12], they used entropy features extracted from time-frequency expansion. These entropy properties were then rescaled for gestational age to characterize the rate at which the uterus evolves towards birth. By using the Gaussian Naive Bayes (GNB) classifier, Principal Components Analysis (PCA), the relevant frequency components were selected, trained with samples prepared under the division-synthesis high sampling scheme, and a success rate of 75% was achieved. Huseyin et al. [13] achieved 90% accuracy using the neural network immunity algorithm. They argued that the proposed Dynamic Self-organized Network Inspired by the Immune Algorithm (DSIA) model performs well and that supervised and unsupervised learning techniques can be associated with the DSIA model. In their study, Xu et al. [14] evaluated studies in the literature addressing barriers to EHG signal analysis and machine learning algorithms. They stated that RMS and power spectrum are candidates for measuring changes in EHG signal and are frequently used in related studies. They stated that the approximate entropy and sample entropy values did not show very satisfactory results due to the interference of different noisy sources in the recorded EHG signal. Similarly, Lyapunov exponent, linear/non-linear correlation etc. They also stated that attempts to introduce new sizes such as They noted that when EHG signals were recorded long before birth, the signal-to-noise ratio was lower. They argued that recent research has focused on the classification of contractions during pregnancy rather than directly predicting preterm labor. Nsugbe et al. [15] used Linear Series Decomposition Learner (LSDL) to predict preterm birth from EHG and tocodynamometer signals in his study. It used two different classifier algorithms. By using LSDL, they determined that less storage space is needed for data and achieved a success rate close to 100%. They noted that the EHG signal is attenuated before it reaches the surface and recording instrumentation, and the tocodynamometer signal provides better accuracy for classifiers. The study by Dine et al. [16] used data from 57 women at the University Hospital Landspitali and 79 women at the Center for Obstetrics and Gynecology. In this study, it was aimed to improve and compare the classification between labor and pregnancy contractions. They investigated the effect of graphic parameters in characterizing the evolution of the uterine connection from pregnancy to delivery and distinguishing between pregnancy and labor contractions. They examined the performance of different classification methods from the classifier algorithms (Artificial neural network (ANN), SVM, RF, Recurrent Neural Network (RNN), Long Short-Term Memory (LSTM)) and reached a success rate of 94.46% with the RF algorithm.

In our study, algorithm is proposed in which the effectiveness of the Empirical Wavelet Transform (EWT) approach is also evaluated to predict preterm labor from a single EHG channel. At the same time, machine learning method has been tried to be adopted to classify the data without the need for feature reduction algorithms. The second section of the manuscript includes methods and techniques, the third section includes the results, and the fourth section includes the discussion section where our study is compared with studies in the literature.

II. MATERIALS AND METHODS

A. The Proposed Method

The block diagram of the proposed method is shown in Figure 1. After EHG data was recorded, the data were divided into one-minute windows. Each window data is separated into 5 modes with the EWT approach. The feature matrix was obtained by calculating the sample entropy value from each mode and the average energy value from the signal obtained by recombining the modes. The obtained feature matrix was given as input to the classifier algorithms and term/preterm classification was made.
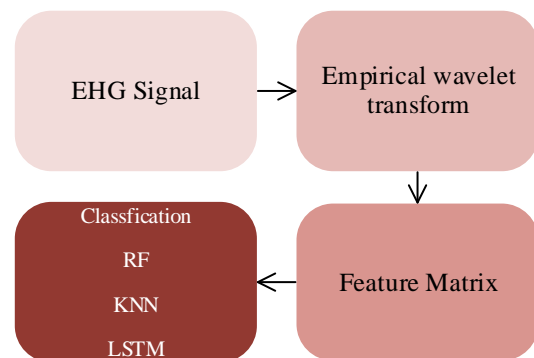
Fig.1. Flow chart of the proposed method

B. Dataset

EHG records in Physionet's Term-Preterm Electrohysterogram Database (TPEHGDB) were obtained from Ljubljana University Medical Center between 1997-2005. There are 300 EHG records, of which 262 are term and 38 are preterm deliveries. These records were divided into two groups according to the weeks of gestation as 143 term and 19 preterm records before the 26th gestational week, 119 term and 19 preterm records at and after the 26th gestational week. The recordings consist of three channels recorded from four electrodes placed on the abdominal surface of pregnant women as shown in Figure 2. Electrodes were placed symmetrically above and below the navel at a distance of 7 cm on the abdominal surface. Using the differences in the electrical potentials of the electrodes, three channels were used, namely Channel 1 (CH1)=E2-E1, CH2=E2-E3 and CH3=E4-E3. Unfiltered channel data, 0.08-4 Hz. filtered in the range of 0.3-3 Hz. filtered in the range and 0.3-4 Hz. 4 separate data are available for each channel, including the channel data filtered

by the Butterworth band-pass filter in the range. Each recording takes 30 minutes. Sampled at 20 Hz with 16-bit resolution in the ±2.5 millivolt range. Due to filtering, the first and last 180 seconds of each record have been removed [17]. In this study, 0.3-4 Hz in channels. Filtered channel data is used in the range. Figure 3 shows the one minute EHG signal from three channels.
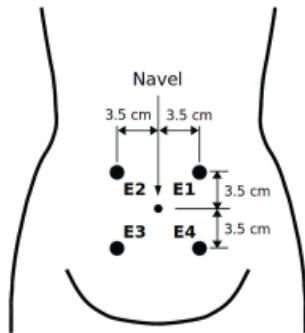
Fig.2. The placement of EHG electrodes [18]
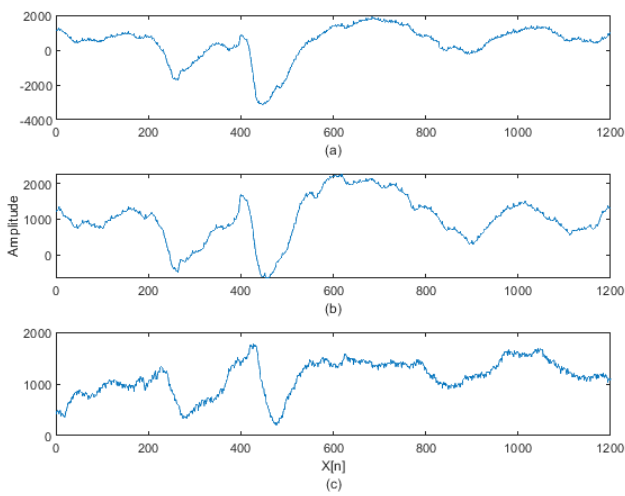
Fig.3. Example of a randomly selected one-minute full-term birth EHG signal (a) Channel 1 (b) Channel 2 (c) Channel 3
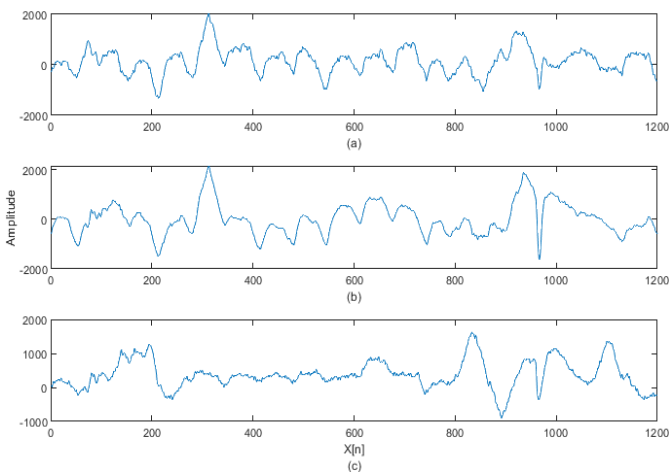
Fig.4. Randomly selected one-minute preterm birth EHG signal sample (a) Channel 1 (b) Channel 2 (c) Channel 3

Figure 4 shows 3 channel data of a randomly selected one-minute window of a person who has given birth prematurely. A randomly selected one-minute data sample from the CH1 channel is shown in the data set. Figure 5(a) shows a cross-section of the data sample that is term birth, while Figure 5(b) shows a cross-section of the data sample that is preterm.
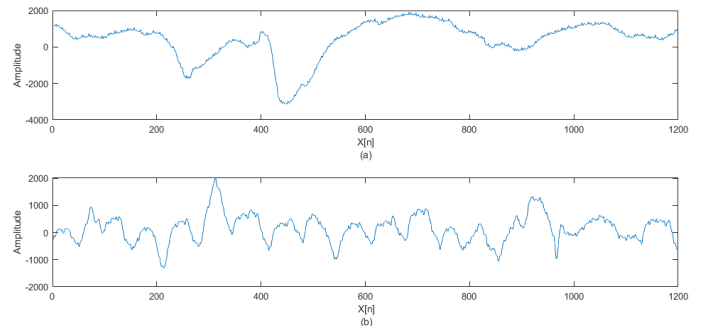
Fig.5. One-minute EHG channel data (a) term birth data (b) preterm birth data

C. Feature Extraction

The conversion of raw data into numerical features that can be processed without losing its originality is called feature extraction. It allows easier processing of data in large data sets. In this study, sample entropy and average energy values obtained from EWT and EWT modes are used as features.

2.3.1 Empirical wavelet transform

Adaptive methods used to analyze a signal are of great importance for the detection of information contained in the signal. The purpose of adaptive methods is to identify modes that represent the signal based on the information contained in the signal and to establish an appropriate basis. EWT is a proposed technique operating in the frequency space to detect different modes of the signal and generate empirical wavelets to represent the signal. Empirical wavelets mean generating a set of wavelets adapted to the processed signal. Modes are the main components of the signal that completely represent the signal. This method works in four steps. 1) Fast Fourier Transform algorithm is used to obtain the spectrum of the processed signal. 2) Calculate the local maximums of the spectrum. 3) Boundaries are detected and divided into windows. 4) Empirical wavelets are generated and the signal is decomposed into its different components [19-21]. Figure 6 shows an example of a normal birth EHG signal from a randomly selected 1-minute epoch and the EWT modes derived from this signal. Figure 7 shows the preterm EHG signal sample from an epoch and the EWT modes obtained from this signal. The feature matrix was obtained with the data obtained from these 5 modes in this study.
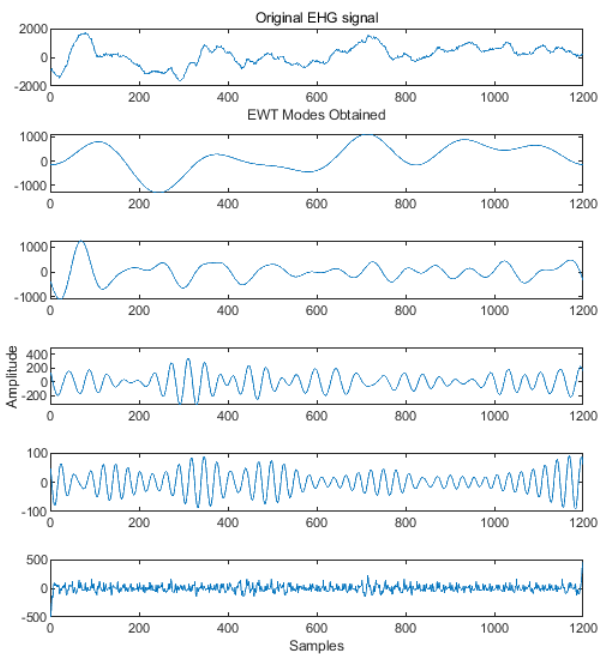
Fig.6. One-minute term EHG signal sample and EWT modes
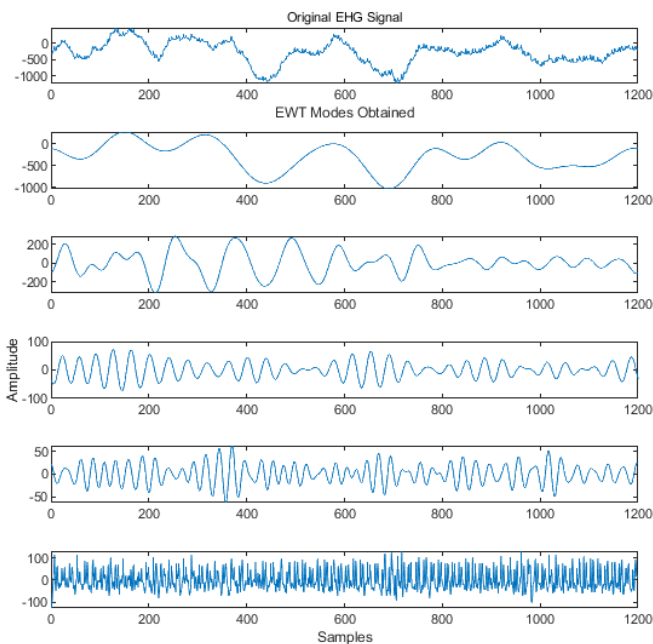
Fig.7. One minute preterm EHG signal example and EWT modes

2.3.2 Sample entropy

Sample Entropy has been proposed to measure the complexity of the array. It is basically a negative logarithm of the conditional probability of sequences of a data vector. If a vector of length N repeated for m points, it will repeat for m+1 points. Therefore, high sample entropy value means lower regularity and more complexity in the data [22, 23]. It is expressed mathematically as in Equation (1).

$$SampEn = -log\frac{A}{B} \qquad (1)$$

where B is the total number of matches of length m and A is the total number of forward matches of length m+1.

2.3.3 Average energy

Indicates the amount of power in the signal. It represents the power of ripple. It is expressed mathematically as in Equation (2) [22, 24].

$$AvEn = \frac{1}{N}\sum_{n=1}^{N}(X_n)^2 \qquad (2)$$

D. Classification

The concept of artificial intelligence, which is one of the common working areas in many different disciplines, which is frequently encountered in recent years, is called self-improving systems that try to imitate human intelligence. The main purpose of the studies is to enable machines to think like humans and to create an autonomous system that can decide on its own. The classification process, which is a part of these processes, is the process of classifying the values in a data set. This method, which aims to separate the data and assign it to the class it belongs to; It is used in many fields such as analysis of biomedical signals, computer aided diagnosis systems. There are many different classifier algorithms according to their calculation methods. When choosing algorithms, the method that will minimize the error in the classification phase is investigated and preferred [25-27]. In this study, using the feature vectors obtained as a result of the previous stages, classification process was performed with KNN, RF and LSTM algorithms, which are widely used in the literature.

2.4.1 Random forest

The RF algorithm was developed by Leo Breiman. It is an algorithm that consists of many independent decision trees and chooses the appropriate one. It is one of the preferred algorithms in many studies because it is a feasible method on classification and regression problems. It uses multiple randomly generated decision trees to classify the data. In the first step, the data that can distinguish the best among the randomly selected data is selected. The nodes are divided into branches and the tree structure is developed by randomly selected. Creates a decision tree for each instance. Estimated value results of each decision tree are obtained. It performs voting for each value formed as a result of the prediction. Finally, the result is reached by choosing the most voted value for the prediction. Two parameters must be defined by the user to start the RF algorithm [28, 29]. These parameters used to determine the best split are the maximum depth and the number of trees in the random forest [30]. In this study, the maximum depth was determined as 70 and the number of trees as 50, and the classification process was carried out with the help of the RF algorithm.

2.4.2 K-nearest neighbors

The KNN algorithm is based on separation from each other by calculating the distance between the data using distance functions. It determines the classification according to the majority of neighboring data. Each data point is associated with labels in its nearest neighbors. Therefore, this algorithm works

on the assumption that similar data are close to each other. The KNN algorithm has two user-specified parameters that affect the classification results. One of them is the number of K neighbors and the other is the distance function. Two parameters are determined by the user [31, 32]. In this study, K=3 neighborhood and Euclidean distance function are based. The Euclidean Distance calculation used to calculate the given distance between two data is given in Equation (3) [33].

$$Distance = \sqrt{\sum_{i=1}^{n}(p_i - q_i)^2} \qquad (3)$$

Here $p_i - q_i$ represent two data..

2.4.3 Long short-term memory

The long-short-term memory model is known as a recurrent RNN neural network. The problems experienced in the training of traditional RNN neural networks have been completely eliminated in LSTM. LSTM architecture basically consists of input, output, forget gates and memory cells. The cell remembers values at random intervals. All three doors regulate the entry and exit of information entering the cell. It is frequently used in time series signals such as biomedical signals because it can learn long-term dependencies. Because of its ability to learn long-term correlations in the series, LSTM networks have the ability to accurately model complex multivariate sequences. [34, 35]. The topology of the designed LSTM consists of an input layer, an LSTM layer, a dropout layer, and an output layer, as shown in Figure 8. There are 4 layers in the designed architecture. The developed model has an LSTM network layer with tanh activation and dropout to prevent over-learning. The model was implemented in Matlab environment. The number of cells in the LSTM layer was determined as nine, the learning coefficient (β) was chosen as 0.001 and Adam optimization was used in the model.
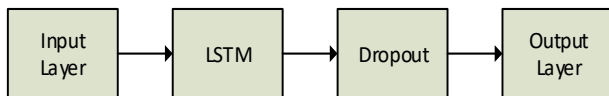
Fig.8. The LSTM neural network model used in the study

2.5 Evaluation Metrics

Confusion matrix is generally used to evaluate the performance of classification algorithms used in machine learning and similar fields. The confusion matrix is also called the classification accuracy table. The data in this table are obtained by comparing the classified value with the reference values [36]. Many metrics can be calculated from this matrix to evaluate the performance of the classifier models. In this study, Precision (Pre), Recall (Re) and Accuracy (Acc) metrics were calculated to evaluate the performance of the classifiers. These metrics are calculated as shown in Equations (4), (5) and (6) [37].

$$Pre = \frac{TP}{TP+FP} x100 \qquad (4)$$

$$Re = \frac{TP}{TP+FN} x100 \qquad (5)$$

$$Acc = \frac{TP+TN}{TP+TN+FP+FN} x100 \qquad (6)$$

where TP and FN represent the number of correctly and incorrectly classified cases, and TN and FP represent the number of correctly and incorrectly classified cases. The Precision metric shows how many of the values classified as positive are actually positive. Recall is a metric that shows how much of the values that should be classified as positive are classified as positive. To validate the performance of the classifiers, 80% of randomly selected data from the entire dataset was used for training and the remainder was used for testing.

III. RESULTS

Premature birth is one of the health problems that negatively affect human life. The mother at risk of preterm birth should stay in the hospital after the birth and the treatment should be applied carefully to both the baby and the mother. In addition, preterm babies may have more health problems in their later years than babies born at normal time. Since human life is at stake, being able to predict this problem will be a solution to many permanent or non-permanent problems in the future or immediately after birth [38, 39]. The first step in the study is to classify preterm and full-term birth signals from EHG signals recorded in the physionet database with machine learning techniques. For this, the data is divided into one-minute windows and a label is assigned for each window. Using EWT, each window data was analyzed in five modes and features were extracted from each of the discretized EHG modes. Obtained features were given as input to three different classifier algorithms and the results were evaluated. The other step in the study is to classify the data recorded before and after the twenty-sixth week from the EHG signals recorded in the same database as preterm or term birth among themselves. For this, the data is divided into windows as in the first step and labels are assigned to each window. Using EWT, each window data was analyzed in five modes and features were extracted from each of the discretized EHG modes. The obtained features were given as input to the classifier algorithms and the results were evaluated. Except for the LSTM algorithm, the classification success of other algorithms was found to be higher in CH3 data. As a result of the classification made with CH3 data, the success rate of the RF algorithm was 98.19%. This rate was followed by the classification result made with the KNN-3 algorithm. The lowest classification success rate was obtained as 87.83% as a result of the classification made with the LSTM algorithm.

The time for classifier algorithms to classify test data is determined as 0.28 seconds for the RF algorithm, this time for LSTM. 2.02 seconds was determined as 1.34 seconds for the KNN algorithm. The hardware features of the computer on which the study is performed are "Intel(R) Core(TM) i3-6006U CPU @ 2.00GHz" and 4 GB Ram. The RF algorithm performed very fast compared to both KNN algorithm and LSTM, which is a deep learning architecture. Table 2 shows the success rates obtained as a result of the classification of the EHG signals obtained before the 26th week and labeled as preterm or term delivery. Similar to the results in Table 1, a high success rate

was achieved by using the RF algorithm with the data received from the CH3 channels. This rate was followed by LSTM and KNN-3 algorithm results, respectively. When Table 2 is examined in terms of the classification times of the test data, the RF algorithm was found to be the fastest algorithm with 0.06 seconds.

TABLE 1
CLASSIFIER PERFORMANCE RESULTS OF DIFFERENT CHANNEL CONFIGURATIONS CREATED FOR PRE-TERM AND TERM CLASSIFICATION

Classifier	Channel name	Precision (%)	Recall (%)	Acc. (%)	Elapsed time for test data (second)
KNN-3	CH1	79.70	84.50	84.51	1.2
	CH2	81.10	84.90	84.90	1.2
	CH3	95.10	95.20	95.15	1.34
LSTM	CH1	76.10	87.10	87.05	1.18
	CH2	87.10	87.80	87.83	1.62
	CH3	87.10	87.80	87.83	2.02
RF	CH1	81.70	87.70	87.61	0.17
	CH2	90.10	90.40	90.42	0.13
	CH3	98.20	98.20	98.19	0.28

TABLE 2
PERFORMANCE METRICS AND DURATIONS OBTAINED AS A RESULT OF THE CLASSIFICATION OF SIGNALS TAKEN BEFORE THE TWENTY-SIXTH WEEK OF PREGNANCY AND LABELED AS PRETERM/TERM BIRTH

Classifier	Channel name	Precision (%)	Recall (%)	Acc. (%)	Elapsed time for test data (second)
KNN-3	CH1	79.60	84.70	84.65	0.44
	CH2	80.60	84.80	84.75	0.36
	CH3	82.60	86.20	86.22	0.88
LSTM	CH1	76.10	87.01	87.05	1.2
	CH2	86.70	87.30	87.26	1.3
	CH3	76.10	87.01	87.05	1.2
RF	CH1	89.20	87.70	87.68	0.06
	CH2	77.70	86.60	86.63	0.06
	CH3	89.20	89.00	89.03	0.06

Table 3 shows the success rates obtained as a result of the classification of signals obtained after the twenty-sixth week and labeled as preterm or term birth. Similar to the results in Tables 1 and 2, the highest success rate was achieved with the RF algorithm. Considering the classification times of the test data, the times close to the times in Table 2 were obtained, as expected.

TABLE 3
PERFORMANCE METRICS AND DURATIONS OBTAINED AS A RESULT OF THE CLASSIFICATION OF SIGNALS OBTAINED AFTER THE TWENTY-SIXTH WEEK OF PREGNANCY AND LABELED AS PRETERM/TERM BIRTH

Classifier	Channel name	Precision (%)	Recall (%)	Acc. (%)	Elapsed time for test data (second)
LSTM	CH1	74.9	86.40	85.82	1.08
	CH2	74.9	86.40	85.65	1.36
	CH3	86.70	87.60	87.63	0.05
RF	CH1	82.80	86.70	86.65	0.06
	CH2	83.60	86.90	86.90	0.06
	CH3	74.9	86.40	86.41	1.33
KNN-3	CH1	77.80	82.60	82.61	0.27
	CH2	82.70	84.80	84.82	0.27
	CH3	81.70	85.10	85.06	0.5

When the results obtained are examined in terms of success rates and processing load, it has been observed that the LSTM model, which is a deep learning architecture, has quite a long time to classify test data compared to RF and KNN models. The RF algorithm, known as fast, performed better than other algorithms in terms of processing load in the classification of EHG datasets. As expected, LSTM algorithm did not perform better than other algorithms in terms of processing load compared to RF and KNN algorithms. RF outperformed other algorithms in terms of both success rate and processing load.

The success of the classifier algorithms is directly related to the obtained features. Therefore, the EWT method used on EHG signals and the obtained features contribute to the success rates. The efficiency of both the classifier algorithms and the EWT method has been demonstrated by the classification study performed separately for each channel. EWT has been evaluated in signal processing methods in many different areas, but its effectiveness on EHG signals has not been evaluated in any study. Compared to the new methods, it is shown that the features used and the created model distinguish term and preterm data well. Thanks to signal analysis and machine learning algorithms on EHG signals, this and similar studies are promising in terms of preterm birth diagnosis with 100% classification accuracy.

IV. DISCUSSION

In this study, an algorithm that can classify from a single channel using EHG signals to recognize preterm birth is presented. The classification of preterm and term delivery was considered important rather than early or late recording of EHG records. The study is based on the EWT-based feature extraction approach. High accuracy rates have been achieved with the RF classifier, which is a successful model with less processing load, by calculating the processing load. Results from other studies using the TPEHGDB database are compared with this study in Table 4.

TABLE 4
COMPARISON OF STUDIES CONDUCTED WITH THE SAME DATA SET

Author	Database	Channel name	Best classifier	Train/Test Method	Acc.	Term /Preterm

Study	Dataset	Filter	Method	Validation	Performance	Data
Fergus et al. [8_9]	TPEHGDB	0.34–1 Hz. filter on Channel 3	LMNC, RBNC, RNNC combined	80% train, 20% test	90%	262/38
Huseyin et al. [12_13]	TPEHGDB	0.3–3 Hz. filter on Channel 3	DSIA	60% train, 25% validation, 15% test	90%	262/38
Vinothini et al. [9_10]	TPEHGDB	0.3–3 Hz. filter on Channel 3	RF	5-fold cross validation	98.6%	143/19
Far et al. [10_11]	TPEHGDB	0.08- 4 Hz. filter on Channel 1	SVM	10-fold cross validation	99.7%	262/38
Lou et al. [11_12]	TPEHGDB and ICLEHG	0.3–4 Hz. filter on Channel 3	GNB	80% train, 20% test	75%	262/38
This	TPEHGDB	0.3–4 Hz. filter on Channel 3	RF	80% train, 20% test / 10-fold cross validation	98.19% / 98.10%	262/38

When the studies in Table 4 are examined, it can be seen that the highest classifier performance was obtained in the study conducted by Far SM et al. [11]. I believe that the preferred channel data, filter range and classifier algorithm have an impact on achieving this success rate. I believe that the small number of data in the data set used in the study conducted by Vinothini S et al. [10] affects the performance. In the study conducted by Vinothini S et al. [10], the RF algorithm gave successful results, similar to the manuscript. Higher performance was achieved in this manuscript compared to other studies in Table 4. Unlike the studies in the literature, a different feature extraction method was applied to EHG data by using the EWT approach. However, the results obtained show that the applied method and technique are successful. In addition, it has been revealed that the performances of classifier algorithms can be analyzed one by one in terms of processing load and can be integrated into embedded systems. Many of the studies in the literature are analyzed in terms of method technique, but not in terms of processing load. In this respect, I believe that it has made a significant contribution to the literature. I could not find any study in the literature that used EHG data sets and was based on the EWT approach. Therefore, the evaluation of the effectiveness of the EWT approach on EHG data has been introduced to the literature with this manuscript.

V. Conclusion

In recent years, the development of artificial intelligence techniques has played an important role in the biomedical field. Thanks to this situation, it has become easier and faster to remove biological patterns in biomedical signals. In addition, feature extraction from data, evaluation of various methods and techniques on biomedical signals are widely used for solving problems. This article presents an EWT-based algorithm for accurate classification of term and preterm births using a single EHG channel. At the same time, EHG records before and after the twenty-sixth week were scored separately and the results were evaluated. Different classifiers were used based on the EWT approach to classify term and preterm records. The results show that the optimal classifier is RF with 98.20% precision, 98.20% recall and 98.19% accuracy, both in terms of performance and overhead. These results are encouraging for machine learning and show that the proposed approach is worth pursuing. The adequacy of the extracted features and the method according to the classification results made with the data obtained from different channels has been verified.

The limitation of the study is the small number of preterm samples. To eliminate this situation, synthetic data can be used or real hospital data can be added to the study. Adding synthetic data can reveal an over-learning situation in terms of machine learning. Therefore, it may be a more accurate way to balance the data set by adding hospital records obtained from pregnant women who gave birth prematurely to the data set. In future studies, more extensive research is planned to reach an error-free model (100% accuracy) with different machine learning algorithms and techniques.

References

[1] P. Gondane, S. Kumbhakarn, P. Maity, K. Kapat. "Recent Advances and Challenges in the Early Diagnosis and Treatment of Preterm Labor." Bioengineering, 2024. https://doi.org/10.3390/bioengineering11020161.

[2] M. Delnord, J. Zeitlin. "Epidemiology of late preterm and early term births – An international perspective." Seminars in Fetal and Neonatal Medicine, 2019. https://doi.org/10.1016/j.siny.2018.09.001.

[3] J. Xu, Z. Chen, J. Zhang, Y. Lu, X. Yang, A. Pumir. "Realistic preterm prediction based on optimized synthetic sampling of EHG signal." Computers in Biology and Medicine, 2021. https://doi.org/10.1016/j.compbiomed.2021.104644.

[4] J. Peng, D. Hao, L. Yang, M. Du, X. Song, H. Jiang, Y. Zhang, D. Zheng. "Evaluation of electrohysterogram measured from different gestational weeks for recognizing preterm delivery: a preliminary study using random forest." Biocybernetics and Biomedical Engineering, 2019. https://doi.org/10.1016/j.bbe.2019.12.003.

[5] C. Gao, S. Osmundson, D.R.V. Edwards, G.P. Jackson, B.A. Malin, Y. Chen. "Deep learning predicts extreme preterm birth from electronic health records." Journal of Biomedical Informatics, 2019. https://doi.org/10.1016/j.jbi.2019.103334.

[6] H.H. Chang, J. Larson, et al. "Preventing preterm births: analysis of trends and potential reductions with interventions in 39 countries with very high human development index." The Lancet, 2013. https://doi.org/10.1016/S0140-6736(12)61856-X.

[7] J.A. Mccoshen, P.A. Fernandes, M.L. Boroditsky, J.G. Allardice. "Determinants of reproductive mortality and preterm childbirth. In: Bittar EE, Zakar T (ed) Advances in Organ Biology." Elsevier, 1996, pp 195-223.

[8] M. Shahrdad, M.C. Amirani. "Detection of preterm labor by partitioning and clustering the EHG signal." Biomedical Signal Processing and Control, 2018. https://doi.org/10.1016/j.bspc.2018.05.044.

[9] P. Fergus, I. Idowu , A. Hussain, C. Dobbins. "Advanced artificial neural network classification for detecting preterm births using EHG records." Neurocomputing, 2015. https://doi.org/10.1016/j.neucom.2015.01.107.

[10] S. Vinothini, N. Punitha, P.A. Karthick, S. Ramakrishnan. "Automated detection of preterm condition using uterine electromyography based topological features." Biocybernetics and Biomedical Engineering, 2021. https://doi.org/10.1016/j.bbe.2021.01.004.

[11] S.M. Far, M. Beiramvand, M. Shahbakhti, P. Augustyniak. "Prediction of preterm delivery from unbalanced EHG database." Sensors, 2022. https://doi.org/10.3390/s22041507.

[12] H. Lou, H. Liu, Z. Chen, Z. Zhen, B. Dong, J. Xu. "Bio-process inspired characterization of pregnancy evolution using entropy and its application in preterm birth detection." Biomedical Signal Processing and Control, 2022. https://doi.org/10.1016/j.bspc.2022.103587

[13] A.J. Hussain, P. Fergus, H. Al-Askar, D. Al-Jumeily, F. Jager. "Dynamic neural network architecture inspired by the immune algorithm to predict preterm deliveries in pregnant women." Neurocomputing, 2015. https://doi.org/10.1016/j.neucom.2014.03.087

[14] J. Xu, Z. Chen, H. Lou, G. Shen, A. Pumir. "Review on EHG signal analysis and its application in preterm diagnosis." Biomedical Signal Processing and Control, 2022. https://doi.org/10.1016/j.bspc.2021.103231

[15] E. Nsugbe, "Novel uterine contraction signals decomposition for enhanced preterm and birth imminency prediction." Intelligent Systems with Applications, 2022. https://doi.org/10.1016/j.iswa.2022.200123

[16] K. B. E. Dine, N. Nader, M. Khalil, C. Marque. "Uterine synchronization analysis during pregnancy and labor using graph theory, classification based on neural network and deep learning." IRBM, 2022. https://doi.org/10.1016/j.irbm.2021.09.002

[17] PhysioNet, The term–preterm EHG database (TPEHG-DB), (physionet.org), 2012.

[18] F. Jager, S. Libensek, K. Gersak. The term-preterm EHG dataset with tocogram (TPEHGTDS)[data set], 2018.

[19] R. Kumar, I. Saini. "Empirical wavelet transform based ECG signal compression." IETE Journal of Research, 2014. https://doi.org/10.1080/03772063.2014.963173.

[20] C. K. Jha, M. H. Kolekar. "Empirical mode decomposition and wavelet transform based ECG data compression scheme." IRBM, 2021. https://doi.org/10.1016/j.irbm.2020.05.008.

[21] A. Anuragi, D. S. Sisodia. "Empirical wavelet transform based automated alcoholism detecting using EEG signal features." Biomedical Signal Processing and Control, 2020. https://doi.org/10.1016/j.bspc.2019.101777.

[22] M. Almeida, H. Mourino H, A. G. Batista, S. Russo, F. Esgalhado, C. R. P. Reis, F. Serrano, M. Ortigueira. "Electrohysterography extracted features dependency on anthropometric and pregnancy factors." Biomedical Signal Processing and Control, 2022. https://doi.org/10.1016/j.bspc.2022.103556.

[23] Y. H. Wang, I. Y. Chen, H. Chiueh, S. F. Liang, "A low-cost implementation of sample entropy in wearable embedded systems: an example of online analysis for sleep EEG." in IEEE Transactions on Instrumentation and Measurement, 2021. https://doi.org/10.1109/TIM.2020.3047488.

[24] D. C. Dickin, R. K. Surowiec, H. Wang. "Energy expenditure and muscular activation patterns through active sitting on compliant surfaces." Journal of Sport and Health Science, 2017. https://doi.org/10.1016/j.jshs.2015.10.004.

[25] E. Tuncer, E. D. Bolat, "Classification of epileptic seizures from electroencephalogram (EEG) data using bidirectional short-term memory (Bi-LSTM) network architecture." Biomedical Signal Processing and Control, 2022. https://doi.org/10.1016/j.bspc.2021.103462.

[26] Y. Mohia, F. Ouallouch, M. Lazri et al. "Classification of precipitation ıntensities from remote sensing data based on artificial ıntelligence using RF multi-learning." J. Indian Soc. Remote Sens., 2023. https://doi.org/10.1007/s12524-023-01665-5.

[27] E. Celik, T. Dal, T. Aydın. "Comparison of data mining classification algorithms for sentiment analysis." European Journal of Science and Technology Vol.27, 880-889, 2021.

[28] V. Srivardhan. "Adaptive boosting of random forest algorithm for automatic petrophysical interpretation of well logs." Acta Geodaetica et Geophysica, 2022. https://doi.org/10.1007/s40328-022-00385-5.

[29] D. R. Edla, K. Mangalorekar, G. Dhavalikar, S. Dodia. "Classification of EEG data for human mental state analysis using random forest classifier." Procedia Computer Science, 2018. https://doi.org/10.1016/j.procs.2018.05.116.

[30] E. Tuncer, E. D. Bolat, "Channel based epilepsy seizure type detection from electroencephalography (EEG) signals with machine learning techniques." Biocybernetics and Biomedical Engineering, 2022. https://doi.org/10.1016/j.bbe.2022.04.004.

[31] K. M. Sunnetci, A. Alkan. "KNN and decision trees based SPPM demodulators applicable to synchronous modulation techniques." Journal of the Faculty of Engineering and Architecture of Gazi University, 2022. https://doi.org/10.17341/gazimmfd.890721.

[32] J. Hu, H. Peng, J. Wang, W. Yu. "kNN-P: A kNN classifier optimized by P systems." Theoretical Computer Science, 2020. https://doi.org/10.1016/j.tcs.2020.01.001.

[33] O. F. Ertugrul, M. E. Tagluk. "A novel version of k nearest neighbor: Dependent nearest neighbor." Applied Soft Computing, 2017. https://doi.org/10.1016/j.asoc.2017.02.020.

[34] S. Tanisman, A. A. Karcioglu, A. Ugur, H. Bulut. "Forecasting of bitcoin price using LSTM neural network and ARIMA time series models and comparision of methods." European Journal of Science and Technology, 32:514-520, 2021.

[35] K. M. Chinea, J. Ortega, J. F. Gomez-Gonzalez et al. "Effect of time windows in LSTM networks for EEG-based BCIs." Cogn Neurodyn, 2022. https://doi.org/10.1007/s11571-022-09832-z.

[36] S. Ruuska, W. Hamalainen, S. Kajava, M. Mughal, P. Matilainen, J. Mononen. "Evaluation of the confusion matrix method in the validation of an automated system for measuring feeding behaviour of cattle." Behavioural Processes, 2018. https://doi.org/10.1016/j.beproc.2018.01.004.

[37] J. Yoo, I. Yoo, I. Youn, et al. "Residual one-dimensional convolutional neural network for neuromuscular disorder classification from needle electromyography signals with explainability." Computer Methods and Programs in Biomedicine, 2022. https://doi.org/10.1016/j.cmpb.2022.107079.

[38] Z. Peng et al. "A continuous late-onset sepsis prediction algorithm for preterm ınfants using multi-channel physiological signals from a patient monitor." in IEEE Journal of Biomedical and Health Informatics, 2023. https://doi.org/10.1109/JBHI.2022.3216055.

[39] X. Song, X. Qiao, D. Hao, L. Yang, X. Zhou, Y. Xu, D. Zheng. "Automatic recognition of uterine contractions with electrohysterogram signals based on the zero-crossing rate." Sci Rep., 2021. https://doi.org/10.1038/s41598-021-81492-1.

BIOGRAPHIES

Erdem TUNCER received M.Sc. degrees in Electronics & Computer Education from Kocaeli University, Turkey, in 2015. He received Ph.D. degree in Biomedical Engineering from Kocaeli University, Turkey in 2022. He is currently working as an electronics teacher at the Ministry of National Education. His active research interests are signal processing, artificial intelligence, machine learning.

Research Article

Design and Analysis of MEMS-Based Capacitive Power Inverter Using Electrostatic Transduction

Salih Rahmi Turan, Osman Ulkir and Melih Kuncan

Abstract—In this study, a capacitive microelectromechanical system (MEMS) based DC/AC power inverter design for renewable energy applications is proposed, and analyzed. In the proposed approach, electrostatic actuation is preferred to develop a DC/AC power inverter with varying phase overlap lengths for solar energy systems. The developed inverter is based on MEMS to achieve miniaturized performance, producing smooth sine wave output, efficiently obtaining the signal frequency, and low power consumption. The proposed inverter has a thickness of 325 µm, an active settlement area of 45x45x0.585 mm^3, and an initial capacitance value of 2.9 pF. In addition, a 50-Hz mechanical resonance frequency was used to be compatible with the frequency of the city network. It can convert voltage values between 0.5 V and 24 V DC with a MEMS power inverter. Because the inverter is based on a capacitive structure, it provides near-zero power consumption. The frequency and waveform of the converted DC/AC signal match the AC signal of a power grid with an efficiency of 5%.

Index Terms—Electrostatic actuation, MEMS, miniaturization, power inverter, renewable energy.

I. INTRODUCTION

THE DEMAND in the renewable energy market is increasing every year. Solar energy systems are one of the most promising renewable energy generation technologies. The primary purpose of these systems is to reduce costs and increase efficiency [1]. Power inverters are one of the essential considerations in most alternative energy systems for converting DC energy from photovoltaic generators to AC energy. Today, various studies are being conducted to increase the efficiency of these high-order power inverters [2-4]

Salih Rahmi Turan, is with Institute of Science, Siirt University, Siirt, Turkey(e-mail: srahmituran@hotmail.com).

https://orcid.org/0000-0001-5826-0786

Osman Ulkir, is with Department of Electric and Energy, Mus Alparslan University, Mus, Turkey(e-mail: o.ulkir@alparslan.edu.tr).

https://orcid.org/0000-0002-1095-0160

Melih Kuncan, is with Department of Electric and Electronics Engineering, Siirt University, Siirt, Turkey(e-mail: melihkuncan@siirt.edu.tr).

https://orcid.org/0000-0002-9749-0418

Commercial transducer systems consist of power electronic switches made of semiconductors such as silicon carbide (SiC) or gallium nitride (GaN) [5, 6]. However, these systems have disadvantages such as on-state loss, switching loss of power devices, complex control system configurations, low efficiency, and high costs. All of these disadvantages are partially eliminated by PWM inverters [7]. Particularly popular in medium and high power applications, the multilevel inverter has many switches to control. This number of switches increases the probability of failure of the power electronics driving circuit. A multilevel inverter generates a sine wave associated with harmonics that depend on the switching frequency in power electronics [8-10]. These harmonics cause high leakage current and high-frequency noise, affecting the PV power system performance and causing easy failure of the PV power system [11, 12]. Today, the improvement of inverter systems is to develop DC/AC inverter performance, increase the temperature to improve reliability, increase the operating voltage to adapt to high-voltage PV systems, improve frequency regulation, and reduce cost [13-15].

Recent studies have offered approaches to overcome the harmonic problem and other shortcomings of the power inverters [16-18]. These approaches faced issues such as cumbersome and expensive, a large number of auxiliary switches increasing system complexity, high voltage stress of switches, large size and weight of passive components, and complex control system. In addition, the electromechanical power inverter method has been proposed as an alternative to the power electronics inverter [19, 20].

Microelectromechanical systems (MEMS) will contribute to the development of power inverters because they offer an approach to the miniature bulk device, high efficiency, and low-cost manufacturing [21, 22]. This approach is a micro processing technology used since the late 1980s. MEMS technology has many applications, such as radio frequency, accelerometer gyroscope, sensor and actuator technology, biomedical, thermodynamics, telecommunications, and so on [23-26]. Electrostatic actuation is the most important for MEMS technology, which has different actuation methods such as piezoelectric, electromagnetic, and thermal principles [27, 28]. MEMS DC/AC capacitive power inverters are comb-driven electrostatic actuators commonly used in MEMS applications, consisting of two interconnected finger structures. One comb is fixed, and the other is attached to a compatible

suspension [29, 30]. The inclusion of this structure in solar PV system will significantly improve power inverter technologies because of its miniature size, high efficiency and faster response, lower production cost, and lower power consumption [31, 32].

This paper presents a new capacitive electromechanical power inverter's modeling, design, and simulation results. This study aims to obtain information about the compatibility of MEMS inverter with the system by voltage time analysis and to convert DC voltage to AC voltage in the form of a smooth sinusoidal wave by using the solar energy system. The suggested MEMS design is based on a comb drive structure for generating two sets of the variant capacitor. One with two sets of electrodes where one is moving and the other is fixed. Because the designed MEMS system is capacitive based, there will be no need for power consumption in the conversion process. The MEMS capacitive resonator structure provides the sensitivity and mass detection of electrons, and low frequency, low power consumption, low cost, and minimum power loss are targeted. Based on the results obtained, it is predicted that it can be used in different electronic applications. Modeling and simulation studies of MEMS power inverter were made using modelling software.

II. MATERIALS AND METHODS

A. Structural Design of MEMS Power Inverter

The MEMS-based DC/AC power inverter is structurally designed with a mechanical resonator and variable capacitors. The mechanical resonator consists of a seismic mass. Electrodes surround these masses to form the moving part of the variable capacitors (Fig. 1). MEMS resonators have been used in sensor design for many years. These resonators actively perceive mass, force, and electronic transformations and adapt to the system. The variable capacitor forms the intertwined moving part with adjacent electrodes in the seismic mass. As it can be understood from here, the seismic mass will be sensitive to mechanical vibration and cause a mechanical displacement.

The design consists of fixed comb electrodes, moving comb electrodes, a proof mass suspended by double folded flexure beams, and a shuttle mass. The electrons fixed to the anchors are composed of the electrons in the moving combs and the mass suspended by the beams (Fig. 1). Here, deviations occur because it creates a capacitive effect on the moving parts. This means that as the capacitance on one side increases, the capacitance on the other will also increase. One of the two capacitors formed here acts as a driver capacitor, while the other acts as a converter. When the comb structure is examined, it should be designed so that one of the fingers on the moving part is extended while the other is short. Because it reduces deviations, it is exposed to and enables us to obtain more capacitance formation.

MEMS capacitors were mechanically examined in two groups. These are differential variable capacitors or follower variable capacitors. The design in Fig. 1 is a follower variable capacitor type MEMS device [33].
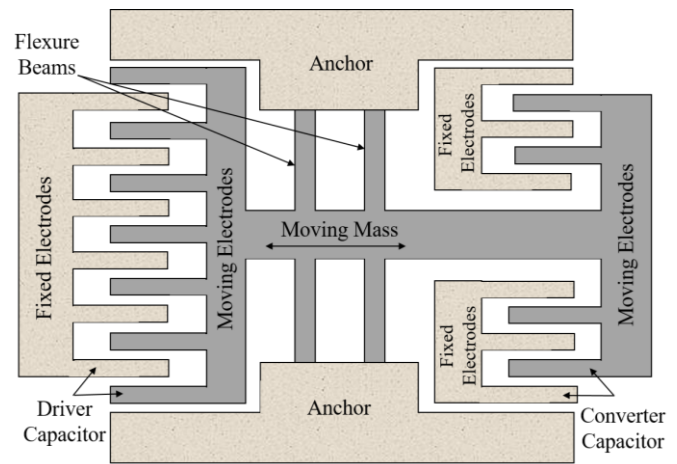
Fig.1. The design of the proposed MEMS power inverter

Differential variable capacitors have two independent stators. However, as the rotor is rotated, the capacity of one section of the differential variable capacitor increases while that of other section decreases [34]. This keeps the capacitance constant while maintaining the sum of the two stators. These capacitors can therefore be used in capacitive potentiometric circuits. In follower variable capacitors, both capacitance devices exhibit simultaneous in- phase capacitance variation.

Mechanical movement of the seismic mass in the MEMS device can be achieved in two ways. One is accomplished by creating vibration with an external force, as in accelerometers and energy storage circuits [35]. The other is applying an external AC signal as MEMS resonators [36]. In this study, the capacitive MEMS device to be operated electrostatically is powered by an electrical AC signal to implement DC/AC power conversion. Because the AC voltage used in the city network in our country is 50 Hz and 220V, the frequency is taken as 50 Hz in this study. In addition, the classical MEMS settlement area was preferred. The design specifications are demonstrated in Table I.

TABLE I
DESIGN SPECIFICATIONS OF THE MEMS INVERTER

Sl. No.	Specification	Values
1	Active settlement area	$45 \times 45 \times 0.585$ mm^3
2	Maximum mechanical deflection	15 μm
3	Driver initial capacitance	92 fF
4	Reference AC voltage	120 V
5	Load resistance	100 MΩ
6	Solar DC input	24 V
7	Frequency	50 Hz

B. Operating Principle of MEMS Power Inverter

Using the proposed MEMS technology, a capacitance-based power inverter was modeled, and simulation studies were carried out. The implementation of DC/AC conversion to the designed inverter system is given in Fig. 2a. MEMS transducers operate based on the principle of converting mechanical signals into electrical signals or vice versa on a miniature scale.
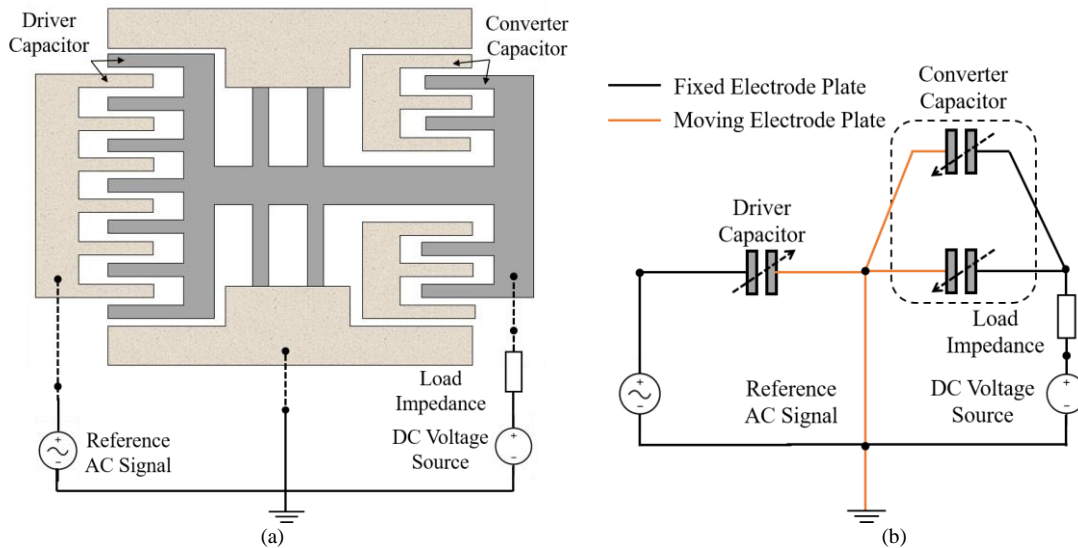
Fig.2. Capacitive MEMS power inverter (a) System implementation (b) Equivalent electrical circuit diagram

These transducers typically consist of tiny structures etched from semiconductor materials like silicon, incorporating mechanical components such as beams, diaphragms, or cantilevers, along with electrical components like capacitors or piezoelectric materials. When subjected to mechanical stimuli like pressure, acceleration, or vibration, these structures undergo minute physical deformations, resulting in changes in electrical properties, such as capacitance, resistance, or voltage.

The power inverter converts the DC signal from the solar system to power inverter converts the DC signal from the solar system to AC usable signal. It is sufficient to apply a small AC signal to the MEMS switch input for the system to work. The DC voltage generated by the solar cell is applied to the MEMS device, and a converter capacitance is generated through the driver capacitance. These data are isolated in the ground section. Changing the reference AC signal here causes the efficiency of the converted DC/AC signal and the system to change.

The equivalent electrical circuit diagram of the system is shown in Fig. 2b. Here, the reference AC signal is connected in parallel with the driver capacitor. This AC signal induces an alternating electrostatic force across the driving capacitor electrodes, causing mechanical displacement of the seismic mass. In this case, the converter leads to the same deflection of the capacitor electrodes. As a result, a change in capacitance occurs. Electrically, the capacitance change of the DC converter capacitor induces an AC electric current. This current is expressed as the converted DC/AC current flowing through the load. Thanks to the ground that provides the electrical isolation between the driver and the converter capacitors, it prevents the reverse flow of AC current, which allows us to accept the power consumption as zero theoretically.

The photovoltaic systems are off-grid and on-grid photovoltaic systems connected to the grid. In the grid-connected system, the electricity produced by the solar panels is arranged in the grid-connected inverter, and the conversion is performed to be transferred to the electricity grid. If the battery is not used in these systems, the photovoltaic system may be disabled in case of a power outage in the network. The battery support is required in grid-connected photovoltaic systems.

In systems separate from the grid, the electricity produced by the solar panels is regulated by the charge controller and stored in the batteries. The electricity stored in the batteries as DC is converted into AC electricity with the help of inverters. As can be understood from both systems, the direct current produced by the solar panels should be converted into alternating current with the help of DC/AC inverters. This study aims to obtain an efficient power inverter by integrating MEMS technology into a classical photovoltaic system. A block diagram representing a MEMS power inverter system has been incorporated into the conventional solar PV system (Fig. 3).
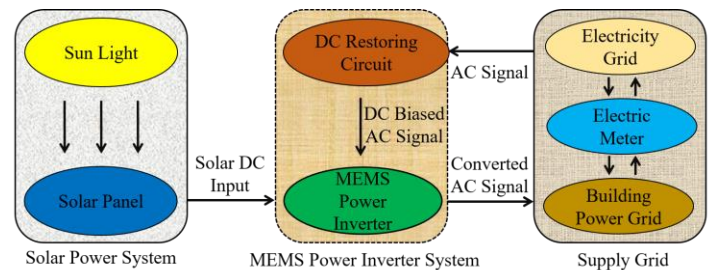
Fig.3. Solar PV system with MEMS power inverter unit

C. Mathematical Modelling of MEMS Power Inverter

The implementation of DC/AC conversion to the designed MEMS inverter system is shown in Fig. 2a. The basic modeling of the MEMS power inverter design is based on the electrical and mechanical electrostatic field approach in mechanical resonators. This approach consists mass-spring- damper system, variable capacitor, and electrical circuit. The model consists of seismic mass, mechanical springs, damping element, and mechanical stop (Fig. 4). The model variable capacitors are driver capacitor C_1, and converter capacitor C_2. The electrical circuit in the model consists of the load impedance Z_L, reference AC voltage source V_{AC}, and a solar DC input voltage source V_{DC}. The model can be mathematically symbolized by extracting the system force balance equation as follows [37]:

$$m_m \ddot{x}_m + b_m \dot{x}_m + k_m x_m = \overrightarrow{F_{ex}} + \overrightarrow{F_s} + \overrightarrow{F_{es}} \qquad (1)$$

Here m_m is the total mass amount, b_m is the viscosity damping coefficient, k_m is the mechanical spring constant, and k_s is the mechanical stop constant. The symbol F_{ex} is external mechanical stimulation caused by mechanical vibration. In this study, the external mechanical excitation force is considered to be zero. Because external vibration is neglected. The symbol F_s is the mechanical stopping force vector formed by the seismic mass. This force value is calculated as follows:

$$F_s = k_s x_s \qquad (2)$$

$$F_s = \begin{cases} 0, & -x_s \le x \le x_s \\ k_s(x + x_s), & x < -x_s \\ k_s(x - x_s), & x > x_s \end{cases} \qquad (3)$$

Here x_s denotes the displacement of the mechanical stop. The expression F_{es} in equation 1 is the total electrostatic force. This force is proportional to the square of the applied voltage. A capacitance variation is observed here because the electrostatic force will cause displacement in the overlapping length. Capacitance is inversely proportional to voltage [38]. Therefore, the proposed MEMS inverter system is a compatible design in low-power applications and is suitable for low-cost, and low-power applications. This force is usually calculated based on the capacitance variation (C) and the capacitor voltage (V). The derivative of this variation gives the resonator deviation ($\frac{dC}{dx}$).

$$F_{es} = \frac{1}{2} \cdot \frac{dC}{dx} \cdot V^2 \qquad (4)$$

The calculation of the capacitance in equation 3 depends on the geometry of the capacitor. For the variable capacitor shown in Fig. 2, the overlap area between the electrodes is the variable parameter. In line with these parameters, the capacitance is calculated as follows:

$$C = \frac{2\varepsilon_0 \varepsilon_r N_e (L_0 + \bar{x}) + t_e}{g} = C_0 \left(1 + \frac{\bar{x}}{L_0}\right) \qquad (5)$$

In this equation, ε_0 is the permeability of the vacuum, ε_r is the middle dielectric constant, N_e is the number of electrons in the moving capacitor, L_0 is the first overlapping length of the electrode, t_e is the thickness of the electrode, g is the gap between the moving and fixed electrodes.
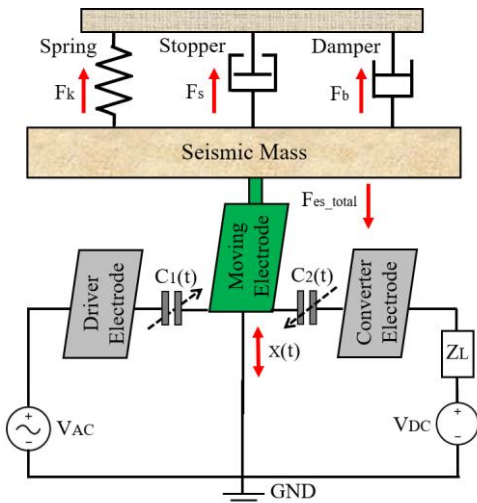
Fig.4. Electromechanical model of proposed MEMS power inverter

Capacitors work with DC voltage using charging and discharging methods. When it is full, it will work like an open circuit, so the current will be zero. When AC voltage is applied, it behaves like a resistor and changes depending on the frequency and capacitance of the capacitor. The symbol $\bar{x}$ in equation 5 represents the deviation vector. This value can have a positive or negative sign depending on the displacement direction of the electrons. Accordingly, the resonator deflection of the capacitor changes as follows:

$$\frac{dC}{dx} = \begin{cases} \frac{c_0}{L_0}; \bar{x} = x \\ \frac{c_0}{L_0}; \bar{x} = -x \end{cases} \qquad (6)$$

For the proposed MEMS power inverter, using the formula in equation 4, the total electrostatic force is calculated as follows. This force depends on the derivatives of the driver and converter capacitors and the square of their voltage.

$$F_{es\_total} = \frac{1}{2}\left(\frac{dC_1}{dx}V_{C_1}^2 \mp \frac{dC_2}{dx}V_{C_2}^2\right) \qquad (7)$$

The voltages of the variable capacitors in the MEMS inverter are affected by the response of the electrical circuit. As can be seen from the simplified electromechanical model in Fig. 4, due to the parallel connection of the driver capacitor and the AC reference voltage, the voltage on the driver capacitor V_{C_1} is equal to the reference AC voltage V_{AC}. Calculating the voltage across the converter capacitor V_{C_2} is obtained by applying Kirchhoff's voltage law in the loop of the elements connected in series. According to this law, the algebraic sum of the potential differences in any loop must equal zero. Here, the DC voltage source is V_{DC}, load impedance Z_{LC} and converter capacitor C_2 are connected in series (Fig. 4). As a result, equation 8 is calculated as follows:

$$V_{C_2} = V_{DC} - i(t)Z_L \qquad (8)$$

The converter voltage in equation 8 is directly proportional to the electric current induced in the circuit. In addition, the converter voltage V_{C_2}, the electrical charge stored in the converter capacitor can calculated in terms of Q_{C_2} and C_2 capacitance as follows:

$$V_{C_2} = \frac{Q_{C_2}}{C_2} \qquad (9)$$

D. Matlab/Simulink Model Implementation

The mathematical model of the proposed MEMS power inverter in Section C is implemented and solved using Matlab/Simulink software. The developed Simulink model consists of four separate parts. The first of these is the MEMS resonator, which represents the mass-damper-spring model used in normal MEMS systems. The mechanical actuation of the MEMS resonator only changes owing to the change in the electrostatic force of the system. The velocity and displacement values are examined according to the acceleration of the resonator. Here, the limit deviation function determines whether the resonator has undergone displacement or not. The second part is the variable capacitor part, where the circuit is completed by calculating the feedback of the circuit and the electrostatic force, which is the input terminal. The third part is the inverter circuit used to calculate the driver and converter capacitors of each circuit element according to the capacitance.
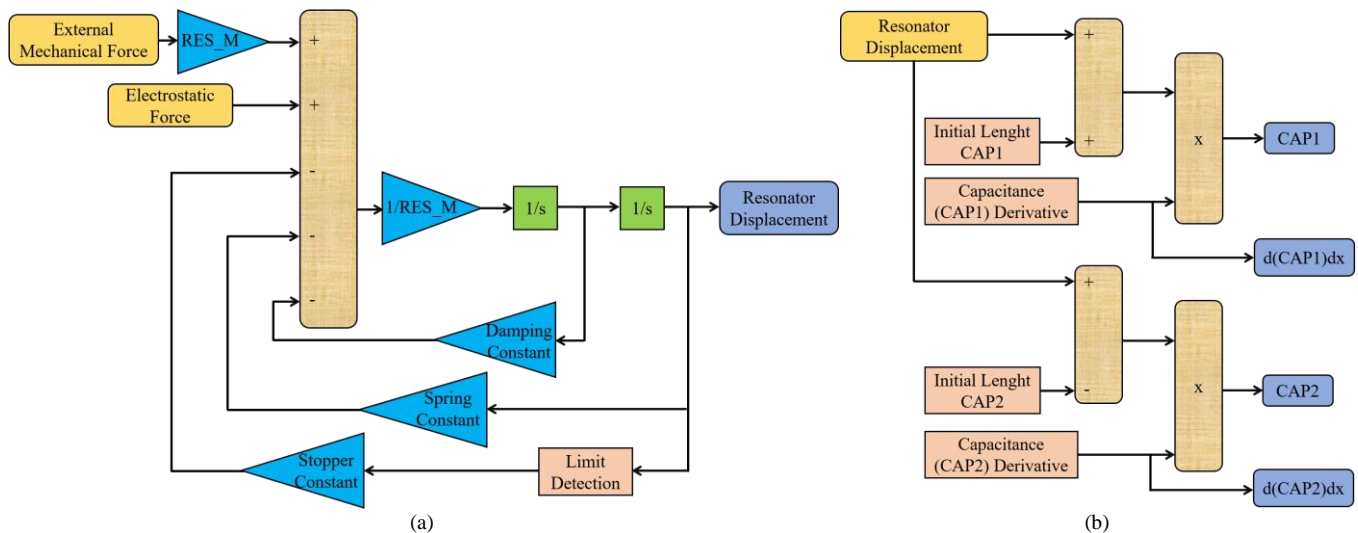
Fig.5. Simulink model of the mechanical resonator and variable capacitor (a) Mechanical resonator (b) Variable capacitor

The fourth part is the electrostatic force that occurs in the system when the MEMS resonator starts to work. The displacement of the MEMS resonator is used to extract the instantaneous values of the driver and converter capacitors at the input terminal.

The model of the MEMS resonator and the variable capacitor created in Simulink is given in Fig. 5. equations (1), (2), and (3) in Section mathematical modelling of MEMS power inverter calculate the velocity and displacement of the mass-spring-damper resonator according to its acceleration. The output of the block is zero when it does not reach the bias limit. When it reaches the deflection limit, it equals the collision force. There are two inputs in the block diagram, mechanical excitation, and electrostatic force. The mechanical excitation input expresses the vibration from the environment and is entered as zero in this simulation study. The other input is the electrostatic force obtained from the electromechanical model of the MEMS system. Another unit in Fig. 5 is the MEMS capacitor. In equations (5) and (6), the values of the converted capacitors that occur with the effect of the displacement of the MEMS capacitor are obtained. The input terminal of this unit is the displacement of the MEMS resonator. In addition, capacitance

derivatives are calculated according to the deviation required to calculate the electrostatic force of the system in equation (7).

The Simulink model of electric DC/AC inverter circuit and electrostatic force is given in Fig. 6. The electrical charge stored in the capacitor is calculated such that the voltage converted by equations (8) and (9) is proportional to the induced current. Thus, the voltage and current of each element in the circuit, driver capacitor, converter capacitor, and load resistance, are calculated. In this unit, AC reference voltage, solar cell voltage, driver, and converter capacitor values are applied as inputs. The other unit in Fig. 6 is the section where the electrostatic force is created. The power inverter system uses equation (7) to calculate the force. This force can be obtained.

The flow diagram of the MEMS power inverter modeled in Simulink in Section D is given below (Fig. 7). This diagram consists of the electrical actuation signal, electrostatic force, variable capacitor, MEMS resonator, power inverter circuit, solar cell system, and solar energy. In the initial position, the mechanical resonator is in equilibrium. This indicates that there is no displacement. A reference AC voltage is first applied to the power inverter system. The AC voltage is transferred to the section where the electrostatic force occurs.
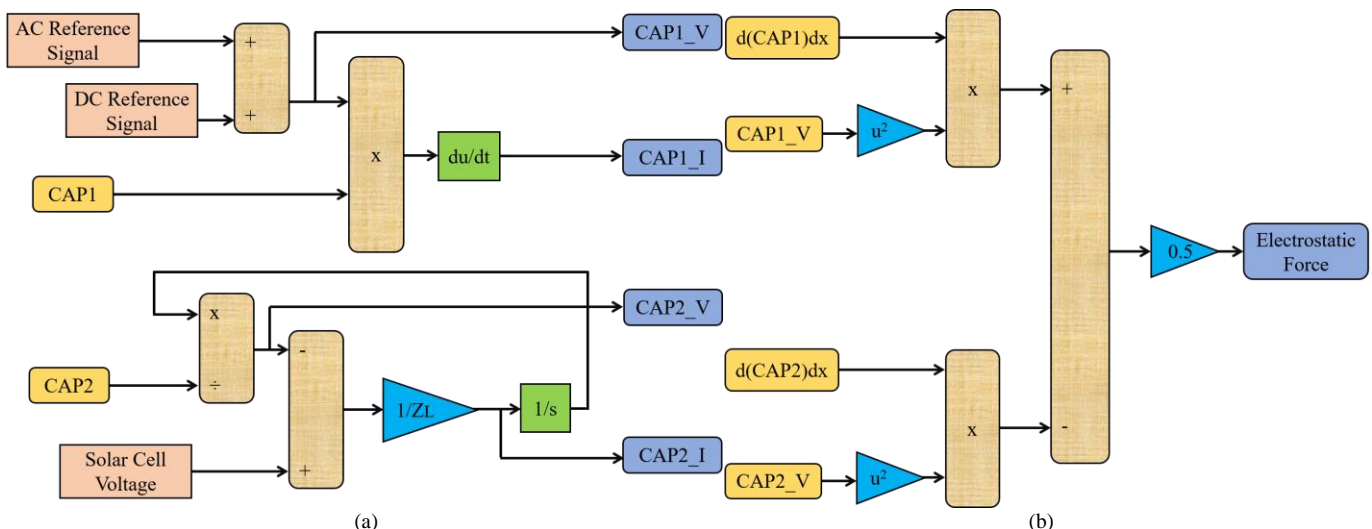
Fig.6. Simulink model of power inverter circuit and electrostatic force (a) Power inverter circuit (b) Electrostatic force
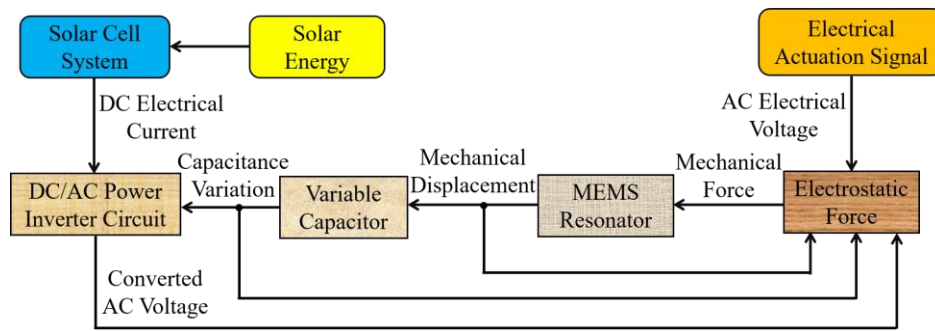
Fig.7. Signal flow schema of the Matlab/Simulink model

This section describes the unit that receives the mechanical feedback components from the MEMS resonator and the MEMS capacitor, the electrical feedback components from the electrical start signal, and the converted AC voltage from the electrical DC/AC inverter circuit. As the output of this unit, a mechanical vibration force is transferred to the MEMS resonator.

The output of the resonator block is the mechanical displacement signal transferred to the variable capacitor section for the calculation of new capacitor values. The result obtained by calculating the new values in the capacitor section is transferred to the DC/AC inverter circuit with the instantaneous capacitance value of the DC current coming from the solar cell system. As a result, the output voltage that emerges in the circuit with these inputs, i.e., the converted AC Signal, is calculated. This signal is transferred to the electrostatic force unit. Thus, the MEMS power inverter system is repeated without the need for a new AC reference voltage, and the DC/AC inverter is also converted.

III. RESULTS AND DISCUSSION

A. Simulation Results

In this section, the design and simulation results of a DC/AC inverter that can be used in renewable energy applications are presented. The design is analyzed in photovoltaic systems. As a result of the analysis, MEMS DC/AC inverter results close to the normal inverter were obtained. The graphical results of the mathematical model created to observe the effect of capacitance values were observed in Matlab/Simulink software by applying different scenarios. The design criteria in Table 1 were used in all scenarios. As a result of the analysis, the change of capacitance according to displacement and electrical potential was examined. In addition, the efficiency of the voltage converted by the reference input voltage and the electrostatic force with the output signal was calculated.

Because the main frequency is 50 Hz in our country, the resonant frequency and the frequency of the reference AC voltage connected to the circuit are taken as 50 Hz. The MEMS residential area was chosen to be within the conventional dimensions. For the circuit to work, the main voltage connected to the circuit is 120 V AC, and the driver capacitance connected in series to the mains is 0.092 pF. The DC voltage from the solar panel can be between 0.5V and 48V. This study, the voltage converted according to the capacitance change at 0.5V and 24V DC voltages is simulated.

A comparison of the generated models was made using parameters such as electric potential distribution, displacement, and capacitance change. The potential electric distribution and displacement data are calculated for both models below with an operating voltage of 24 V. Two different models were designed for the capacitance analysis according to displacement. The results obtained from the compared models are shown in Fig. 8. The displacement increased as the capacitance value increased. The displacement and capacitance values are higher in Model 2. The 1st model showed an increase based on the max displacement range (1250 nm - 1260.62 nm), while the 2nd model showed an increase based on the max displacement range (2190 nm – 2193.885 nm).
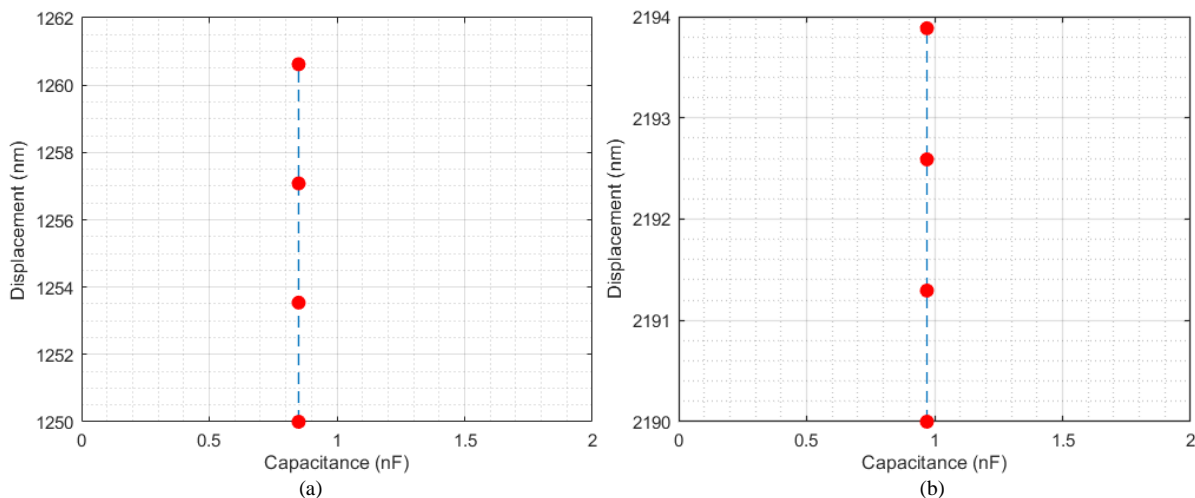
Fig.8. Capacitance values versus displacement for models (V=24V, C1=0.85nF, C2=0.97nF) (a) Displacements for model 1 (b) Displacements for model 2
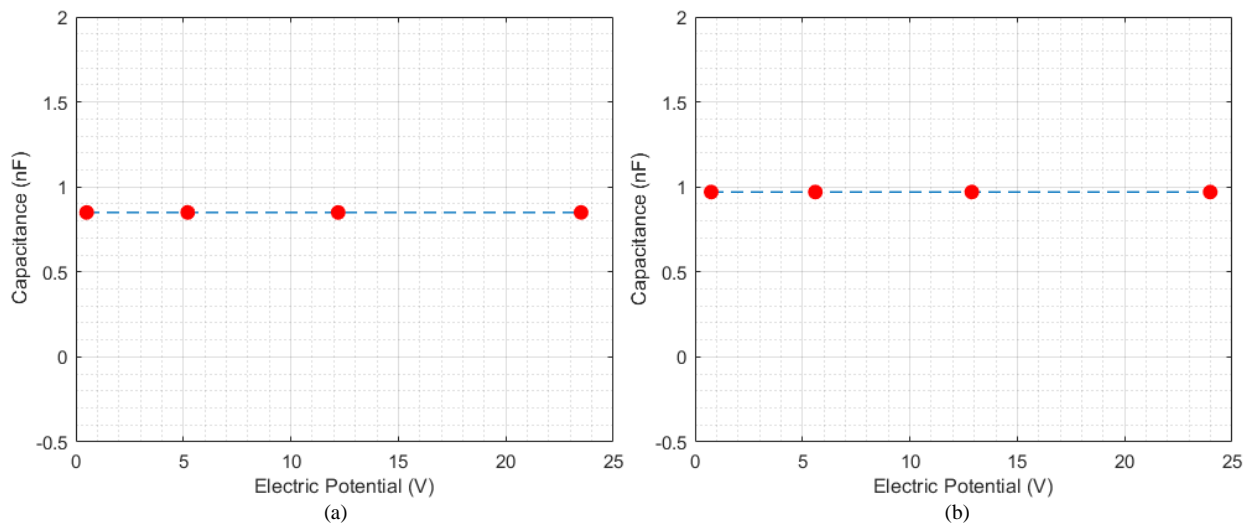
Fig.9. Electrical potential values versus capacitance for models (V=24V, C1=0.85nF, C2=0.97nF) (a) Capacitance for model 1 (b) Capacitance for model 2

Depending on the number of fingers in the MEMS comb structure, it shifted toward the Y axis with the increase in the overlap length of the capacitors overlapping in displacement.

Two different models were designed for capacitance analysis according to the electrical potential. The displacement depending on the capacitance value was investigated by selecting the input voltage as 24 V. The fixed and mobile electrons in the MEMS comb structure caused displacement on the surface and an increase in the electrical potential due to the change in capacitance. Since the increase in the electrical potential means the increase in the overlap area of the capacitors, the converter facilitates the increase of the capacitance throughout the circuit. The results obtained from the compared models are given in Fig. 9. As can be seen from the graphs, the electrical potential increases as the capacitance value increases. In addition, the electrostatic force and displacement increased as the capacitance increased according to the voltage changes between the electrical potential surfaces.

The electrostatic force and capacitance values of the moving electrodes were observed to change the capacitance caused by the fixed and moving electrodes. Since the reference AC voltage will cause vibration in the system, it will affect the electrostatic force. As the vibration coming to the resonator increases, the electrostatic force will increase. Because of the operating voltage, the electrostatic force between the two electrodes is proportional to the square of the applied voltage. Its variation with different voltage values is given in Fig. 10a. The electrostatic force also causes displacement in the overlap length. This then causes a change in capacitance. Because the capacitance is inversely proportional to the voltage, its variation with voltage is shown in Fig. 10b. Developing low-power large-scale integration (VLSI) applications is critical to current technology [39]. The proposed MEMS power inverter model can be used for low-cost and low-power applications.

When the converted voltage analysis is performed according to the reference input voltage, a sinusoidal graph appears like a standard DC/AC inverter. In the simulation, a frequency of 50 Hz was applied. Initially, the input voltage was taken as 0V, and the output voltage conversion was provided at low capacitance values. The voltage-time graph converted at a capacitance value of 97 fF at a voltage of 0.5V DC is shown in Fig. 11a. Then, the capacitance value was increased by applying a voltage to the input. Again, a sinusoidal graph is obtained at the output. The voltage conversion graph of 0.5V DC voltage at 3900 fF with an input voltage of 120V is given in Fig. 11b.
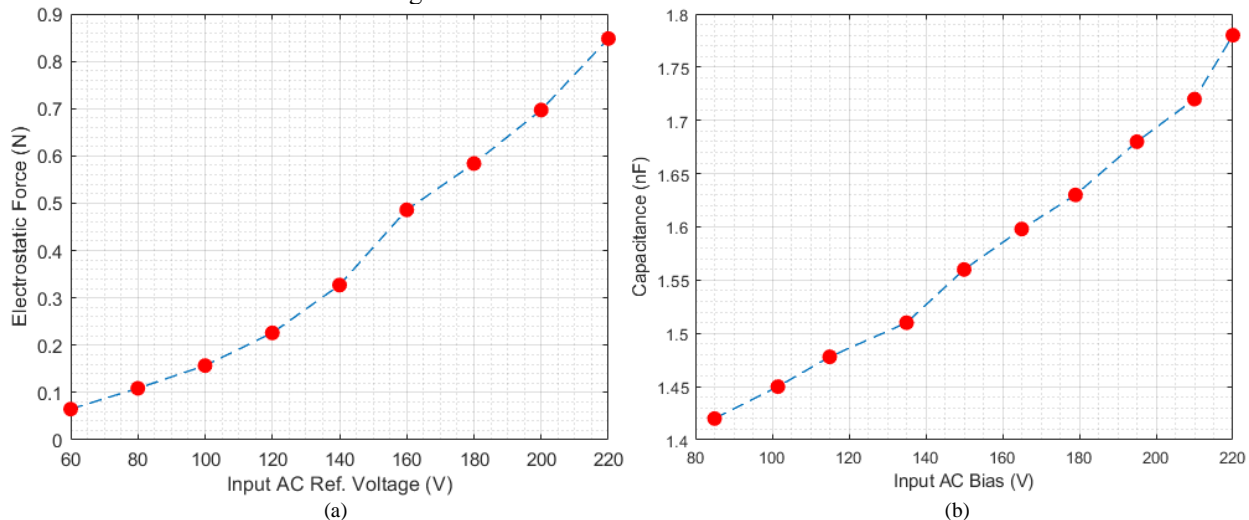
Fig.10. Electrostatic force and capacitance values versus reference voltage value (a) Electrostatic Force for model 1 (b) Capacitance for model 2
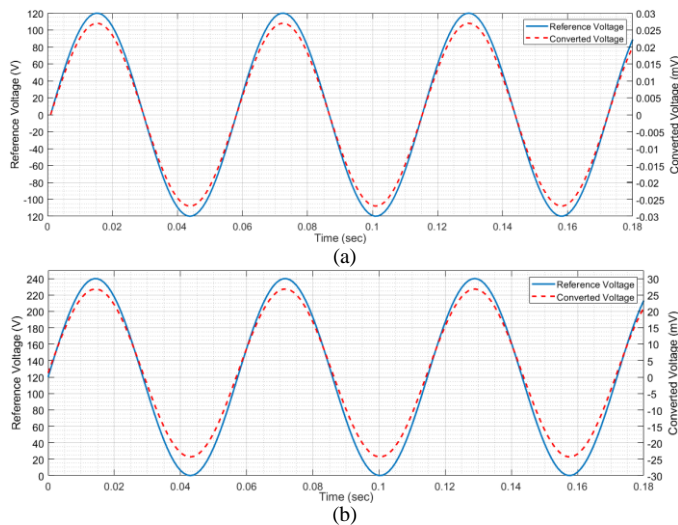
Fig.11. Voltage–time response simulation of MEMS inverter (a) Converted voltage graph versus 0 V reference input voltage (b) Converted voltage graph versus 120 V reference input voltage.

Finally, the efficiency performance of the MEMS power inverter is evaluated. Efficiency was calculated by changing the reference voltage and converting the capacitance values of the two different designs at 0.5 V DC voltage (Table II). The purpose of the designed inverter is to obtain the maximum AC amplitude signal from the DC input signal.

TABLE II
THE EFFICIENCY OF MEMS POWER INVERTER RELATIVE TO THE REFERENCE VOLTAGE

Efficiency (%)	V_L(mV)	V_{DC}(V)	Converter capacitance (fF)	Reference voltage (V)
0.002828	0.02	0.5	97	0
0.002121	0.015	0.5	97	0
0.001414	0.01	0.5	97	0
0.000707	0.005	0.5	97	0
6.161728	43.57	0.5	3900	120
5.436237	38.44	0.5	3900	120
2.938736	20.78	0.5	3900	120
1.467954	10.38	0.5	3900	120

The efficiency of the design with the input voltage applied and the capacitance increased is better. Here, the efficiency (η), is calculated by the root mean square value of the DC input signal from the solar system and the resulting converted voltage V_L. The efficiency results calculated for capacitance changes at 0.5V voltage are given in Table 3. When the results were examined, it was determined that high efficiency could be obtained at high capacitance values. Tables II and III reveal that augmenting the converter capacitance enhances the efficiency of the MEMS power inverter, while elevating the supplied DC voltage notably amplifies the converted DC/AC voltage V_L.

TABLE III
THE EFFICIENCY OF THE MEMS POWER INVERTER RELATIVE TO THE DIFFERENT CAPACITANCE

Efficiency (%)	V_L(mV)	V_{DC}(V)	Converter capacitance (fF)
0.0033	0.024	0.5	97
0.16	1.112	0.5	97
6.29	44.48	0.5	3900
6.3	44.54	0.5	3900

B. Discussion

A unique aspect of this work is the use of a capacitive MEMS-based power inverter designed for renewable energy applications. The use of MEMS technology in the field of power electronics is quite new, and little research has been done in this field. The role of power inverters in renewable energy systems is of great importance, and smaller, lighter and more efficient alternatives need to be investigated instead of traditional inverters. This study explores the potential of MEMS technology in power inverters and offers an original design for renewable energy applications. In addition, characterization of the inverter through simulation enables rapid evaluation of the performance of the design and provides valuable preliminary information before experimental prototype production. In this way, the efficiency of the design process increases and a more improved product is obtained.

In a study on how to improve the capacitive performance of MEMS-based transducers, MEMS-based DC/AC capacitive transducers of different materials and structures were tested [40]. At low input voltage, the capacitance increased due to curvature in the MEMS comb structure, which caused the deviation. In addition, the increase in the number of combs caused an increase in the electrostatic force. In the data obtained as a result of the simulation, the electrostatic force increased due to the increase in the number of combs and caused an increase in the capacitance. These results support the study. In another study, a MEMS-based low-power capacitive inverter design for renewable energy applications is presented, and the electrical and mechanical performances of two different MEMS structures are investigated by ignoring power losses at zero harmonic values [41]. In the study, less instability was obtained at the maximum displacement of the overlap length. In this article, the increase in the electrostatic force with the increase of the comb length was understood, and the efficiency and output signal obtained from the DC/AC inverter with the capacitance effect was examined. The results obtained are similar to this study. In a study on the efficiency calculation of MEMS power inverters, up to 6% efficiency was obtained [42]. In this study, efficiency was calculated in capacitance changes at 0.5V and 24V DC voltage, and it was determined that high efficiency could be obtained at high capacitance values. In this article, when the efficiency of the system was made by increasing the input voltage at 0.5V DC voltage and changing the capacitance values, it was observed that the efficiency increased as the capacitance value increased, and results similar to the study were obtained.

The simulation results and previous studies were compared, and it was understood how important capacitance is in MEMS technology. Depending on the capacitance, electrostatic force formation has been observed in MEMS devices. In renewable energy systems, the converted voltage in DC/AC inverters can benefit from MEMS technology to achieve maximum conversion with minimum loss. Elements affecting the designed DC/AC inverter have been determined, and it has been tried to use them in the most efficient way. With the mathematical equations and simulation results, the importance of the number and length of combs to be used in the MEMS system has been understood. The quality of the converted signal increases with the change in capacitance and electrostatic force.

As a result of simulation studies, the DC/AC conversion is possible with low-power applications.

This study discussed the design of a capacitive MEMS-based power inverter for renewable energy applications and its characterization through simulation. In the future, as an important continuation of this study, the design may need to be validated experimentally and the prototype tested in real environments. Field tests can be conducted to determine the performance of the inverter under real-world conditions and evaluate the effectiveness, reliability and integration ability of the optimized design. Additionally, a comprehensive study can be conducted examining the compatibility of the inverter with different renewable energy sources and its behavior under various operating conditions. However, innovative approaches such as improved control strategies or the use of new materials and manufacturing techniques can also be explored to increase the efficiency of the inverter. These studies can contribute to making renewable energy systems more efficient and reliable and promote progress in the field of MEMS-based power electronics.

IV. CONCLUSION

In this study, a capacitive MEMS-based power inverter design for renewable energy applications was developed, and characterization was carried out through simulation. Unlike conventional inverters, this inverter offers low costs, high efficiency, and low power consumption. The proposed inverter has a thickness of 325 μm, an active settlement area of 45x45x0.585 mm^3, and an initial capacitance value of 2.9 pF. An electromechanical model was used to observe the voltage-time response of the power inverter. Simulation studies of the mathematical model created on this model were performed in Matlab/Simulink. In the simulation studies, the displacement, electrostatic force, and capacitance responses of the proposed MEMS inverter over different models were obtained. As a result of these findings, the power inverter transformed the DC voltage from the solar system into a true sinusoidal waveform and a perfect AC voltage signal with the AC signal of the power grid. Because the proposed inverter is based on a capacitive structure, it provides close to zero power consumption. As a result of the efficiency calculations, the frequency and waveform shape of the converted DC/AC signal was matched to the AC signal of a power grid with a conversion efficiency of 5%. The losses of the designed MEMS DC/AC inverter can be minimized by the material used, the number of combs, and their length. In addition, the efficiency can be further increased by changing the electrostatic force and choosing the appropriate input voltage and suitable capacitor. With MEMS technology, DC/AC inverters with a near-perfect sinusoidal wave output will be made for ease of maintenance, and inexpensive electronic devices will be produced by obtaining inverters with longer service life.

ACKNOWLEDGMENT

REFERENCES

[1] H. Husin, M. Zaki, "A critical review of the integration of renewable energy sources with various Technologies" Protection and Control of Modern Power Systems, vol. 6, 1, 2021, pp. 1-18.

[2] B. K. Santhoshi, K. Mohanasundaram, L. A. Kumar, "ANN-based dynamic control and energy management of inverter and battery in a grid-tied hybrid renewable power system fed through switched Z-source converter" Electrical Engineering, vol. 103, 5, 2021, pp. 2285-2301.

[3] M. H. Ahmed, M. Wang, M. A. S. Hassan, I. Ullah, "Power loss model and efficiency analysis of three-phase inverter based on SiC MOSFETs for PV applications" IEEE Access, vol. 7, 2019, pp. 75768-75781.

[4] P. C. Vratny, H. Kuhn, M. Hornung, "Influences of voltage variations on electric power architectures for hybrid electric aircraft" CEAS Aeronautical Journal, vol. 8, 1, 2017, pp. 31-43.

[5] K. J. Chen, O. Häberlen, A. Lidow, "GaN-on-Si power technology: Devices and applications" IEEE Transactions on Electron Devices, vol. 64, 3, 2017, pp. 779-795.

[6] O. M. Rodríguez-Benítez, M. Ponce-Silva, J. A. Aquí-Tapia, A. Claudio-Sánchez, "Comparative performance and assessment study of a current-fed dc-dc resonant converter combining si, sic, and gan-based power semiconductor devices" Electronics, vol. 9, 11, 2020, pp. 1-15.

[7] T. Kaliannan, J. R. Albert, D. M. Begam, P. Madhumathi, "Power quality improvement in modular multilevel inverter using for different multicarrier PWM" European Journal of Electrical Engineering and Computer Science, vol. 5, 2, 2021, pp. 19-27.

[8] M. K. Das, K. C. Jana, A. Sinha "Performance evaluation of an asymmetrical reduced switched multi-level inverter for a grid-connected PV system" IET Renewable Power Generation, vol. 12, 2, 2018, pp. 252-263.

[9] M. Pichan, H. Rastegar, "Sliding-mode control of four-leg inverter with fixed switching frequency for uninterruptible power supply applications" IEEE Transactions on Industrial Electronics, vol. 64, 8, 2017, pp. 6805-6814.

[10] A. Sinha, K. C. Jana, M. K. Das, "An inclusive review on different multi-level inverter topologies, their modulation and control strategies for a grid connected photo-voltaic system" Solar Energy, vol. 170, 2018, pp. 633-657.

[11] P. Shah, X. Zhao, "Leakage current mitigation technique in solar PV array system using passive filter" IEEE Transactions on Energy Conversion, vol. 38, 1, 2022, pp. 463-478.

[12] M. U. Sardar, T. Vaimann, L. Kütt, A. Kallaste, B. Asad, S. Akbar, K. Kudelina, "Inverter-Fed Motor Drive System: A Systematic Analysis of Condition Monitoring and Practical Diagnostic Techniques" Energies, vol. 16, 15, 2023, pp. 5628.

[13] F. Obeidat, "A comprehensive review of future photovoltaic systems" Solar Energy, vol. 163, 2018, pp. 545-551.

[14] M. Dreidy, H. Mokhlis, S. Mekhilef, "Inertia response and frequency control techniques for renewable energy sources: A review" Renewable and Sustainable Energy Reviews, vol. 69, 2017, pp. 144-155.

[15] Y. Slimani, A. Selmi, E. Hannachi, M. A. Almessiere, "Impact of ZnO addition on structural, morphological, optical, dielectric and electrical performances of BaTiO3 ceramics" Journal of Materials Science: Materials in Electronics, vol. 30, 10, 2019, pp. 9520-9530.

[16] J. Druant, T. Vyncke, F. De Belie, P. Sergeant, J. Melkebeek, "Adding inverter fault detection to model-based predictive control for flying-capacitor inverters" IEEE Transactions on Industrial Electronics, vol. 62, 4, 2014, pp. 2054-2063.

[17] Y. Liu, B. Ge, H. Abu-Rub, D. Sun, "Comprehensive modeling of single-phase quasi-Z-source photovoltaic inverter to investigate low- frequency voltage and current ripple" IEEE Transactions on Industrial Electronics, vol. 62, 7, 2014, pp. 4194-4202.

[18] A. S. Abbas, R. A. El-Sehiemy, A. Abou El-Ela, E. S. Ali, "Optimal harmonic mitigation in distribution systems with inverter based distributed generation" Applied Sciences, vol. 11, 2, 2021, pp. 765-774.

[19] Y. Peng, Y. J. Zhang, D. T. Liu, L. S. Liu, "Degradation estimation using feature increment stepwise linear regression for PWM Inverter of Electro-Mechanical Actuator" Microelectronics Reliability, vol. 88, 2018, pp. 514-518.

[20] M. Chen, D. Zhou, F. Blaabjerg, "High penetration of inverter-based power sources with VSG control impact on electromechanical oscillation of power system" International Journal of Electrical Power & Energy Systems, vol. 142, 2022, 108370.

[21] X. Guo, Q. Xun, Z. Li, S. Du, "Silicon carbide converters and MEMS devices for high-temperature power electronics: A critical review" Micromachines, vol. 10, 6, 2019, pp. 395-406.

[22] I. V. Uvarov, A. N. Kupriyanov, "Stiction-protected MEMS switch with low actuation voltage" Microsystem Technologies, vol. 25, 8, 2019, pp. 3243-3251.

[23] N. Gupta, S. Dutta, A. Panchal, I. Yadav, S. Kumar, Y. Parmar, "Design and fabrication of SOI technology based MEMS differential capacitive accelerometer structure" Journal of Materials Science: Materials in Electronics, vol. 30, 16, 2019, pp. 15705-15714.

[24] W. Tian, P. Li, L. Yuan, "Research and analysis of MEMS switches in different frequency bands" Micromachines, vol. 9, 4, 2018, pp. 8-15.

[25] I. E. Lysenko, A. V. Tkachenko, E. V. Sherova, A. V. Nikitin, "Analytical approach in the development of RF MEMS switches" Electronics, vol. 7, 12, 2018, pp. 395-415.

[26] O. Ulkir, I. Ertugrul, N. Akkus, S. Ozer, "Fabrication and experimental study of micro-gripper with electrothermal actuation by stereolithography method. Journal of Materials Engineering and Performance, vol. 31, 10, 2022, pp. 8148-8159.

[27] J. Yunas, B. Mulyanti, I. Hamidah, M. Mohd Said, R. E. Pawinanto, "Polymer-based MEMS electromagnetic actuator for biomedical application: a review" Polymers, vol. 12, 5, 2020, pp. 1-18.

[28] A. S. Algamili, M. H. M. Khir, J. O. Dennis, A. Y. Ahmed, S. S. Alabsi, "A review of actuation and sensing mechanisms in MEMS-based sensor devices" Nanoscale Research Letters, vol. 16, 1, 2021, pp. 1-21.

[29] R. Sangno, R. K. Mehta, S. Maity, "MEMS Based Low Power Efficient Capacitive Inverter for renewable energy applications" IEEE VLSI Circuits and Systems Letter, vol. 5, 2, 2019, pp. 1-9.

[30] G. Niu, F. Wang, "A review of MEMS-based metal oxide semiconductors gas sensor in Mainland China" Journal of Micromechanics and Microengineering, vol. 32, 5, 2022, pp. 1-25.

[31] I. Vairavasundaram, V. Varadarajan, P. J. Pavankumar, R. K. Kanagavel, L. Ravi, S. Vairavasundaram, S. "A review on small power rating PV inverter topologies and smart PV inverters" Electronics, vol. 10, 11, 2021, pp. 1296.

[32] U. Akram, M. Nadarajah, R. Shah, F. Milano, "A review on rapid responsive energy storage technologies for frequency regulation in modern power systems" Renewable and Sustainable Energy Reviews, vol. 120, 2020, pp. 109626.

[33] H. Madinei, H. H. Khodaparast, M. I. Friswell, S. Adhikari, "Minimising the effects of manufacturing uncertainties in MEMS energy harvesters" Energy, 149, 2018, pp. 990-999.

[34] E. Ranjbar, A. A. Suratgar, "A composite adaptive controller design for 3-DOF MEMS vibratory gyroscopes capable of measuring angular velocity" Iranian Journal of Science and Technology, Transactions of Electrical Engineering, vol. 43, 2, 2019, pp. 245-266.

[35] A. Mustafazade, M. Pandit, C. Zhao, G. Sobreviela, "A vibrating beam MEMS accelerometer for gravity and seismic measurements" Scientific Reports, vol. 10, 1, 2020, pp. 1-8.

[36] K. Tao, J. Miao, S. W. Lye, X. Hu, "Sandwich-structured two-dimensional MEMS electret power generator for low-level ambient vibrational energy harvesting" Sensors and Actuators A: Physical, vol. 228, 2015, pp. 95-103.

[37] Y. Wang, H. Chen, B. Gao, X. Xiao, R. Torquato, F. C. Trindade, "Harmonic resonance analysis in high-renewable-energy-penetrated power systems considering frequency coupling" Energy Conversion and Economics, vol. 3, 5, 2022, pp. 333-344.

[38] M. A. Haj-ahmed, M. S. Illindala, "The influence of inverter-based DGs and their controllers on distribution network protection" In 2013 IEEE Industry Applications Society Annual Meeting, 2013, pp. 1-9.

[39] S. Vidhyadharan, R. Yadav, S. Hariprasad, S. S. Dan, "An advanced adiabatic logic using Gate Overlap Tunnel FET (GOTFET) devices for ultra-low power VLSI sensor applications" Analog Integrated Circuits and Signal Processing, vol. 102, 1, 2020, pp. 111-123.

[40] R. Sangno, R. K. Mehta, S. Maity, "Improvement in capacitive performances of efficient micro electro mechanical system (MEMS) based power inverter" Cogent Engineering, vol. 5, 1, 2018, 1455407.

[41] R. Sangno, R. K. Mehta, S. Maity, "MEMS Based Low Power Efficient Capacitive Inverter for renewable energy applications" IEEE VLSI Circuits and Systems Letter, vol. 5, 2, 2019, pp. 1-9.

[42] H. A. Kloub, E. M. Hamad, "Electromechanical modeling and designing of capacitive MEMS DC/AC interactive power inverter for renewable energy applications" Microsystem Technologies, vol. 23, 4, 2017, pp. 863-874.

BIOGRAPHIES

Salih Rahmi Turan graduated from Kocaeli University, Engineering Faculty, Koala, in 2012 and received Ph.D. degree in Science and Engineering Institute from Marmara University, Istanbul, Turkey, in 2019. Now he works at Mus Alparslan University. His current research interests include micro electro mechanical system, additive manufacturing, renewable energy, additive manufacturing.

Osman Ulkir graduated from Kocaeli University, Engineering Faculty, Kocaeli, in 2012, and received M.Sc. degree from Marmara University, Institute of Pure and Applied Sciences, in İstanbul, Turkey, in 2015. He has been started Ph.D. studying in department of Mechatronics Engineering, Marmara University, Institute of Pure and Applied Sciences in 2015. He is currently working as an assistant professor in mechatronics engineering department at Mus Alparslan University. His special field of interest mechatronics system design, MEMS, biomechatronics systems, signal processing, lower limb orthosis, additive manufacturing and data-driven predictive control.

Melih Kuncan received a B.S. degree in mechatronics engineering from Kocaeli University, Kocaeli, Turkey, in 2010, an MS degree in mechatronics engineering from Kocaeli University, Kocaeli, in 2013, and a Ph.D. degree in mechatronics engineering from Kocaeli University, Kocaeli, Turkey, in 2017. He is an Associate Professor in the Department of Electrical and Electronics Engineering, Siirt University. His areas of research include measurement, signal processing, medical signals, diagnosis, bearing fault, bearing fault diagnosis, fault classification and artificial intelligence.

Research Article

Shannonian Maximum Entropy Balking Threshold Mechanism (BTM) for a Stable $M/G/1$ Queue with Significant Applications of $M/G/1$ Queue Theory to Augmented Reality (AR)

Ismail A. Mageed

Abstract— **An exposition is undertaken to analytically derive validate the Shannonian Maximum Entropy BTM for the underlying stable queue. Most importantly, the analytic derivation of the upper and lower bounds 0f the absolute difference between Shannonian Cumulative service time distribution functions (CDFs) with and without balking. Typical numerical experiments are provided. Additionally, some applications of $M/G/1$ queue theory to AR are given. Some challenging open problems are addressed combined with closing remarks and future research directions.**

Index Terms— **BTM, Maximum Entropy (ME), CDF, energy, $M/G/1$ queue theory, AR.**

I. INTRODUCTION

IN principle, this current work supplies a complementary part of the research conducted (c.f., [1]). As the authors now feel the task completion and demonstration with both analytic expressions as well as illustrative data to interpret the newly devised research results.

It is commonly thought that obtaining precise performance distributions is often impossible, which encourages the use of alternative solution analysis methods such as ME and the diffusion approximation [2-7]. Using queueing models with balking, multiple real-world systems, such as commercial service systems and call centres where clients may learn about expected delays, and traffic-flow control in transportation networks, have all been effectively appraised [8-17].

2. PANORAMIC OVERVIEW ON [1]

I A MAGEED is with Department of Computer Science, University of Bradford, United Kingdom,(e-mail: drismail664@gmail.com).

https://orcid.org/0000-0002-3691-0773

In [15], a ME solution to QLD for a stable $M/G/1$ queue, includes a generalized geometric distribution (GGeo), as well as average Queue length (MQL), normalization status, and prior knowledge about the queue's stability (or flow conservation), via optimisation constraint p(0) (or equivalent use).

$$F_t = 1 - \frac{2}{c^2+1} e^{-\frac{2}{c^2+1}\mu t}, t \geq 0, \mu > 0 \qquad (1)$$

where the mean is $(1/\mu)$, and the square coefficient of variation is C^2 (SCV).

The discrete Half Normal distribution (dHN) [15] reads

$$p(n) = \frac{\theta^n q^{\frac{n(n-1)}{2}}}{\sum_{n=0}^{\infty} \theta^n q^{\frac{n(n-1)}{2}}} = p(0)\theta^n q^{\frac{n(n-1)}{2}}, n = 0,1,2\dots, \theta > 0, 0 < q < 1 \qquad (3)$$

θ and q are Lagrangian coefficients-dependent parameters.

Theorem 1 [17] The GdHN is the ME distribution given by

$$p(n) = \begin{cases} p(0), & n = 0 \\ p(0)\tau_s \phi^n r^{\frac{n(n-1)}{2}}, & n = 1,2,3\dots \end{cases}, \tau_s, \phi, r > 0, \qquad (4)$$

where τ_s, ϕ and r are distribution parameters in terms of the Lagrangian coefficients, such that
$(x_3)^{-1} = \tau_s = 2/(1 + C_{s,1,s}^2), \left(x_1 x_2^{-(2E[N]-1)}\right) = \phi$ and

$x_2 = r^{\frac{1}{2}}, x_1, x_2$ and x_3 are the Lagrangian coefficients corresponding to the first moment, variance and $p(0)$ prior moment information constraints respectively, with $p(0)$ written as

$$p(0) = \left(1 + \sum_{n=1}^{\infty} \tau_s \phi^n r^{\frac{n(n-1)}{2}}\right)^{-1} \qquad (5)$$

Theorem 2[1] The exactness of $p(n)(c.f.,(4))$ holds for $f_{s,B}(\mu, \tau_s, x_2, \beta, t)$ is GE_V- type, which reads as

$$f_{s,B}(\mu, \tau_s, x_2, \beta, t) = (1 - \tau_s^V)u_0(t) + \mu(\tau_s^V)^2 e^{-\mu \tau_s^V t} \qquad (6)$$

where $\tau_s^V = \tau_s r^{\frac{\beta}{2}}, u_0(t)$ reads as

$$u_0(t) = \begin{cases} \infty, & t = 0 \\ 0, & t \neq 0 \end{cases}$$

such that
$\int_{-\infty}^{\infty} u_0(t)dt = 1, (\tau_s, r)$ (c.f., (4)) and β is the inequality parameter, satisfying

$$n^2 = \alpha n + \beta \qquad (7)$$

We call α the factorization parameter.

$$n^2 = \alpha n + \beta \qquad (8)$$

Corollary 3

The family of families $\{F_{s,B}(\mu, \tau_s, x_2, \beta, t)\}$ are the corresponding GEV type CDFs for $\{f_{s,B}(\mu, \tau_s, x_2, \beta, t)\}$ (c.f., (6)) are determined by

$$F_{s,B}(\mu, \tau_s, x_2, \beta, t) = 1 - \tau_s^V e^{-\mu \tau_s^V t} \qquad (9)$$

with (τ_s, β, r) (c.f., Theorem 2) and $\tau_s^V = \tau_s r^{\frac{\beta}{2}}$. When $q \to 1$, $F_{s,B}(\mu, \tau_s, x_2, \beta, t)$(c.f., (9)) $\to F_s(t) = 1 - \tau_s e^{-\tau_s \mu t}$ (c.f., [15]) with $\tau_s = \frac{2}{c_{s,1,s}^2 + 1}$.

Corollary 4(c.f., [1])

For $f_{B,s}$ of Equ. (6), mean values and SCVs read as follows:

$$E(s_{B,S}) = \frac{1}{\mu} \qquad (10)$$

$$E(s_{B,S}^2) = \frac{2}{\mu^2 \tau_s^V} \qquad (11)$$

$$C_{B,S}^2 = \frac{E(s_{B,S}^2)}{(E(s_{B,S}))^2} - 1 = \frac{(2 - \tau_s^V)}{\tau_s^V} \qquad (12)$$

Provided that (τ_s, β, r) (c.f., Theorem 2) and $\tau_s^V = \tau_s r^{\frac{\beta}{2}}$.

[1] mainly contributes to:

- First time ever reaveling of the SDF of the Shannonian Balking solution of the stable $M/G/1$ queueeing system.
- First time ever reaveling of the corresponding family 3.of families of CDFs of the derived SDFs.
- First time ever reaveling of the corresponding family of families of mean values and SCVs.
- The generalization of the results in [15].

The following theorem is essential in the undertaken proofs.

Preliminary Theorem (PT) [18]

Let f be a function that is defined and differentiable on an open interval (c,d).
(I) If $f'(x) > 0 \ \forall x \in (c,d)$, then f is increasing on (c,d) (13)
(II) If $f'(x) < 0 \ \forall x \in (c,d)$, then f is decreasing on (c,d) (14)

This paper's road map is. Section 2 overviews the short paper upon which this current paper is aimed to be an extension of it. In section 3, we derive the new results. Section 4 deals with experimental setup to numeriacally demonstrate the validity of our new rersults. Section 5 is devoted to the provision of some potential applicatications of $M/G/1$ theory to AR. Some influential emerging open problem from this paper combined with closing remarks and the next phase of research are given in section 6.

3. NEW RESULTS

In what follows, two new theorems are devised, namely, the Shannonian maximum entropy BTM and the Shannonian Balking Differrence (SBD)Theorem.
In the following Theorem, we are defining for the first time, the generic threshold for up to which Shannonian Balking service time cumulative distribution function for the $M/G/1$ queue will be monotonic decreasing and after which, it will be increasing. This will open a new ground to understand the effect of the parameters of the on the behaviour of the Shannonian Balking service time cumulative distribution function.

Theorem 3 For $F_{s,B}(\mu, \tau_s, x_2, \beta, t)$ (c.f., (9)), it holds that:
(i) $F_{s,B}(\mu, \tau_s, x_2, \beta, t)$ is forever increasing in μ, t for all values of $t \geq 0$, $\mu > 1, 1 > \tau_s > 0, x_2, \beta$ are real numbers (15)
(ii) $F_{s,B}(\mu, \tau_s, x_2, \beta, t)$ is forever increasing in τ_s, $1 > \tau_s > 0$ if and only if we can find $\varrho > 0$ satisfying

$$\varrho = -\left(\frac{(ln(\mu_{inimum} x_2^\beta t))}{ln(\tau_s)_{minimum}}\right) - 1 \qquad (16)$$

μ, t for all values of $t \geq 0$,
$\mu > 1, 1 > \tau_s > 0, x_2, \beta$ are real numbers.

(iii) $F_{s,B}(\mu, \tau_s, x_2, \beta, t)$ is forever decreasing in τ_s, $1 > \tau_s > 0$ if and only if we can find $\varrho > 0$ satisfying

$$t \leq \frac{1}{\mu x_2^\beta \tau_s} \qquad (17)$$

μ, t for all values of $t \geq 0$,
$\mu > 1, 1 > \tau_s > 0, x_2, \beta$ are real numbers.

Proof.

(i)We have $F_{s,Balking}(t) = 1 - \tau_s x_2^\beta e^{-\mu \tau_s x_2^\beta t}$. By the preliminary theorem, it holds that $F_{s,Balking}(t)$ is (increasing)(decreasing) if and only if

$$\frac{\partial F_{s,Balking}(t)(\mu, \tau_s, x_2, \beta, t)}{\partial \mu} < 0 (\geq 0) respectively \qquad (c.f.,(13))$$

We have

$$\frac{\partial F_{s,Balking}(t)(\mu, \tau_s, x_2, \beta, t)}{\partial \mu} = \mu(\tau_s x_2^\beta)^2 e^{-\mu \tau_s x_2^\beta t} \qquad (18)$$

Hence, it is notable by (13) that $\frac{\partial F_s(\mu, \tau_s, t)}{\partial \mu} > 0$ for all values, $\mu, t, \tau_s > 0, 1 > \tau_s > 0$. It follows that $F_s(t)$ is increasing for all values, $\mu, t, \tau_s > 0, 1 > \tau_s > 0$, $\beta = n(n - \alpha)$ for all positive real numbers α, β. On the other hand, let $\frac{\partial F_{s,Balking}(t)(\mu, \tau_s, x_2, \beta, t)}{\partial \mu} \leq 0$, which implies

$\mu(\tau_s x_2^\beta)^2 e^{-\mu \tau_s x_2^\beta t} \leq 0$. This is impossible since

$\mu, t, \tau_s > 0, 1 > \tau_s > 0$ and $e^{-\mu \tau_s x_2^\beta t} \geq 0$. Hence, the contradiction follows.

Following the same approach, $F_{s,B}(\mu, \tau_s, x_2, \beta, t)$ is forever increasing in t for all values of $t \geq 0$, $\mu > 1, 1 > \tau_s > 0, x_2, \beta$ are real numbers.

(ii) We have $F_{s,B}(\mu, \tau_s, x_2, \beta, t) = 1 - \tau_s x_2^\beta e^{-\mu\tau_s x_2^\beta t}$. By the preliminary theorem, it holds that $F_{s,B}(\mu, \tau_s, x_2, \beta, t)$ is increasing in τ_s if and only if $\frac{\partial F_{s,B}(t)(\mu,\tau_s,x_2,\beta,t)}{\partial \tau_s} > 0$, (i.e.,)

$$-x_2^\beta e^{-\mu\tau_s x_2^\beta t} + \tau_s(x_2^\beta)^2 e^{-\mu\tau_s x_2^\beta t} > 0 \qquad (19)$$

This implies

$$-x_2^\beta e^{-\mu\tau_s x_2^\beta t}(1 - x_2^\beta \mu\tau_s t) > 0 \qquad (20)$$

by (20), $F_{s,B}(\mu, \tau_s, x_2, \beta, t)$ is forever increasing in τ_s if and only if $(1 - x_2^\beta \mu\tau_s t) < 0$, which implies $t > \frac{1}{\mu x_2^\beta \tau_s}$. It is implied that there exists a positive number $\varrho \in (0, \infty)$ such that if $t = \frac{((\tau_s)_{min})^{-\varrho}}{\mu_{min} x_2^\beta \tau_s} = \frac{((\tau_s)_{min})^{-(\varrho+1)}}{\mu_{min} x_2^\beta}$. Hence, it follows that

$$\varrho = -\left(\frac{(ln(\mu_{inimum} x_2^\beta t))}{\ln(\tau_s)_{minimum}}\right) - 1 \qquad (c.f., (16))$$

(iii) Following the same argument, assume $t \leq \frac{1}{\mu x_2^\beta \tau_s}$. Hence, it follows that $(1 - x_2^\beta \mu\tau_s t) \geq 0$. Consequently, $\frac{\partial F_{s,B}(t)(\mu,\tau_s,x_2,\beta,t)}{\partial \tau_s} \leq 0$. This provides the sufficient and necessary condition for $F_{s,B}(\mu, \tau_s, x_2, \beta, t)$ to be decreasing in τ_s.

Theorem 4

The difference $\mathcal{D}$ of values between $F_{s,Balking}(\mu, \tau_s, x_2, \beta, t)$ (c.f., (9)) and, $F_s(\mu, \tau_s, t)$(c.f., [15]) satisfies

$$\left(1 - F_s(\mu, \tau_s, t)\right)\left(x_2^\beta e^{-\mu\tau_s(x_2^\beta-1)t} + 1\right)$$
$$\geq \mathcal{D} \geq \left(1 - F_s(\mu, \tau_s, t)\right)(x_2^\beta e^{-\mu\tau_s(x_2^\beta-1)t} - 1), \qquad (21)$$
$$\mathcal{D} = |F_{s,Balking}(\mu, \tau_s, x_2, \beta, t) - F_s(\mu, \tau_s, t)|$$

Proof

We have

$$\mathcal{D} = |F_{s,Balking}(\mu, \tau_s, x_2, \beta, t) - F_s(\mu, \tau_s, t)|$$
$$= |\tau_s x_2^\beta e^{-\mu\tau_s x_2^\beta t} - \tau_s e^{-\mu\tau_s t}|$$
$$= \tau_s e^{-\mu\tau_s t}|x_2^\beta e^{-\mu\tau_s(x_2^\beta-1)t} - 1|$$
$$= \left(1 - F_s(\mu, \tau_s, t)\right)|x_2^\beta e^{-\mu\tau_s(x_2^\beta-1)t} - 1| \qquad (22)$$

By the modulus inequality,

$$|a| + |b| \geq |a - b| \geq |a| - |b| \qquad (23)$$

$$\left(1 - F_s(\mu, \tau_s, t)\right)\left(x_2^\beta e^{-\mu\tau_s(x_2^\beta-1)t} + 1\right)$$
$$\geq \mathcal{D} \geq \left(1 - F_s(\mu, \tau_s, t)\right)(x_2^\beta e^{-\mu\tau_s(x_2^\beta-1)t} - 1). \text{ QED}$$
P.S. As $\beta \to 0$, $\mathcal{D} \to 0$, as $F_{s,Balking}(\mu, \tau_s, x_2, \beta, t) \to F_s(\mu, \tau_s, t)$.

In the following section, we are showing numerically the effect of the variance parameter on the increasability and decreasility of the cumulative balking service time distribution function.

4. EXPERIMENTAL SETUP

Case study One, $n = 1$

For $n = 1, \alpha = \beta = 0.5, \tau_s = 0.5, 0.6, 0.7, \mu \in [2, 7.5]$. Let $x_2 = 0.8$. Looking at figure 1, it can be seen that the threshold value is $t = 0.1$. By the Shannonian Balking Threshold Theorem, this threshold exists by the existence of a positive real number $\varrho \epsilon (0, 2)$ such that

$$\varrho = -\left(\frac{(\boldsymbol{ln}(\mu_{inimum} x_2^\beta t))}{\ln(\tau_s)_{minimum}}\right) - \mathbf{1}$$

By calculations, we have
$$\varrho = -\left(\frac{(\boldsymbol{ln}((0.1)(2)(0.8^{0.5})))}{ln\ 0.5}\right) - \mathbf{1} = 1.482892142.$$
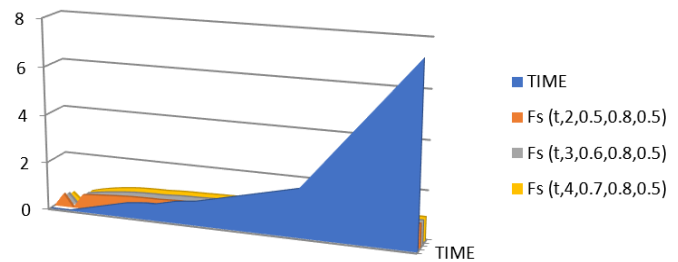
Figure 1. How time impacts $F_s(\mu, \tau_s, t), n = 1$

Case study Two, $n = 3$

Let $n = 3, \alpha = 2, \beta = 3, \tau_s = 0.5, \mu \in [2, 7.5]$. Let $x_2 = 3.5$. Observing figure 2, we can see that the threshold value is $t = 0.1$. By the Shannonian Balking Threshold Theorem, this threshold exists by the existence of a positive real number $\varrho \epsilon (0, \infty)$ such that

$$\varrho = -\left(\frac{(ln(\mu_{inimum} x_2^\beta t))}{\ln(\tau_s)_{minimum}}\right) - 1$$

By calculations, we have $\varrho = -\left(\frac{(ln((0)(2)(2^2)))}{ln\ 0.5}\right) - 1$. Hence, it holds that $\varrho \to \infty$. in other words, the threshold is satisfied for a sufficiently large ϱ.
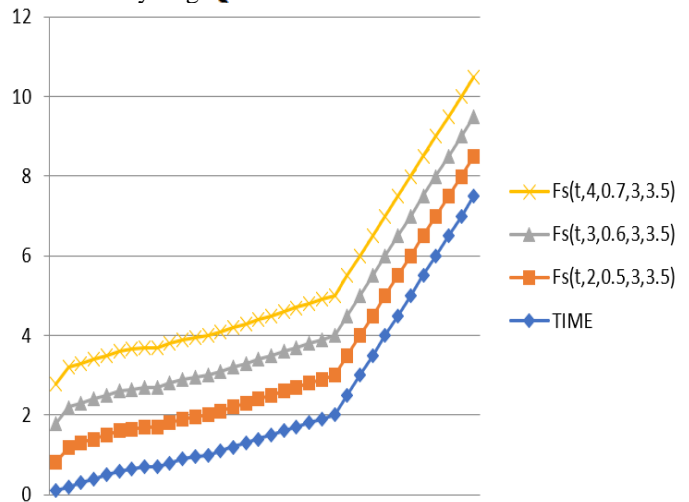
Figure 2. How time impacts $F_s(\mu, \tau_s, t), n = 3$

5. $M/G/1$ THEORY APPLICATIONS TO AR

[19] discussed the challenge of providing trusted and updated information for AR services over a terahertz (THz) cellular network and explained the relationship linking an $M/G/1$ queue dynamics and the ruin's risk, which can be used to re-define the system's reliability explicitly in PAoI.

In the context of an AR system, the authors [19] proposed a queuing model that splits the system into two as a guarantee among users-fair scheduling policy, while also allowing for urgent requests to be prioritized.   This is visually demonstrated by figure 3(c, f., [19]). The proposed model aims to prevent outdated and potentially harmful information from being sent to AR users.

Figure 4. Average peak AoI versus user count [19].

Figure 3. An illustration of the proposed queuing model for analysing the freshness of AR content updates. The model splits the queuing system into two limited-sized queues, one for prioritizing urgent requests and another for fair scheduling of requests. (c.f., [19]).
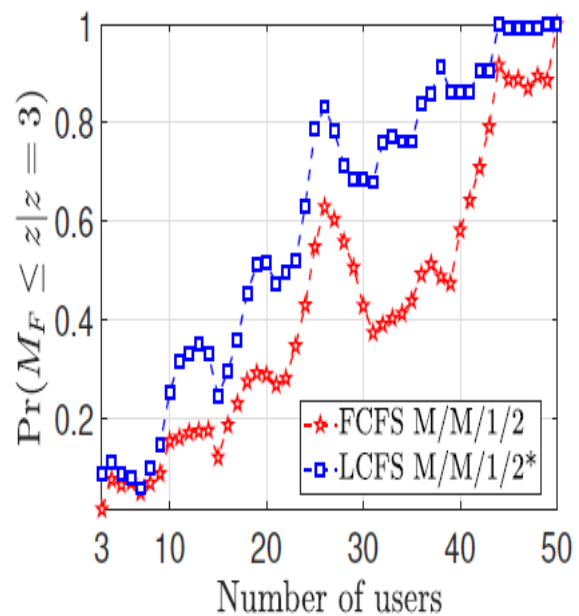
Figure 5. The probability of the worst-case peak AoI being less than z = 3 versus the number of users [19].

Figures 4 and 5(c.f., [19]) demonstrate the impact of the number of users on up-to-date information in a THz cellular network. With the increase of users, the peak average Age of Information (AoI) decreases due to the simultaneous arrival of more packets, generating information updates to the allocated server of the network.

Extended Reality (XR)[20], which includes Virtual Reality and Augmented Reality, has the potential to revolutionize virtual and telepresence experiences. Figure 6 (c,f., [20]) describes a simplified architecture of a Cloud XR system. This architecture is important for providing an immersive experience but presents challenges in terms of real-time video quality adaptation and network resource allocation.
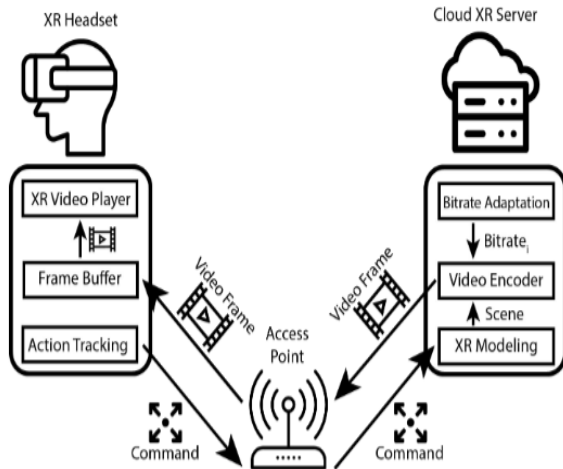
Figure 6. Cloud XR architecture's sample (c.f., [20])

The authors of [20] studied the performance of adaptive XR video streaming in the presence of high-priority interfering traffic and discussed the existing literature on the $M/G/1$ queue system and its probabilistic properties, so the authors[20] used their model to estimate the maximum bitrate of an XR video stream in a scenario where the network capacity is limited and the stalling probability should be less than 0.01.

Figure 7 shows that the actual capacity of the network for the XR video is up to 50% lower than what can be obtained with a certain equation due to the variance of the resource consumption by the commands growing with the command rate.
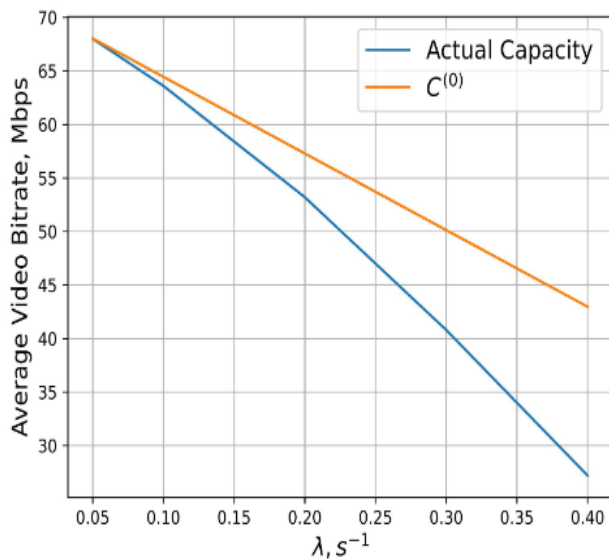
Figure 7. Network capacity estimation (c.f., [21])

The average computation delay for tasks processed by a BS can be calculated by modeling the service process as an

$M/G/1$ queue and analysing its sojourn time, which includes both service time and waiting time.

Figure 8(c.f., [21]) highlights the importance of effective service caching decisions in accommodating different types of services and improving overall system performance.
"Cached service" refers to the storage of frequently accessed data or services at base stations (BSs) in a wireless network. Figure 8 highlights the importance of cooperation in accommodating more types of services and improving overall system performance. Notably, the number of services is denoted by k.
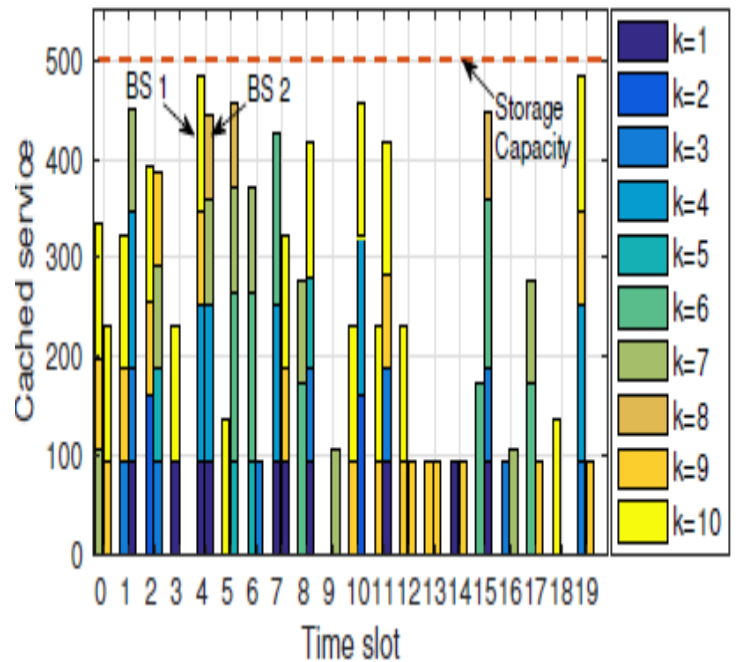
Figure 8. Cached service

6. CONCLUSION, OPEN PROBLEMS AND NEXT RESEARCH PHASE

An explanation is given to confirm the Shannonian Maximum Entropy BTM for the underlying stable queue analytically. Most crucially, the upper and lower bounds of the absolute difference between with and without Shannonian Cumulative service time distribution functions are derived analytically. There are examples of typical numerical experiments offered. In addition, several queue theory applications to AR are shown. Some difficult open problems are addressed, as well as closing remarks and future research objectives.
The current paper has several emerging open problems.

Open Problem One

Having arrived at the stage where Shannonian Balking mechanism has been fully captured in both analytic and

numerical domains. The current resesarch generates some open problems as follows:

- What will the overall derivations for the undertaken balking mechanism if we add more higher order moments to the constraints?
- Coming to a situation, where other higher order entropies that generalize Shannon's entropy with the same set of constraints, which will the derivations look like? More interestingly, will the derived formalism be a generalisation to the results of [1] and this current paper?

Open Problem Two

Numerous potential open problems are generated by the established model in [19].

- Following [19], is possible to extend their established model to a more complex and realistic high-priority traffic pattern. They are asking if their model can be adapted to better account for video encoding idiosyncrasies, such as different types of frames in a video stream, their sizes, and their impact on Quality of Service (QoE). This open problem highlights the potential for further research and development in the field of network optimization.
- Can we broaden the model to include interference from other videos? Finally, a more sophisticated optimisation technique can be employed to lower the computational cost of calculating the optimal bitrate adaption function for a particular network state. Using this technique, we may perform optimisation with finer granularity and provide improved QoE to end users.

- **Open Problem Three**

In the undertaken model(c,f., [21]) gives rise to open problems, such as incorporating user-cell association decisions and allowing workload transfer among peer base stations to balance task workload.

The next phase of research includes attempting to solve the highlighted open problems and expanding on the exploration of more applications of $M/G/1$ theory to other fields of science.

REFERENCES

[1] I.A.Mageed, et al, "M/G/1 queue with Balking Shannonian Maximum Entropy Closed Form Expression with Some Potential Queueing Applications to Energy", 2022 Global Energy Conference (GEC). IEEE, 2022.

[2] E.T.Jaynse, "Information Theory and Statistical Mechanics", Physical Review, 106, 1957, 620 - 630.

[3] E.T.Jaynes, E.T., "Where do we Stand on Maximum Entropy?", in Proc. The Maximum Entropy Formalism Conference, M.I.T., USA, 1978.

[4] S.-C.Fang,et al, "Entropy optimization and mathematical programming,1997, Kluwer Academic Publishers, Boston.

[5] J.Shore, and R. Johnson, "Axiomatic derivation of the principle of maximum entropy and the principle of minimum cross-entropy", IEEE Transactions onInformation Theory,1980, 26, 26-37.

[6] J.Shore, "Information theoretic approximations for M/G/1 and G/G/1 queuing systems",1982, Acta Informatica, 17, 43.

[7] J.Cantor,et al, "Information theoretic analysis for a general queueing system at equilibrium with application to queues in tandem", Acta Informatica,1986, 23 ,657-678.

[8] F.A.Haight, "Queueing with Balking", Biometrika, 1957,44 (1957) 360-369.

[9] L.Liu, " Service Systems with Balking Based on Queueing Time ,PhD Thesis", Department of Statistics and Operations Research, University of North Carolina at Chapel Hill, USA, 2007.

[10] O.J.Boxma, and B.J. Prabhu, "Analysis of an M/G/1 Queue with Customer Impatience and an Adaptive Arrival Process", 2009,Technical Report Eurandom; Vol. 2009028, Eindhoven University of Technology, Eindhoven, The Netherlands.

[11] F.Baccelli,et al, "Single-Server Queues with Impatient Customers", 1984, Advances in Applied Probability, 16, 887-905.

[12] P.M.Morse, " Queues, Inventories and Maintenance: The Analysis of Operational Systems with Variable Demand and Supply", 1958,First ed., John Wiley & Sons, Inc.

[13] A.W.Kemp, "Steady-state Markov chain models for certain q-confluent hypergeometric distributions", 2005,Journal of Statistical Planning and Inference, 135, 107.

[14] A.W.Kemp, "The Discrete Half-Normal Distribution", in: Arnold, B.C., Balakrishnan,N., J.M. Sarabia,J.M. & Minguez, R. (Eds.) Advances in Mathematical and Statistical Modeling, Birkhäuser Boston,2008, pp. 353-360.

[15] M.A.El-Affendi,and D.D.Kouvatsos," A maximum entropy analysis of the M/G/1 and G/M/1 queueing systems at equilibrium", 1983,Acta Informatica, 19,339.

[16] D.D.Kouvatsos, "A Maximum Entropy Analysis of the G/G/1 Queue at Equilibrium", 1988, The Journal of the Operational Research Society, 39, 183-200.

[17] N.Shah, "Entropy Maximisation and Queues With or Without Balking", 2014,PhD Thesis, Department of Computing, University of Bradford.

[18] P.V.Gapeev , et al, " Optimal double stopping problems for maxima and minima of geometric Brownian motions", Methodology and Computing in Applied Probability. 2022 Jun;24(2):789-813.

[19] C.Chaccour and W.Saad, "On the ruin of age of information in augmented reality over wireless terahertz (THz) networks", InGLOBECOM 2020-2020 IEEE Global Communications Conference 2020 Dec 7 (pp. 1-6). IEEE.

[20] M.Liubogoshchev, et al, "Adaptive cloud-based extended reality: Modeling and optimization", IEEE Access. 2021 Feb 26;9:35287-99.

[21] J.Xu , et al, " Joint service caching and task offloading for mobile edge computing in dense networks",In IEEE INFOCOM 2018-IEEE Conference on Computer Communications 2018 Apr 16 (pp. 207-215). IEEE.

BIOGRAPHIES

ISMAIL A MAGEED Dr. Ismail A Mageed completed his doctorate in Applied Probability at The University of Bradford, United Kingdom. His current research interests include the unification of queueing theory with information theory and information geometry. His leading research on the relativization of queuing theory and discovering the geodesic equation of motion for transient queues was greatly received by the world research community. Mageed's research on finding the analytic solutions of the longstanding simulative approach of The Pointwise Stationary Fluid Flow Approximation theory (PSFFA) was an exceptional discovery to advance PSFFA theory. Mageed has published numerous papers in many highly reputable journals and conferences. He is also a reviewer of several prestigious journals. Mageed's research has been internationally recognized as being revolutionary by providing several breakthroughs. Dr Mageed has published a chapter in a book of the best eight queueing theorists in the world by ISTE WILLEY. He is currently leading several research teams in UK, India, Africa, and Saudi Arabia. He is also a fellow of the Royal Statistical Society (RSS), a member of INTISCC (Austria), IEANG (world council of engineering) and a life member of the Islamic Society of Statistical Sciences.

The Use of Data Transmission Technique Via Power Line Communication

Murat Sen and Seda Ustun Ercan

Abstract—**The smart grid requires the use of communication methods. One of these communication methods is power line communication (PLC). In this study, TMDSPLCKITV4 evaluation boards are programmed with the G3-PLC standard and operated as transmitter and receiver in low voltage distribution grid. Then, the distances between the transceiver points, the load characteristics were changed and the received signal strength indication, signal noise ratio, bit error rate and package error rate values for each modulation type of the G3-PLC standard were measured in real time. According to these measured values, the success of the PLC has been demonstrated. In general, it is observed that the number of erroneous data bits increases in each modulation type under pulsed variable load. Robust mod and binary phase shift keying modulation types appear to be the most successful modulation types with the least number of erroneous data bits when all experimental conditions are considered.**

Index Terms—**Smart grid, power line communication, modulation, TMDSPLCKITV4, G3-PLC**

I. INTRODUCTION

THERE IS an estimation that worldwide electrical energy consumption will increase by 60% in 2030 to approximately 37000 TWh [1]. The need to meet the energy demand increase should be managed in an environmentally friendly manner when the concepts of carbon emissions and fossil fuel use are considered. Naturally, this situation will significantly increase the dependence on renewable energy sources. But the problem is that today's electricity grids are not designed to meet the growing energy demand or to support electricity generation from renewable energy sources. For this reason, the need for updating the existing electricity grid arises. Updating the existing grid reveals the concept of a "Smart Grid". The smart grid introduces new load groups to the system,

Murat SEN, is with the department of Electrical-Electronics Engineering, Ondokuz Mayıs University, Samsun, Turkey. (e-mail: murat.sen@omu.edu.tr)

https://orcid.org/0000-0002-8439-3862

Seda Ustun Ercan, is with the department of Electrical-Electronics Engineering, Ondokuz Mayıs University, Samsun, Turkey. (e-mail:sedau@omu.edu.tr)

https://orcid.org/ 0000-0002-8688-5852

such as grid-integrated electric vehicles. This technology holds promise for both the smart grid and reducing the environmental impact of vehicles [2]. In addition, it is also possible to see different power electronics switching elements and converters in smart grids. DC-AC Inverters that can be managed with different control techniques are examples of this situation [3].

The smart grid generally consists of a communication technology that will provide data communication between two points in electricity generation, transmission and distribution systems. With this structure, the smart grid provides a two-way energy flow and communication signal transmission in power systems, thus revealing a large-scale control and communication infrastructure [4]. The use of communication technologies in applications such as smart grids and the Internet of Things has led to the development of next-generation technologies such as 6G [5, 6]. However, it is more important to effectively utilize the communication technologies that are already accepted. Currently, communication technologies for the smart network are divided into two main groups as wired and wireless communication methods [7]. All communication methods inherently have some advantages and disadvantages, but communication methods used for smart grids are expected to have essential features such as high data transmission rate, low signal degradation, high flexibility and coverage, sustainability, low cost, strong encryption, compatibility with hybrid communication operations [8]. PLC provides communication using existing power grid lines. Therefore, it provides technical, economic benefits and wide usage area.

Considering all these situations, PLC has been an active research area for smart grid implementations that has been effectiveness for years [9]. PLC stands out for smart grid implementations with its benefits such as wide coverage, flexible and long-distance communication, low cost, ease of installation, stable operation in fixed grid conditions [10]. On the other hand, the PLC signal can be negatively impacted by electromagnetic interference resulting from high frequency switching in the distribution grid. Additionally, changes in impedance within the communication channel used for data transmission can lead to attenuation of the PLC signal. PLC can be used at the medium voltage level of the electrical grid for operations such as fault monitoring, breaker status monitoring, transformer parameters acquisition and distributed generation monitoring [11]. Besides this, PLC can be used for remote detection of broken insulators, fuse locations, cable breakage and deflection tracking at high voltage levels [12]. PLC is suitable as communication technology in SCADA systems, which are known as remote monitoring and management systems. In addition, it is possible to monitor the real-time

remote monitoring of the Sag event, known as the sudden voltage drop in the grid by examining the status of the PLC signal [13]. Smart grid operations, where the PLC communication method is used most widely and extensively, are located in the LV electricity distribution grid. The most preferred operation of the PLC method is AMR which the reading results of smart meters is obtained remotely [14].

In this paper, TI TMDSPLCKITV4 evaluation boards are programmed in Narrowband (NB) G3 -PLC standard and perform real time in LV distribution grid. Then, parameters such as distance, load, modulation type were changed in the laboratory and data transmission between two points was carried out with PLC technology under different conditions. It is seen that most of the studies in the PLC literature are simulations but this study produces real time real data for thanks to TMDSPLCKITV4. This study produces a pre-field output about the PLC usage suitability of the grid where PLC will be used by running evaluation cards in the LV grid in the laboratory. Another contribution is the most suitable PLC modulation type can be detected easily according to grid conditions like load and distance. In addition, evaluation cards software provides the opportunity to change the data package size used in the transceiver communication, the data package sending frequency and the total number of the data package to be sent, making a very important contribution to determining the data characteristics to be included in the communication before the field implementation and provides experiments in the laboratory.

II. THE THEORY OF POWER LINE COMMUNICATION

PLC technology is defined as the realization of data communication between sending and receiving ends by a signal containing information while carrying out generation, transmission and distribution operations in the grid by using the existing electrical grid. The advantages of using PLC are listed as minimizing the need for a new installation, no coverage area problem and no need for antenna use. On the other hand, the disadvantages of using PLC can be listed as the fact that the power lines are not designed for communication purposes, the communication channel conditions are constantly changing, the number of switching in the grid is excessive, the signals carrying data are corrupted by exposure to interference.

For the use of the PLC method, three basic parameters must be considered; the impedance value of the PLC channel, the noise that the PLC channel will be exposed to in the grid and the signal attenuation that may occur during data transfer between sending and receiving ends. If the impedance value of the Tx / Rx circuit is the same as the channel impedance on which the data communication is provided, the parameters of the signal that will carry the data sending and receiving ends two points will be transmitted to the line in an optimum way. Noises in the power grid directly affect the frequency and amplitude values of the carrier signals that provide data communication between sending and receiving ends with the disruptive effect is created by them. Signal attenuation depends on the length of the power line where point to point data communication is provided and the number of cable splices on this line. Higher signal attenuations are observed in industrial areas than in rural and urban areas for PLC technology [15].

Impedance, noise and signal attenuation parameters are evaluated by measuring BER, PER, SNR and RSSI values for PLC technology. NB-PLC is one of the structures of PLC with its standards and modulation types [16]. NB-PLC is the most prominent structure of PLC communication types. G3-PLC and PRIME standards of NB-PLC technology are extensively studied and widely used standards. NB-PLC is known as a type of PLC used to get smart meter data remotely in the power grid. The organization named CENELEC in Europe has determined the frequency bands for NB-PLC level use [17]. The CENELEC standard uses the frequency range 3 kHz – 148.5 kHz. CENELEC has divided the operating frequency range into four sub-frequency bands to ensure efficient and trouble-free operation, considering the diversity of operations. One of these sub-bands is CENELEC A band that uses the 9 kHz – 95 kHz frequency range, is reserved only for distribution and generation service providers and is available for smart grid implementation, primarily AMR [18].

The data-carrying signal must be made suitable for the PLC channel where communication will be occurred to use PLC technology. In this way, the characteristic of one of the phase, amplitude or frequency parameters of the data-carrying signal must be transformed according to the regulatory signal, in other words, it must be modulated. Modulation types are basically phase shift keying (PSK), amplitude shift keying and frequency shift keying. The case of using more than one carrier for signal transmission in the PLC channel is expressed as multi-carrier modulation. The most well-known structure of multi-carrier modulation is the orthogonal frequency division multiplexing (OFDM) technique [19]. In the OFDM technique, the PLC channel increases efficiency by saving bandwidth when the subcarriers are positioned orthogonally for data transmission in the segmented frequency range [20]. In addition, OFDM is robust against interference in the NB-PLC channel. It shows low sensitivity to time matching errors. It is suitable for Fourier transform operations and is robust against fading caused by multipath propagation. On the other hand, OFDM is sensitive to frequency synchronization problems and phase noise. OFDM is known as the most widely used technique in NB-PLC types smart grid AMR implementations with this mentioned working structure, especially with PSK methods [21]. OFDM based PSK modulations are used as binary phase shift keying (BPSK), quartet phase shift keying (QPSK), octal phase shift keying (8PSK) according to the phase angles and bit values they use. It is possible to have an idea about the success of data communication with OFDM-based PSK modulations in NB-PLC level by performing BER analysis [22].

G3-PLC, PRIME and IEEE1901.2 structures are very common among NB-PLC communication technology standards. The frequency range of 35.938 kHz – 90.625 kHz in the CENELEC-A sub-band is used by OFDM-based G3-PLC. Besides the G3-PLC, another globally accepted standard is the PRIME standard. The PRIME contains 97 subcarriers while the G3-PLC contains 36 subcarriers [23]. Although PRIME maximum data rate can reach 128.6 kbps and its uncomplicated structure, it has been proven that the G3-PLC is more robust and powerful than the PRIME [24]. The G3-PLC standard consists of physical layer, data link layer, network layer and transport layer. In the physical layer (PHY), the OFDM

technique process steps of the G3-PLC standard are included together with the process steps specific to G3-PLC. For this reason, PHY is the most important layer where the G3-PLC standard is defined and its execution structure is located. The media access control (MAC) sublayer, located as a lower layer in the data link layer, allows the transmission of MAC packets using the PLC channel through which communication is made [25, 26]. It provides verification control by notifying the upper layers that the transmission is positive or negative and enables the establishment of the network structure between communicating points by associating nodes.

III.   MATERIAL, METHOD AND EXPERIMENTAL FINDINGS

All experiments were done in a laboratory environment as real time by TI TMDSPLCKITV4 evaluation boards which have been programmed with the OFDM based G3-PLC standard in the NB-PLC communication type CENELEC A band. Two evaluation board products, one for the Tx side and one for the Rx side, were used to evaluate the operating situations of PLC technology under different conditions in LV distribution grid.

G3-PLC standard was uploaded to the evaluation boards via "Code Skin" program. These boards work like gateways for transmitting and receiving data at Tx and Rx points on the PLC channel. In this way, by changing the load and distance conditions between Tx and Rx points, RSSI, SNR, BER, and PER values for each modulation type of the G3-PLC standard, including ROBO, BPSK, QPSK, 8PSK, were captured thanks to evaluation boards software and all experimental findings were obtained. "Intermediate Mode (IM)" of TMDSPLCKITV4 board was used for all experiments. IM program can show the RSSI, SNR, BER, PER values which are the communication quality basic parameters in the PLC channel, in real time and graphically according to the modulation type.

The setups in which all the experiments were executed in the laboratory environment are shown in Fig.1. In these images, evaluation boards positioned as Tx and Rx points which are responsible for performing data transmission are seen. Also power line connection scheme of TMDSPLCKITV4 can be seen.

All experiments were performed with the IM program. The regulated data unit parameters are aligned as follows; the data packet sending time interval is 1000 (the selected time parameter is multiplied by the value of 10 µs by the program, in this case, there is a time difference of 0.01 s between each data packet), the total number of data packets to be sent for each test is 1000 and the size of a data packet is 100 bytes. All graphs were obtained with updated data at 3-second intervals throughout the test period on the Rx side. In addition, the same cable cross-section was used in all experiments.

Experiment-1 was performed to measure the effect of signal attenuation in BPSK modulation type without load at 5m and 25m distances. The results of 5m distance no load condition is shown as Fig.2. It is seen that in Fig.3., the RSSI value indicating the received signal power is 116 dBµV with a distance of 5m between Tx and Rx in the no load condition in BPSK modulation type. Also, there is no bit error value. On the other hand, in Fig.3., the results are obtained when the distance

is increased to 25m in the same modulation type and no-load condition. It is seen that in Fig.3. the RSSI value is measured as 113 dBµV at a distance of 25 m under the same test conditions. When compared with the experiment performed at 5m distance in Fig.2. there is a signal attenuation of 3 dBµV due to the increase in distance, but this signal attenuation did not cause any error bit.

(a)

(b)

(c)
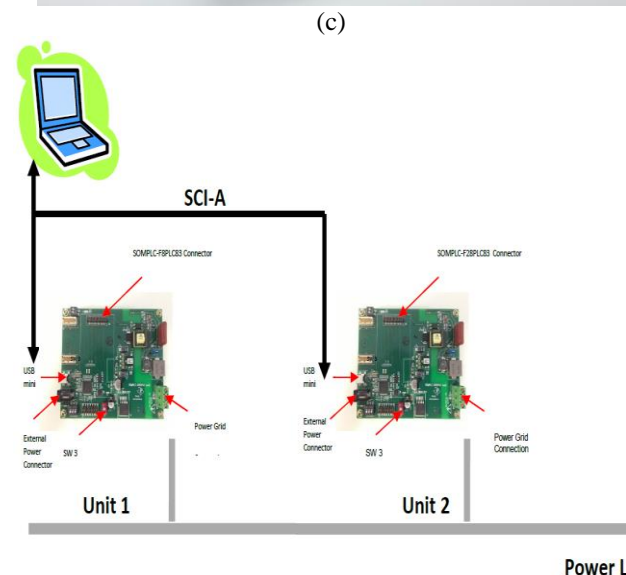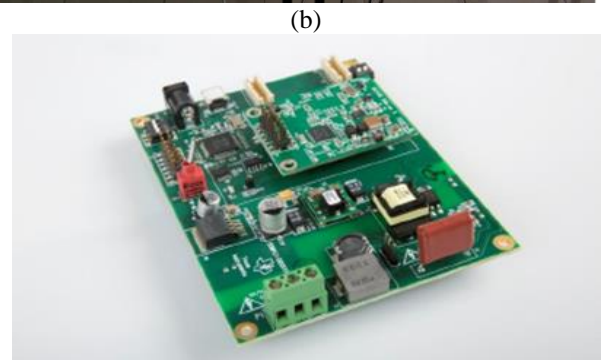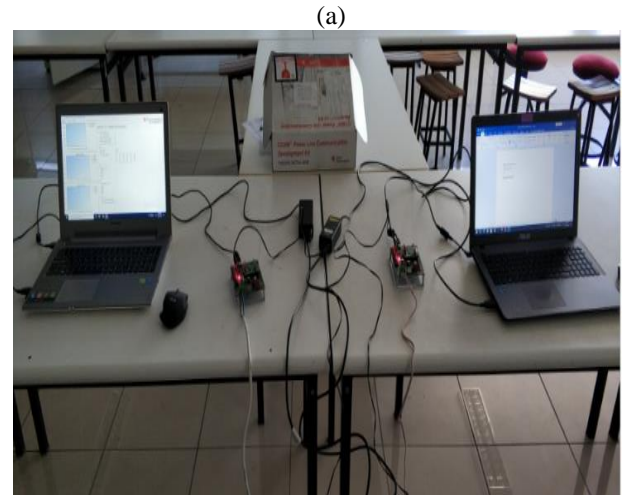
Fig.1. (a) Tx and Rx points in the experimental setup (b) TMDSPLCKITV4 (c) TMDSPLCKITV4 power line connection

QPSK, 8PSK, respectively. The results of Experiment-2 are shown in Fig. 4., 5., 6., 7. and Table 1.
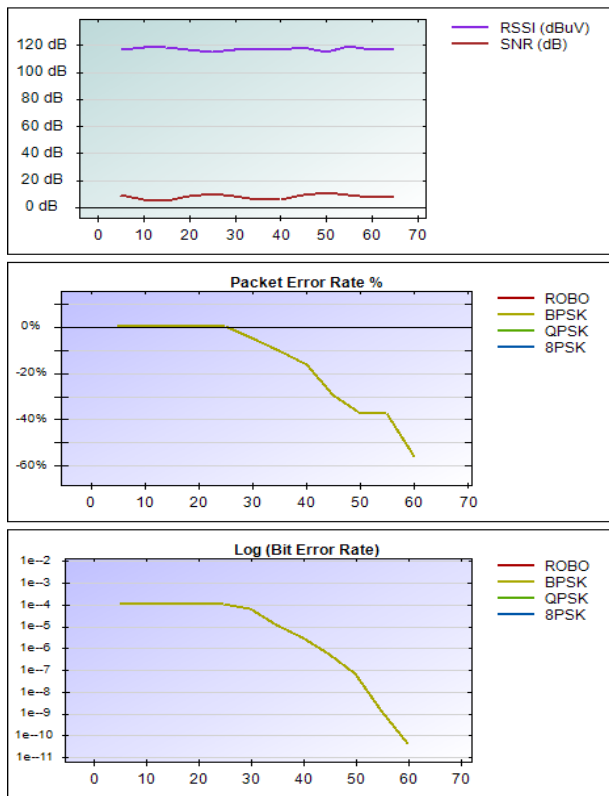
Fig.2. Experiment-1 no load, BPSK, 5m
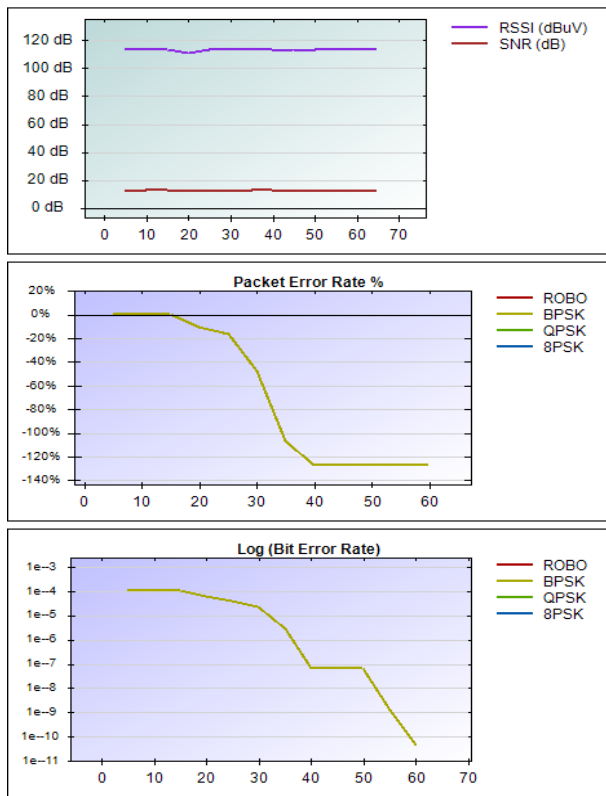
Fig.3. Experiment-1 no load, BPSK, 25m
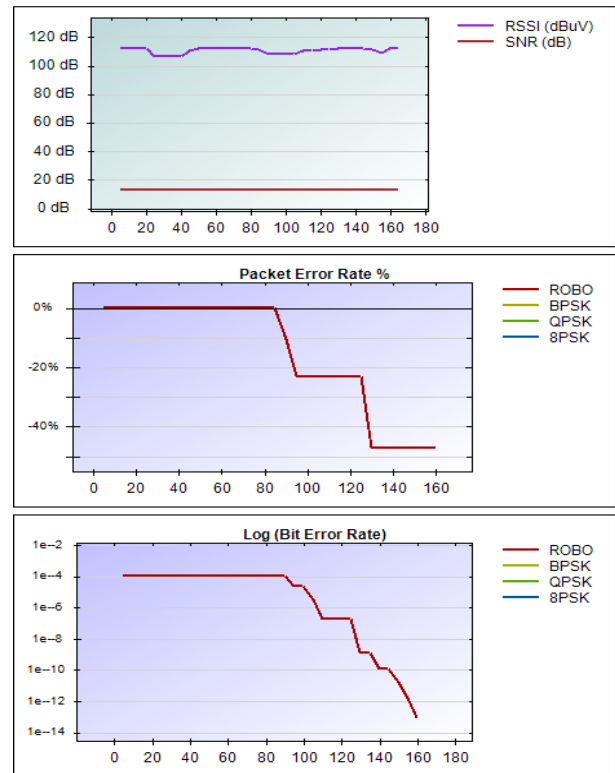
Fig.4. Experiment-2 3300W constant ohmic load, ROBO, 25m
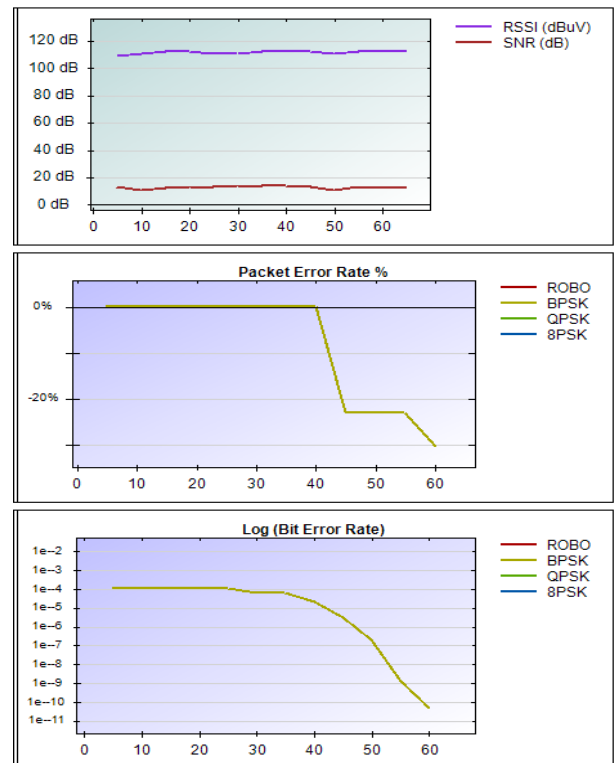
Fig.5. Experiment-2 3300W constant ohmic load, BPSK, 25m

25m distance between Tx-Rx and 3300W constant ohmic load conditions were used for Experiment-2. PLC tests were performed separately in the modulation types ROBO, BPSK,
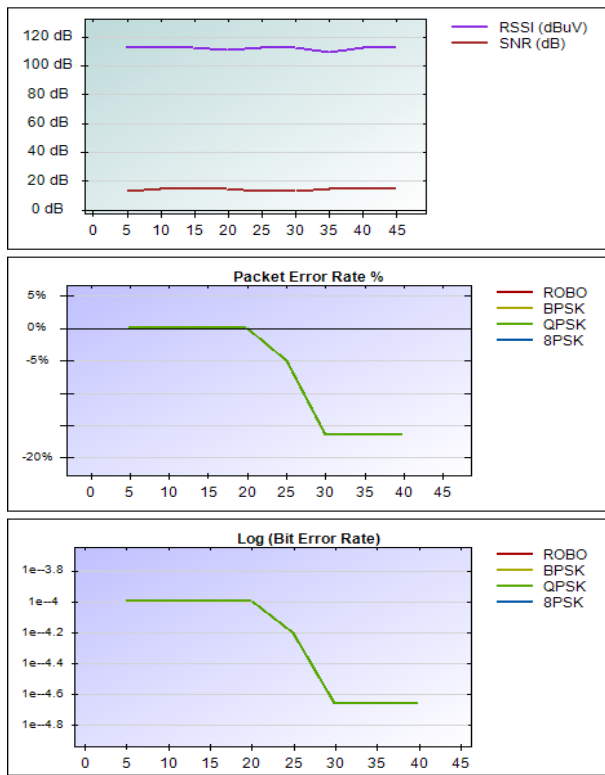
Fig.6. Experiment-2 3300W constant ohmic load, QPSK, 25m
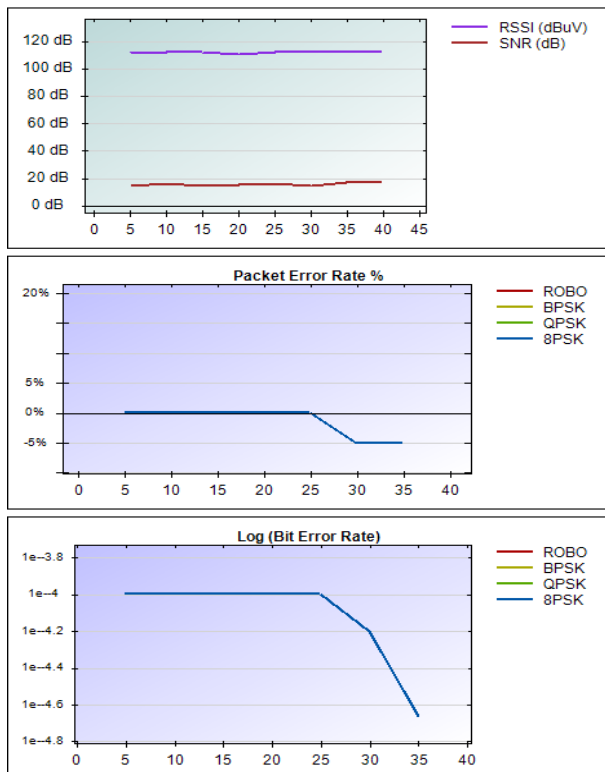
Fig.7. Experiment-2 3300W constant ohmic load, 8PSK, 25m

Experiment-3 was performed using a total load of 3300W including 1800W constant ohmic load and additional 1500W Pulsed Variable Load (PVL) at 5m distance between Tx-Rx. Pvl is a type of load with frequent changes in impedance and current values due to its characteristic feature. Since PVL directly affects the communication channel parameters with this

structure, it determines the realization of data transmission with PLC. All tests were conducted with modulation types ROBO, BPSK, QPSK, 8PSK, respectively for Experiment-3. All results for Experiment-3 are shown in Figures 8, 9, 10, 11 and Table-2.
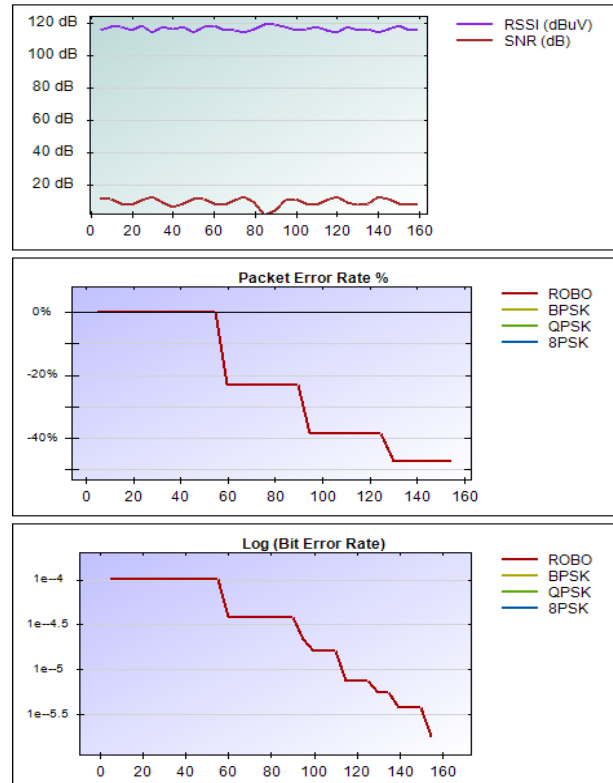
Fig.8. Experiment-3 1800W constant ohmic load, and 1500W PVL, ROBO, 5m
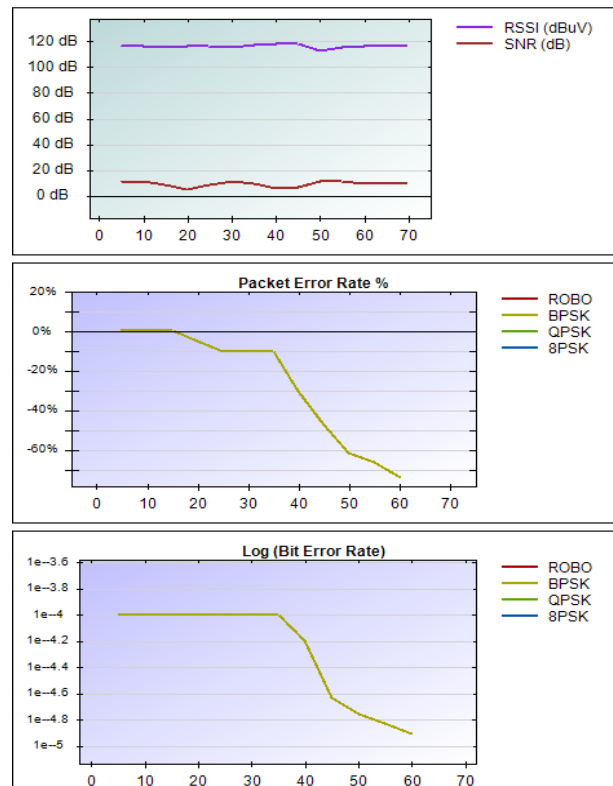
Fig.9. Experiment-3, 1800W constant ohmic load, 1500W PVL, BPSK, 5m
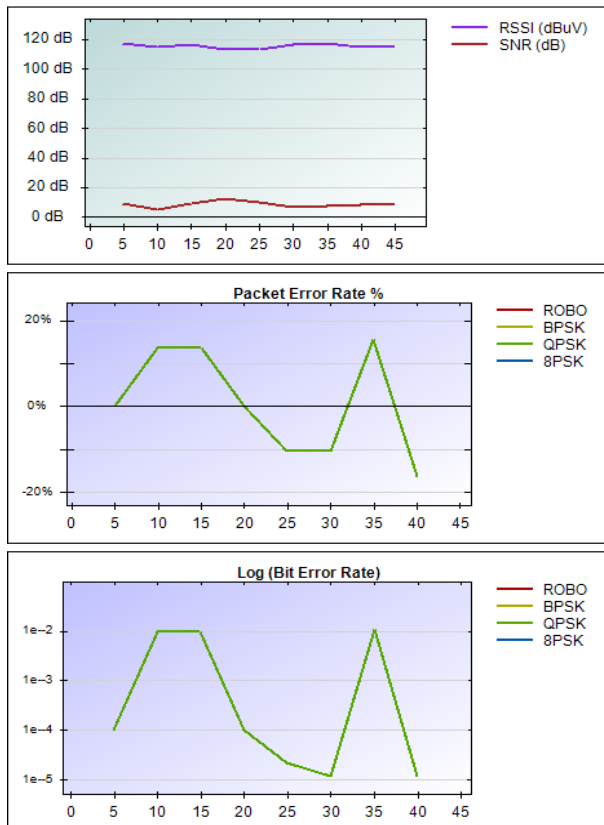
Fig.10. Experiment-3 1800W constant ohmic load, 1500W PVL, QPSK, 5m
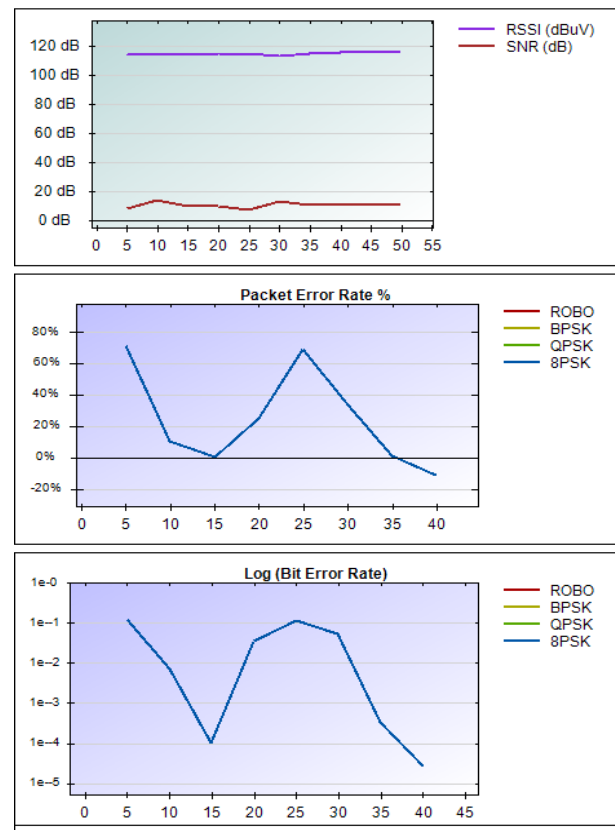
Fig. 11. Experiment-3 1800W constant ohmic load, 1500W PVL, 8PSK, 5m

TABLE I
RESULTS OF EXPERIMENT-2

Modulation Type	Distance	Load	BER	SNR(dB)
ROBO	25m	3300 Watt	1e-13	13
BPSK	25m	3300 Watt	1e-10	12
QPSK	25m	3300 Watt	1e-4.6	14
8PSK	25m	3300 Watt	1e-4.7	17

TABLE II
RESULTS OF EXPERIMENT-3

Modulation Type	Distance	Load	BER	SNR(dB)
ROBO	5m	1800 Watt+1500 Watt (PVL)	1e-5.7	7
BPSK	5m	1800 Watt+1500 Watt (PVL)	1e-4.9	9
QPSK	5m	1800 Watt+1500 Watt (PVL)	1e-2	8
8PSK	5m	1800 Watt+1500 Watt (PVL)	1e-1	11

IV. CONCLUSION

PLC signal attenuation was investigated with Experiment-1. The 3dBµV attenuation in the RSSI value because of the distance increase did not cause any bit errors. So the variation of the distance between Tx and Rx points does not significantly affect the signal attenuation. Experiment-2 was conducted with only constant load and it shows that all modulation types of G3-PLC are suitable for smart grid communication in stable grid conditions such as residential or rural AMR operations.

According to the results of Experiment-3 which has a 1500W pulsed variable load, SNR values decreased for all modulation types. Depending on this, the highest data bit errors and BER values were seen in PVL tests with low SNR values. Bad SNR values and high BER, PER values caused data bit errors and data packet errors, especially in the QPSK and 8PSK modulations. In PVL tests, although SNR values decreased in ROBO and BPSK modulations and BER values increased significantly compared to the results in only constant load conditions, no data bit error and data packet errors were not seen. Thus, it has been revealed that only ROBO and BPSK

modulation types should be used for smart grid communication in unstable grid conditions.

Especially, Experiment-3 shows that sudden load changes in the grid, namely impedance changes, impose restrictions on the use of PLC and error bits that occur during data communication reduce PLC success. When we compare this situation with the signal attenuation problem in Experiment-1, it is possible to say that sudden impedance changes are a bigger problem for PLC than signal attenuation. As seen in the results mentioned above, the most resistant modulation type against impedance changes due to sudden load changes is ROBO. In addition, it should be noted that when using 8PSK and QPSK, there should be no sudden changes in the grid load status, otherwise bit errors may occur during data communication.

With this study, the modulation type that should be used according to the grid conditions is determined in the laboratory before the field installation. In addition, the data size of the smart grid implementation, data transmission frequency and the number of data packets are set and tested, allowing data communication regulation before field installation (For example, customizing AMR meter, load profile, short read out and long read data packets). Beside this as explained in section 3, the receiver and transmitter exchanged data packets with high data size and frequency at short intervals. Stress test conditions were created to clearly demonstrate the success status of the PLC, and the load effects were measured in real-time.

The smart grid and the internet of things are developing day by day and this development will accelerate in the near future. This means that the need for data communication between sending and receiving points will increase rapidly and new frequency bands will be required to meet this need. In this way, all existing communication methods that can be used in smart grid operations should be utilized with the highest efficiency. This study showed that PLC is a suitable and proven communication method so it should be more widespread.

REFERENCES

[1] Shlebik T., Fadel A., Mhereeg M., Shlebik M. 2017. The development of a simulation-based smart grid communication management system using MATLAB. International Conference on Green Energy Conversion Systems (GECS), Tunisia.

[2] Erdogan B., Tan A., Savrun M. M., Cuma M.U., Tumay M. 2023. Design and analysis of a high-efficiency resonant converter for EV battery charger. Balkan Journal of Electrical and Computer Engineering 12(1):198-205.

[3] Deniz E. 2021. Medium and large vector-based SVPWM technique for five-phase two-level inverter. European Journal of Technique 11(2):209-216.

[4] Kabalci Y. 2016. A survey on smart metering and smart grid communication. Renewable and Sustainable Energy Reviews: 302-318.

[5] Hamamreh J.M., Iqbal S. 2023. Precoded universal MIMO superposition transmission for achieving optimal coverage and high throughput in 6G and beyond networks. Balkan Journal of Electrical and Computer Engineering 11(1):25-34

[6] Mageed I.A. 2023. Cosistency axioms of choices for Ismael's entropy formalism (IEF) combined with information theoretic (IT) applications to advance 6G networks. European Journal of Technique 13(2):207-213

[7] Zhou X., Ma Y., Gao Z., Wang H. 2017. Summary of smart metering and smart grid communication. IEEE International Conference on Mechatronics and Automation (ICMA), 300-304. Japan.

[8] Yaqoob I., Hashem I.A.T., Mehmood Y., Gani A., Mokhtar S., Guizani S. 2017. Enabling communication technologies for smart cities. IEEE Communications Magazine 55(1):112-120.

[9] Lopez G., Matanza J., De La Vega D., Castro M., Arrinda A., Moreno J.I., Sendin A. 2019. The role of power line communications in the smart grid revisited: applications, challenges and research initiatives. IEEE Access 7: 117346-117368.

[10] Yigit M., Gungor V.C., Tuna G., Rangoussi M., Fadel E. 2014. Power line communication technologies for smart grid applications: A review of advances and challenges. Computer Networks 70: 366-383.

[11] Galli S., Scaglione A., Wang Z. 2011. For the grid and through the grid. The role of power line communications in the smart grid. Proceedings of the IEEE 99(6):998-1027.

[12] J.F., Silveira P.M., Martinez M.L.B., Perez R.C., Dallbello A.C. 2009. New approach to improve high-voltage transmission line reliability. IEEE Transactions on Power Delivery 24 (3): 1515-1520.

[13] Villiers W., Cloete J.H., Wedepohl L.M., Burger A. 2007. Real-time Sag monitoring system for high-voltage overhead transmission lines based on power-line carrier signal behavior. IEEE Transactions on Power Delivery 23(1):389-395.

[14] Usman A., Shami S.J. 2013. Evolution of communication technologies for smart grid applications. Renewable and Sustainable Energy Reviews 19:191-199.

[15] Cavdar I.H. and Karadeniz E. 2008. Measurements of impedance and attenuation at CENELEC bands for power line communications systems. Sensors 8(12):8027-8036

[16] Sharma K., Saini L.M. 2017. Power-line communications for smart grid: Progress, challenges, opportunities and status. Renewable and Sustainable Energy Reviews 67:704-751

[17] Berger L.T., Schwager A., Garzas J.J.E. 2013. Power line communications for smart grid applications. Journal of Electrical and Computer Engineering:1-16

[18] Masood B. and Baig S. 2016. Standardization and deployment scenario of next generation NB-PLC technologies. Renewable and Sustainable Energy Reviews 65:1033-1047.

[19] Gotz M., Rapp M., Dostert K. 2004. Power line channel characteristics and their effect on communication system design. IEEE Communications Magazine 42(4): 78-86.

[20] Omri A., Fernandez J. H., Pietro R. 2023. Subcarrier index modulation for OFDM based PLC systems. IEEE Symposium on Computers and Communications (ISCC). Tunisia, 649-655.

[21] Ndjiongue A.R., Ferreira H.C. 2019. Power line communications (PLC) technology: More than 20 years of intense research. Transactions on Emerging Telecommunications Technologies 30 (7): 1-20.

[22] Moaveninejad S., Kumar A., Scazzoli D., Piti A., Magarini M., Bregni S., Verticale G. 2017. BER evaluation of post-meter PLC services in CENELEC-C band. IEEE 9th Latin-American Conference on Communications (LATINCOM). Guatemala, 1-6.

[23] Sadowski Z. 2015. Comparison of PLC-PRIME and PLC-G3 protocols. International School on Nonsinusoidal Currents and Compensation (ISNCC). Poland, 1-6.

[24] Hoch M. 2011. Comparison of PLC G3 and PRIME. 2011 IEEE International Symposium on Power Line Communications and Its Applications. Italy, 165-169.

[25] Ngcobo T. and Ghayoor F. 2019. Study the topology effect on a G3-PLC based AMI network. Southern African Universities Power Engineering Conference/Robotics and Mechatronics/Pattern Recognition Association of South Africa (SAUPEC/RobMech/PRASA). South Africa, 629-633.

[26] Razazian K. and Bali M. C. 2023. Evaluating various machine learning techniques in selecting different modulations in G3-PLC protocol. IEEE International Symposium on Power Line Communications and its Applications (ISPLC). United Kingdom, 55-60.

BIOGRAPHIES

Murat SEN was born in Turkey. He received the B.Sc. degree in electrical engineering from Kocaeli University, Turkey in 2010 and the M.Sc. degree in electrical and electronic engineering from Ondokuz Mayıs University, Samsun, Turkey in 2021. He is currently Ph.D. student in the department of electrical and

electronic engineering at Ondokuz Mayıs University and works as a lecturer at Yeşilyurt Demir Çelik Vocation School Electronic Technology Program of Ondokuz Mayıs University. His research interests include power line communication, electric distribution, smart grid and smart metering.

Seda USTUN ERCAN was born in Turkey. She received the B.S, M.Sc. and Ph.D. degrees in electrical and electronic engineering from Ondokuz Mayıs University, Samsun, Turkey, in 2005, 2009 and 2016, respectively. She was a Postdoctoral researcher in electrical and electronic engineering from the University of Nottingham in United Kingdom. She is currently an Assistant Professor at the department of electrical and electronics engineering in Samsun, Turkey. Her research interests include power line communication and digital signal processing.

Research Article

Analysis of Food Supply Chain Process by Block Chain Based Approach

Mesut Gun, Eyup Emre Ulku* and Ilayda Ulku

Abstract— **The developments in technology and the emergence of new technologies have increased the expectations for the supply chain to have a more efficient, traceable and transparent structure. Although the legal regulations and standards of blockchain technology have not been clearly revealed yet, it is thought that it will solve many problems with its application in the food supply chain. In this context, the use of blockchain technology in the food supply chain, its advantages and disadvantages and today's application examples were examined by making a literature review. As a result of the study, it has been seen that blockchain technology provides significant added value to the food supply chain and is a solution to many problems of today's traditional supply chain.**

I. INTRODUCTION

THE CURRENT supply chain is a linear business model. However, increasing international competition and increasing outsourcing with globalization increase the number of members in the supply chain day by day [1]. Depending on the situation, the supply chain process of a product may include multiple international borders, different state and customs processes, many invoices and payment stages, as well as multiple individuals or institutions, and comprehensive and multidimensional transactions that can take months depending on the nature of the transaction. All these complexities negatively affect performance and increase risks in the supply chain. Delays in transactions, increased costs, loss of trust between the parties are some of the prominent risks [2].

MESUT GUN, is with Program of Computer Engineering, Institute of Pure and Applied Sciences, University of Marmara, Istanbul, Turkey, (e-mail: mesut.gun.72@gmail.com).
https://orcid.org/0009-0006-4952-9855

EYUP EMRE ULKU, is with Department of Computer Engineering, Faculty of Technology, University of Marmara, Istanbul, Turkey (e-mail: emre.ulku@marmara.edu.tr).
https://orcid.org/0000-0002-1985-6461

ILAYDA ULKU, is with Department of Industrial Engineering University of Istanbul Kültür University, Istanbul, Turkey, (e-mail: i.karabulut@iku.edu.tr).
https://orcid.org/ 0000-0003-0464-7007

In addition, the confidence of consumers was shaken in the food safety crisis that emerged with the increase of food-related problems. According to the World Health Organization [3], food safety is one of the most important causes of the most common health problems in the world. Therefore, consumers want to be aware of every process from the production to consumption of the products. This situation causes consumers to prefer businesses where they can track food.

First of all, it is thought that blockchain technology, which has found an application area in the field of finance, will lead to important solutions in many areas. There is no need for a third party for transactions made with this technology. As each transaction takes place, it is processed into the encrypted block by the supply chain member performing that transaction. Each block is linked to previous and next blocks and cannot be changed or deleted by a single chain member. With the blockchain, which is an autonomous technology, transactions can be made automatically by connecting to conditions.

The decentralized nature of the blockchain increases its validity by providing control over the change of information. In addition, thanks to this distributed structure, an error is not collected in a single point and attacks on the network are prevented. However, this digital ledger, which is not guaranteed by any third party, required measures to be taken on important issues such as the risk of users cheating. For this reason, all transactions are processed into the public ledgers of computers that hold an identical copy of each ledger, giving the entire network the power of surveillance. These ledgers are constantly updated when users make their transactions [4].

This nature of blockchain is seen as a potential solution to many problems in the supply chain. With a blockchain-based structure, every changeover of a product from manufacture to sale can be documented, creating a permanent product history. In this way, it may be possible to significantly reduce time delays, additional costs and human errors that hinder today's operations. By using smart contracts, automated control and action flows can be realized during the movement of a product on the chain (such as transferring Z units of money after a product reaches stage X and passes Y control). When we evaluate it from the perspective of the customer, users can be informed about the arrival process of the product they bought and make a more conscious decision.

The aim of this study is to reveal what kind of gains can be achieved by applying blockchain technology to the food supply chain, what obstacles will be encountered and for what

purposes it is used. For this purpose, in the first chapter, the definition of supply chain and the analysis of the main problems such as the difficulty of traceability of today's supply chain processes, lack of trust and lack of coordination between the parties are given. In the second part, what is blockchain technology and its uses in the food supply chain are mentioned. In the third chapter, the advantages and disadvantages of Blockchain technology in a supply chain area are discussed. In the fourth chapter, the supply chain applications of blockchain technology in the field of food are given. In the last part, there is the general evaluation and conclusion part.

II.   SUPPLY CHAIN

A.   Supply Chain and Supply Chain Management

The supply chain can be defined as a chain that connects all the links (suppliers, production centers, warehouses, distribution centers, retailers, etc.) from the raw material supply to the end users [5] as shown in Figure 1. The supply chain is a dynamic process that includes the continuous flow of materials, funds and information across many functional areas. In other words, a company's supply chain; raw material producers convert raw materials and semi-finished products into finished products. In other words, they are all the elements that create value during the manufacturing processes, and then during the delivery of the finished products to the final consumer in the distribution channels [6]. These processes rely on rules, trust, and security provided by third parties that manage this flow [7].

Although the structure of the supply chain varies widely from company to company and from industry to industry, it can be seen in both service and manufacturing organisations. The supply chain structurally begins with the purchase and acquisition of the goods to be sold. It then turns to inventory management and warehouse management to support sales. It ends with the delivery of the products to the customers [8]. But that has changed with the boom of the internet, technological innovation, and the global demand-driven economy. Today's supply chain is no longer a linear as in Figure 1. It is a complex structure [9] consisting of different networks that can be accessed 24 hours a day. At the heart of these networks are consumers who demand that their orders be fulfilled when and how they want it. When, where, how and in the desired quantity, the orders are delivered to the customer in a cost-effective way has become a success method [10]. What is important in supply chain management is the correct planning of activities such as stock levels, supply and demand balance, cost and asset management, cash flow, production and logistics. Therefore, every company should work with a suitable supply chain strategy and design.

Effective management of the supply chain ensures increasing customer satisfaction, reducing the cycle time (from receiving the customer order to the manufacturer to collect the customer's payment), reducing inventory-related costs, and reducing product errors. It should be organized in a way that has sufficient information sharing, roles and responsibilities, and reporting relationships defined [11]. The importance and complexity of supply chain management is increasing exponentially due to the increasing number of customers with increasing demands and increasing competition in the market.

Fig.1. Supply Chain Process

B.   Functioning and Basic Problems of Today's Supply Chain

With the globalization of today's supply chain, many people, companies and institutions become parties to the supply and logistics operation processes, the documents in the transactions are many in variety and number, they include more than one country and each of these countries has different legal rules. Since it is difficult to trace transactions and documents, it causes both high cost, confusion and time loss due to reasons such as loss of documents and the risk of creating fake documents. In addition, the payments between the parties take days and as the products pass through various countries and regions until they arrive at the destination, the traceability of the products becomes difficult as documents can be lost and counterfeited.

The history of traceability dates back to the early 1930s, when some European countries wanted to prove the origin of

high-quality foods such as French champagne. Traceability is a complex issue as it requires the involvement and collaboration of actors throughout the entire supply chain to track a product's history. In practice, chain traceability can be achieved if businesses keep records of their suppliers and customers and share this information with every member along the entire supply chain. Traceability is used to improve food safety, use in quality control activities, fight fraud and manage complex chains. For example, the traditional model of a supply chain starts with the manufacturer and importer as shown in Fig. 2. The next stage is the exporter, manufacturer, and wholesaler. This stage is the intermediate stage that processes the basic products. The last stage is retailer. In summary, there is a linear model in the traditional supply chain from manufacturers and importers to retailers. The disadvantage of this model is that the consumer does not have

a method of verifying the production and distribution stages of the food to be purchased.

Fig.2. Traditional Supply Chain

Since the process is not transparent, the fact that the buyers know the origin and value of the products makes it difficult to determine whether any fraudulent or illegal transaction was committed, by whom, when and where, that is, the responsible person. In addition, the lack of transparency causes a lack of trust between the parties. Trust in the supply chain is defined as the willingness to believe in business partners that can be trusted. Effective supply chain planning based on information sharing and trust among chain members is one of the most fundamental elements of successful supply chain practices. In supply chain relations, trust and risk issues are of great importance, since there is a high degree of independent action between companies within the chain. In addition, trust is considered as an important asset that increases the performance of the companies involved by increasing cooperation, reducing transactions and costs, facilitating market transactions, and improving the ability of companies to keep up with complex and uncertain environments [12].

Another problem in supply chain management is the lack of coordination of activities between the parties. If this problem is solved, businesses will gain benefits such as "reducing costs, increasing service level, using resources more effectively and reacting faster and more efficiently to changes in the market" in supply chain processes [13].

III. BLOCKCHAIN TECHNOLOGY

Although there is no single agreed definition of blockchain technology, in the most basic terms, it is managed by many computers called nodes, which is not under the control of a single person or organization, uses hashing algorithms for verification of transactions and consensus protocols for approval, sorts transactions with timestamp, and is approved. It is a distributed data recording system that keeps an identical copy at all nodes by linking transactions one after another with cryptography and hashing functions, and the data it contains is almost impossible to change and reverse [14].

This word first came to the fore with Satoshi Nakamoto's concept of Bitcoin in 2008. In fact, in Satoshi Nakamotu's article (Nakamoto, 2008), the term "blockchain" is not used directly, while the system is described as the building block where the transactions are recorded, and the addition of each approved block to each other with a special algorithm is expressed as a chain, and then it has been used as a blockchain [14]. The blocks in the blockchain are connected to each other linearly and chronologically [15]. In each block, there is the block order, the block title summary, the summary of the title of the connected and previous block, the time stamp of the time the block was created, the random value and the values of the transfer operations as represented in Fig. 3.

One of the most important characteristics of blockchain is its distributed and shared structure. Therefore, blockchain-based systems have the potential to eliminate costs and conflicts caused by existing intermediaries. Thus, it promises more data integrity, distribution, an environment of trust that does not require intermediaries, and lower transaction costs [16].

We can say that blockchain technology has experienced two revolutions in its history so far; Bitcoin and Ethereum. Bitcoin is the distributed form of the technology called Blockchain 1.0, which provides only data recording and security. In this way, it provided important developments in the financial sector.
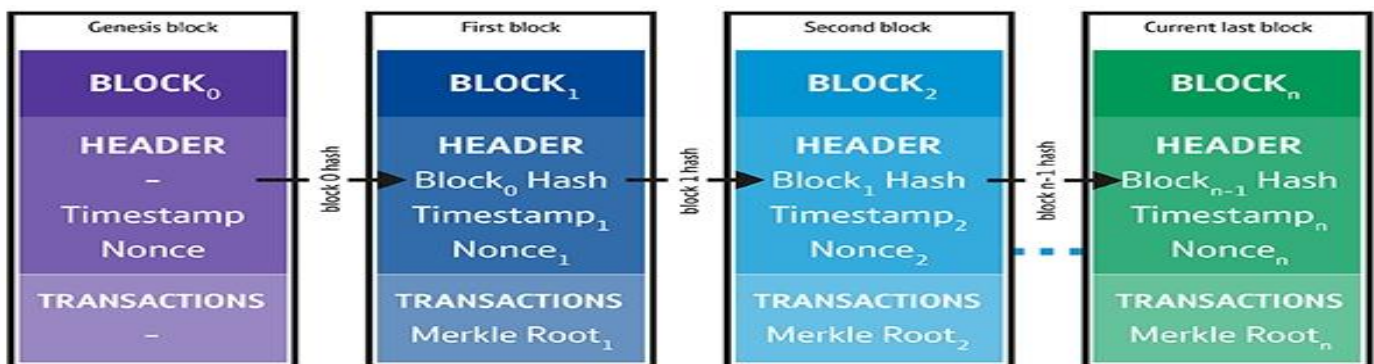
Fig.3. Blokchain Structure [17]

Ethereum, on the other hand, is a platform called Blockchain 2.0, created with the blockchain infrastructure within the framework of Vitalin Buterin's smart contract concept. The reason why Ethereum is so important; It is both an easy-to-apply and a reliable platform for smart contracts, which date

back to pre-blockchain technology. Smart contracts have smart contract accounts like blockchain accounts [18].

The system verifies that every node included in the contract complies with the terms of the contract as a result of coding the details of the information such as the algorithms to be

implemented by the contract and the calculations to be made and uploaded to the Ethereum website. It is very important that the contract is prepared correctly and completely. Otherwise, as in the project called DAO, a user can take advantage of any vulnerability of the smart contract and transfer the money in the contract account to another account [19].

A. Use of Blockchain Technology in Supply Chain

The transparent structure and cryptology feature of the blockchain technology and the decentralized structure of the information flow between the parties offer important opportunities for trust and full-time communication. It offers radical solutions to the problems of miscommunication and product history in the traditional supply chain. With the participation of all supply chain stakeholders in the blockchain network, it is possible to document the permanent and secure product history from raw material to the final product [18]. Necessary notifications reach all rings of the supply chain thanks to the full-time information flow. In this way, a perfect balance of supply and demand is formed.

With blockchain technology, in order to prevent food-related health problems and to renew the consumer's trust in food businesses, it is possible to monitor the processes and conditions of food in the supply chain process, control of the additives and chemicals used, detection of contamination levels, and thus traceability from field to fork [20]. This traceability is done through the radio frequency identification (RFID) tag, QR code, barcode, GPS tag, chip of the internet of things technology. It is one of the important advantages of this technology to monitor every movement from production to sales, to observe the process transparently by consumers, and to prevent imitation and adulteration because food product information cannot be changed [21]. In addition, many food safety problems such as the horse meat scandal, salmonella in eggs, listeria in cheese, E. coli 0157:H7 in hamburgers and food counterfeiting reveal the importance of traceability. In such a food safety issue, the parties in the chain can see where the harmful substances come from, batch numbers, factory and processing data, expiration dates, shipment details and which stores they are delivered to, thanks to blockchain technology [26]. To give an example, Migros supply chain security and transparency [22]; Walmart, food product history and certificates; Provenance, tracking all kinds of food materials from production to consumption; Everledger, wine movements and warehouse information [23]; jd.com uses blockchain technology to track the entire retail process in the fight against fraud.

Another area of use is to prevent losses in perishable food resources. For example, although our country ranks first in the world in vegetable and fruit production, serious losses are experienced during transportation and marketing, as well as decay and deterioration. In order to detect and prevent these losses, it will be possible to monitor the processes from the harvest of vegetables and fruits to their storage, distribution and sale to the customer.

The delay in payments in the supply chain is one of the most important reasons for the bottleneck in the process. Thanks to the smart contracts in blockchain technology, it contributes to the acceleration of financial money transfer transactions of international enterprises, reducing transaction costs and eliminating the risk of fraud [24, 25].

A lot of paperwork is done during the shipping process. These processes cause both time and money loss. It is estimated that the cost of processing documents related to the trade made accounts for 15 to 50 percent of the physical transportation costs. For example, many businesses still use printed bills of lading on paper. This situation creates the need for a department that organizes the documents within the organizational structures of the logistics service providers and the personnel working there. The existence of bill of lading or documentation departments will also come to an end, as the need for printed documents will be eliminated with the blockchain [26, 27].

Smart contracts are computer programs that determine the rules of the blocks that will be formed in the Blockchain. Smart contracts are the determination of the necessary rules and laws in the network infrastructure to be established and this is seen transparently by all participants [28]. As seen in Figure 4, the application process consists of four parts: physical flow, information flow, blockchain and smart contract. On the physical flow side, there are the stakeholders of the supply chain. There is a flow of information between stakeholders in every supply chain. Throughout the supply chain, each stakeholder records information in blocks in the blockchain. These blocks are connected with each other and turn into a chain that includes all the tasks done up to the end of the supply chain, all the stakeholders involved and information specific to a customer. Smart contracts are created by automatically filling in agreed-upon contracts using information found in a blockchain. In smart contract, on chain It is not possible to make any changes without the agreement of the parties involved. For example, a payment is automatically made after all contractual terms for a delivery that has already occurred (eg quantity, quality, timing, etc.) are met [25].
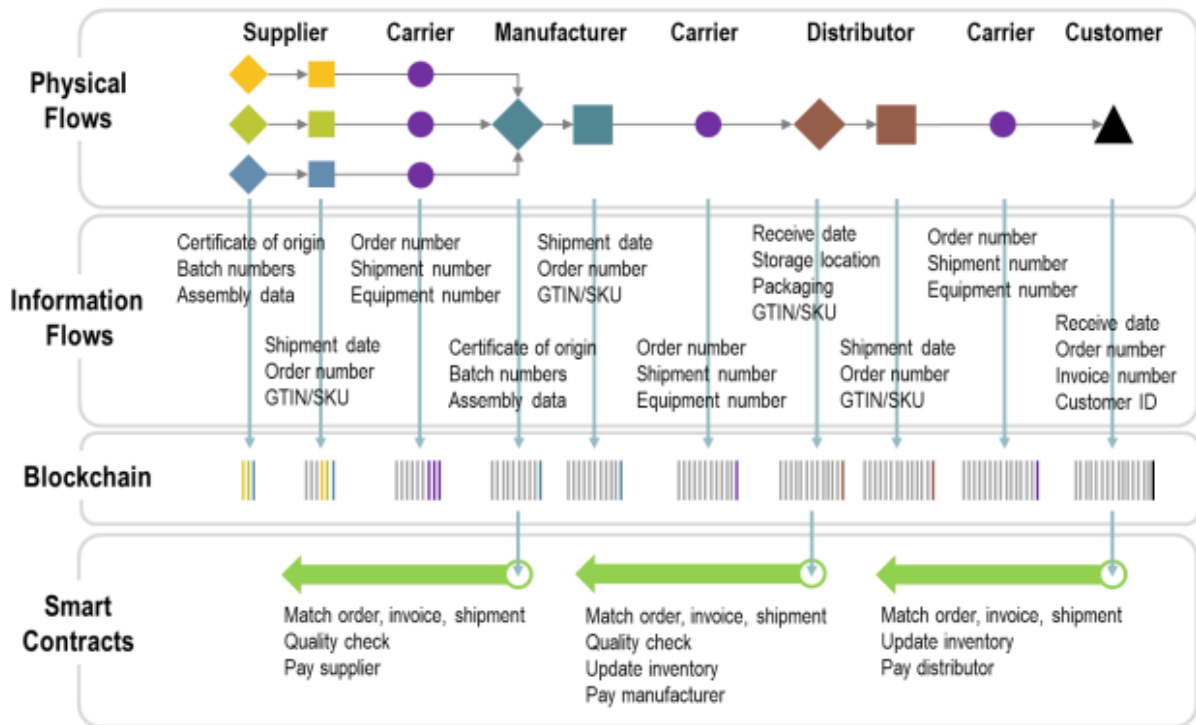
Fig.4. Blockchain applications in the supply chain [25]

IV. ADVANTAGES AND DISADVANTAGES OF USING BLOCK CHAIN IN SUPPLY CHAIN

The use of blockchain technology in the supply chain has many advantages. The first of these is security. Security is at the highest level. Due to the structure of the blockchain, the records cannot be changed, the data is verified multiple times and uploaded to the system upon agreement of all parties.

With the digitization of document transfers and the acceleration of data flow, it provides efficiency and cost advantages, especially in cross-border activities. Considering an activity consisting of tens of people and organizations in more than one country, such a high rate of error and delay is high and records need to be reproduced many times.

Another advantage is that it provides traceability. For the quality and safety of the products, it is possible to trace them throughout the supply chain from field to table. In this way, it is ensured that consumers consume reliable, transparent, traceable and quality products, thus eliminating the food safety concerns of consumers.

Blockchain also bridges the gap between small sellers and large sellers. According to IOHK director of product Aparna Jue, small coffee farmers in countries like Ethiopia may lack the capital to invest in the traceability solutions needed to complete traceability from source to source. In this case, it is unlikely that small coffee farmers will be selected as suppliers to multinational companies. Therefore, only a few large suppliers dominate the market. By using blockchain in industries like coffee and agriculture, all farmers can access traceability solutions with their GPRS-enabled mobile phone, eliminating notorious intermediaries. This enables SMEs to be

secure and transparent, supporting large supply chains and economic growth [29].

After the second step in the supply chain, tracking becomes difficult. Difficult to follow-up causes many details to be overlooked and security vulnerabilities such as theft, smuggling, loss, and counterfeit product transportation.

Since the supply chain includes multiple processes and processes, problems such as loss of documents and misarrangement may occur, no matter how careful attention is paid. Thanks to the smart contracts of the blockchain technology, such problems are reduced as the processes do not require any manual operations. In addition, high paperwork costs and the need for paperwork personnel in the supply chain process are avoided.

Another advantage is that, thanks to smart contracts, human-induced errors are minimized, as processes normally performed by humans are performed automatically. In addition, problems such as loss of documents and incorrect arrangement of documents are eliminated.

Thanks to the smart contracts in the blockchain technology, payments can be made faster, transaction costs are lower and the risk of fraud is eliminated.

Blockchain also bridges the gap between small sellers and large sellers. Aparna Jue, IOHK product director, said: "Considering the coffee industry, small coffee farmers in countries like Ethiopia, for example, may lack the capital to invest in the traceability solutions needed to complete traceability from source to source. But this is not the case for larger coffee producers, who not only have access to more resources but also the latest technologies. While larger farmers can use these systems to secure certificates for the sustainability, traceability and validity of their coffee beans, smaller farmers lack access to the technology needed to keep

these records. Small farmers are unlikely to be selected as suppliers to multinational companies without this information. Therefore, only a few large suppliers dominate the field. Using blockchain in industries like coffee and agriculture, all farmers need access to traceability solutions. With a basic GPRS-capable cell phone of the kind that has been around for 20 years, farmers can become part of a global network. Blockchain enables the transportation and traceability of their products via a phone app, eliminating notorious middlemen. This enables SMEs to be secure and transparent, supporting large supply chains and economic growth." [30].

Moreover, it is not dependent on a central authority. This allows transactions to run faster and costs to be lower. However, this advantage also paves the way for disadvantages. Because this system, which works without being tied to a place, can be configured in different ways for different purposes by various software developers. This means that the chains are not standard and if the chain members have any problems, they cannot be solved easily because there is no interlocutor. This is the main reason why investors are more cautious about blockchain applications [29].

One of the obstacles to the use of blockchain technology is how well it will be accepted in the supply chain industry. Because there are obstacles such as the fact that the stakeholders are at different levels in terms of compliance with blockchain technology, the stakeholders do not want to abandon their past habits, the material and moral burden of adapting to technology and changing the way of doing business is high, compliance problems between stakeholders, and legal differences between countries.

The difficulty of understanding this technology is also an important obstacle to the use of blockchain technology. Because to understand blockchain technology, it is necessary to have the working principle, system and security knowledge of the blockchain. Therefore, stakeholders should receive training in these areas [31].

Another obstacle to the use of blockchain technology in the supply chain is that the relevant legal regulations are still in the preparation stage. Issues such as the legal binding and infrastructure of smart contracts, whether records in the blockchain can be accepted as evidence are also disadvantages of blockchain technology.

Since the blockchain includes all records from the first transaction, the scalability problem arises as the size of the registry grows over time. In addition, transactions can be made in a certain way per second in the blockchain. As the number of participants in the blockchain increases, the number of transactions will naturally increase, so the response time to transactions will increase.

The fact that the blockchain technology is not yet technologically mature and does not become a standard application is another obstacle to the use of this technology. In addition, high development costs and the possibility of failure of startups are barriers to the use of blockchain technology. Because if the attempt is unsuccessful, it will cause loss of both money and time.

In addition, since the blockchain is a new technology and has decentralized autonomous organizations, authorization problems are of great concern, and in case of a data breach or legal dispute, the question of who will be held legally responsible and how to deal with the regulations and laws related to the limits of authority comes to mind [32].

V. FOOD SUPPLY CHAIN APPLICATIONS OF BLOCK CHAIN TECHNOLOGY

A. Transparent Path

The Transparent Path platform displays the food journey from farm to consumer in real time. It allows companies to manage food safety and research the origin of food. This platform combines sensor technology, third-party auditors and decentralized blockchain applications to provide a transparent real-time view.

B. TE-FOOD

It is the world's largest public blockchain-based farm-to-table food tracking system used by Migros, Switzerland's largest grocery chain. With the application of TE-FOOD, transparency is provided for Migros customers. How does this blockchain system work? Suppliers are required to enter data into the Electronic Product Code Information Service (EPCIS). Information added to the EPCIS system is added to Migros' blockchain network. Finally, consumers who scan the QR code can access detailed information about the products, just like Carrefour and Walmart.

C. Ripe.io

It offers enterprise blockchain technology for the food and agriculture industry to create greater trust and transparency between food manufacturers, distributors and customers. By making use of sensor data, the data of the source of the food is processed into a blockchain-based system, providing transparency from field to fork. It is a technology platform where everyone from the producer to the distributor is involved, contributes to data and follows the journey of food.

This blockchain technology platform was first used to grow tomatoes. By collecting farmer data and information about temperature, humidity and tomato chemistry from sensors, it is aimed to grow better tomatoes. In this way, farmers will be able to meet market demand effectively and produce high quality, sustainable products. In addition, distributors will be able to monitor the process effectively and receive real-time information about food safety and delivery, while consumers will be able to monitor the stages of the product they purchase throughout the supply chain.

D. CBH Group

Australia's largest grain producer, CBH Group, has begun trials to use blockchain technology for shipping its products. Grain growers' cooperative has started to use a blockchain-based system in order to track the origin of the grain from the producers and document its quality. The main purpose of the system to be used is to show the data in the supply chain to potential buyers and to increase the trust in grain warehouses [33].

Research Article

E. AgriDigital

The AgriDigital initiative was established in 2015 and emerged in agricultural supply chains.It was established to solve emerging problems on a blockchain-based basis. The company's mainits field of activity is in grain supply chains, but in the fields of rice and cotton industry is also working.

AgriDigital supports grain producers, buyers, wholesalers, intermediaries, shippers and agricultural on a single platform using blockchain technology brings together. Thus, stakeholders can make smart contracts over this structure, can carry out delivery and payment transactions instantly. A cloud-based application Besides, AgriDigital operates using blockchain protocol layers. While establishing AgriDigital, in order to find solutions to the agricultural problems given below developed.

- Inability of farmers to receive their payment as soon as they deliver their products,
- Inability of buyers to have sufficient financial resources during the procurement of agricultural products,
- Investment due to the inability of investors to monitor and control the supply chain abstain from,
- Since consumers do not know where the food comes from and under what conditions, anxiety in purchasing transactions [34].

F. Provenance

Thanks to the online platform that the company has established, information among its customers enabling them to change. Transparency between partners in information sharing is important although it is open to those with authority, it cannot be changed. The most important application The aim is to verify the origin of the product, especially in the field of food, and to ensure that the fake use of certificates precedes it. Thus, the traceability of the products will increase and the brands will achieve the desired quality attachment will be achieved. Provenance's data solutions, by tagging with smart tags it can be integrated into any physical product online or via mobile application. For example, which supply chain does Indonesian tuna fish from the shore to the end consumer? It has been successfully followed that it has gone through all stages [34].

VI. CONCLUSION

The supply chain is a whole consisting of the stakeholders involved from the production of a product to reaching the consumer. The supply chain can be very simple in structure as well as very complex and complex. Today's supply chain management structure cannot be a solution to the problems of this complex and complex structure. Blockchain technology is thought to be a solution to many of these problems.

In this study, the advantages and disadvantages of blockchain technology, which has applications in many sectors, especially in finance, if it is applied to the food supply chain, for what purposes it can be used and application examples are emphasized. It has been seen that it will provide significant added value. However, although it has become popular today, more research is needed on the application of blockchain technology in the food supply chain. In addition, since Blockchain technology has not yet completed its technological competence and due to its complex nature, a detailed analysis process is required before it can be implemented.

References

[1] N. Kshetri, "Blockchain's roles in meeting key supply chain management objectives". International Journal of Information Management, 2018.

[2] M. Christopher. "Logistics and Supply Chain Management". Financial Times Prentice Hall.cument, 2011.

[3] World Health Organization – WHO. (2022, May 19). Food safety. Retrieved July 13, 2023, from https://www.who.int/news-room/fact-sheets/detail/food-safety

[4] G. Volpicelli. "Support The Guardian". Retrieved July 13, 2023, from https://www.theguardian.com/technology/2018/mar/10/blockchain-music-imogen-heap-provenance-finance-voting-amir-taaki.

[5] Gıda Bilimi.com. Retrieved July 13, 2023, from https://www.gidabilimi.com/en/component/content/article/62-makale/3097-tedarik-zinciri-yonetimi?Itemid=157.

[6] M. Al-Mashari, M. Zairi "Supply Chain Re-engineering Using Enterprice Resource Planning (ERP) Software of a SAP R/3 Implementation Case", International Journal of Physical Distribution and Logistics Management, 30 (3/4), 2000, 296-313.

[7] A.K. Pundir, J. Devpriya, M. Chakraborty, and L. Ganpathy. "Technology Integration for Improved Performance: A Case Study in Digitization of Supply Chain with Integration of Internet of Things and Blockchain Technology". 9th Annual Computing and Communication Workshop and Conference (CCWC), 2019, 170- 176.

[8] F. Çizmeci. Tedarik Zinciri Yönetimi, Alfa Basım Yayım, Ocak, 2002.

[9] Oracle. SCM (Tedarik Zinciri Yönetimi) Nedir? Retrieved July 13, 2023, from https://www.oracle.com/tr/scm/what-is-supply-chain-management/.

[10] R. B. Handfield and E. L. Nicholas. "Introduction to Supply Chain Management", Prentice-Hall, Inc., New Jersey, 1999.

[11] Deloitte. Tedarik Zinciri Stratejisi and Organizasyonu. Retrieved July 13, 2023, from https://www2.deloitte.com/tr/tr/pages/operations/solutions/supply-chain-management-services/supply-chain-strategy-and-organization-services.html.

[12] A. E. Şengün. "Alıcı-tedarikçi ilişkilerinde güven and güvensizliğin mübadele performansı üzerine etkileri: Ankara mobilyacılar sitesi örneği". Yönetim Araştırmaları Dergisi, 7 (1-2), 2007, 5-38.

[13] C. M. Tsou. "On the strategy of supply chain collaboration based on dynamic inventory target level management: A theory of constraint perspective". Applied Mathematical Modelling 37 (7), 2013: 5204-14. https://doi.org/10.1016/j.apm.2012.10.031.

[14] Ç. Karahan and A. Tüfekçi. "Blok Zincir Teknolojisinin İç Denetim Faaliyetlerine Etkileri: Fırsatlar and Tehditler",.Denetişim Dergisi, 9, 2019, 19-56.

[15] F. Tian. "An agri-food supply chain traceability system for china based on RFID & Blockchain technology". Service Systems and Service Management (ICSSSM), 13th International Conference on. IEEE, 24-26 June, 2016. Kunming, China.

[16] J. Berryhill, T. Bourgery and A. Hanson. "Blockchains Unchained: Blockchain Technology and its Use in the Public Sector"., OECD Working Papers on Public Governance, No. 28, 2018. Paris: OECD Publishing. http://dx.doi.org/10.1787/3c32c429-en

[17] M. E. Eker. "Blockchain Nedir?".Retrieved July 13, 2023, from https://www.mehmetemineker.com/blockchain-interoperability/.

[18] S. Çağında and S. Topal. "Proof of Meet Konsensüs Protokolünün Gıda Taşımacılığı Üzerine Bir Uygulaması". 2020. https://dergipark.org.tr/en/download/article-file/1287494

[19] B. Yıldız. "Dijital dönüşüm Sürecinde blok zinciri teknolojisi and akıllı sözleşmeler". Dijital Dönüşüm Trendleri. Filiz Kitabevi. Kasım, 2019. 120-143.

[20] B. Keleş ve G. Ova , "Gıda Tedarik Zinciri Yönetiminde Bilgi Teknolojileri Kullanımı", Adnan Menderes Üniversitesi Ziraat Fakültesi Dergisi, c. 17, sayı. 1, ss. 137-143, Tem. 2020, doi:10.25308/aduziraat.695732.

Research Article

[21] D. Gerdan, C. Koç, and M. Vatandaş. "Gıda ürünlerinin izlenilebilirliğinde blok zinciriteknolojisi kullanımı". Tarım Makinaları Bilimi Dergisi. 2020. 16(2): 8-14.

[22] L. N. Yılmaz. "Bir Tedarik Zinciri Uygulaması: Migros Blockchain". 2021. Retrieved July 13, 2023, from https://medium.com/@iublocktech/bir-tedarik-zinciri-uygulamas%C4%B1-migros-blockchain-d1606afe1316.

[23] Everledger. Can blockchain wine help put a cork on forgery? Retrieved July 13, 2023, from https://everledger.io/can-blockchain-wine-help-put-a-cork-on-forgery/.

[24] J. Francis. "Closing The Hall Of Mirrors, How Blockchain Will Simplify And Transform The Suppy Chain". 2018. Accenture Consulting.

[25] J. P. Rodrigue. "Efficiency and sustainability in multimodal supply chains", International Transport Forum Discussion Paper, No. 2018-17, Organisation for Economic Co-operation and Development (OECD), International Transport Forum. 2018. Paris, http://dx.doi.org/10.1787/12f93f71-en

[26] N. Hackius and M. Petersen. "Blockchain in logistics and supply chain: Trick or treat", In Proceedings 8-13, October 2017. 112-113. Hamburg International Conference of Logistics (HICL).

[27] R. Ö. Yıldız and S. Baştuğ. "Blok zincir teknolojisi kapsamında elektronik konşimento", 2018.

[28] F. A. Tian. "Supply chain traceability system for food safety based on HACCP, blockchain & Internet of things". 2017. In 2017 International conference on service systems and service management.

[29] İ. Bakan and Z. H. Şekkeli. "Blok Zincir Teknolojisi ve Tedarik Zinciri Yönetimindeki Uygulamaları. 2019. https://dergipark.org.tr/tr/download/article-file/733144.

[30] A. Hurst. "Blockchain use cases within transport and logistics. 2020, 24 July. Retrieved July 13, 2023, from https://www.information-age.com/blockchain-use-cases-within-transport-logistics-16419/.

[31] J. Dai. "A Dissertation for the degree of Doctor of Philosophy. Three Essays on Audit Technology: Audit 4.0, Blockchain, and Audit App." 2017. New Jersey: The State University of New Jersey.

[32] A. Chalker. "Why Internal Auditors Must Care About Blockchain." 2018. Retrieved July 13, 2023, from https://blog.protiviti.com/2018/06/12/internal-auditors-must-care-blockchain/

[33] Fintech İstanbul. "Tarım sektörü de Blockchain kullanmaya başlıyor." 2017. Retrieved July 13, 2023, from . Retrieved July 13, 2023, from https://fintechistanbul.org/2017/08/07/tarim-sektoru-de-blockchain-kullanmaya-basliyor/

[34] H. Kaya. "Sektörel and Operasyonel Blokzincir Uygunluk Analizlerinde Kullanılacak Kriterlerin Belirlenmesi". 2019. Retrieved July 13, 2023, from http://acikerisim.ybu.edu.tr:8080/xmlui/handle/123456789/2064.

BIOGRAPHIES

MESUT GUN In 2022, he started his graduate education at Marmara University, Computer Engineering Department. He worked as IT Manager and software engineer at Jiber and Sümer Lojistik A.Ş (P&G). His research interests are project management, software engineer, IT auditing, machine learning and cryptocurrency.

EYUP EMRE ULKU He is an Assistant Professor in the Department of Computer Engineering at Marmara University, Turkey. He completed his Ph.D. in Computer Engineering at Marmara University in 2018. His research interests include wireless communications, ad hoc networks, image processing, deep learning and educational technologies in engineering education.

ILAYDA ULKU She earned her Ph.D. degree in Industrial Engineering at Marmara University in 2019. In 2010, she joined as a Research Assistant in the Istanbul Kültür University at Industrial Engineering Department where she currently serves as an Assistant Professor since 2019. Her current research interests are Mathematical Programming, Scheduling, Data Mining, and Supply Chain Management.

Research Article

MobileMRZNet: Efficient and Lightweight MRZ Detection for Mobile Devices

Necmettin Bayar, Kubra Guzel and Deniz Kumlu

Abstract—**The Machine Readable Zone (MRZ) is a standardized section found on identification documents (IDs) that adhere to the International Civil Aviation Association (ICAO) Document 9303. The MRZ region contains sensitive personal information about the document holder, and a portion of this information is utilized to establish communication between the passive chip within the ID and a mobile device via Near Field Communication (NFC) protocol. This communication is crucial as the data retrieved from the ID's chip is subsequently used in authentication steps such as face or fingerprint recognition. Thus, accurate detection of the personal information within the MRZ region is vital. In this research study, we propose a fast and lightweight approach for MRZ region detection called MobileMRZNet, which is based on the BlazeFace model. The MobileMRZNet architecture is specifically designed for mobile Graphical Processing Units (GPUs) and enables rapid and precise detection of MRZ regions. To train and evaluate the model, a dataset consisting of both simulated and real data was created using Turkish national IDs. The BlazeFace model was reconfigured and trained specifically for MRZ region detection. The detector, based on BlazeFace and trained on augmented real and simulated data, demonstrates excellent generalization capabilities for deployment with real IDs. Both qualitative and quantitative results confirm the superiority of our proposed method. The mean Intersection over Union (IoU) for the first frame, without utilizing any layout alignment for IDs, achieves an accuracy of approximately 81\%. For character recognition, the method achieves 100\% accuracy after three consecutive frames. The model operates in less than 10 milliseconds on a mobile device, and its size is around 400 KB, making it significantly fast, lightweight, and robust compared to any existing MRZ detection methods.**

Index Terms—**Biometric identification, Blazeface model, ID Cards, MRZ Detection, Travel Documents.**

I. INTRODUCTION

IDENTITY DOCUMENTS (IDs) play a vital role in ensuring national security and enabling citizens to engage in various activities such as voting, traveling, and accessing government and private sector benefits. The accurate verification of IDs allows governments to effectively monitor their citizens, identify illegal immigrants, prevent identity theft, track criminals, monitor terrorism activities, and identify individuals who may pose a risk to national security. Moreover, governments provide services specifically tailored to their citizens, and IDs serve as a means to streamline service delivery by ensuring that only eligible citizens receive these services, minimizing any potential errors or misuse by non-citizens.

When the brief history of IDs are checked, it is evident that they first appeared around 1876. However, they did not become widely accessible until the early 20th century [1]. The introduction of photographic IDs occurred in 1915, following the well-known Lody-Spy scandal [2]. Prior to 1985, there was no global standardization for IDs. It was in 1985 that ISO/IEC 7810 established standardized guidelines for the shape, size, and content of IDs, which were further refined in 1988 through ISO/IEC 7816. As technology advanced, radio frequency identification (RFID) chips were integrated into IDs, enabling the storage of sensitive personal information alongside biometric data like photographs and fingerprints. The most recent standards for IDs are defined by the International Civil Aviation Association (ICAO), and the majority of countries worldwide have aligned their ID systems with these standards [3].

The International Civil Aviation Organization (ICAO) document 9303 establishes the standardized guidelines for machine-readable travel documents, including national IDs, passports, and more. Presently, over 190 countries have adopted these standards and incorporate machine-readable zones (MRZs) within their respective IDs.

The MRZ is a specific section on IDs that contains sensitive personal information about the document holder. It is designed to streamline and expedite the scanning process for government-issued documents such as IDs and passports. The information within the MRZ can be read using optical character recognition (OCR) methods, such as the Tesseract OCR engine, as the characters in the MRZ region have a unique font called OCR-B. To enhance the accuracy and performance of the OCR engine, it is crucial to accurately detect the exact MRZ region on IDs beforehand [4].

The MRZ region is commonly used as part of the authentication process, with some of its information utilized to access the chip within IDs via the Near Field Communication (NFC) module of mobile phones. NFC comprises a collection of short-range wireless technologies that establish a reliable

Necmettin Bayar, is with Artificial Intelligence Department, Kobil Technology, Istanbul, Turkey, (e-mail: necmettin.bayar@kobil.com).
https://orcid.org/0000-0003-2367-828X

Kubra Guzel, is with Artificial Intelligence Department, Kobil Technology, Istanbul, Turkey, (e-mail: kubra.guzel@kobil.com).
https://orcid.org/0009-0002-8401-6983

Deniz Kumlu, is with Artificial Intelligence Department, Kobil Technology, Istanbul, Turkey, (e-mail: deniz.kumlu@kobil.com).
https://orcid.org/0000-0002-7192-7466

connection between the passive chip on IDs and mobile devices, typically requiring a distance of 4cm or less [5]. To initiate communication via NFC and retrieve sensitive personal or biometric information from the chip, control over the data written on the ID's MRZ region, such as the date of birth, document number, and expiration date, is necessary. Once this information is provided to the chip, a communication process known as the hand-shake protocol begins, allowing the extraction of highly secure personal information, facial biometric images, and fingerprints from the ID's chip. This information is highly reliable for identity verification, as it is difficult to manipulate, tamper with, or falsify the data stored within the chip. Additionally, passive and active authentication processes implemented on the chip help ensure the integrity of the information, guarding against cloning, tampering, and manipulation [6]. As a result, the use of NFC-based IDs authentication has gained popularity, particularly in financial and banking mobile applications.

Several methods have been proposed for MRZ detection and character reading [7-17]. The initial method lacked a dedicated detection module and required users to manually align their IDs with a specific template on the device screen, followed by manual cropping to obtain the MRZ region. However, this heuristic approach heavily relied on the user's ability to align the ID properly, leading to inaccuracies if alignment was not precise [7]. Subsequently, methods were introduced that employed binarization of the MRZ region using adaptive thresholding. Horizontal and vertical histogram projections were utilized to decompose the document image into character parts, and character recognition algorithms were applied to extract the desired information [8, 9]. However, these methods were found to be less robust in scenarios with nonuniform illumination and situations involving occlusion, making them unsuitable for sensitive mobile applications. In a different approach, a combination of Fuzzy Adaptive Resonance Theory (ART)-based Radial Basis Function (RBF) network and Principal Component Analysis (PCA) algorithm was proposed for passport recognition [10]. This method involved isolation and connected component analysis, filtering and selecting clustered lines of text, and converting the input image to a binary image prior to component search. However, this method relied on video frames and fusion of results from multiple frames, which increased processing time. Furthermore, the complexity of the algorithm made it unsuitable for mobile implementation, and it was specifically designed for passport documents.

Neural network (NN) based models have been proposed for MRZ detection as well. In a study by Khan et al. [11], a combination of Convolutional Neural Network (CNN) and Artificial Neural Network (ANN) was employed for accurate recognition of the passport MRZ region, even when dealing with passport images of varying sizes and skewed orientations. To achieve effective character segmentation, the method included MRZ line detection using a connected component analysis algorithm and skew correction using a perspective transform algorithm. The results of this approach showed

promise, but it should be noted that the method is complex and specifically applied to passport images, limiting its applicability to other types of IDs.

A recent MRZ region detection model named MRZNet, proposed by Li et al. [12], has demonstrated remarkable performance compared to other existing MRZ detection models. MRZNet is based on MobileNetV2 architecture [13]. The authors conducted a comprehensive comparison with Tesseract-based methods [14], a deep learning-based commercial solution [15, 16], and end-to-end NN based text spotting approaches [17, 18]. They reported that their method outperforms existing solutions by a significant margin and can effectively extract MRZ information from passports of various sizes and content. However, similar to other existing solutions, the running time of the method and the size of the model may not be optimal for mobile device implementation. Additionally, it should be noted that the evaluation of MRZNet's results was specifically focused on passports and not on other types of travel documents, limiting its generalizability to those document types.

Our proposed model has been rigorously compared with two well-known models, PassportEye [14] and UltimateMRZ [15] utilizing two publicly available datasets (MIDV-500 [19] and MIDV-2019 [20], in addition to a dataset specifically generated for this study. These comprehensive comparisons offer insights into the performance of our model in terms of character error rate (CER), model size, and inference time, highlighting its capabilities and advantages for the mobile platforms.

A. Types of Graphics

The MRZ is a designated section within IDs that holds sensitive personal information of the document holder. Currently, the majority of countries incorporate MRZ regions in their IDs. The specifications and formats of the MRZ region are defined by the ICAO document 9303 [3]. The specific layout and content of the MRZ region may vary depending on the type of document, such as passports, national IDs, or other travel documents.

- "Type 1" refers to a common format for national IDs, which are typically similar in size to credit cards. In this format, the MRZ region of the ID contains three lines, each consisting of 30 characters.
- "Type 2" refers to a less common format for IDs, which deviates from the typical credit card-size. In this format, the MRZ region of the ID contains two lines, and each line consists of 36 characters.
- "Type 3" refers to the standard format used for passports. In this format, the MRZ region of the passport contains two lines, with each line consisting of 44 characters.

The commonly used ID formats are Type 1 and Type 3 IDs. Type 1 IDs is 85.6 × 54.0 mm (3.37 × 2.13 in) in size such as credit cards. The MRZ data in Type 1 IDs consists of three rows, with each row containing 30 characters. The characters used in the MRZ region are limited to uppercase letters "A–Z", digits "0–9", and the filler character "<". Type 3 is a passport

162

and contains two rows of 44 characters in each and the characters are the same as in Type 1.

Indeed, the MRZ region specifications can vary depending on the document types and countries. In the case of Turkish national IDs, the MRZ region consists of three lines, with each line containing 30 characters. On the other hand, Turkish passports have a different MRZ format, with two lines and each line consisting of 44 characters. In the scope of the study, the focus was primarily on "Type 1" and "Type 3" IDs, which are typical for national IDs and passports, respectively, in Turkey. However, the methodology and findings of the study can also be applicable to standardized foreign IDs that comply with the ICAO specifications.

The decomposition of the MRZ region in the simulated Turkish ID are presented in Fig. 1. Highlighted information inside the red boxes in the Fig. 1 can be described in correct order as follows;

- (First line) Document Type "I" is for ID card, country code, document number, control digit, national identification number.
- (Second line) Date of birth, control digit, sex "M" refers to male and "F" refers to female, expiration date of the document, control digit, nationality, control digit.
- (Third line) Surname, Name.

Fig.1. MRZ region in simulated Turkish ID document and decomposition of the MRZ region.

Accurate detection of the document number, date of birth, and expiration date from IDs is crucial for initiating communication with the passive chip inside the IDs using mobile devices. The information extracted from the MRZ region, including these specific details, is used to establish a connection with the chip via OCR technology. If any of the characters in the MRZ region are recognized incorrectly, the communication process will not initiate. In such cases, the MRZ region detection process will restart until all the characters are successfully recognized by the OCR engine, ensuring the accuracy and reliability of the extracted information.

Many financial institutions and banks have adopted digital onboarding systems to attract new customers and facilitate secure account access. One integral component of this process is the detection of the MRZ region, particularly in the widely used "Know Your Customer" (KYC) onboarding system. KYC is a regulatory requirement and a set of processes and procedures that businesses, especially in the financial sector, must follow to verify and identify their customers. The KYC

process involves gathering and verifying relevant information about customers to ensure their identities, assess potential risks, and prevent illegal activities such as fraud, money laundering, and terrorist financing. The KYC process typically involves obtaining identification documents, verifying the authenticity of the documents, collecting additional information about the customer, and conducting risk assessments. This information is used to establish the customer's identity, understand their financial activities, and ensure compliance with legal and regulatory obligations.

Absolutely, accurate and efficient detection of the MRZ region at the beginning of the KYC steps is highly crucial. The MRZ region contains vital information about the customer. By accurately detecting and extracting this information, businesses can establish the customer's identity with confidence and ensure the integrity of the onboarding process. Reliable extraction of crucial information from the MRZ region enables businesses to verify the customer's identity more effectively, streamline the onboarding process, and reduce the risk of errors or fraudulent activities. It facilitates the automatic population of customer data, eliminating the need for manual entry and minimizing potential human errors. By setting a strong foundation through accurate and efficient MRZ region detection, businesses can enhance the overall KYC process, improve customer experience, and ensure compliance with regulatory requirements. It helps establish trust and confidence in the onboarding process, ultimately leading to a successful and streamlined customer onboarding journey.

In this study, we have developed a specialized MRZ detection solution that is optimized for mobile devices, ensuring both speed and accuracy. Our approach is based on the BlazeFace model, a lightweight deep learning model created by Google. By training our model with a combination of real and simulated data that we generated, we have achieved impressive results in detecting the MRZ region. Our proposed method offers fast and precise detection capabilities for the MRZ region, making it applicable for various types of IDs such as national IDs, passports, and visas. The training process involved significant effort to ensure optimal performance, resulting in reliable and efficient detection results. By leveraging the power of deep learning and tailoring the model specifically for mobile devices, our solution provides a practical and effective approach for MRZ detection. It offers the potential to enhance identification processes, improve efficiency, and enable secure and reliable document verification in a mobile environment.

The rest of the paper is organized as follows. In section 2, MRZ region and its importance is discussed. Section 3 introduces the popular BlazeFace model for object detection. In section 4, proposed approach is introduced, and the dataset details and experimental results are explained in section 5. The paper is concluded in Section 6.

II. BLAZEFACE MODEL

BlazeFace is proposed by [21] for lightweight and well performing face detection method on mobile devices. In their test cases, some flagship mobile devices can run at sub-millisecond in face detection. It is inspired from MobilNetV1/V2 architectures [13, 22] and single shot multibox

detector (SSD) models [23]. The first model is exploited for feature extraction and the second model is exploited for GPU-friendly anchor scheme. In addition, alternative approach is applied to the non-maximum suppression (NMS) algorithm for additional refinement at the final stage. BlazeFace is primarily used for face detection purposes and it is also combined with mobilefacenets [24] in the recent study [25].

Many models are using traditional convolution netwroks (generally, it is *3×3* kernel size) on the input image and the computational cost can be significant. From the computational view, input image has a size *s×s×c*, where *s* is the image dimensions and *c* is the number of channel and the convolution kernel is *k×k×d* where *k* is the kernel dimension and *d* is the number of kernels. Then, total number of operations will be ds^2ck^2 for the normal convolution case. In MobileNetV1/V2 depth-wise separable convolution computation is used which consists of depth-wise and point-wise convolutions. For the same size input image and kernel like in the normal convolution case, depth-wise and point-wise convolutions' computations will become s^2ck^2 and s^2cd, respectively. Thus, total computation for the depth-wise separable convolution will be $s^2ck^2 + s^2cd$ and their ratio becomes factor of $\frac{d}{s^2}$. There is factor of $\frac{k^2d}{k^2+d}$ decrease between the normal convolution and depth-wise separable convolution [22]. This reduction in computation makes the MobileNetV1/V2 models more computationally efficient while still maintaining good performance. It allows for faster inference and makes these models suitable for resource-constrained environments, such as mobile devices.

In addition, between the depth-wise and point-wise convolution operations, the latter one takes more time not only due to the arithmetic operations but also due to fixed costs and memory access factors. Thus, increasing the kernel size of the depth-wise part is cheap and does not explode running time of the model. In [22], the use of a *5×5* kernel size in the depth-wise convolution operation has been shown to be effective in increasing the receptive field size and improving the performance of the model. This approach provides a balance between computational efficiency and capturing more comprehensive information from the input data. By optimizing the kernel sizes and balancing computational costs, the BlazeFace model achieves a good trade-off between model efficiency and receptive field enlargement, making it suitable for real-time applications on mobile devices.

To further accelerate the progression of the receptive field size, a double BlazeBlock is introduced in addition to the single BlazeBlock. The double BlazeBlock is designed to effectively capture larger contextual information and enhance the understanding of complex visual patterns. The double BlazeBlock consists of two consecutive sets of convolutional layers, depth-wise separable convolutions, and non-linear activation functions. Each set of convolutions is followed by a down-sampling operation, typically achieved through max pooling or strided convolutions, which reduces the spatial dimensions of the feature maps. By stacking two BlazeBlocks together, the receptive field of the model is increased, allowing it to capture more global information and contextual dependencies. The double BlazeBlock architecture enables the

network to learn more robust and discriminative features, enhancing its ability to accurately detect and classify objects. This progression in receptive field size is particularly beneficial for tasks that involve objects with varying scales or complex spatial relationships. Both single and double Blazeblock architectures are shown in Fig. 2
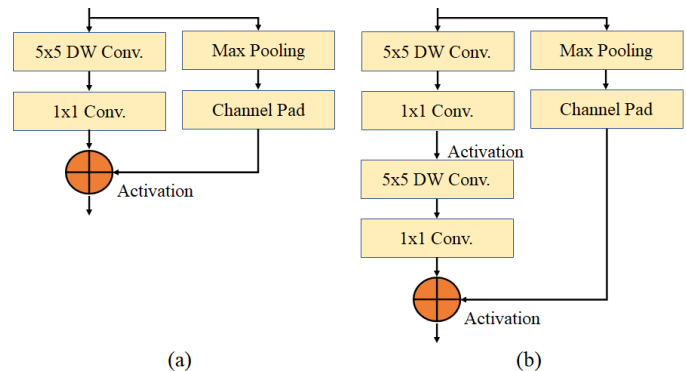
Fig.2. (a) Single Blazeblock, (b) double Blazeblock.

By incorporating the double BlazeBlock into the network architecture, the model can effectively handle larger and more diverse visual inputs, making it suitable for applications such as object detection, scene understanding, and image classification.

For the feature extraction part, the input RGB image (face image) is *128×128*, BlazeFace model architecture contains 5 single BlazeBlocks and 6 Double BlazeBlocks. The highest channel resolution is 96 and the lowest spatial resolution is 8 ×8.

In addition, the classical non-maximum suppression algorithm (the final bounding box depends only one of the candidate anchor) is replaced with blending strategy that predicts the regression parameters of bounding boxes as weighted mean between overlapping estimations. In [21], it is mentioned that this replacement brought 10\% increase in the accuracy for the detection results.

III.   PROPOSED METHOD

The BlazeFace model [21], originally developed for face detection and facial landmark detection on mobile devices, has proven to be effective with its lightweight design and high-speed architecture. It performs comparably well to other popular face detection models while offering the advantages of its lightweight nature. Leveraging the performance of the BlazeFace model in face detection, we have modified it to detect the MRZ region in IDs.

In our modified model which is shown in Fig. 3, the layers of the BlazeFace model remain the same, but the input sizes have been increased from 128 to 320. This allows for the collection of features from the 9th layer output and the last layer output, increasing the total anchor count. While a lower anchor count may reduce inference time, it can also compromise model performance. Thus, anchor counts and schemes have been updated to achieve better detection performance.

Typically, face detection models assume that the aspect ratio of the detected face's width and height is equal to 1, and prior boxes are set accordingly. However, in the case of the MRZ region, it has been determined that the aspect ratio for width to height is approximately 4. Therefore, the aspect ratio value for
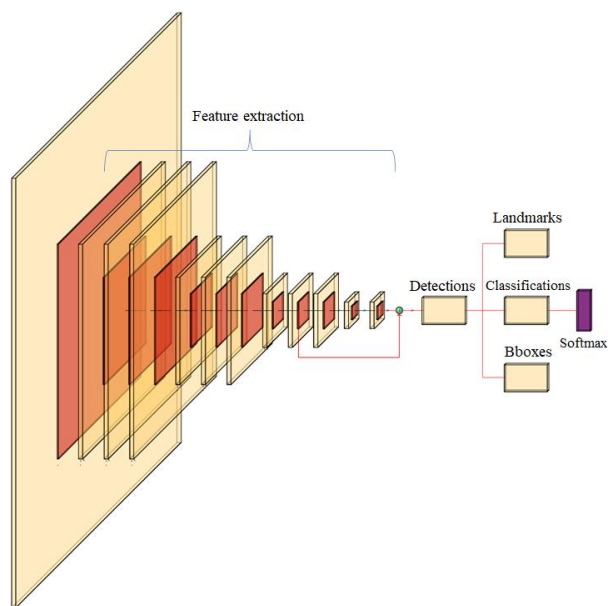
Fig.3. Block diagram of our proposed model.

the prior boxes has been changed to 4, and specialized anchor calculations have been performed to improve the results. In the experimental results, it has been observed that setting the aspect ratio as 3 performs better than 4 due to an additional non-maximum suppression step in the final stage. A higher aspect ratio may result in wider bounding boxes, which can negatively impact subsequent processes on the detected region.

Another difference between the face detection model and the MRZ region detection model is that the MRZ region model does not require the detection of landmarks. Therefore, the landmark layer can be dropped to reduce model weight and increase inference speed.

Overall, the modified MRZ region detection model based on BlazeFace offers accurate and efficient detection of the MRZ region in IDs, leveraging the strengths of the original BlazeFace model while making necessary adjustments for the specific requirements of MRZ region detection.

IV. EXPERIMENTAL RESULTS

In the experimental part of this study, BlazeFace model [21] was trained on a dataset comprising real and simulated IDs. The model was then evaluated on a range of test datasets, including simulated IDs, real IDs, and publicly available ID samples. We conducted both quantitative and visual analyses to assess the performance of our proposed model in detecting the MRZ region.

Quantitative results were obtained by measuring various performance metrics such as accuracy, precision, recall, and F1 score. These metrics provide objective measures of the model's ability to accurately detect the MRZ region in different types of IDs.

Additionally, we presented visual results to demonstrate the effectiveness of our proposed model. This involved showcasing the model's detection results on sample ID images, highlighting the accurately detected MRZ regions. Visual representations help provide a clear understanding of how well the model

performs in identifying the MRZ region within various ID samples.

By combining quantitative analysis with visual evidence, it is aimed to provide a comprehensive evaluation of our proposed model's MRZ region detection performance. These results contribute to validating the accuracy and effectiveness of our model in reliably detecting the MRZ region in IDs, regardless of whether they are simulated, real, or sourced from publicly available samples.

Fig.4. (a) Blank Turkish national ID, (b) randomly filled Turkish national ID.

A. Simulated Dataset

To address the security concerns surrounding sensitive personal information on national IDs, the availability of public datasets or real IDs for research purposes is limited. In order to overcome this limitation, we have created a new simulated dataset specifically tailored for national Turkish IDs, while ensuring compatibility with other national IDs adhering to ICAO standards [3].

During the construction of the simulated dataset, the static text was kept consistent across all IDs, only modifying the dynamic text components. Certain information on the IDs, such as the date of birth, expiration date, and national identification number, maintain a fixed length of characters. However, other text fields, such as the name and surname, vary in length. To account for this variability, we randomly generate the length of the name and surname using a Gaussian distribution to simulate realistic variations.

By utilizing this simulated dataset, we are able to train and evaluate our MRZ detection model effectively while respecting privacy and security concerns associated with real IDs. The simulated dataset allows us to capture the essential characteristics and variability of national IDs, enabling robust and accurate performance assessment of our proposed model.

Firstly, the dynamic text part of the ID, which contains sensitive information, is removed using an inpainting algorithm. This algorithm fills in the areas corresponding to the dynamic text with appropriate background patterns, resulting in an empty national Turkish ID as depicted in Fig. 4(a). Next, the empty ID is populated with randomly selected digits, letters, and the "<" symbol to replicate the actual content and order of the dynamic text. This process ensures that the simulated data closely resembles the characteristics and structure of real IDs. The resulting simulated data for the ID is illustrated in Fig. (b).

By employing this method, diverse range of simulated IDs were generated while preserving the privacy and security of individuals. The inpainting algorithm enables the removal of sensitive information, and the subsequent random filling process ensures the variability and realism of the simulated data.

Fig.5. Sample Turkish national IDs with different backgrounds in the simulated dataset.

Fig.6. MRZ detection results for the simulated Turkish national IDs.

To create a diverse and comprehensive simulated dataset, 40 different fake national Turkish IDs are randomly generated based on the template shown in Fig. (b). These simulated IDs are then printed with high quality to resemble actual physical IDs. In order to capture variations in image quality, background, and hand grip positions, multiple photos of each printed ID are taken using different scenarios. This is done using three different mobile devices: Samsung, iPhone, and Xiaomi. As a result, a total of 1,300 photos are obtained, covering approximately 50 different backgrounds. To further enhance the variability and robustness of the dataset, data augmentation techniques are applied. This includes

manipulating factors such as color, illumination, sharpness, blurriness, and other relevant parameters. Through data augmentation, the size of the simulated dataset is increased to 130,000 IDs. Fig. 5 illustrates different sample IDs from our simulated dataset, showcasing the diversity and realism achieved through the combination of random generation, high-quality printing, diverse photo scenarios, and data augmentation techniques.

B. Real Dataset

To address the limitations of using only simulated data, we recognize the importance of incorporating real data into the training dataset. However, due to security concerns and the sensitive nature of personal information on real IDs, it is challenging to find publicly available real ID datasets.

In this study, we managed to obtain a small set of 4 different genuine national Turkish IDs. These IDs were recorded in video format, capturing them in various scenarios with 100 different backgrounds. From each recorded video, 7 frames were extracted, resulting in a total of 700 real ID images. To increase the diversity and quantity of the real dataset, data augmentation techniques were applied to the extracted real ID images. This augmented the total number of real IDs to 70,000, providing a more comprehensive training dataset.

While increasing the number of real data can be beneficial for model performance, it was necessary to keep the quantity limited due to security concerns and the sensitive nature of the information contained in real IDs. By carefully balancing the inclusion of real and simulated data, it is aimed to enhance the quality, quantity, and diversity of the training dataset while ensuring the privacy and security of individuals' personal information.

C. Training Configuration

To enhance the quality, quantity, and diversity of the training data, we combined the simulated dataset with the limited real dataset. This approach is commonly used in the literature to improve model performance. The real dataset consisted of a small number of unique identity cards, which were augmented to increase the data diversity.

The initial training dataset comprised 2000 images before augmentation. Data augmentation techniques were applied to both the simulated and real datasets, resulting in a final dataset of approximately 200,000 images. The augmentation numbers were optimized by assessing the model's performance.

During training, an initial learning rate of 0.001 was set, and four learning rate decay steps were implemented over the course of 200 epochs. The input images had three channels and a size of 320×320 pixels. A batch size of 512 was used in training. Three different optimizers, namely Adam, stochastic gradient descent (SGD), and root mean squared propagation (RMSProp), were tested. The best results were achieved with RMSProp.

Model performance evaluation was conducted at different intervals during the training process. Up to the 100th epoch, evaluation was performed every 10 epochs, and after that, it was done every 5 epochs.

The training process was carried out on a workstation equipped with an Ubuntu 20.04 operating system, 128 GB of RAM, and 2 Nvidia Rtx A5000 GPUs. The total training time

for the approximately 200,000 images was approximately 4 days. It was observed that the model's performance reached a convergence point after the 130th epoch, and there was no significant improvement beyond that point.

D. Detection Results

In this study, BlazeFace model [21] was trained for the MRZ detection for the first time. For the training part, simulated and real ID card dataset is constructed where the following scenario is tested;

- Scenario: Training on the simulated and real Turkish national IDs dataset and testing on the simulated, real and publicly available IDs.

The performance of the proposed model was evaluated using both visual and quantitative measures. The visual results are presented in Fig. 6, and Fig. 7 (a)-(c), showcasing the MRZ region detection for different types of IDs, including simulated IDs, real Turkish national IDs, and IDs, passports, and visas from various countries.

Fig. 6 demonstrates the successful MRZ region detection for simulated IDs with different backgrounds. The bounding boxes accurately enclose the MRZ region, ensuring that all relevant text information is contained within them. This allows for subsequent processing with OCR engines.

Fig. 7(a) shows the visual results for real Turkish national IDs, with sensitive personal information hidden for security reasons. The bounding boxes are well-fitted to the MRZ region, even in cases with different orientations, distances, and backgrounds. The model is capable of handling challenging scenarios such as IDs held by hand, where the shape of the ID card may be distorted or occluded. Unlike methods that rely on the shape of the ID card, our model focuses solely on the MRZ region, enabling successful detection even in distorted or occluded cases.

Figs. 7(b) and (c) present the MRZ region detection results for IDs, passports, and visas from different countries worldwide. Despite the training dataset being solely based on Turkish IDs, the proposed model exhibits excellent generalization ability. It can successfully detect the MRZ region in various travel documents and IDs from different countries, demonstrating its superior performance and generalization capability.

Overall, the visual results demonstrate the effectiveness and robustness of the proposed model in detecting the MRZ region in a wide range of ID types and scenarios.

Quantitative results were also obtained to evaluate the performance of the model. Fig. 8 illustrates the average precision, which exceeds 96%. This high precision score is achieved by setting a high confidence threshold during the testing stage. Despite the high threshold, there are very few cases of missed detection. The precision-recall curve shows that the model maintains a consistently high precision even as the recall increases, indicating its robustness in detecting the MRZ region.

Accurate localization of the MRZ region is crucial for the OCR process. To evaluate this aspect, the Accuracy vs. IoU threshold is presented in Fig. 9.

Fig.7. MRZ detection results (a)) the real Turkish national IDs, (b) publicly available ID cards for different nations,, and (c) publicly available other travel documents such as passports and visas.

The red point on the graph shows that our model achieves an accuracy above 80% when the IoU threshold is set at 0.75. Our experimental results indicate that the Tesseract OCR engine performs well with MRZ regions that have an IoU threshold of 0.75 or higher, based on the average results of our tests.

80\%. This indicates that using templates for IDs allows for more accurate MRZ region detection, especially in the first few frames and often in the first frame.
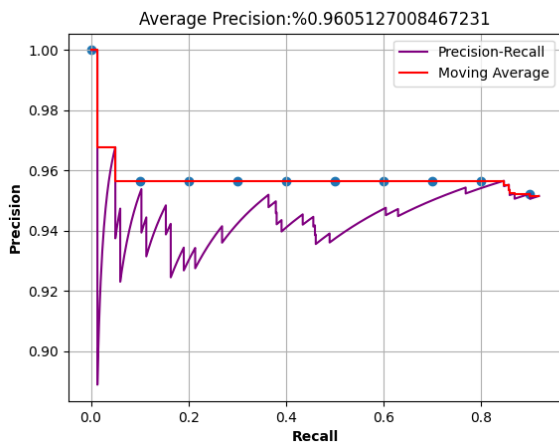
Fig.8. Precision vs Recall curve of trained model with average precision.

Fig.9. Accuracy vs. IoU threshold curve of trained model with average accuracy.

Furthermore, the model's performance was assessed in capturing MRZ regions in the wild using a mobile device camera. Fig. 10 demonstrates that even without aligning to a specific template, our model achieves an accuracy rate of over

In summary, the quantitative results confirm the high performance and accuracy of the proposed model in detecting the MRZ region, and its compatibility with OCR engines for extracting text information from the MRZ regions of various IDs captured by mobile devices.

E. Quantitative Analysis and Comparison

For this experiment, we employed MIDV-500 [19] and MIDV-2019 [20] datasets, and our dataset, comparing the results with existing models from the literature. While MIDV-500 and MIDV-2019 include passport MRZ regions, our model is solely trained on Turkish ID cards. Consequently, the results obtained on these datasets demonstrate the generalizability and cross-dataset performance of our proposed model. It's worth noting that PassportEye is designed for use with passports exclusively, and therefore, it did not yield results in our ID card dataset. As for PassportEye [14] and UltimateMRZ [15], we utilized the pre-trained models as provided in their original publications. The performance comparisons are tested over videos since for our use case, video clip of the ID card is taken until it recognizes the characters in the MRZ region. For each individual video, if character error rate (CER) is lower than 50% for one of the frame, it is considered as a successful detection.

The results are outlined in Table I. In publicly available datasets like MIDV-500 and MIDV-2019, UltimateMRZ obtains the top position, with PassportEye following closely. In these datasets, our proposed model exhibits lower performance compared to these two models. Several factors contribute to this difference. 1) Our model is primarily trained on ID card MRZ regions, and while it generalizes well to passports, it has not been exposed to passport MRZ regions during training. 2) We deliberately excluded extreme cases in MRZ videos from our dataset. Since our mobile application guides users to capture videos of their ID cards with a good quality. This guided approach streamlines our model's architecture but may result in reduced performance when dealing with more diverse angles and scenarios. In our dataset, our model outperforms UltimateMRZ. PassportEye, designed primarily for passports, doesn't yield valid results with ID cards, as expected. Since our dataset only contains ID card videos, it's reasonable to conclude that incorporating passport images into our training data could potentially lead to competitive results for datasets like MIDV-500 and MIDV-2019.

TABLE I
MRZ DETECTION RESULTS (%) BASED ON CER

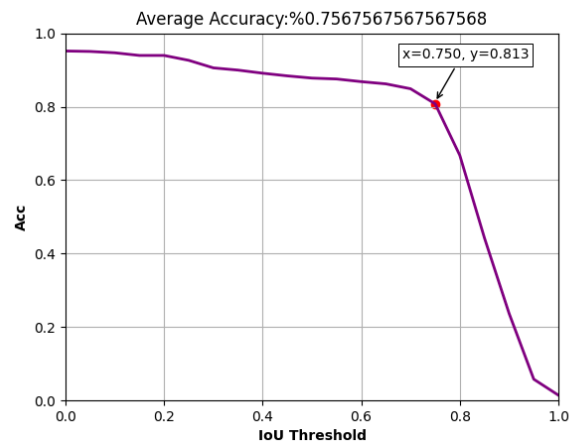| Dataset	UltimateMRZ	PassportEye	MobileMRZNet
MIDV-500	93.33	90.66	90
MIDV-2019	90	88.33	75
Ours	88.46	-	90.80

In Table II, we provide a comparison of model sizes and inference times. All methods were tested on the following hardware and environment: Intel Core i7-7820HQ @ 2.9GHz, 16GB DDR4-2400 MHz, NVIDIA Quadro M620, on a Windows 10 64-bit platform. Our proposed model is significantly more lightweight than UltimateMRZ, being nearly 2.5 times smaller, and it surpasses PassportEye by a factor of 50 in terms of model size. Furthermore, for inference time comparison, our proposed model outperforms both UltimateMRZ and PassportEye, with the latter exhibiting a particularly substantial difference in running-time performance.

The results presented in both Table I and Table II provide strong evidence supporting the suitability of our proposed methods for mobile platforms, aligning with the claims made in this study.

TABLE II
MODEL SIZE AND INFERENCE TIME COMPARISON

Model	Size (MB)	Time (Sec.)
UltimateMRZ	2.6	0.16
PassportEye	23.5	1.11
MobileMRZNet	1.06	0.12

V. CONCULUSION

The proposed MRZ region detection model offers an efficient and lightweight solution specifically tailored for mobile devices. The construction of a realistic simulated dataset addresses the challenge of limited publicly available MRZ datasets, considering the need to protect sensitive information. By training the BlazeFace model on the combined real and simulated IDs dataset, the proposed model outperforms existing MRZ region detection models in terms of detection performance, robustness, and computational efficiency. The model is well-suited for mobile devices and demonstrates generalization capabilities to other travel documents such as passports and visas from different countries. Overall, the proposed model represents a significant advancement in MRZ region detection, offering improved accuracy and efficiency for various applications.

VI. ACKNOWLEDGEMENT

REFERENCES

[1] R. Hall, G. Dodds, S. Triggs, "The World of William Notman," David R. Godine, pp. 46-47, 1993.

[2] J. Doulman, D. Lee, "Every Assistance & Protection: A History of the Australian Passport," Federation Press, p. 56, 2008.

[3] International Civil Aviation Organization (ICAO), "Machine Readable Travel," 7th ed., Parts 2-7, 2015.

[4] J. Monnerat, S. Vaudenay, M. Vuagnoux, "About machine-readable travel documents," Springer, 2007.

[5] R. Want, "Near field communication," IEEE Pervasive Computing, vol. 10, no. 3, pp. 4-7, 2011.

[6] P. K. Chan, C. S. Choy, C. F. Chan, K. P. Pun, "Preparing smartcard for the future: from passive to active," IEEE Transactions on Consumer Electronics, vol. 50, no. 1, pp. 245-250, 2004.

[7] A. Hartl, C. Arth, D. Schmalstieg, "Real-time detection and recognition of machine-readable zones with mobile devices," 10th International Conference on Computer Vision Theory and Applications, vol. 3, pp. 79-87, 2015.

[8] Y. V. Visilter, S. Y. Zheltov, A. A. Lukin, "Development of OCR system for portable passport and visa reader," In Document Recognition and Retrieval VI, Vol. 3651, pp. 194-199, 1999.

[9] Y.-B. Kwon, J.-H. Kim, "Recognition based verification for the machine-readable travel documents," In 7th International Workshop on Graphics Recognition, pp. 1-10, 2007.

[10] K.-B. Kim, S. Kim, "A passport recognition and face verification using enhanced fuzzy ART based RBF network and PCA algorithm," Neurocomputing, vol. 71, pp. 3202-3210, 2008.

[11] J. Kim, "Recognition of Passport MRZ Information Using Combined Neural Networks," Journal of Korea Society of Digital Industry and Information Management, vol. 15, no. 4, pp. 149-157, 2019.

[12] Y. Liu, H. James, O. Gupta, D. Raviv, "MRZ code extraction from visa and passport documents using convolutional neural networks," International Journal on Document Analysis and Recognition (IJDAR), vol. 25, no.1, pp. 29-39, 2022.

[13] M. Sandler, A. Howard, M. Zhu, A. Zhmoginov, L. C. Chen, "Mobilenetv2: Inverted residuals and linear bottlenecks," In Proceedings of the IEEE conference on computer vision and pattern recognition, pp. 4510-4520, 2018.

[14] K. Tretyakov, "PassportEye: Extraction of machine-readable zone information from passports, visas, and ID-cards via OCR," GitHub, 2016. [Online]. Available: https://github.com/konstantint/PassportEye.

[15] UltimateMRZ, doubango.org, 2020. [Online]. Available: https://github.com/DoubangoTelecom/ultimateMRZ-SDK. Accessed: Oct. 01, 2023.

[16] D. Kostro, M. Zasso, "MRZ detection via image-js," GitHub, 2020. [Online]. Available: https://github.com/image-js/mrz-detection.

[17] P. Lyu, M. Liao, C. Yao, W. Wu, X. Bai, "Masktextspotter: An end-to-end trainable neural network for spotting text with arbitrary shapes," In Proceedings of the European Conference on Computer Vision (ECCV), pp. 67-83, 2018.

[18] L. Xing, Z. Tian, W. Huang, M. R. Scott, "Convolutional Character Networks," arXiv:1910.07954, 2019.

[19] V. V. Arlazarov, K. Bulatov, T. Chernov, V. L. Arlazarov, "MIDV-500: A dataset for identity document analysis and recognition on mobile devices in video stream," Computer Optics, vol. 43, pp. 818-824, 2019.

[20] K. Bulatov, D. Matalov, V. V. Arlazarov, "MIDV-2019: Challenges of the Modern Mobile-Based Document OCR," ICMV 2019, pp. 114332N1-114332N6, 2020.

[21] V. Bazarevsky, Y. Kartynnik, A. Vakunov, K. Raveendran, M. Grundmann, "BlazeFace: Sub-millisecond neural face detection on mobile GPUs," arXiv preprint arXiv:1907.05047, 2019.

[22] A. G. Howard, M. Zhu, B. Chen, D. Kalenichenko, W. Wang, T. Weyand, H. Adam, "Mobilenets: Efficient convolutional neural networks for mobile vision applications," arXiv preprint arXiv:1704.04861, 2017.

[23] W. Liu, D. Anguelov, D. Erhan, C. Szegedy, S. Reed, C. Y. Fu, A. C. Berg, "SSD: Single shot multibox detector," In European Conference on Computer Vision, pp. 21-37, Springer, Cham, 2016.

[24] S. Chen, Y. Liu, X. Gao, Z. Han, "Mobilefacenets: Efficient CNNs for accurate real-time face verification on mobile devices," In Chinese Conference on Biometric Recognition, pp. 428-438, 2018.

[25] N. Bayar, K. Güzel, D. Kumlu, "A Novel BlazeFace Based Pre-processing for MobileFaceNet in Face Verification," 45th International Conference on Telecommunications and Signal Processing (TSP), pp. 179-182, 2022.M. Yilmaz, "The Prediction of Electrical Vehicles' Growth Rate and Management of Electrical Energy Demand in Turkey." Green Technologies Conference (GreenTech), 2017 Ninth Annual IEEE. Denver, US, 2017.

BIOGRAPHIES

Necmettin Bayar received B.S. degree from the Department of Electronic Engineering, Gebze Technical University, Kocaeli, Turkey, in 2018 and completed his master degree from Istanbul Technical University in 2023. He is working as AI Developer in private company. His research interests cover image processing, signal processing, machine learning, deep learning, ai based radar imaging, SAR/ISAR imaging.

Kübra Güzel eceived B.S. degree from the Department of Electronic and Communication Engineering, Kocaeli University, Kocaeli, Turkey, in 2022. She works as AI Developer in private company. Her interests cover image processing, signal processing, machine learning, deep learning.

Deniz Kumlu received B.S. degree from the Department of Electrical and Electronics Engineering, Turkish Naval Academy, Istanbul, Turkey, in 2007 with honor degree, M.S. degree from the Ming Hsieh Department of Electrical Engineering, Viterbi School of Engineering, University of Southern California, Los Angeles, CA, USA, in 2012, where he studied with the special fellowship granted from the Turkish Naval Forces. He obtained Ph.D. degree from the Department of Electronic and Communication Engineering, Istanbul Technical University, Istanbul, Turkey, in 2018 with best thesis award of the year. He is currently serving as a senior researcher in private sector. He is Senior IEEE member and his research interests include image processing, signal processing, machine learning, deep learning, and radar signal processing applications.

Research Article

Determining Fault Location in Transmission Lines Using Differential Equation Algorithms

Cenk Gezegin

Abstract—**A transmission line, in the context of electrical engineering and power systems, is a high-voltage or high-tension line that is used to transmit electrical power over long distances from power generation sources (such as power plants) to substations, where the electricity is then distributed to homes, businesses, and industrial facilities. Transmission lines are the backbone of the electrical grid, serving as the highways for electricity delivery. Their efficient and reliable operation is essential for ensuring that electricity is generated, transmitted, and distributed effectively, meeting the needs of consumers while maintaining grid stability and resilience. Transmission line protection refers to a set of techniques and devices used in electrical power systems to detect and respond to faults or abnormal conditions that can occur in high-voltage transmission lines. These lines are a critical part of the electrical grid and are responsible for transporting electricity over long distances from power generation plants to distribution substations.**

This paper proposes a different differential equation algorithm to locate faulty section on transmission lines. As seen from performance curves, the proposed protection algorithm is able to distinguish normal and faulty conditions.

Index Terms— **Transmission Line, Protection, Differential Equations, Fault Location.**

I. INTRODUCTION

TRANSMISSION LINE, in the context of electrical engineering and power systems, is a specialized high-voltage power conductor used to transport electricity over long distances from power generation sources (such as power plants) to distribution substations, industrial facilities, and residential areas. Transmission lines are a crucial component of the electrical grid, and they serve several important purposes [1].

Long-Distance Power Transport: Transmission lines are designed to efficiently carry large quantities of electrical power over long distances, which is essential because power generation facilities are often located far away from where the electricity is needed. They bridge the gap between power generation and the distribution network.

Voltage Transformation: High-voltage transmission lines allow for the efficient transmission of electricity over long distances with minimal losses. However, before electricity is

CENK GEZEGİN, is with Department of Electrical and Electronic Engineering of Ondokuz Mayis University, Samsun, Turkey (e-mail: cenk.gezegin@omu.edu.tr).

https://orcid.org/0000-0002-4442-904X

distributed to homes and businesses, it needs to be stepped down to lower voltages at substations. This voltage transformation reduces energy losses and makes it safer for distribution.

Grid Stability: Transmission lines help maintain the stability and reliability of the electrical grid by enabling the flow of electricity between different regions and balancing supply and demand. They allow for power to be rerouted in case of outages or unexpected changes in demand.

Grid Expansion and Reliability: As populations grow and energy demands increase, expanding and upgrading transmission infrastructure becomes crucial. Building new transmission lines or upgrading existing ones is essential to ensure a reliable and robust power supply.

Integration of Renewable Energy: Transmission lines play a significant role in integrating renewable energy sources, such as wind and solar farms, into the grid. These renewable energy sources are often located in remote areas, and transmission lines are needed to transport their electricity to urban centers.

Economic Benefits: A robust transmission infrastructure can support economic growth by enabling the development of industries and businesses that rely on a stable and abundant power supply. It also helps lower energy costs by facilitating access to diverse sources of electricity generation.

Redundancy and Reliability: Transmission lines are typically designed with redundancy to ensure reliability. If one line experiences a fault or needs maintenance, power can often be rerouted through alternate lines to minimize disruptions.

Power Quality: Transmission lines help maintain the quality of power delivered to end-users by regulating voltage levels and reducing electrical noise and disturbances during transmission.

Transmission lines are essential for the efficient, reliable, and safe delivery of electrical power over long distances. They form the backbone of the electrical grid, supporting the functioning of power systems and enabling economic growth and the integration of renewable energy sources. Maintaining and upgrading transmission infrastructure is critical to ensuring a stable and resilient power supply for communities and industries [2].

A. The Importance Of Line Protection

Transmission line protection refers to a set of techniques and devices used in electrical power systems to detect and respond to faults or abnormal conditions that can occur in high-voltage transmission lines. These lines are a critical part of the electrical grid and are responsible for transporting electricity

over long distances from power generation plants to distribution substations. The primary goal of transmission line protection is to ensure the safety and reliability of the power system by quickly isolating faults or disturbances on the transmission lines while minimizing disruption to the rest of the grid. Here are some key aspects of transmission line protection [3].

Fault Detection: Transmission lines can experience various types of faults, such as short circuits, ground faults, and open circuits.

Fast Response: It is crucial to respond to faults swiftly to prevent damage to equipment and to minimize the extent of power outages.

Relay Protection: Protective relays are devices that monitor the electrical parameters of the transmission line and make decisions to trip circuit breakers or disconnect the faulty section in case of a fault.

Communication: In modern power systems, protection relays often use communication networks to exchange information with each other and with the central control system.

Zone Protection: Transmission lines are often divided into protection zones, and relays are set up to protect specific sections of the line.

Redundancy: Redundant protection systems are often employed to increase reliability.

Coordination: Protection schemes are coordinated with other elements of the power system, such as transformers, generators, and substations, to ensure that the correct section of the line is isolated and that other equipment is protected from damage.

This paper suggests a new differential equation algorithm to calculate R and L variables on transmission lines. Section 2 gives a brief explanation about proposed technique.

II. MATERIAL AND METHOD

Transmission line protection methods are techniques and devices used to safeguard high-voltage electrical transmission lines from faults and abnormal conditions. These methods are critical for maintaining the reliability and stability of power systems. Here are some common transmission line protection methods related to our study [4].

Differential Protection: Differential relays compare the currents entering and leaving the transmission line. If there is a significant difference, indicating a fault within the protected zone, the relay will trip the circuit breaker.

Distance Protection: Distance relays measure the impedance of the transmission line and calculate the distance to the fault location. If a fault is detected within a predefined distance, the relay operates to isolate the faulted section.

Impedance-Based Protection: Impedance relays monitor the impedance of the transmission line. A change in impedance can indicate a fault, and the relay will operate to trip the circuit breaker.

Transformer and Capacitor Protection: Specialized protection schemes are used for transformers and capacitor banks connected to transmission lines to prevent damage to these assets in case of faults.

Ground Fault Protection: Ground fault protection methods detect when a transmission line has a connection to ground, indicating a fault. Ground fault relays can trip circuit breakers to isolate the fault. The proposed method serves differential, distance and impedance protection methods.

A. Differential Equation Technique

Because it gives a simple and rapid solution for locating faults in transmission lines, the differential equation approach is widely utilized in transmission lines. This approach is originally developed for the serial parameters of the transmission line at various sampling frequencies. Fig. 1 shows single phase transmission line with distributed parameters. Total resistance (R) is 8Ω and total inductance (L) is set to 32mH.

The proposed approach is based on Eq. (1) and requires voltage and current samples.

$$v(t) = Ri(t) + L\frac{di(t)}{dt} \qquad (1)$$

In Eq. (1), R and L are the serial distributed transmission line parameters, $v(t)$ is the beginning line voltage, and $i(t)$ is the current flowing along the serial branch. Eq. (1) must be adjusted in light of the existence of the fault point resistance. The line's R and L parameters may be easily determined using the Eq. (1) expressed in different time intervals. Eq. (1) is traditionally rewritten using a trapezoidal integration method at various intervals (3 samples and 6 samples, respectively) and utilized as a defect location discovery technique. Using this approach, the serial R and L characteristics of a line may be determined sensitively, especially in short lines that are unaffected by parallel capacity. While Eq. (1) has two unknown parameters, the magnitudes ($v(t)$ and $i(t)$) are known. As a result, rewriting Eq. (1) in two distinct time periods yields Eqs. (2) and (3) [5,6].

The integral terms in Eqs. (2) and (3) are restructured using the trapezoidal method, yielding Eq. (4).

$$\int_{t0}^{t1} v(t)dt = R\int_{t0}^{t1} i(t)dt + L[i(t_1) - i(t_0)] \qquad (2)$$

$$\int_{t1}^{t2} v(t)dt = R\int_{t1}^{t2} i(t)dt + L[i(t_2) - i(t_1)] \qquad (3)$$

The integral terms in Eqs. (2) and (3) are restructured using the trapezoidal method, yielding Eq. (4).

$$\int_{t0}^{t1} v(t)dt = \frac{\Delta t}{2}[v(t_1) + v(t_0)] = \frac{\Delta t}{2}[v_1 + v_2] \qquad (4)$$

The above method is also very well-known as trapezoidal integration rule (TIR). In this paper, other integration numerical methods are also tried and the parameter estimation results are compared.

http://dergipark.gov.tr/bajece
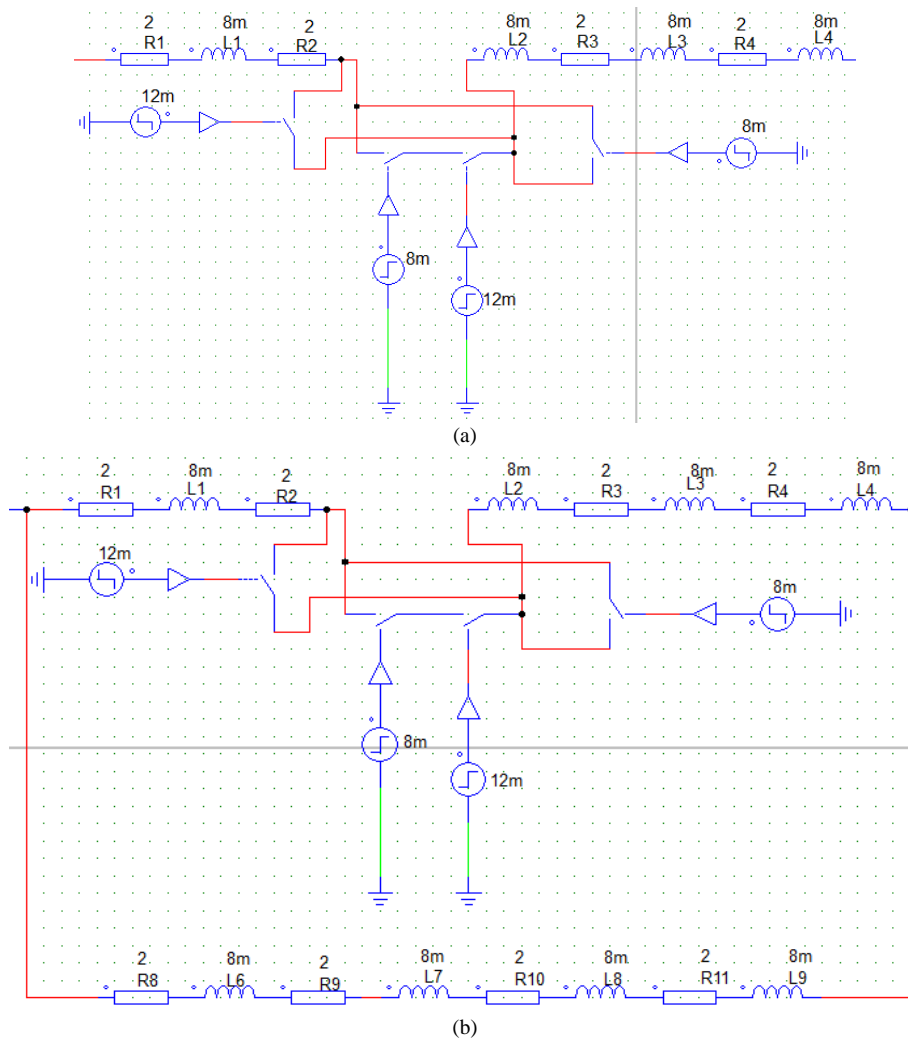
Fig. 1 Transmission line under investigation, (a) series and (b) parallel

1) Short Window

The TIR technique is commonly stated as Eq. (5), and it employs two voltage and three current samples to estimate the parameters.

$$\begin{bmatrix} \dfrac{\Delta t}{2}(i_{k+1}+i_k) & (i_{k+1}-i_k) \\ \dfrac{\Delta t}{2}(i_{k+2}+i_{k+1}) & (i_{k+2}-i_{k+1}) \end{bmatrix} \begin{bmatrix} R \\ L \end{bmatrix} = \begin{bmatrix} \dfrac{\Delta t}{2}(v_{k+1}+v_k) \\ \dfrac{\Delta t}{2}(v_{k+2}+v_{k+1}) \end{bmatrix} \quad (5)$$

2) Long Window

Especially Eq. (6) is concerned, singular value decomposition method must be used to solve the line parameters system matrices because there are few known parameters despite the unknown parameters. Eq. (5) and Eq. (6) are still used as a conventional DEA techniques and a numerical distance protection relay algorithm in transmission lines.

$$\begin{bmatrix} \dfrac{\Delta t}{2}(i_{k+1}+i_k) & (i_{k+1}-i_k) \\ \dfrac{\Delta t}{2}(i_{k+2}+i_{k+1}) & (i_{k+2}-i_{k+1}) \\ \dfrac{\Delta t}{2}(i_{k+3}+i_{k+2}) & (i_{k+3}-i_{k+2}) \\ \dfrac{\Delta t}{2}(i_{k+4}+i_{k+3}) & (i_{k+4}-i_{k+3}) \\ \dfrac{\Delta t}{2}(i_{k+5}+i_{k+4}) & (i_{k+5}-i_{k+4}) \end{bmatrix} \begin{bmatrix} R \\ L \end{bmatrix} = \begin{bmatrix} \dfrac{\Delta t}{2}(v_{k+1}+v_k) \\ \dfrac{\Delta t}{2}(v_{k+2}+v_{k+1}) \\ \dfrac{\Delta t}{2}(v_{k+3}+v_{k+2}) \\ \dfrac{\Delta t}{2}(v_{k+4}+v_{k+3}) \\ \dfrac{\Delta t}{2}(v_{k+5}+v_{k+4}) \end{bmatrix} \quad (6)$$

3) Very Long Window

Similarly, Eq. (7) must be used to solve the line parameters system matrices because there are few known parameters despite the unknown parameters.

$$\begin{bmatrix} \frac{\Delta t}{2}(i_{k+1}+i_k) & (i_{k+1}-i_k) \\ \frac{\Delta t}{2}(i_{k+2}+i_{k+1}) & (i_{k+2}-i_{k+1}) \\ \frac{\Delta t}{2}(i_{k+3}+i_{k+2}) & (i_{k+3}-i_{k+2}) \\ \frac{\Delta t}{2}(i_{k+4}+i_{k+3}) & (i_{k+4}-i_{k+3}) \\ \frac{\Delta t}{2}(i_{k+5}+i_{k+4}) & (i_{k+5}-i_{k+4}) \\ \frac{\Delta t}{2}(i_{k+6}+i_{k+5}) & (i_{k+6}-i_{k+5}) \\ \frac{\Delta t}{2}(i_{k+7}+i_{k+6}) & (i_{k+7}-i_{k+6}) \\ \frac{\Delta t}{2}(i_{k+8}+i_{k+7}) & (i_{k+8}-i_{k+7}) \end{bmatrix} \begin{bmatrix} R \\ L \end{bmatrix} = \begin{bmatrix} \frac{\Delta t}{2}(v_{k+1}+v_k) \\ \frac{\Delta t}{2}(v_{k+2}+v_{k+1}) \\ \frac{\Delta t}{2}(v_{k+3}+v_{k+2}) \\ \frac{\Delta t}{2}(v_{k+4}+v_{k+3}) \\ \frac{\Delta t}{2}(v_{k+5}+v_{k+4}) \\ \frac{\Delta t}{2}(v_{k+6}+v_{k+5}) \\ \frac{\Delta t}{2}(v_{k+7}+v_{k+6}) \\ \frac{\Delta t}{2}(v_{k+8}+v_{k+7}) \end{bmatrix} \quad (7)$$

Eqs. (6) and (7) are assumed ill-conditions matrixes. While ill-conditioned matrices don't have a specific visual form, they exhibit certain characteristics that make them numerically unstable and challenging to work with. A hermitian matrix is a square matrix that is equal to the transpose of its conjugate matrix. The diagonal elements of a hermitian matrix are all real numbers, and the element of the (i, j) position is equal to the conjugate of the element in the (j, i) position.

Here's a breakdown of key concepts:

a) ill-Conditioning

It arises when a matrix is close to being singular (non-invertible), which means its determinant is nearly zero.

Small changes in the matrix's entries can lead to disproportionately large variations in its inverse or in solutions to linear systems involving it.

b) Condition Number

A numerical measure of how sensitive a matrix is to changes in its entries.

Mathematically, it's defined as the ratio of the largest singular value of the matrix to its smallest singular value. Larger condition numbers indicate greater ill-conditioning. Furthermore, an ill-conditioned matrix is a matrix that is nearly singular or singular, meaning that its condition number is very large. The condition number of a matrix measures how sensitive the solution of a linear system is to changes in the input data. A large condition number indicates that the matrix is ill-conditioned, and small changes in the input data can result in large changes in the output.

For example, consider a system of linear equations Ax=b. If A is ill-conditioned, small changes in b can result in large changes in x, making the solution sensitive to input perturbations [7-9].

B. Simulation Studies

Energy transmission lines can be divided into three according to their length. Lines from 0 to 100 km are called short lines. Lines between 100-250 km are called medium-length lines. Lines of 250 km and longer are called long transmission lines and necessary calculation methods and line parameters are found. If we examine transmission lines from an electrical perspective, line parameters and lengths are in question. Since our investigations are generally transmission lines using alternating current, all quantities used in alternating current will be in question here. Transmission lines have an ohmic resistance (R). This resistance is approximately 1.5 times higher than that in direct current due to the skin phenomenon. On the other hand, due to the fluxes surrounded by the currents flowing in neighboring conductors, self and mutual inductances of the phase conductors occur [10-12].

Since we work with sinusoidal currents, the term inductive reactance, which is a function of the network frequency, is used instead of inductance. The ohmic resistance and inductive reactance of the line are considered to be connected in series to each other, and the series sum of these two quantities, impedance, is used to characterize the line.

In this study, short lines are used for parameters using DEA algorithms. The theorical background is as follow. A two-gate circuit representation of a power transmission line is given in Fig. 2.
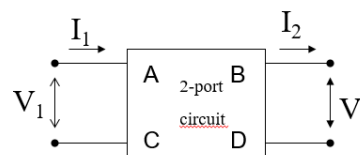
Fig.2. Two-door circuit representation with ABCD parameters

The relations between the inputs and outputs shown in the Figure 2 are given as below.

$$V_1 = A \cdot V_2 + B \cdot I_2 \text{ and } I_1 = C \cdot V_2 + D \cdot I_2 \quad (8)$$

It is in the form. If we write the expressions as a matrix

$$\begin{bmatrix} V_1 \\ I_1 \end{bmatrix} = \begin{bmatrix} A & B \\ C & D \end{bmatrix} \cdot \begin{bmatrix} V_2 \\ I_2 \end{bmatrix} \quad (9)$$

If the four-terminal circuit is symmetrical, A and D are equal and unitless. The units of B and C are Ω (ohm) and S (Siemens = 1/Ω), respectively. Provided that this symmetry is achieved AD - BC = 1 and the system is balanced.

In this study, two-busbar serial and one-bar parallel transmission lines were used. Line impedances for both transmission lines are selected as 8+j10.5 ohms.

1) Series Connection of Two Four-Term Circuits

In case two short lines with line constants A_1, B_1, C_1, D_1 and A_2, B_2, C_2, D_2 are connected in series, common ABCD coefficients will be calculated by DEA.
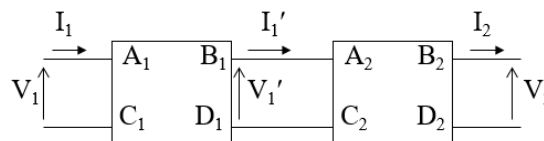
Fig.3. Series connection of two four-pin circuits

Here, the ABCD coefficients are $A=A_1A_2+B_1C_2$, $B=A_1B_2+B_1D_2$, $C=C_1A_2+D_1C_2$ and $D=C_1B_2+D_1D_2$, respectively.

Series Transmission Line Distributed Parameters
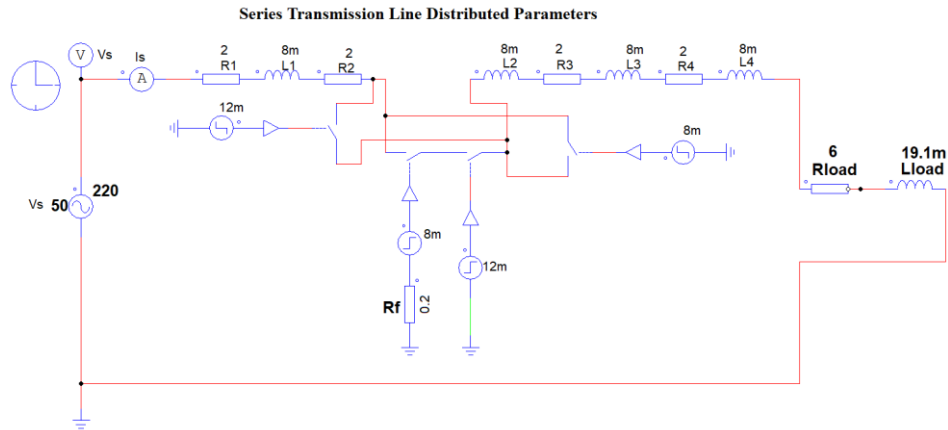
Fig.4. Serial transmission line distributed parameters

Parallel Transmission Line Distributed Parameters
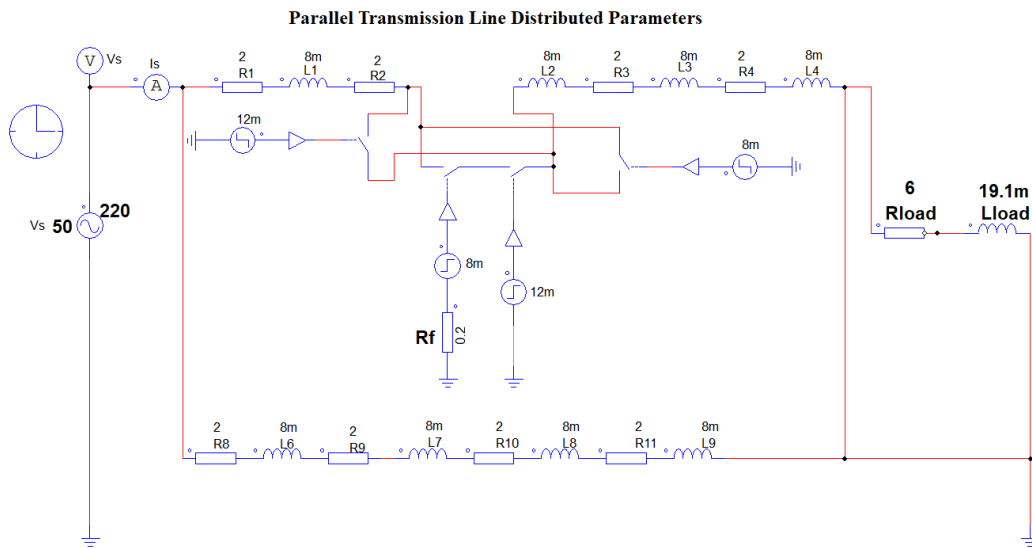
Fig.5. Parallel transmission line distributed parameters

2) Parallel Connection of Two Four-Pin Circuits

Figure 5 shows parallel connection of two four-pin.
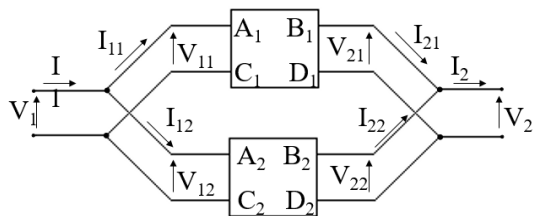
Fig.6. Parallel connection of two four-pin circuits

$$\begin{bmatrix} V_1 \\ I_1 \end{bmatrix} = \begin{bmatrix} \dfrac{A_1B_2+A_2B_1}{B_1+B_2} & \dfrac{B_1B_2}{B_1+B_2} \\ C_1+C_2\dfrac{(A_1-A_2)(D_2-D_1)}{B_1+B_2} & \dfrac{D_1B_2+D_2B_1}{B_1+B_2} \end{bmatrix} \cdot \begin{bmatrix} V_2 \\ I_2 \end{bmatrix} \quad (10)$$

Here, the ABCD coefficients are as follow.

Simulation studies cover sampling frequency (Fs) and median filtering to choose best option. Figure 7 shows series distributed line parameters of R3, R6, R3m, R6m and L3, L6, L3m, L6m without filtering and with filtering. Figure 7 shows parallel distributed line parameters of R3, R6, R3m, R6m and L3, L6, L3m, L6m without filtering and with filtering. Tables 1-4 show the effects of Fs and median filter degrees. As seen Tables 1-4 the technique is robust and does not require the higher Fs values.

Eq. 7 shows 9 point transmission line parameter. Eq. 7 does not required since 6-point method accurate estimating parameters of R and L.
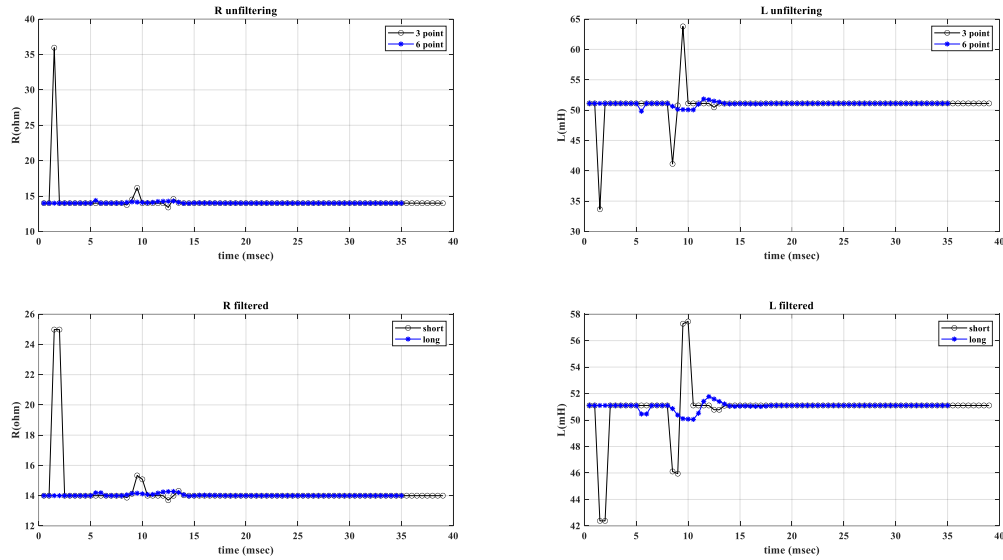
Fig.7. Parallel distributed *R* and *L* parameters (Fs=2kHz, filter degree of 3)

TABLE I
THE EFFECTS FS WITH RESPECT OF CORRELATION
COEFFICIENTS VALUES FOR SERIES LINE (FILTER DEGREE OF 3)

Fs (Hz)	R3 and R3m	L3 and L3m	R6 and R6m	L6 and L6m
2000	**0.0666**	0.2990	**0.8265**	0.8726
2500	0.0399	0.2868	0.6540	**0.8812**
3333	0.0031	**0.3141**	0.3471	0.8439
5000	0.0087	0.2702	0.2195	0.8929
10000	0.0027	0.2609	0.0816	0.8969

TABLE II
THE EFFECTS FS WITH RESPECT OF CORRELATION COEFFICIENTS
VALUES FOR SERIES LINE (FILTER DEGREE OF 6)

Fs (Hz)	R3 and R3m	L3 and L3m	R6 and R6m	L6 and L6m
2000	-0.0057	**-0.0086**	**0.7785**	0.8042
2500	**-0.0124**	-0.0063	0.6233	**0.8288**
3333	-0.0097	-0.0045	0.3284	0.7968
5000	-0.0072	-0.0027	0.2085	0.8495
10000	-0.0030	-0.0013	0.0776	0.8553

TABLE III
THE EFFECTS FS WITH RESPECT OF CORRELATION COEFFICIENTS
VALUES FOR PARALLEL LINE (FILTER DEGREE OF 3)

Fs (Hz)	R3 and R3m	L3 and L3m	R6 and R6m	L6 and L6m
2000	0.0685	0.3004	**0.8310**	**0.8712**
2500	**0.0431**	**0.2879**	0.6587	0.8794
3333	0.0034	0.3144	0.3488	0.8421
5000	0.0086	0.2708	0.2214	0.8914
10000	0.0028	0.2614	0.0817	0.8957

TABLE IV
THE EFFECTS FS WITH RESPECT OF CORRELATION COEFFICIENTS
VALUES FOR PARALLEL LINE (FILTER DEGREE OF 6)

Fs (Hz)	R3 and R3m	L3 and L3m	R6 and R6m	L6 and L6m
2000	**-0.0131**	**-0.0086**	**0.7851**	0.8043
2500	-0.0126	-0.0064	0.6279	**0.8271**
3333	-0.0398	-0.0050	0.3269	0.7949
5000	-0.2893	-0.0027	0.2102	0.8481
10000	0.0454	-0.0013	0.0778	0.8542

Keep in mind that this approach is for simple linear differential equations representing lines. More complex scenarios may involve higher-order differential equations or nonlinear relationships, requiring different techniques for solution.

The following codes give the implementation of R3, L3, R6, and L6 in Matlab[TM], respectively.

```
R3(k)=((g(k+1)+g(k))*(a(k+2)-a(k+1))-
((g(k+2)+g(k+1))*(a(k+1)-a(k))))/...
    ((a(k+1)+a(k))*(a(k+2)-a(k+1))-
(a(k+2)+a(k+1))*(a(k+1)-a(k)));
dt=(t(n)-t(n-1));                                    (11)

L3(k)=(dt/2)*((a(k+1)+a(k))*(g(k+2)+g(k+1))-
((a(k+2)+a(k+1))*(g(k+1)+g(k))))/...
((a(k+1)+a(k))*(a(k+2)-a(k+1))-(a(k+2)+a(k+1))
*(a(k+1)-a(k)));

R6(k)=((g(k)+2*g(k+1)+2*g(k+2)+2*g(k+3)+2*g(k+4
)+g(k+5))*(a(k+10)-a(k+5))-(g(k+5)+2*g(k+6)
+2*g(k+7) +2*g(k+8)+2*g(k+9) +g(k+10))*(a(k+ 5)-
a(k)))/((a(k)+2*a(k+1)+2*a(k+2)+ 2*a(k+3)
+2*a(k+4)+ a(k+5))* (a(k+10)-a(k+5))-(a(k+5)+
2*a(k+6)+2*a(k+7) +2*a(k+8)+ 2*a(k+9)+a(k+10))
*(a(k+5)-a(k)));
dt=(t(n)-t(n-1));                                    (12)

L6(k)=(dt/2)*((a(k)+2*a(k+1)+2*a(k+2)+2*a(k+3)+2*
a(k+4)+a(k+5))*(g(k+5)+2*g(k+6)+2*g(k+7)+2*g(k+
8)+2*g(k+9)+g(k+10))-
(a(k+5)+2*a(k+6)+2*a(k+7)+2*a(k+8)+2*a(k+9)+a(k
+10))*(g(k)+2*g(k+1)+2*g(k+2)
+2*g(k+3)+2*g(k+4)+g(k+5)))/((a(k)+2*a(k+1)+2*a(
k+2)+2*a(k+3)+2*a(k+4)+a(k+5))*(a(k+10)-a(k+5))-
(a(k+5)+2*a(k+6)+2*a(k+7)+2*a(k+8)+2*a(k+9)+a(k
+10))*(a(k+5)-a(k)));
```

http://dergipark.gov.tr/bajece

III. Conclusion

The protection of transmission lines is essential due to their vulnerability to a myriad of risks, including natural disasters, equipment failures, and malicious activities. Disruptions to these lines can have far-reaching consequences, leading to widespread power outages, economic losses, and societal disruptions. Therefore, implementing robust protection measures is imperative to ensure the reliability and availability of electrical power.

The protection of transmission lines is a multifaceted endeavor that requires a holistic approach, combining engineering ingenuity, advanced technologies, and comprehensive planning. As our dependence on electrical power continues to grow, ensuring the resilience of transmission lines becomes increasingly vital. By embracing innovative solutions, prioritizing regular maintenance, and integrating robust cybersecurity measures, we can build a power infrastructure that is not only reliable but also resilient in the face of evolving challenges. In doing so, we fortify the backbone of our power grid, securing a stable and uninterrupted supply of electricity for the benefit of society as a whole.

Calculating parameters and characteristics of transmission lines involves several key factors such as impedance, propagation velocity, and attenuation. The calculations can vary depending on the type of transmission line. In this study, single representation of 3-phase line (1-125km) is used for calculating R and L parameters using DEA. As seen from Table1-4 the methods predict R and L parameters even at low Fs.

In future study, fault detection and location in power systems with a high density of inverter based generation, to overcome the issues of reverse power flow using DEA.

References

[1] Y. Liu, B. Wang, X. Zheng, D. Lu, M. Fu and N. Tai, "Fault Location Algorithm for Non-Homogeneous Transmission Lines Considering Line Asymmetry," in IEEE Transactions on Power Delivery, Vol. 35, No. 5, pp. 2425-2437, Oct. 2020, doi: 10.1109/TPWRD.2020.2968191.

[2] "IEEE Approved Draft Guide for the Parameter Measurement of AC Transmission Lines," in IEEE P1870/D7, October 2018 , Vol., No., pp.1-90, 20 March 2019.

[3] Z. Yang, K. Zhang, Y. Wang, Q. Zhao, F. Xiao and T. Wang, "A New Backup Protection for Transmission Lines Based on Substation-area Current Information," 2020 IEEE 4th Conference on Energy Internet and Energy System Integration (EI2), Wuhan, China, 2020, pp. 2347-2352, doi: 10.1109/EI250167.2020.9346906.

[4] D. Yildiz, S. Karagol and O. Ozgonenel, "Estimation of online transmission line parameters and fault location by using different differential equation algorithms," 2015 9th International Conference on Electrical and Electronics Engineering (ELECO), Bursa, Turkey, 2015, pp. 1034-1038, doi: 10.1109/ELECO.2015.7394500.

[5] N. Alimbekova, A. Berdyshev and D. Baigereyev, "Parallel Implementation of the Algorithm for Solving a Partial Differential Equation with a Fractional Derivative in the Sense of Riemann-Liouville," 2021 IEEE International Conference on Smart Information Systems and Technologies (SIST), Nur-Sultan, Kazakhstan, 2021, pp. 1-6, doi: 10.1109/SIST50301.2021.9465922.

[6] H. Sun and X. Li, "Computer Programming Optimization Based on Numerical Algorithms of Fractional Differential Equations," 2021 IEEE 3rd International Conference on Civil Aviation Safety and Information Technology (ICCASIT), Changsha, China, 2021, pp. 809-813, doi: 10.1109/ICCASIT53235.2021.9633409.

[7] R. Banerjee, D. Mukherjee, P. K. Guchhait, S. Chakraborty, J. Bhunia and A. Pal, "Numerical Approach for Finding the Solution of Single Term Nonlinear Fractional Differential Equation," 2020 IEEE 1st International Conference for Convergence in Engineering (ICCE), Kolkata, India, 2020, pp. 260-263, doi: 10.1109/ICCE50343.2020.9290561.

[8] M. Ratchagit and H. Xu, "Parameter Identification of Stochastic Delay Differential Equations Using Differential Evolution," 2022 37th International Technical Conference on Circuits/Systems, Computers and Communications (ITC-CSCC), Phuket, Thailand, 2022, pp. 1-3, doi: 10.1109/ITC-CSCC55581.2022.9894864.

[9] M. Yılmaz, "Real Measure of a Transmission Line Data with Load Fore-cast Model for The Future", Balkan Journal of Electrical and Computer Engineering, Vol.6, No.2, 2018, 141 - 145, 10.17694/bajece.419646.

[10] S. M. Çürük, V. Özkaner, "A Measurement Based Study to Assess Power Line Communication Network Throughput Performance", Balkan Journal of Electrical and Computer Engineering, Vol.7, No.1, 2019, 27 - 33, 10.17694/bajece.457390.

[11] M.A. Özçelik, "A Micro Hybrid Wind-Pv Based On Grid Energy System With Enhanced Efficiency", European Journal of Technique (EJT), Vol.7, No.2, 2017, 109 – 118.

[12] M. A. Özçelik, A. Aycan" Experimental Investigation of the Variation of Power and Iron-Copper Losses in the Loaded Operation of the Transformer", European Journal of Technique (EJT), Vol.12, No.2, 2022, 152 - 155, 10.36222/ejt.1196829.

BIOGRAPHIES

CENK GEZEGİN was born in Amasya in 1982. He graduated from Kocaeli University Electrical Education Department in 2002. He received his M.Sc. and Ph.D. degrees from Ondokuz Mayis University, Department of Electrical and Electronics Engineering in 2006 and 2018, respectively. From 2007 to 2020, he served as Head of the Electricity and Energy Department of Vocational School of Amasya University, Department of Technical Sciences. He has been working as an Assist. Prof. in the Department of Electrical and Electronics Engineering at Ondokuz Mayis University since 2020. His main research interests include hotspots in transformers, technical and economic analysis of renewable energy systems, and power quality in electrical networks, hotspots in transformers, technical and economic analysis of renewable energy systems, and power quality in electrical networks.

Multi-Channel CooperativeSpectrum Sensing and Scheduling for Cognitive IoT Networks

Abdulkadir Celik

Abstract—This paper presents a novel multi-channel cooperative spectrum sensing and scheduling (MC_2S_3) framework for spectrum and energy harvesting cognitive Internet of Things (IoT) networks. We address the challenge of maximizing network throughput by formulating a combinatorial problem that jointly optimizes the sensing scheduling of primary channels (PCs), the assignment of IoT devices for sensing scheduled PCs, and the clustering and allocation of IoT nodes to efficiently use discovered idle PCs; subject to spectrum utilization and collision avoidance constraints. Recognizing the inherent complexity of the underlying NP-hard mixed-integer non-linear programming (MINLP) problem, we propose a decomposition strategy that decouples the master problem into PC exploration and exploitation subproblems. In the exploration phase, we derive closed-form solutions for optimal sensing durations and detection thresholds that satisfies spectrum utilization and collision avoidance constraints, which are then used to develop a priority metric to rank PCs. The proposed PC ranking informs a sequential PC scheduling and IoT sensing assignment approach that exploits a linear bottleneck assignment (LBA) strategy, proceeding until further scheduling does not enhance network utility. For the exploitation phase, we leverage a non-orthogonal multiple access (NOMA) strategy to multiplex multiple IoT nodes on a single PC, employing an iterative linear sum assignment (LSA) method for efficient allocation to maximize utilization of idle PCs. Numerical results validate the efficacy of our proposed methodologies, reaching an accuracy of approximately 99% in the order of milliseconds, significantly outperforming time complexity of brute-force benchmarks.

Index Terms—Internet of Things, Cognitive Radio Networks, Cooperative Spectrum Sensing, Energy Detection, Energy Harvesting.

I. INTRODUCTION

THE PROLIFERATIO of the Internet of Things (IoT) has dramatically intensified the demand for efficient spectrum management strategies in cognitive radio networks (CRNs) [1], [2]. In particular, stands at the forefront of this challenge, facilitating a collaborative mechanism for IoT devices to detect and utilize underutilized spectrum bands across multiple primary channels (PCs), thereby addressing the spectrum scarcity problem [3]. This endeavor unfolds through two critical phases: *spectrum exploration* and *spectrum exploitation*, each harboring distinct complexities and optimization prospects.

During the spectrum exploration stage, the essence of multi-channel cooperative spectrum sensing scheduling (MC_2S_3) unfolds as multiple IoT nodes concurrently sense various PCs, reporting their findings to a central decision maker, typically

Abdulkadir Celik Computer, Electrical and Mathematical Sciences and Engineering (CEMSE) Division, King Abdullah University of Science and Technology (KAUST), Thuwal, KSA 23955-6900.
(e-mail: abdulkadir.celik@kaust.edu.sa)
https://orcid.org/ 0000-0001-9007-9979

a secondary base station (SBS) [4]. The overarching goal is to minimize the exploration time by swiftly identifying the greatest number of potentially idle PCs with a high probability of being unoccupied. The duration of PC exploration predominantly hinges on the assignment of IoT nodes to sense scheduled PCs, ultimately determined by the node with the longest sensing time. Therefore, the overall channel exploration time is set by the slowest IoT as the SBS cannot make a decision until receiving local decisions from all IoT nodes. Moreover, requiring more IoT nodes to cooperate on sensing improves the detection accuracy of MC_2S_3. This necessitates a judicious balance between the speed of detection and the accuracy of cooperatively identifying idle spectrum opportunities. Another subtle yet critical issue is that a PC with a high probability of being idle may incur a high sensing duration if there is no IoT nodes with good sensing quality on that PC. Thus, scheduling such a PC to be sensed may deteriorate overall spectrum discovery and available throughput for the IoT network, underscoring the importance of a joint optimization strategy for both PC scheduling and IoT sensing assignment. It is also worth noting that jointly optimizing sensing and scheduling tasks to minimize the spectrum exploration time not only maximizes the time remaining for the spectrum exploitation but also minimizes the MC_2S_3 energy consumption and maximizes the available time for wireless energy harvesting [5].

The *spectrum exploitation* phase focuses on the effective allocation of identified idle PCs and the strategic clustering of IoT devices, aiming to maximize the utility of limited spectrum resources. In densely populated IoT networks, where the demand for vacant PCs far exceeds the supply, achieving high-quality service (QoS) becomes a formidable challenge. Here, non-orthogonal multiple access (NOMA) techniques offer a promising solution by allowing multiple users to share the same spectrum resources through distinct identification methods such as power levels or codes, thereby enhancing spectrum efficiency [6]. However, the implementation of traditional power-domain NOMA schemes involves complexities related to grant acquisition and power weight calculations, which could introduce computational and signaling overheads, especially in uplink transmissions [7]. To circumvent these challenges, our study explores a grant-free operational model, where transmit powers are predetermined, and the reception disparity is tactically managed during the clustering phase by grouping IoT nodes with distinct channel characteristics into the same cluster.

Addressing the intertwined challenges of efficient spectrum sensing, optimal scheduling, and effective exploitation of discovered spectrum often falls within the real of combinatorial problems, whose computational complexity is prohibitive even

for moderate size of networks. Accordingly, this paper contributes to the advancement of cognitive IoT networks through developing fast yet efficient solutions for enhancing network throughput, energy efficiency, and overall performance in the face of growing spectrum demands.

A. Related Works

Cooperative Spectrum Sensing (CSS) has emerged as a pivotal technology to address the challenges of spectrum scarcity in cognitive IoT networks, focusing on optimizing spectral and energy efficiency while ensuring minimal interference with primary network (PN). This subsection reviews recent advancements in CSS, highlighting various strategies aimed at optimizing sensing operations, energy consumption, and network throughput.

Heuristic Solutions and Optimization Techniques have been proposed to address the challenges in CSS, aiming at improving energy efficiency and network utility. Chauhan et al. introduced a CSS scheme using a greedy-based heuristic solution to enhance network utility and energy efficiency in heterogeneous multi-channel CRNs. This approach adaptively optimizes the sensing duration based on the received signal-to-noise ratio (SNR) [8]. On the other hand, Cao et al. proposed a PSO-based CSS strategy, focusing on system throughput and energy efficiency optimization. This strategy balances sensing performance and energy consumption effectively [9]. Likewise, Kaschel et al. explored energy-efficient solutions for dynamic CRNs, proposing a framework to predict energy consumption in CSS tasks, minimizing energy consumption with low-complexity algorithms [10]. Moreover, a green approach with an emphasis on high energy efficiency through spectrum sensing and power allocation optimization is proposed in [11], demonstrating significant energy efficient improvements. Finally, Al-Kofahi et al. proposed Spectrum Sensing as a Service (SSaS) approach to optimize sensor selection to minimize energy consumption with a sub-optimal greedy algorithm [12]. In [13] and [14], statistical and systematic approaches are offered to evaluate network lifetime and identifying correlations between spectrum sensing, clustering algorithms, and energy-harvesting technology, respectively. Finally, Wu et al. explored the impact of user characteristics on CSS performance in mobile CRNs, proposing a dynamic detection scheme to optimize performance [15].

Machine Learning (ML) Approaches have also been utilized to enhance sensing accuracy and efficiency in CSS. Ning et al. presented a reinforcement learning-enabled CSS scheme for CRNs, optimizing the scanning order of channels and the selection of cooperative partners to improve detection efficiency [16]. Shi et al. employed multiple ML algorithms, including unsupervised and supervised learning techniques, to tackle the challenges of complex sensing models in CSS [17]. Moreover, Ahmed et al. integrated CR technology with IoT, employing SVM for spectrum sensing and allocation, demonstrating high reliability in frequency band allocation [18].

Game-Theoretic Models have been applied to extend network lifetime and improve sensing quality and cooperation among sensors. Bagheri et al. proposed a novel game-theoretic sensor selection algorithm for MCSS in WSNs, focusing on extending the network lifetime while ensuring the quality of sensing [19]. Rajendran et al. introduced a distributed coalition formation game with a genetic algorithm for optimal coalition head selection in CSS among SUs, enhancing sensing accuracy and minimizing energy consumption [20].

Cooperative Prediction and Sensing Schemes have also been studied to minimize energy consumption and maintain spectral efficiency. Chauhan et al. proposed a cooperative spectrum prediction-driven sensing scheme employing long short-term memory networks for local spectrum prediction, aiming at reducing energy consumption [21]. Gharib et al. proposed a heterogeneous multi-band multi-user CSS scheme for IoT in CR networks, improving detection performance and CRN throughput through optimized leader selection and cooperative sensing [22].

B. Main Contributions

The main contributions of this paper can be summarized as follows:

- We consider MC_2S_3 for spectrum and energy harvesting cognitive IoT networks. An optimal problem formulation is provided to maximize overall IoT network throughput through joint optimization of sensing scheduling of PCs, assignment of IoTs to sense scheduled PCs, and clustering and allocating IoT nodes to exploit discovered idle PCs; subject to collision and spectrum utilization constraints of CSS. The proposed system model considers practical aspects including channel reporting errors as well as channel switching and reporting latency.
- Since the optimal problem falls into the class of mixed-integer non-linear programming (MINLP) problem, which is known to be NP-hard, we propose a decomposition approach to decouple it into PC exploration and exploitation sub-problems. For the PC exploration sub-problem, we derive optimal sensing durations and detection thresholds in closed-form to inform a PC ranking mechanism based on a newly proposed priority metric. PCs are scheduled sequentially according to their priority, and IoT nodes are assigned using a linear bottleneck assignment (LBA) strategy to minimize exploration time. This process continues until additional PC scheduling does not further benefit the network's utility.
- For the exploitation phase, upon identifying a set of idle PCs, we organize IoT nodes into clusters and allocate them to discovered idle PCs. Given the potential disparity between the number of IoT nodes and available idle PCs, we employ a non-orthogonal multiple access (NOMA) strategy. This allows for the multiplexing of multiple IoT nodes on a single PC. Allocation is done using an iterative linear sum assignment (LSA) method, adding IoT nodes to an idle PC until all nodes are allocated, thus maximizing the utilization of available spectrum resources.
- Our numerical analysis demonstrates that the proposed methodologies achieve approximately 99% accuracy in

milliseconds, a significant improvement over traditional brute-force approaches that exhaustively search all possible combinations to identify optimal sensing schedules and IoT node clustering.

C. Paper Organization and Notations

The remainder of paper is organized as follows: Section II delineates the system model. Section III provide details of MC_2S_3, multi-modal energy harvesting, and NOMA-based IoT data transmission. Section IV formulates the optimal problem and outline the proposed solution methodology. Section V presents proposed decomposed approach and explain its algorithmic implementation. Section VI provide numerical results. Finally, Section VII papers with a few remarks.

Notations: Throughout the paper, sets and their cardinality are denoted with calligraphic and regular uppercase letters (e.g., $|\mathcal{A}| = A$), respectively. Vectors and matrices are represented in lowercase and uppercase boldfaces (e.g., $\boldsymbol{a}$ and $\boldsymbol{A}$), respectively. The ith member of a vector and set is denoted by $\boldsymbol{a}[i]$ and $\mathcal{A}\{i\}$, respectively. Likewise, matrix $\boldsymbol{A}$'s entry on i^{th} row and j^{th} column is denoted by $\boldsymbol{A}[i,j]$. Subscripts m, n, and i are used for indexing PCs, IoT nodes, and idle PCs, respectively.

II. SYSTEM MODEL

This section introduces system models for PN, secondary network (SN), and underlying models for sensing, reporting, and communication channels.

A. Primary Network

We consider a PN which is licensed to operate on M downlink PCs, whose index set is denoted by $\mathcal{M}$, each with a bandwidth of W Hz. The PN consists of a single primary base station that communicates with its associated primary users over dedicated PCs. Primary transmissions operate on a synchronous communication protocol with time-slot duration of T. The actual occupancy state of a PC is denoted by $O_m \in \{0,1\}$, with $O_m = 1$ if PC_m is busy, $O_m = 0$ otherwise. The binary hypotheses correspond to the idle and busy PC states are denoted as $\mathcal{H}_m^0$ and $\mathcal{H}_m^1$, respectively. The PC traffic is modeled as an independent and identically distributed (i.i.d.) random process such that π_0^m and π_1^m represent the apriori probability of being idle and busy for PCs, respectively. We assume that these apriori probabilities are obtained over long-term observations and known to the SN.

B. Secondary Network

The SN comprises of N time synchronous energy and spectrum harvesting IoT devices, whose index set is denoted by $\mathcal{N}$. The SN is orchestrated by a SBS that also follows a time-slotted operation synchronized to the PN. As shown in Fig. 1, each time-slot of duration T is split into two stages: multi-channel *exploration* and *exploitation*. In the multi-channel exploration stage, the IoT devices collaboratively searches for the available bands by means of a MC_2S_3 policy, wherein the SBS assigns a set of PCs to each IoT device for sequential
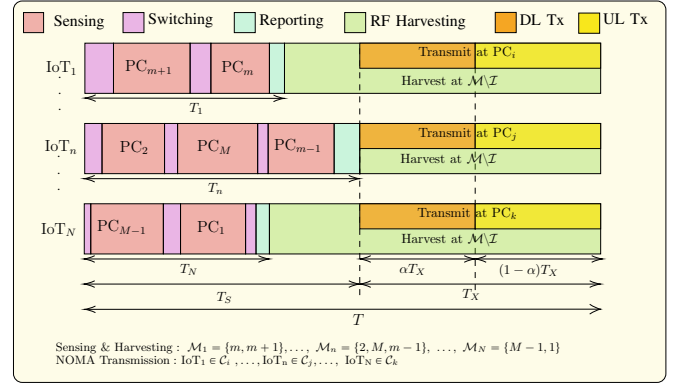
Figure 1: Time-slotted operation of the secondary network.

sensing, which requires IoT devices to switch channel and adjust their operating frequency to the assigned channels. Accordingly, the binary sensing assignment matrix is denoted by $\mathbf{X} \in \{0,1\}^{M \times N}$, whose elements are given by

$$x_m^n = \begin{cases} 1 & \text{, if } IoT_n \text{ is assigned to sense } PC_m \\ 0 & \text{, otherwise} \end{cases}, \quad (1)$$

$\forall m \in \mathcal{M}, \forall n \in \mathcal{N}$. Hence, the set of PCs assigned to IoT_n for sequential sensing is represented by $\mathcal{M}_n = \{m \mid x_m^n = 1, \forall m\}$, whose cardinality is $M_n = \sum_n x_m^n$. Likewise, the cluster of IoT nodes that cooperatively sense PC_m is denoted by $\mathcal{N}_m = \{n \mid x_m^n = 1, \forall n\}$, whose cardinality is $N_m = \sum_m x_m^n$. To reach a better global decision, MC_2S_3 typically requires PCs to be sensed by a certain number of IoTs, i.e., $N_m \geqslant \bar{N}$.

However, sensing all PCs may require IoTs to search over a large number of PCs and results in limited exploration time, especially when $\bar{N} \gg \frac{N}{M}$. At this point, PC sensing scheduling becomes paramount, which is represented by $\mathbf{y} \in \{0,1\}^M$ with $y_m = 1$ if PC_m is scheduled for sensing, $y_m = 0$ otherwise. Following the completion of sequential sensing, IoTs report their local decisions on channel occupancy states to the SBS that makes global decisions and broadcasts the list of I idle PCs, $\mathcal{I}$. Denoting overall sensing, switching, and reporting duration for IoT_n by T_n^s, the overall multi-channel search time is determined by the IoT taking the longest channel search time (e.g., IoT_n in Fig. 1) as the SBS needs to receive all reports to reach a conclusion.

In the multi-channel exploitation stage, IoT devices are scheduled to transmit data over the residual time after the multi-channel exploration. Denoting the number of sample matrix as $\boldsymbol{S} \in \mathbb{N}^{M \times N}$, the overall transmission duration is given by $T_X(\boldsymbol{X}, \boldsymbol{y}, \boldsymbol{S}) = T - T_S(\boldsymbol{X}, \boldsymbol{y}, \boldsymbol{S})$, during which IoT devices exploit the discovered idle PCs, $\mathcal{I}$, and busy PCs, $\mathcal{M}\backslash\mathcal{I}$, for data transmission and RF energy harvesting, respectively. During the exploitation stage, the SN operates in a NOMA fashion, wherein IoT devices are clustered to exploit idle PCs. Accordingly, the binary PC allocation and IoT clustering matrix is denoted by $\mathbf{Z} \in \{0,1\}^{M \times N}$, whose elements are given by

$$z_m^n = \begin{cases} 1 & \text{, if } IoT_n \text{ transmits at } PC_m \\ 0 & \text{, otherwise} \end{cases}, \forall m \in \mathcal{M}, \forall n \in \mathcal{N},$$

$$(2)$$

based on which, the IoT cluster transmitting at PC_m is denoted by $\mathcal{C}_m = \{n \mid z_m^n = 1, \forall n\}$, $\forall m$, $|\mathcal{C}_m| = C_m \leqslant \lceil \frac{N}{M} \rceil$.

C. Channel Model

The sensing channel gain matrix between the PBS and IoT devices is denoted by $\mathbf{H} \in \mathbb{R}^{\mathbf{M} \times \mathbf{N}}$, whose elements h_m^n, $\forall m \in [1, M]$, $\forall n \in [1, N]$, are given by

$$h_m^n = G_m G_n K_m \left[\frac{d_0}{d_m^n} \right]^{\theta} 10^{\psi_m^n/10} \tag{3}$$

where G_t is the transmitter gain of the PBS, G_n is the receiver gain of IoT_n, $K_m = \frac{c}{4\pi d_0 f_m}$, c is the speed of light, f_m is the carrier frequency of the PC_m, d_0 is a reference distance, d_m^n is the distance between the PBS and IoT_n, θ is the path loss exponent, $10^{\psi_m^n/10}$ is the log-normal shadowing, and ψ_m^n is a normal random variable representing the variation in received power with a standard deviation of σ_m^n, i.e., $\psi_m^n \sim \mathcal{N}(0, \sigma_m^n)$. The reporting between SBS and IoT_n occurs on a dedicated control channel, which is denoted by g_n^s and follows the composite channel gain similar to (3). Likewise, the transmission channel gain matrix between the SBS and IoT devices is denoted by $\tilde{\mathbf{H}} \in \mathbb{R}^{\mathbf{M} \times \mathbf{N}}$, whose elements, $\tilde{h}_m^n$, can also be obtained following the same model presented in (3). We assume all channels to be quasi-static which experience flat fading during the sensing, reporting, and transmission phases.

III. MULTI-CHANNEL COOPERATIVE SPECTRUM SENSING AND ENERGY HARVESTING

In this section, we delineate the spectrum exploitation and exploration stages by providing the technical details of multi-channel cooperative spectrum sensing, multi-modal energy harvesting, and IoT data transmission.

A. Spectrum Exploration Stage

Since our main focus in this paper is the scheduling aspects of the CSS, we prefer *energy detection* as a generic method because it does not require any apriori information regarding the PN's physical layer features. Without loss of generality, let us focus on spectrum sensing of PC_m with IoT devices belong to $\mathcal{N}_m$. First, $IoT_n \in \mathcal{N}_m$ measures the energy of received signal on $PC_m \in \mathcal{M}$ for a number of samples, S_m^n, and compares it with a detection threshold, ε_m^n, to reach a local decision on the idle and busy states of PC_m.

The overall channel search time for IoT_n comprises of three phases: 1) Energy detection duration, T_n^{ed}; 2) channel switching time T_n^{sw}; and 3) reporting time, T_n^r. Denoting the sampling frequency and interval by W and $\tau_s = 1/W$, the number of samples determines the energy detection duration for IoT_n, $\forall n \in \mathcal{N}_m$ on PB_m as $\tau_n^n = S_m^n \tau_s$. We assume that the channel switching time obeys triangularity and linearity properties [23], i.e., $\beta |f_{\mathcal{M}_n\{i\}}^c - f_{\mathcal{M}_n\{j\}}^c|$, $i \neq j, 1 \leqslant i, j \leqslant M_n$, where β is a switching factor that depends on hardware parameters and power consumption and $f_{\mathcal{M}_n\{i\}}^c - f_{\mathcal{M}_n\{j\}}^c$ is the central frequency of the PC_i/PC_j, $(i, j) \in \mathcal{M}_n$. Accordingly, the channel search time for IoT_n can be expressed as

$$T_n^s(\boldsymbol{X}, \boldsymbol{y}, \boldsymbol{S}) = T_n^{ed} + T_n^{sw} + T_n^r \tag{4}$$

where

$$T_n^{ed} = \tau_s \sum_m S_m^n x_m^n y_m, \tag{5}$$

$$T_n^{sw} = \beta \left| f_{\mathcal{M}_n\{i\}}^c - f_0^c \right| + \sum_{i=1}^{M_n} \beta \left| f_{\mathcal{M}_n\{i\}}^c - f_{\mathcal{M}_n\{i-1\}}^c \right|, \tag{6}$$

$$T_n^r = \tau_r \sum_m x_m^n y_m, \text{ and} \tag{7}$$

f_0^c is the central frequency of the last PC sensed in the previous time slot. Following from (4), the overall multi-channel exploration time is given by

$$T_S(\boldsymbol{X}, \boldsymbol{y}, \boldsymbol{S}) = \max_{n \in \mathcal{N}} \{T_n^s(\boldsymbol{X}, \boldsymbol{y}, \boldsymbol{S})\}. \tag{8}$$

For a normalized noise variance and large enough S_m^n, the probability of false alarm, $P_{m,n}^f \triangleq \mathcal{P}[\mathcal{H}_m^1 | \mathcal{H}_m^0]$, and the probability of detection, $P_{m,n}^d(S_m^n, \varepsilon_m^n) \triangleq \mathcal{P}[\mathcal{H}_m^1 | \mathcal{H}_m^1]$, are respectively given by [24]

$$P_{m,n}^f(S_m^n, \varepsilon_m^n) = \mathcal{Q}\left[(\varepsilon_m^n - 1) \sqrt{S_m^n} \right], \tag{9}$$

$$P_{m,n}^d(S_m^n, \varepsilon_m^n)(t) = \mathcal{Q}\left[(\varepsilon_m^n - \gamma_m^n - 1) \sqrt{\frac{S_m^n}{2\gamma_m^n + 1}} \right], \tag{10}$$

where γ_m^n is the received sensing signal-to-noise-ratio (SNR) at IoT_n on the PC_m and $\mathcal{Q}(x) = \frac{1}{\sqrt{2\pi}} \int_x^{+\infty} e^{-y^2/2} dy$ denote the right-tail probability of a normalized Gaussian distribution.

Notice in (9) and (10) that both probabilities are jointly determined by the detection threshold and number of samples, i.e., sensing duration. Since false alarm and detection probabilities are key metrics to measure sensing accuracy, a joint optimization of these variables is necessary to reach predetermined thresholds. After the sequential local sensing process, the IoT_n sends its binary result $u_m^n \in \{0, 1\}$ to the SBS over a binary symmetric channel (BSC), which is received by the SBS as $\tilde{u}_m^n$. The error probability of the BSC is defined as $p_m^n = \mathcal{P}[\tilde{u}_m^n = 0 | u_m^n = 1] = \mathcal{P}[\tilde{u}_m^n = 1 | u_m^n = 0]$. Accordingly, the SBS receives the local false alarm and detection probabilities as

$$\tilde{P}_{m,n}^f(S_m^n, \varepsilon_m^n) = p_m^n [1 - P_{m,n}^f] + [1 - p_m^n] P_{m,n}^f \tag{11}$$

$$\tilde{P}_{m,n}^d(S_m^n, \varepsilon_m^n) = p_m^n [1 - P_{m,n}^d] + [1 - p_m^n] P_{m,n}^d \tag{12}$$

The SBS collects $\tilde{u}_m^n$, $\forall m, \forall n$, and makes the global decision using the k-out-of-N decision fusion test

$$\mathcal{K}_m = \sum_{n \in \mathcal{N}_m} \tilde{u}_m^n x_m^n \underset{\mathcal{H}_m^0}{\overset{\mathcal{H}_m^1}{\gtrless}} \kappa_m, \tag{13}$$

where $1 \leqslant \kappa_m \leqslant N_m$ is the voting rule. For instance, $\kappa_m = 1$, $\kappa_m = N_m$, and $\kappa_m = \lceil \frac{N_m}{2} \rceil$ are referred to as OR, AND, and majority voting rules, respectively. $\mathcal{K}_m$ follows Binomial distribution if $\tilde{u}_m^n$'s are i.i.d, which naturally requires all reported local detection and false alarm probabilities to be identical If the i.i.d condition is satisfied, the global false alarm $Q_m^f(S_m^n, \varepsilon_m^n) = \mathcal{P}[\mathcal{K}_m \geqslant \kappa_m | \mathcal{H}_m^0]$ and detection $Q_m^d(S_m^n, \varepsilon_m^n) = \mathcal{P}[\mathcal{K}_m \geqslant \kappa_m | \mathcal{H}_m^1]$ probabilities

can be expressed by using the probability mass function (pmf) of the Binomial variable as follows

$$Q_m^f(S_m^n, \varepsilon_m^n) = \mathcal{P}\left[\mathcal{K}_m \geqslant \kappa_m | \mathcal{H}_m^0\right] = \qquad (14)$$

$$\sum_{i=\kappa_m}^{N_m} \binom{N_m}{i} \left(\tilde{P}_m^f(S_m^n, \varepsilon_m^n)\right)^i \left(1 - \tilde{P}_m^f(S_m^n, \varepsilon_m^n)\right)^{N_m - i},$$

$$Q_m^d(S_m^n, \varepsilon_m^n) = \mathcal{P}\left[\mathcal{K}_m \geqslant \kappa_m | \mathcal{H}_m^1\right] = \qquad (15)$$

$$\sum_{i=\kappa_m}^{N_m} \binom{N_m}{i} \left(\tilde{P}_m^d(S_m^n, \varepsilon_m^n)\right)^i \left(1 - \tilde{P}_m^d(S_m^n, \varepsilon_m^n)\right)^{N_m - i}.$$

Indeed, opportunistic spectrum access schemes typically require spectrum utilization constraint, i.e., $Q_m^f(S_m^n, \varepsilon_m^n) \leqslant \bar{Q}_f$, and collision avoidance constraint, i.e., $Q_m^d(S_m^n, \varepsilon_m^n) \geqslant \bar{Q}_d$, are satisfied at the same time. For instance, predetermined thresholds of $\bar{Q}_f = 0.01$ and $\bar{Q}_d = 0.99$ ensure that idle and busy channels are utilized and correctly detected 99% of the time, respectively. Since both $Q_m^f(S_m^n, \varepsilon_m^n)$ and $Q_m^d(S_m^n, \varepsilon_m^n)$ are determined by the cluster size, N_m, the global false alarm and detection probability constraints require reported local false alarm and detection probabilities to respectively satisfy

$$\tilde{P}_m^{f,\star}(N_m) \leqslant \begin{cases} 1 - \sqrt[N_m]{1 - \bar{Q}_f} & , \kappa_m = 1 \\ \sqrt[N_m]{\bar{Q}_f} & , \kappa_m = N_m \end{cases}, \qquad (16)$$

$$\tilde{P}_m^{d,\star}(N_m) \geqslant \begin{cases} 1 - \sqrt[N_m]{1 - \bar{Q}_d} & , \kappa_m = 1 \\ \sqrt[N_m]{\bar{Q}_d} & , \kappa_m = N_m \end{cases}, \qquad (17)$$

which can be solved numerically for other voting rules, $1 < \kappa_m < N_m$. In order to satisfy both i.i.d. conditions and global constraints, $\text{IoT}_n \in \mathcal{N}_m$ needs to adjust its local false alarm and detection probabilities according to the erroneous BSC channel conditions as

$$P_{m,n}^{f\star}(N_m) \leqslant \frac{\tilde{P}_m^{f,\star}(N_m) - p_m^n}{1 - 2p_m^n}, \qquad (18)$$

$$P_{m,n}^{d\star}(N_m) \geqslant \frac{\tilde{P}_m^{d,\star}(N_m) - p_m^n}{1 - 2p_m^n}, \qquad (19)$$

which follows from (11) and (12), respectively.

B. Multi-Modal Energy Harvesting

In addition to scavenging energy from other ambient sources, e.g., flexible solar patches, IoT devices are also assumed to harvest RF energy from busy PCs. The energy arrival rate for RF and non-RF energy modalities are denoted bu $\chi_{m,n}^{RF}$ and χ_{sol}^n [J/s] which depends on received power on PC_m and light intensity along with hardware specifications (e.g., energy conversion and storing efficiency, etc.), respectively. Indeed, energy detectors can be designed to support both spectrum sensing and RF energy harvesting on the same platform through power splitting or time switching [25]. Following the spectrum searching, each IoT switch themselves to the PC with the highest reception power, yielding the total harvested energy of $E_h^n = \chi_{sol}^n T + \text{argmax}_m \{\chi_{m,n}^{RF}(T - T_S(\boldsymbol{X}, \boldsymbol{y}, \boldsymbol{S}))\}$, where the first and second terms are harvested energy from RF and solar ambient sources, respectively. Since the non-RF energy harvesting is independent of MC_2S_3, we will focus our attention on the RF energy harvesting. In case

of time switching mode, the harvested RF energy can only be maximized by minimizing the channel exploration phase, which will be the main focus of the formulated problem and developed solution methodology in the sequel.

C. IoT Data Transmission

The efficient use of discovered idle spectrum is of utmost importance, especially for dense SNs trying to utilize limited vacant PCs of a PN exhibiting frequent traffic characteristics, i.e., $I \ll N$. In such scenarios, exploitation of OMA to avoid interference may not provide required QoS demands for numerous IoT nodes that merely depends on the free spectrum. At this point, NOMA can offer high spectrum efficiency by multiplexing several users in the same time/frequency resource by distinguishing each with discrete codes, power levels, etc. For instance, NOMA allows SN to serve at most $C = \lceil \frac{I}{N} \rceil$ IoT nodes at each vacant PC. The traditional power-domain NOMA schemes requires grant acquisition and optimal power weight calculations, which may incur computational complexity and signaling overhead, especially in the UL transmission. Therefore, we consider a grant-free operation where transmit powers are set a predetermined level while power reception disparity is implicitly implemented during the clustering phase by admitting IoT nodes with distinct channels into the same cluster.

Without loss of generality, let us elucidate how NOMA can facilitate data transmission for the ith IoT cluster, $\mathcal{C}_i$, by dividing exploration duration into $\alpha T_X(\boldsymbol{X}, \boldsymbol{y}, \boldsymbol{\mathcal{S}})$ and $(1 - \alpha)T_X(\boldsymbol{X}, \boldsymbol{y}, \boldsymbol{\mathcal{S}})$ for DL and UL traffic, respectively. $\alpha \in [0, 1]$ is a design parameter and can be set based on temporal traffic characteristics of the SN. Due to the quasi-static channel assumption and time-division multiplexing during the same time slot, the DL/UL common channel gains of $\mathcal{C}_i$ sorted in descending order can be denoted by $\tilde{\boldsymbol{h}_i} = [\tilde{h}_i^1, \ldots, \tilde{h}_i^j, \ldots, \tilde{h}_i^{C_i}]$. Hence, the received DL and UL signals for $\text{IoT}_j, j \in \mathcal{C}_i$, are respectively given by

$$\breve{r}_i^j = \left(\sum_{j \in \mathcal{C}_i} \sqrt{P_s^i} \breve{\omega}_i^j \breve{s}_j\right) \tilde{h}_i^j + n, \qquad (20)$$

$$\hat{r}_i^j = \sum_{j \in \mathcal{C}_i} \sqrt{P_j} \tilde{h}_i^j \hat{\omega}_i^j \hat{s}_j + n, \qquad (21)$$

where $P_s^i \triangleq P_{\max}^s / I$ is the maximum DL transmission power at PC_i such that the maximum transmit power of the SBS, $P_{\max}^s$, is equally shared by clusters and members within cluster, P_j is the maximum transmit power of IoT_j, $\breve{\omega}_i^j / \hat{\omega}_i^j$ is the DL/UL power allocation of IoT_j, $\breve{s}_j / \hat{s}_j$ is the DL/UL message for IoT_j, and $n \sim \mathcal{N}(0, \sigma^2)$ is the additive white Gaussian thermal noise, $\sigma^2 = N_0 W$ is the thermal noise power, and N_0 is the thermal noise power spectral density. It is worth noting that cluster members' channel gains play the crucial role of power weights to ensure power reception disparity, which primarily determines the spectral efficiency of NOMA schemes. At the receiver side, a successive interference cancellation (SIC) receiver iteratively decodes the messages in the order of reception power and removes decoded messages
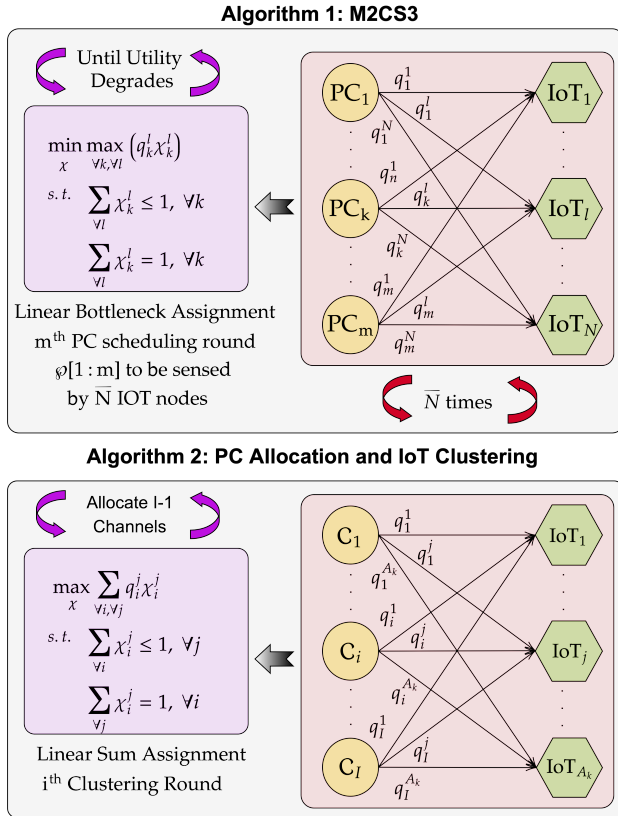
Figure 2: Depiction of Alg. 1 (up) and Alg. 2 (down).

to reduce interference at each time step, leading to following DL and UL SINRs

$$\breve{\gamma}_i^j = \frac{|\tilde{h}_i^j|^2 \breve{\omega}_i^j}{\epsilon \sum_{k=1}^{j-1} |\tilde{h}_i^j|^2 \breve{\omega}_i^k + \sum_{l=j+1}^{C_i} |\tilde{h}_i^j|^2 \breve{\omega}_i^l + \sigma^2/P_s^i}, \quad (22)$$

$$\widehat{\gamma}_i^j = \frac{|\tilde{h}_i^j|^2 \widehat{\omega}_i^j}{\sum_{k=1}^{j-1} |\tilde{h}_i^k|^2 \widehat{\omega}_i^k + \epsilon \sum_{l=j+1}^{C_i} |\tilde{h}_i^l|^2 \widehat{\omega}_i^l + \sigma^2/P_j}. \quad (23)$$

Accordingly, the combined bidirectional data rate of IoT_j on PC_i is given by

$$R_i^j = \left[\alpha \log_2(1 + \widehat{\gamma}_i^j) + (1-\alpha) \log_2(1 + \breve{\gamma}_i^j) \right], j \in \mathcal{C}_i \quad (24)$$

which can also be denoted as $R_i^j(\boldsymbol{Z})$ by setting $\boldsymbol{Z}[i, \mathcal{C}_i] = 1$ and multiplying ω_a^b terms with $\boldsymbol{Z}[a, b]$ elements in (22).

IV. PROBLEM FORMULATION AND SOLUTION METHODOLOGY

The throughput maximization of cognitive IoT networks depends on two main criteria:

1) Discovery of the highest possible number of idle PCs to maximize the spectrum available for IoT nodes. At this point, joint optimization of sensing scheduling variables (i.e., $\boldsymbol{X}, \boldsymbol{y}$), are of paramount importance to schedule PCs with a high probability of being idle and low sensing duration.

2) The optimal utilization of discovered idle PCs through effective PC allocation and IoT clustering.

Accordingly, overall throughput achievable by the SN can be expressed as in (25), where the first and second parts are

related to spectrum exploration and exploitation problems. Following from (25), optimal formulation of the spectrum exploration and exploitation problem can be obtained as follows

$$\mathbf{P_o}: \max_{\substack{\boldsymbol{X}, \boldsymbol{y}, \boldsymbol{Z} \\ \boldsymbol{\mathcal{S}}, \boldsymbol{\mathcal{E}}}} \quad R(\boldsymbol{X}, \boldsymbol{y}, \boldsymbol{Z}, \boldsymbol{\mathcal{S}}, \boldsymbol{\mathcal{E}})$$

$$C_o^1: \quad \text{s.t.} \quad \bar{Q}_d \leqslant Q_m^d(S_m^n, \varepsilon_m^n), \ \forall m \in \{m| \ y_m = 1\}$$

$$C_o^2: \quad Q_m^f(S_m^n, \varepsilon_m^n) \leqslant \bar{Q}_f, \ \forall m \in \{m| \ y_m = 1\}$$

$$C_o^3: \quad x_m^n \leqslant y_m, \ \forall m; \forall n$$

$$C_o^4: \quad \bar{N} y_m \leqslant \sum_{n \in \mathcal{N}} x_m^n, \ \forall m$$

$$C_o^5: \quad \overline{S} \leqslant S_m^n \leqslant T/T_s, \ \forall m; \forall n \qquad ,$$

$$C_o^6: \quad 0 \leqslant T - T_S(\boldsymbol{X}, \boldsymbol{y}, \boldsymbol{\mathcal{S}}),$$

$$C_o^7: \quad \sum_{m \in \mathcal{M}} z_m^n \leqslant 1, \ \forall n$$

$$C_o^8: \quad \sum_{n \in \mathcal{N}} z_m^n \leqslant \left\lceil \frac{N}{M} \right\rceil, \ \forall m$$

$$C_o^9: \quad \boldsymbol{X} \in \{0,1\}^{M \times N}, \boldsymbol{y} \in \{0,1\}^M,$$

$$\boldsymbol{Z} \in \{0,1\}^{M \times N}, \boldsymbol{\mathcal{S}} \in \mathbb{N}^{+M \times N}, \boldsymbol{\mathcal{E}} \in \mathbb{R}^{B \times M}$$

where $\boldsymbol{\mathcal{S}}$ is a positive real matrix with entries S_m^n, and $\boldsymbol{\mathcal{E}} \in \mathbb{R}^{B \times M}$ is a real matrix with entries ε_m^n. In $\mathbf{P_o}$, C_o^1 and C_o^2 are the collision and spectrum utilization constraints, respectively. C_o^3 ensures that if the PC_m is not scheduled for sensing then no IoT can be assigned to sense the PC_m. C_o^4 requires that a scheduled PC must be sensed by the cooperation of at least $\bar{N}$ IoT nodes. C_o^5 sets the upper bound for number of samples to T/T_s which is the maximum number of samples possible within a timeslot duration and sets the lower bound of $\overline{S}$ on the required number of samples to invoke the central limit theorem to ensure that assumptions are hold for (9) and (10). C_o^6 limits the spectrum exploration time by time slot duration T. C_o^7 assures that an IoT can be admitted to at most one cluster, i.e., can utilize at most one PC. On the other hand, C_o^8 limits cluster size to $\left\lceil \frac{N}{M} \right\rceil$ as explained in the previous section. Finally, C_o^9 defines the variable domains.

$\mathbf{P_o}$ is an MINLP problem which incurs impractical computational complexity even for moderate size of networks. Therefore, developing fast yet high-performance sub-optimal solutions is necessary to achieve satisfactory results for practical purposes. It is obvious from (25) that spectrum exploitation and exploration can be decoupled; hence, $\mathbf{P_o}$ can be decomposed into two problems: 1) MC_2S_3 and 2) clustering of IoT nodes and allocation of discovered idle PCs.

In the following subsections, we will provide solution methodology for these two subproblems. In the former subsection, optimal sensing durations and detection thresholds are derived in closed-form for a given set of IoT nodes. Then, we propose a PC ranking approach based on a priority metric, which is the best achievable utility if PC_m is assigned to the best $\bar{N}$ IoT nodes with the lowest sensing duration. As depicted in Fig. 2, we iteratively schedule the first m PCs to be sensed in the mth iteration, where we assign $\bar{N}$ IoT nodes to sense m PCs iteratively. If there is an improvement in terms of total utility, we proceed with scheduling $m+1$ best PCs to be sensed, otherwise we terminate. In the latter

$$R(\boldsymbol{X}, \boldsymbol{y}, \boldsymbol{Z}, \boldsymbol{S}, \boldsymbol{\mathcal{E}}) = \overbrace{\underbrace{\sum_{\forall m \in \mathcal{M}} y_m \pi_m^0 (1 - Q_m^f(S_m^n, \varepsilon_m^n)) T_X(\boldsymbol{X}, \boldsymbol{y}, \boldsymbol{S})}_{\text{Spectrum Exploration}}}^{\text{Utility Function (Average Total Achievable Throughput)}} \overbrace{\underbrace{\left(\sum_{\forall n \in \mathcal{N}} R_m^n(\boldsymbol{Z}) \right)}_{\text{Spectrum Exploitation}}}^{\text{Total Achievable IoT Rate}}, \qquad (25)$$

subsection, we cluster N IoT nodes and allocate each cluster to previously discovered I idle PCs, which is also done through $\lceil N/I \rceil$ consecutive bi-partite matching as illustrated in Fig. 2.

V. DECOMPOSED SPECTRUM EXPLORATION AND EXPLOITATION

By ignoring the second part of (25) and excluding the irrelevant constraints related to spectrum exploitation, the MC$_2$S$_3$ can be directly obtained from $\mathbf{P_o}$ as

$$\mathbf{P_1} : \max_{\boldsymbol{X}, \boldsymbol{y}, \boldsymbol{S}, \boldsymbol{\mathcal{E}}} \sum_{\forall m \in \mathcal{M}} y_m \pi_m^0 (1 - Q_m^f(S_m^n, \varepsilon_m^n)) T_X(\boldsymbol{X}, \boldsymbol{y}, \boldsymbol{S})$$

$$
\begin{aligned}
C_o^1: \quad &\text{s.t.} \quad \bar{Q}_d \leqslant Q_m^d(S_m^n, \varepsilon_m^n), \ \forall m \in \{m|\ y_m = 1\} \\
C_o^2: \quad &\quad Q_m^f(S_m^n, \varepsilon_m^n) \leqslant \bar{Q}_f, \ \forall m \in \{m|\ y_m = 1\} \\
C_o^3: \quad &\quad x_m^n \leqslant y_m, \ \forall m; \forall n \\
C_o^4: \quad &\quad \bar{N} y_m \leqslant \sum_{n \in \mathcal{N}} x_m^n, \ \forall m \\
C_o^5: \quad &\quad \overline{S} \leqslant S_m^n \leqslant T/T_s, \ \forall m; \forall n \\
C_o^6: \quad &\quad 0 \leqslant T - T_S(\boldsymbol{X}, \boldsymbol{y}, \boldsymbol{S}), \\
C_o^9: \quad &\quad \boldsymbol{X} \in \{0,1\}^{M \times N}, \boldsymbol{y} \in \{0,1\}^M, \\
&\quad \boldsymbol{S} \in \mathbb{N}^{+M \times N}, \boldsymbol{\mathcal{E}} \in \mathbb{R}^{B \times M}
\end{aligned}
$$

which attains the optimal point when $Q_m^f(S_m^n, \varepsilon_m^n) = \bar{Q}_f$ and $Q_m^d(S_m^n, \varepsilon_m^n) = \bar{Q}_d$ as $Q_m^f(S_m^n, \varepsilon_m^n) < \bar{Q}_f$ and $\bar{Q}_d > Q_m^d(S_m^n, \varepsilon_m^n)$ require more strict thresholds and sensing duration, respectively; which reduces throughput and causes suboptimality. As explained in (16) and (17), the false alarm and detection probabilities satisfying $Q_m^f(S_m^n, \varepsilon_m^n) = \bar{Q}_f$ and $Q_m^d(S_m^n, \varepsilon_m^n) = \bar{Q}_d$ can be obtained as $P_{m,n}^{f\star}(\bar{N})$ and $P_{m,n}^{d\star}(\bar{N})$, respectively. By substituting $P_{m,n}^{f\star}(\bar{N})$ and $P_{m,n}^{d\star}(\bar{N})$ into (18) and (19), respectively, then solving for ε_m^n and S_m^n respectively yields the following optimal detection threshold and number of samples

$$\varepsilon_{m,n}^{\star} \leqslant 1 + \frac{\mathcal{Q}^{-1}\left(P_{m,n}^{f\star}\right)}{\sqrt{S_{m,n}^{\star}}}, \qquad (26)$$

$$S_{m,n}^{\star} \geqslant \left[\frac{\mathcal{Q}^{-1}\left(P_{m,n}^{d\star}\right)\sqrt{2\gamma_m^n + 1} - \mathcal{Q}^{-1}\left(P_{m,n}^{f\star}\right)}{\gamma_m^n} \right]^2, \quad (27)$$

which are necessary and sufficient conditions to satisfy $Q_m^f(S_m^n, \varepsilon_m^n) = \bar{Q}_f$ and $Q_m^d(S_m^n, \varepsilon_m^n) = \bar{Q}_d$. By leveraging optimal number of samples, $\boldsymbol{S}^{\star}$, $\mathbf{P_1}$ can be reduced to the

following problem

$$\mathbf{P_1'} : \max_{\boldsymbol{X}, \boldsymbol{y}} \sum_{\forall m \in \mathcal{M}} y_m \pi_m^0 (1 - \bar{Q}_f) T_X(\boldsymbol{X}, \boldsymbol{y}, \boldsymbol{S}^{\star})$$

$$
\begin{aligned}
C_o^1: \quad &\text{s.t.} \quad x_m^n \leqslant y_m, \ \forall m; \forall n \\
C_o^2: \quad &\quad \bar{N} y_m \leqslant \sum_{n \in \mathcal{N}} x_m^n, \ \forall m \\
C_o^3: \quad &\quad 0 \leqslant T - T_S(\boldsymbol{X}, \boldsymbol{y}, \boldsymbol{S}^{\star}), \\
C_o^4: \quad &\quad \boldsymbol{X} \in \{0,1\}^{M \times N}, \boldsymbol{y} \in \{0,1\}^M
\end{aligned}
$$

which is still NP-Hard and requires a fast yet efficient heuristic solution for practical purposes.

The proposed solution is detailed in Algorithm 1, which starts with a channel ranking procedure in Line 2. As explained in Section V-A, the channels are ranked based on their best possible average throughput considering their probability of being idle and channel exploitation time. Then, the optimal sensing duration and priority list returned from PC RANK is used by IoT ASSIGN procedure in Line 3. As explained in Section V-B, IoT ASSIGN procedure iteratively schedules PCs following the priority list such that m^{th} iteration schedules PCs with the highest priority and assign $\bar{N}$ IoTs for each scheduled PC, which is terminated if scheduling $(m + 1)^{th}$ PC degrades the average throughput obtained in the mth iteration. Based on returned sensing scheduling matrices, the SBS broadcasts the sensing lists to IoT nodes in Line 4, which are then report their local decisions in Line 5. The SBS eventually make a decision on the list of idle PCs using the voting rule in (13).

A. PC Priority Ranking

To ensure that $\bar{N}$ reports satisfy global false alarm and detection probabilities (i.e., C_o^1 and C_o^2), Line 9 of the PC RANK first computes required detection and false alarm probabilities reports as per (16) and (17), which are then used in Line 10 to obtain required local detection and false alarm probabilities by taking the BER of the reporting channel into account. Based on the local probabilities, we compute the matrix of optimal number of samples as derived in (27). Thereafter, the for-loop between Lines 12-15 acquires the PC scheduling priority metrics for each PC by repeating the following steps: Line 13 sorts the mth column of $\boldsymbol{S}^{\star}$, $\boldsymbol{S}^{\star}[m, :]$, to reorder IoTs in ascending order of number of samples. Then, Line 14 takes the first $\bar{N}$ element of $\boldsymbol{S}^{\star}[m, :]$ to calculate the average maximum throughput of PC$_m$ if it is sensed by the best $\bar{N}$ possible IoT nodes. Finally, Line 16 returns the priority list following sorting PCs in descending order of their utility performance. With this priority list, having a higher *apriori* probability of being idle becomes as important as having a less sensing duration for better utilization of the idle PCs.

Algorithm 1 : Multi-Channel Cooperative Spectrum Sensing and Scheduling (MC_2S_3)

1: **Input:** $M, N, \bar{N}, \bar{Q}_f, \bar{Q}_d, \bar{S}, T, T_s, \pi_m^0, \boldsymbol{H}, p_m^n$
2: $\wp^\star, \boldsymbol{S}^\star \leftarrow$ PC RANK($\pi_m^o, T, T_s, \bar{N}, \bar{Q}_f$)
3: $\boldsymbol{y}^\star, \boldsymbol{X}^\star \leftarrow$ IOT ASSIGN($\wp^\star, \boldsymbol{S}^\star, \pi_m^0, T, \bar{Q}_f$)
4: The SBS broadcasts sensing and scheduling decisions
5: IoT nodes share decisions $(u_m^n, \forall m, n)$ with the SBS
6: $\mathcal{I} \leftarrow$ as per (13)
7: **return** $\mathcal{I}$

8: **procedure** PC RANK($\pi_m^o, p_m^n, T, T_s, \bar{N}, \bar{Q}_f, \bar{Q}_d$)
9: $\quad \tilde{P}_m^{d,\star}(\bar{N}) / \tilde{P}_m^{f,\star}(\bar{N}) \leftarrow$ as per (16) and (17), $\forall m$.
10: $\quad P_{m,n}^{i^\star}(\bar{N}) \leftarrow$ as per (18) and (19), $i \in \{f, d\}$
11: $\quad \boldsymbol{S}^\star \leftarrow$ Substitute $P_{m,n}^{i^\star}(\bar{N}), i \in \{f, d\}$, into (27)
12: $\quad$ **for** $m = 1 : M$ **do**
13: $\quad\quad \aleph \leftarrow$ SORTASCEND($\boldsymbol{S}^\star[m,:]$)
14: $\quad\quad \wp[m] \leftarrow \pi_m^o(1 - \bar{Q}_f)(T - \sum_{i=1}^{\bar{N}} \aleph[i]T_s)$
15: $\quad$ **end for**
16: $\quad \wp^\star \leftarrow$ SORTDESCEND($\wp_m, \forall m$)
17: **return** $\wp^\star, \boldsymbol{S}^\star$
18: **end procedure**

19: **procedure** IOT ASSIGN($\wp^\star, \boldsymbol{S}^\star, \pi_m^0, T, \bar{Q}_f$)
20: $\quad \tau \leftarrow 0$
21: $\quad$ **for** $m = 1 : M$ **do**
22: $\quad\quad \boldsymbol{X} \leftarrow 0^{M \times N}, \boldsymbol{y} \leftarrow 0^M$
23: $\quad\quad \xi \leftarrow \wp[1 : m]$
24: $\quad\quad \boldsymbol{y}[\xi] \leftarrow 1$
25: $\quad\quad \boldsymbol{Q} \leftarrow \boldsymbol{S}^\star[\xi, :]$
26: $\quad\quad \tilde{\boldsymbol{S}} \leftarrow \boldsymbol{S}^\star[\xi, :]$
27: $\quad\quad$ **for** $i = 1 : \bar{N}$ **do**
28: $\quad\quad\quad \boldsymbol{\delta} \leftarrow$ LINEAR BOTTLENECK ASSIGNMENT($\boldsymbol{Q}$)
29: $\quad\quad\quad$ **for** $j = 1 : m$ **do**
30: $\quad\quad\quad\quad \boldsymbol{X}[j, \boldsymbol{\delta}[j]] \leftarrow 1$
31: $\quad\quad\quad\quad \boldsymbol{Q}[:, \boldsymbol{\delta}[j]] \leftarrow \boldsymbol{Q}[:, \boldsymbol{\delta}[j]] + \tilde{\boldsymbol{S}}[j, \boldsymbol{\delta}[j]]$
32: $\quad\quad\quad\quad \boldsymbol{Q}[j, \boldsymbol{\delta}[j]] \leftarrow \infty$
33: $\quad\quad\quad$ **end for**
34: $\quad\quad$ **end for**
35: $\quad\quad \Phi(m) \leftarrow \sum_{i \in \wp[1:m]} \pi_i^0(1 - \bar{Q}_f)(T - T_S(\boldsymbol{X}, \boldsymbol{y}, \boldsymbol{S}^\star))$
36: $\quad\quad$ **if** $\Phi(m) \geqslant \tau$ **then**
37: $\quad\quad\quad \tau \leftarrow \Phi(m)$
38: $\quad\quad$ **else**
39: $\quad\quad\quad$ **Break**
40: $\quad\quad$ **end if**
41: $\quad$ **end for**
42: **return** $\boldsymbol{y}, \boldsymbol{X}$
43: **end procedure**

44: **procedure** LINEAR BOTTLENECK ASSIGNMENT($\boldsymbol{Q}$)
45: $\quad \boldsymbol{\chi} \leftarrow \max_{\boldsymbol{\chi}} \left\{ \min_{\forall i, \forall j} \{\boldsymbol{Q}[i,j]\boldsymbol{\chi}[i,j]\} \right\}$
46: $\quad\quad$ s.t. $\sum_i \boldsymbol{\chi}[i,j] \leqslant 1, \forall j$
47: $\quad\quad\quad \sum_j \boldsymbol{\chi}[i,j] = 1, \forall i$
48: **return** $\boldsymbol{\chi}$
49: **end procedure**

B. IoT Sensing Assignment

The IoT sensing assignment procedure starts with initialization of utility (i.e., average throughput) threshold in Line 20, followed by a for-loop between Lines 21-39. Line 22 initializes sensing scheduling variables; then Line 23 schedules first m PCs from $\wp$ to be sensed, which is reflected on the PC scheduling variable in Line 24. The columns of scheduled PCs are extracted from $\boldsymbol{S}^\star$ to obtain a cost matrix $\boldsymbol{Q} \in \mathbb{R}^{m \times N}$ in Line 25, which is also stored as $\tilde{\boldsymbol{S}}$ for future purposes.

After that, the inner for-loop between Lines 27-34 assign an IoT to each PC at each iteration, until all PCs are assigned with a total of $\bar{N}$ IoTs for sensing. In Line 28, the LBA is executed to find the best IoT assignments that minimizes the maximum sensing duration among all IoT nodes. The LBA returns a vector $\boldsymbol{\delta} \in \mathbb{N}^m$ whose j^{th} element's value correspond to the index of IoT assigned for sensing PC_j. The first step of for-loop between Lines 29-33 updates the assignment matrix by setting $\boldsymbol{X}[j, \boldsymbol{\delta}[j]] = 1$. Line 31 adds sensing duration of assigned IoT to account for its sensing duties in the next round of assignments. Then, Line 32 updates cost matrix with $\boldsymbol{Q}[j, \boldsymbol{\delta}[j]] = \infty$ for preventing selected IoTs to be assigned to sense the same PC again. Exploiting the sensing scheduling matrices, Line 35 computes the utility function, which is compared with the threshold between Lines 36-40; where threshold is updated if adding m^{th} PC into scheduling matrix improves the throughput, otherwise Line 39 breaks the for loop and corresponding sensing scheduling matrices are returned in Line 42.

C. PC Allocation and IoT Clustering

Given the set of idle PCs are obtained through Algorithm 1, now it is time to focus on the second part of (25) and excluding the irrelevant constraints related to spectrum sensing. Accordingly, PC allocation and IoT clustering can be directly obtained from $\mathbf{P_o}$ as follows

$$\mathbf{P_2} : \max_{\boldsymbol{Z} \in \{0,1\}^{I \times N}} \sum_{\substack{i \in \mathcal{I} \\ n \in \mathcal{N}}} R_i^n(\boldsymbol{Z})$$

$$C_o^1 : \quad \text{s.t.} \quad \sum_{m \in \mathcal{M}} z_m^n \leqslant 1, \ \forall n$$

$$C_o^2 : \quad\quad\quad \sum_{n \in \mathcal{N}} z_m^n \leqslant \left\lceil \frac{N}{I} \right\rceil, \ \forall m$$

which is also a combinatorial problem and NP-hard. The proposed solution is illustrated in Fig. 2 and detailed in Algorithm 2, where initialization starts with sorting IoT nodes based on their channel gain and assigning the IoT node with i^{th} strongest channel to the ith PC among I idle PCs, $i \in [1, I]$. The for-loop between Lines 7-14 iteratively admits IoT nodes into I clusters over $K-1$ iteration. At each iteration, Line 8 first updates the set of admission awaiting nodes, then Line 9 calls COMPUTE COST procedure to generate cost matrix whose index $\boldsymbol{Q}[i,j]$ represent the data rate if $\mathcal{A}_k\{j\}$ is admitted to $\mathcal{C}_i$. In Line 10, the linear sum assignment obtains the matching with the highest sumrate, which is followed by cluster and clustering matrix updates in Lines 12 and 13, respectively.

D. Computational Complexity Analysis

The computational complexity of solving simplified problem $\boldsymbol{P_1'}$ in a brute-force fashion can be obtained by considering following combinations: 1) $\sum_{m=1}^{M} \binom{M}{m}$ is total number of scheduling combinations where $\binom{M}{m}$ selects m PCs out of M PCs, 2) For each of selected m PCs, we need to choose $\bar{N}$ nodes out of N IoT nodes. Accordingly, the overall computational complexity is given by $\mathcal{O}\left(K \sum_{m=1}^{M} \binom{M}{m}\binom{N}{\bar{N}}^m\right)$ where

---

Algorithm 2 : PC Allocation and IoT Clustering

1: **Input:** $N, \mathcal{I}, \alpha, \tilde{\boldsymbol{H}}$
2: $\mathcal{I} \leftarrow$ as per (13)
3: $K \leftarrow \lceil \frac{N}{I} \rceil$
4: $\tilde{\mathcal{N}} \leftarrow$ Sort IoTs in descending order of channel gains
5: $\mathcal{C}_i \leftarrow \tilde{\mathcal{N}}\{i\}, i \in [1, \dots, I]$
6: $\boldsymbol{Z}_i^j \leftarrow 1, j \in \mathcal{C}_i$
7: **for** $k = 1 : K - 1$ **do**
8:     $\mathcal{A}_k \leftarrow \tilde{\mathcal{N}} - \bigcup_{i=1}^{I} \mathcal{C}_i$
9:     $\boldsymbol{Q} \leftarrow$ COMPUTE COST$(\mathcal{A}_k, \mathcal{C}_i, \forall i)$
10:    $\chi \leftarrow\leftarrow$ LINEAR SUM ASSIGNMENT$(\boldsymbol{Q})$
11:    $\mathcal{C}_i \leftarrow \mathcal{C}_i \bigcup \mathcal{A}_k\{j\}, \chi_i^j = 1, \forall(i, j)$
12:    $\boldsymbol{Z}[i, j] \leftarrow 1, \forall j \in \mathcal{C}_i$
13: **end for**
14: The SBS broadcasts PC Allocation and IoT clustering
15: **return** $\boldsymbol{Z}$,

16: **procedure** COMPUTE COST$(\mathcal{A}_k, \mathcal{C}_i, \forall i)$
17:    $\boldsymbol{Q} \leftarrow \boldsymbol{0}^{I \times A_k}$
18:    **for** $i = 1 : I$ **do**
19:        **for** $j = 1 : A_k$ **do**
20:            $\mathcal{T}_i \leftarrow \mathcal{C}_i \bigcup \mathcal{A}_k\{j\}$
21:            $\boldsymbol{Q}[i, j] \leftarrow R_i^j, j \in \mathcal{T}_i$
22:        **end for**
23:    **end for**
24:    **return** $\boldsymbol{Q}$
25: **end procedure**

26: **procedure** LINEAR SUM ASSIGNMENT$(\boldsymbol{Q})$
27:    $\chi \leftarrow \max_{\chi} \sum_{\forall i, \forall j} \boldsymbol{Q}[i, j]\chi[i, j]$
28:        s.t. $\sum_i \chi[i, j] \leq 1, \forall j$
29:            $\sum_j \chi[i, j] = 1, \forall i$
30: **return** χ
31: **end procedure**

K is the number of operations required for each combination. On the other hand, the proposed PC ranking algorithm has $\mathcal{O}(MN \log N + M \log M)$ complexity where the first and second terms are induced from the SORTASCEND and SORTDESCEND operations in Lines 13 and 16, respectively. The complexity of proposed PC allocation and IoT assignment procedure is dominated by the cubic complexity of the LBA [26], yielding $\mathcal{O}\left(\sum_m \bar{N}(\max(m, N))^3\right)$.

On the other hand, the computational complexity of solving simplified problem $\boldsymbol{P_2}$ in a brute-force fashion can be obtained by assigning $K = \lceil \frac{N}{I} \rceil$ IoT nodes to a cluster at each iteration, decrementing the pool of available workers by K after each task assignment, and multiplying the combinations possible for each task. Assuming $\lceil \frac{N}{I} \rceil$ is an integer, the computational complexity becomes $\mathcal{O}\left(\prod_{i=0}^{M-1} \binom{N-iK}{K}\right)$. In case of frequency selective channels, the order of iteration is also need to be taken care of, yielding an overall $\mathcal{O}\left(M! \prod_{i=0}^{M-1} \binom{N-iK}{K}\right)$ complexity for the exhaustive PC allocation and IoT clustering. On the other hand, the computational complexity of Algorithm 2 is mainly driven by two steps: 1) IoT sorting and 2) iterative IoT matching. The IoT sorting in Line 5 has a complexity of $\mathcal{O}(N \log N)$. For PC allocation and IoT clustering, the complexity of for-loop between lines 7-13 is $\mathcal{O}\left(\sum_k^{K-1}(\max(I, A_k))^3\right)$ where .

The overall complexity of the proposed decomposition approach can be furhter simplified in two steps: 1) Algorithm

Table I: Table of default parameters

Par.	Value	Par.	Value	Par.	Value
Q_f	0.01	W	180 KHz	G_m	3 dBi
Q_d	0.99	p_m^n	10^{-3}	G_n	3 dBi
$\bar{N}$	4	τ_r	1 ms	d_0	10 m
$\bar{S}$	30	P_s	30 dBm	σ_m^n	8 dB
T	1 s	P_n	10 dBm	f_c	0.9 GHz

1 has $\mathcal{O}\left(M\bar{N}N^3\right)$ assuming that all PCs are scheduled and $N \geq M$ and 2) Algorithm 2 has $\mathcal{O}\left(KN^3\right)$ assuming $N \geq A_k \geq I$. Finally, the overall algorithm has a complexity of $\mathcal{O}\left((K + M\bar{N})N^3\right)$

VI. NUMERICAL RESULTS

In order to gain a clear insight into the impact of various system parameters on the SN performance, IoT nodes are assumed to have identical system parameters. Since our focus is to demonstrate the effect of spectrum sensing and scheduling on the available RF energy harvesting time, we consider a unitary energy arrival rate for all IoT nodes. Moreover, the channel switching factor is set to be $\beta = 0.1$ ms/MHz [23]. Unless it is explicitly stated otherwise, we employ the parameter values summarized in Table I.
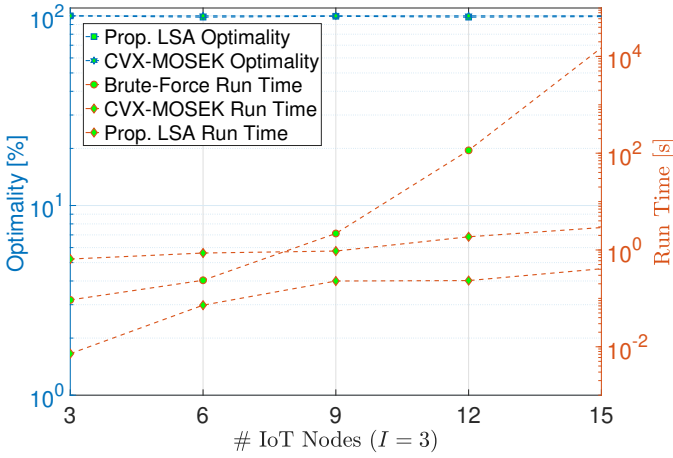
A. Optimality and Run Time Comparison

Before delving into performance evaluation of proposed solutions in a large scale network, we believe it is better to compare optimality and run time complexity with the brute-force approach, where we exhaustively explore all combinations to find the optimal solutions. We start with the comparison of Algorithm 2 as shown in Fig. 3a, where we considering clustering $N = \{3, 6, 9, 12, 15\}$ IoT nodes into $I = 3$ PCs/clusters, yileding following cluster sizes $C = \{1, 2, 3, 4, 5\}$. The proposed iterative LSA approach reaches %98.5 - %99.5 optimality while MOSEK[1] solver of CVX[2] reaches %100 optimality. Fig. 3a clear shows that computational complexity of the brute-force approach increases exponentially as the number of IoT increases even for a very low number of PCs, $I = 3$. To further investigate the optimality and complexity of the proposed iterative LSA approach, we drop brute-force approach and focus on the comparison with the CVX-MOSEK solution for a more realistic network size in Fig. 3b, where we show that our solution reaches %99- %100 optimality while keeping the complexity 2 orders of magnitude less than the CVX-MOSEK.

Given that the efficacy of linear assignment solutions have been shown in Fig. 3a and Fig. 3b, we will focus on comparing proposed M2CS3 approach with the brute-force solution in Fig. 3c, where we consider assignment of $N = 50$ IoT nodes to sense $M = \{4, 8, 12, 16, 20\}$ scheduled PCs. The proposed M2CS3 approach reaches %99.99 performance of brute-force solution in less than 0.1 seconds, proving the efficacy of the PC ranking and LBA-based sensing assignment.

---

[1]MOSEK is a large scale optimization software widely used to solve Linear, Quadratic, Semidefinite and Mixed Integer problems [27].
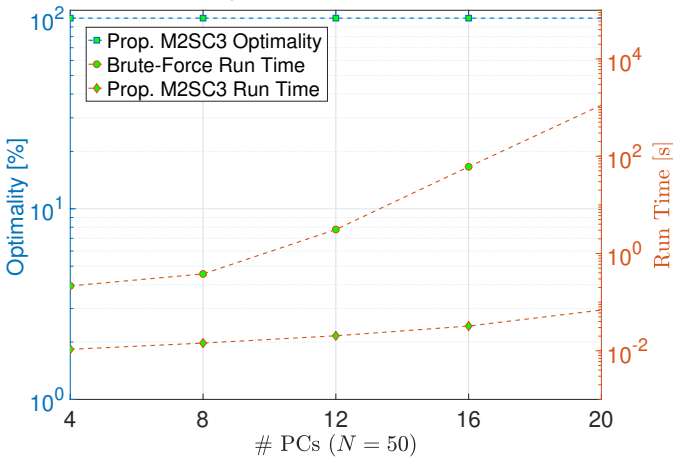[2]CVX is a modeling system for constructing and solving disciplined convex programs [28].

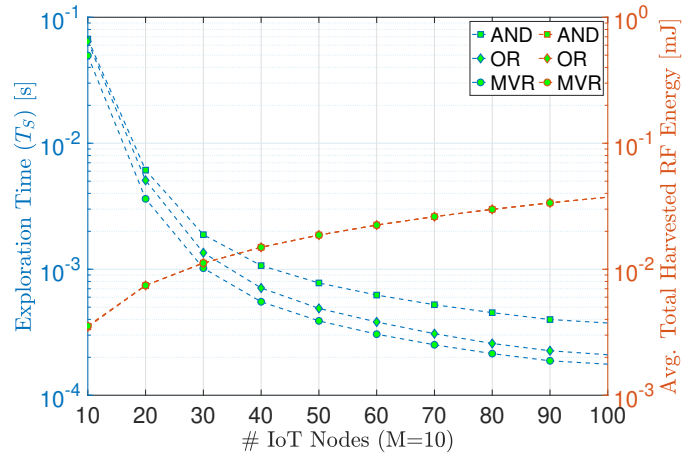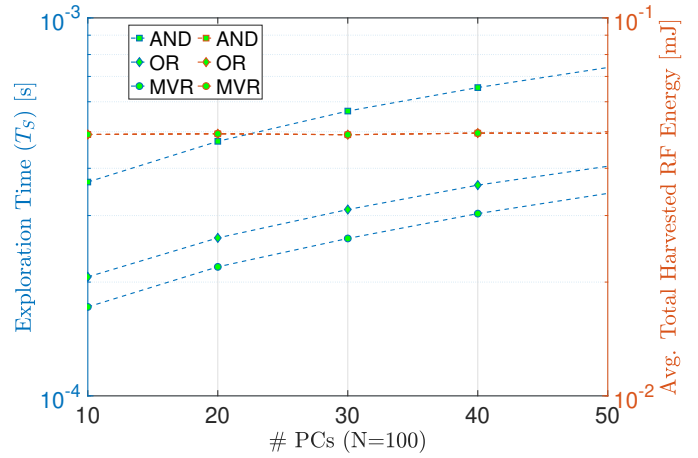(a) Algorithm 2 vs. Brute-Force and CVX-MOSEK.
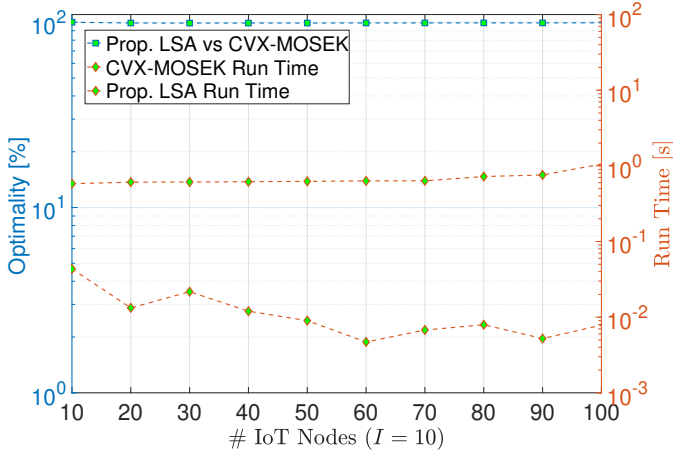
(b) Algorithm 2 vs. CVX-MOSEK.

(c) Algorithm 1 vs. Brute-Force.

Figure 3: The optimality and run time complexity comparison for: a) Algorithm 2 and b) Algorithm 1.

(a) N

(b) M

Figure 4: The impact of number of IoT nodes and PCs on exploration time and average total harvested RF energy.

B. Exploration Time and Harvested Energy

As we already shown the optimality and speed of proposed solutions in the previous section, the rest of this section will consider larger network sizes and exclude comparisons with exhaustive solutions. The channel exploration time, T_S with respect to N for $M = 10$ is shown in Fig. 4a where maximum voting rule and AND rules requires lowest and highest sensing duration, respectively. T_S also reduces as N increases as having more IoT nodes increase the likelihood of having IoT nodes with better sensing attributes. On the other hand, Fig. 4b shows that having more PCs increases the T_S as the likelihood of having PCs with higher probability of being idle increases, which yields more PCs to be scheduled and more time spent for sensing. The impact of T_S on the average total harvested RF energy ($\bar{E}_{RF} = \frac{\chi_{RF}}{M} \sum_m \pi_m^1 \bar{Q}_d (T - T_S)$) is also shown in Fig. 4a and Fig. 4b. Fig. 4a shows that as N increases we have more nodes to harvest RF energy with more exploitation time to harvest energy. On the other hand, the impact of having more PCs is limited since our algorithms focused more on scheduling PCs with higher probability of being idle.

It is also important to investigate N and required number of sensing IoT nodes per PC, $\bar{N}$, for given M. Fig. 5a and
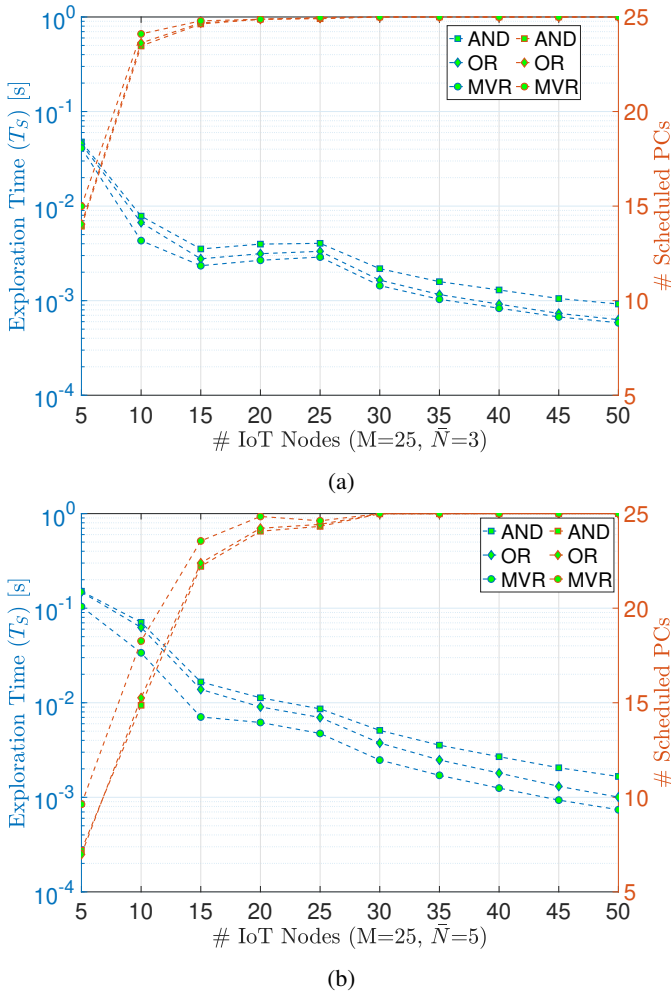
(a)

(b)

Figure 5: Impact of N and $\bar{N}$ on exploration time and # scheduled PCs: a) $\bar{N} = 3$ and b) $\bar{N} = 5$

Figure 6: Algorithm 1 vs. Brute-Force.

Figure 7: Normalized network throughput per IoT node.

Fig. 5b show that $N \leqslant M$ yields under utilization of idle PCs as low number of sensing IoT nodes cause a limited discovery of spectrum. This is also closely related to how many IoT nodes required to sense each PC. Setting a lower $\bar{N}$ can allow us to discover more PCs as $\bar{N} = 3$ and $\bar{N} = 5$ compared in Fig. 5a and Fig. 5b, respectively. Here, the impact of voting rule becomes more obvious as having less T_S allow MVR to schedule more PCs, improving overall idle spectrum discovery. For the same set up, we also show normalized and average network throughput per IoT node in Fig. 6, where $\bar{N} = 3$ and MVR provides a better performance than other schemes. Moreover, it is obvious that even if all PCs are scheduled by $N = 30$, the NOMA scheme was capable of providing similar performance for additional IoT nodes thanks to effective multiplexing of NOMA.

VII. CONCLUSIONS

In this paper, we introduced a comprehensive framework, MC_2S_3, designed to enhance the throughput of cognitive IoT networks through advanced multi-channel cooperative spectrum sensing and scheduling. By tackling the challenge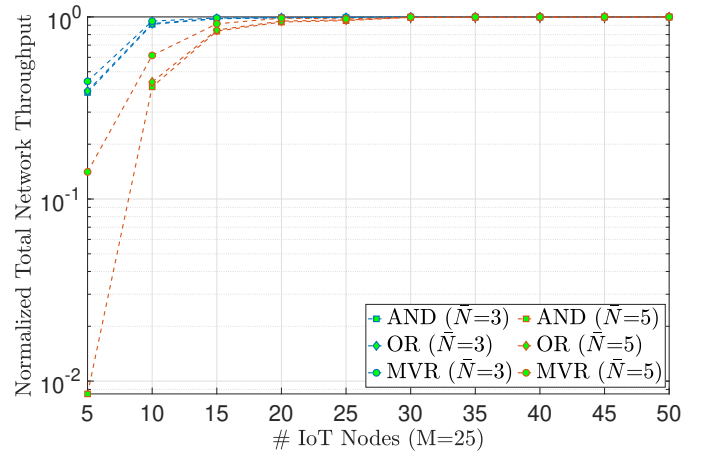 of optimizing network throughput with a novel decomposition strategy, we effectively addressed the NP-hard nature of the joint optimization of sensing scheduling, device assignment, and node clustering within these networks. Our approach, which intelligently divides the problem into manageable sub-problems of PC exploration and exploitation, not only ensures efficient spectrum utilization but also minimizes potential collision with primary networks. The adoption of NOMA for the exploitation phase further underscores our framework's capability to maximize the use of available spectrum resources by accommodating multiple IoT nodes on a single PC. Numerical analysis underscores the superiority of our proposed methodologies, showcasing near-perfect accuracy and significant performance gains over conventional brute-force methods. The implications of our findings are twofold: they pave the way for more efficient cognitive IoT network operations and offer a scalable solution for future spectrum and energy harvesting endeavors. Future work will focus on extending this framework to accommodate dynamic network environments and exploring the integration of machine learning techniques for enhanced decision-making processes.

REFERENCES

[1] A. Celik, I. Romdhane, G. Kaddoum, and A. M. Eltawil, "A top-down survey on optical wireless communications for the internet of things," *IEEE Communications Surveys Tutorials*, vol. 25, no. 1, pp. 1–45, 2023.

[2] M. Khasawneh, A. Azab, S. Alrabaee, H. Sakkal, and H. H. Bakhit, "Convergence of iot and cognitive radio networks: A survey of applications, techniques, and challenges," *IEEE Access*, vol. 11, pp. 71097–71112, 2023.

[3] A. Gharib, W. Ejaz, and M. Ibnkahla, "Distributed spectrum sensing for iot networks: Architecture, challenges, and learning," *IEEE Internet of Things Magazine*, vol. 4, no. 2, pp. 66–73, 2021.

[4] W. Ejaz and M. Ibnkahla, "Multiband spectrum sensing and resource allocation for iot in cognitive 5g networks," *IEEE Internet of Things Journal*, vol. 5, no. 1, pp. 150–163, 2018.

[5] N.-N. Dao, W. Na, A.-T. Tran, D. N. Nguyen, and S. Cho, "Energy-efficient spectrum sensing for iot devices," *IEEE Systems Journal*, vol. 15, no. 1, pp. 1077–1085, 2021.

[6] F. Zhou, Y. Wu, Y.-C. Liang, Z. Li, Y. Wang, and K.-K. Wong, "State of the art, taxonomy, and open issues on cognitive radio networks with noma," *IEEE Wireless Communications*, vol. 25, no. 2, pp. 100–108, 2018.

[7] S. Arzykulov, A. Celik, G. Nauryzbayev, and A. M. Eltawil, "Uav-assisted cooperative cognitive noma: Deployment, clustering, and resource allocation," *IEEE Transactions on Cognitive Communications and Networking*, vol. 8, no. 1, pp. 263–281, 2022.

[8] P. Chauhan, S. K. Deka, B. C. Chatterjee, and N. Sarma, "Utility driven cooperative spectrum sensing scheduling for heterogeneous multi-channel cognitive radio networks," *Telecommunication Systems*, vol. 78, no. 1, pp. 25–37, 2021.

[9] Y. Cao and H. Pan, "Energy-efficient cooperative spectrum sensing strategy for cognitive wireless sensor networks based on particle swarm optimization," *IEEE Access*, vol. 8, pp. 214707–214715, 2020.

[10] H. Kaschel, K. Toledo, J. T. Gómez, and M. J. F.-G. García, "Energy-efficient cooperative spectrum sensing based on stochastic programming in dynamic cognitive radio sensor networks," *IEEE Access*, vol. 9, pp. 720–732, 2021.

[11] A. Ostovar, Y. B. Zikria, H. S. Kim, and R. Ali, "Optimization of resource allocation model with energy-efficient cooperative sensing in green cognitive radio networks," *IEEE Access*, vol. 8, pp. 141594–141610, 2020.

[12] O. M. Al-Kofahi, H. M. Almasaeid, and H. Al-Mefleh, "Efficient on-demand spectrum sensing in sensor-aided cognitive radio networks," *Computer Communications*, vol. 156, pp. 11–24, 2020.

[13] A. Bagheri and A. Ebrahimzadeh, "Statistical analysis of lifetime in wireless cognitive sensor network for multi-channel cooperative spectrum sensing," *IEEE Sensors Journal*, vol. 21, pp. 2412–2421, Jan 2021.

[14] X. Fernando and G. Lăzăroiu, "Spectrum sensing, clustering algorithms, and energy-harvesting technology for cognitive-radio-based internet-of-things networks," *Sensors*, vol. 23, no. 18, 2023.

[15] J. Wu, C. Wang, Y. Yu, T. Song, and J. Hu, "Performance optimisation of cooperative spectrum sensing in mobile cognitive radio networks," *IET Communications*, vol. 14, no. 6, pp. 1028–1036, 2020.

[16] W. Ning, X. Huang, K. Yang, F. Wu, and S. Leng, "Reinforcement learning enabled cooperative spectrum sensing in cognitive radio networks," *Journal of Communications and Networks*, vol. 22, pp. 12–22, Feb 2020.

[17] Z. Shi, W. Gao, S. Zhang, J. Liu, and N. Kato, "Machine learning-enabled cooperative spectrum sensing for non-orthogonal multiple access," *IEEE Transactions on Wireless Communications*, vol. 19, pp. 5692–5702, Sep. 2020.

[18] R. Ahmed, Y. Chen, B. Hassan, and L. Du, "Cr-iotnet: Machine learning based joint spectrum sensing and allocation for cognitive radio enabled iot cellular networks," *Ad Hoc Networks*, vol. 112, p. 102390, 2021.

[19] A. Bagheri, A. Ebrahimzadeh, and M. Najimi, "Game-theory-based lifetime maximization of multi-channel cooperative spectrum sensing in wireless sensor networks," *Wireless networks*, vol. 26, no. 6, pp. 4705–4721, 2020.

[20] M. Rajendran and M. Duraisamy, "Distributed coalition formation game for enhancing cooperative spectrum sensing in cognitive radio ad hoc networks," *IET Networks*, vol. 9, no. 1, pp. 12–22, 2020.

[21] P. Chauhan, S. K. Deka, B. C. Chatterjee, and N. Sarma, "Cooperative spectrum prediction-driven sensing for energy constrained cognitive radio networks," *IEEE Access*, vol. 9, pp. 26107–26118, 2021.

[22] A. Gharib, W. Ejaz, and M. Ibnkahla, "Scalable learning-based heterogeneous multi-band multi-user cooperative spectrum sensing for distributed iot systems," *IEEE Open Journal of the Communications Society*, vol. 1, pp. 1066–1083, 2020.

[23] D. Gözüpek, S. Buhari, and F. Alagöz, "A spectrum switching delay-aware scheduling algorithm for centralized cognitive radio networks," *IEEE Transactions on Mobile Computing*, vol. 12, no. 7, pp. 1270–1280, 2013.

[24] E. C. Y. Peh, Y.-C. Liang, and Y. L. Guan, "Optimization of cooperative sensing in cognitive radio networks: A sensing-throughput tradeoff view," in *2009 IEEE International Conference on Communications*, pp. 1–5, 2009.

[25] S. W. Kim, "Simultaneous spectrum sensing and energy harvesting," *IEEE Transactions on Wireless Communications*, vol. 18, no. 2, pp. 769–779, 2019.

[26] D. F. Crouse, "On implementing 2d rectangular assignment algorithms," *IEEE Transactions on Aerospace and Electronic Systems*, vol. 52, no. 4, pp. 1679–1696, 2016.

[27] M. ApS, "Mosek optimization toolbox for matlab," *User's Guide and Reference Manual, Version*, vol. 4, p. 1, 2019.

[28] M. Grant and S. Boyd, "CVX: Matlab software for disciplined convex programming, version 2.1." http://cvxr.com/cvx, Mar. 2014.

Abdulkadir Celik (Senior Member, IEEE) received M.S. degrees in electrical engineering in 2013 and in computer engineering in 2015, then the Ph.D. degree in co-majors of electrical engineering and computer engineering in 2016, all from Iowa State University, Ames, IA, USA. He was a Postdoctoral Fellow with the King Abdullah University of Science and Technology, Thuwal, KSA, from 2016 to 2020, where he is currently a Senior Research Scientist with the Communications and Computing Systems Laboratory. Dr. Celik is the recipient of IEEE Communications Society's 2023 Outstanding Young Researcher Award for Europe, Middle East, and Africa (EMEA) region. He currently serves as an editor for IEEE Communications Letters, IEEE Wireless Communications Letters, and Frontiers in Communications and Networks. His research interests are in the broad areas of next-generation wireless communication systems and networks.

Optimal Solution of the Dynamic Economic Dispatch by Improved Teaching-Learning-Based Artificial Bee Colony Algorithm

Burçin Ozkaya

Abstract—**Dynamic economic dispatch is one of the most handled problem in modern power system operations. It aims to optimize the output power from thermal generating units over a specified time period to minimize the total fuel cost, while satisfying the several constraints such as generation limits, ramp rate limits, and power balance. In addition to these constraints, the prohibited operating zones and the valve-point loading effect are included the DED problem. In this case, the complexity, nonlinearity, and non-convexity of the DED problem are increases. Therefore, in order to solve the DED problem, a powerful meta-heuristic search (MHS) algorithm are proposed. In this study, an improved teaching-learning-based artificial bee colony (TLABC) algorithm, where the fitness-distance balance based TLABC (FDB-TLABC) and natural-survivor method based TLABC (NSM-TLABC) algorithms were hybridized. To prove the performance of the proposed algorithm, it was applied to solve the DED problem and benchmark problem suites. In the simulation study carried out on benchmark problems, the results of the proposed algorithm and five MHS algorithms were evaluated statistically. According to Friedman test results, the proposed algorithm ranked first with 2.2836 values among them. On the other hand, the proposed algorithm and its rival algorithms were applied to solve the two DED cases. The results of them show that the proposed algorithm achieved superior performance to find the best objective values for both case studies.**

Index Terms—**Dynamic economic dispatch, Natural-Survivor method, Fitness-Distance Balance, NSM-FDB-TLABC algorithm.**

I. INTRODUCTION

IN RECENT years, the dynamic economic dispatch (DED) problem has become a crucial optimization challenge in modern power system operations. It focuses on optimizing the output power from generators over time to minimize fuel costs while adhering to various constraints [1, 2]. When compared to the static ED problem, DED is a very complex problem as it must comply with the generation unit ramp rate limits and plan the output powers of all generation units within a specific time period [3]. On the other hand, the cost function for each generator has been generally simplified as a quadratic function, disregarding the valve-point loading effect (VPLE) arising from

the multiple steam admitting valves. In order to accurately model the DED problem as a real world operation, it is crucial to incorporate the impact of VPLE on the cost of power generators and the constraints such as the generator capacity limits, the ramp-rate limits, the power balance constraints, and the prohibited operation zones (POZs). Considering all of these constraints, the DED problem exhibits non-convex and non-linear properties that make it more complex [3, 4]. To solve this complex DED problem, meta-heuristic search (MHS) algorithms have been applied.

In the literature, several studies have been carried out for the solution of the DED problem using MSH algorithms. Mohammadi-Ivatloo et al. [1] used the imperialist competitive algorithm for solving the DED problem, incorporating the VPLE, transmission losses, and POZs. The performance of the algorithm was proven on a 5-, 10-, and 54-unit test system. Ivatloo et al. [2] proposed a time-varying acceleration coefficients iteration particle swarm optimization for the solution of the DED problem. In the study, transmission losses of the system, VPLE, and POZs were considered. Sonmez et al. [3] used the symbiotic organisms search algorithm for the solution of the DED problem, where it was applied to five case studies created using three scale of test systems and operational constraints. Dai et al. [4] proposed an adaptive hybrid backtracking search optimization algorithm in order to solve the DED problem with VPLE. In the study, six case studies were performed, which were created using three scales of test systems, transmission loss, and POZs. Mohammadi-Ivatloo et al. [5] proposed a hybrid algorithm by combining the immune and genetic algorithms to solve the DED problem, including VPLE and POZs, where the three scales of test systems were taken into account. Mohammadi- Azizipanah-Abarghooee [6] introduced hybrid bacterial foraging and simplified swarm optimization algorithms for solving the DED problem. In the study, the proposed algorithm was applied on four different test systems. Moreover, the cases with and without the inclusion of operational constraints were analyzed. Zhang et al. [7] presented a hybrid bare-bones particle swarm optimization including directionally chaotic search to solve the DED problem with VPLE, where three case studies were considered. Xiong and Shi [8] proposed a hybrid method by combining biogeography-based optimization with brain storm optimization for solving the DED problem, where the transmission loss and VPLE were considered. Here, three scales

Burçin Özkaya, is with Department of Electrical Engineering, Bandirma Onyedi Eylul University, Balıkesir, Turkey, (e-mail: bozkaya@bandirma.edu.tr).

https://orcid.org/0000-0002-9858-3982

of test systems including 5-, 10-, and 30-units were used. Zou et al. [9] introduced a memory-based global differential evolution algorithm for the solution of five case studies of the DED problem considering the VPLE, transmission loss, and POZs. To handle the constraints of the DED problem, a repair technique was proposed. Ghasemi et al. [10] presented a novel version of the particle swarm optimization algorithm to solve the DED problem in 10- and 30-unit test systems, where the four case studies were created using test systems and operational constraints. Zheng et al. [11] proposed an improved version of the invasive weed optimization algorithm to solve the DED problem, including VPLE, POZs, and transmission losses. Here, to prove the performance of the proposed algorithm, six case studies of the DED problem on three different-scales were performed. Santra et al. [12] presented a hybrid method incorporating termite colony optimization and particle swarm optimization algorithms for the solution of the four DED cases, where 5-, 10-, and 30-unit test systems were used. Yang et al. proposed an enhanced exploratory whale optimization algorithm for the solution of the DED problem, where both VPLE and transmission losses were considered. Hu et al. [14] introduced an adaptive backtracking search optimization algorithm including the dual-learning strategy to solve the DED problem with VPLE and transmission losses, where 5-, 10-, and 30-units test systems were considered. Basak et al. [15] introduced a hybrid algorithm based on crow search algorithm and JAYA to solve the DED problem including wind energy sources, where 10- and 15-unit test systems were studied. Yang et al. [16] presented an improved chaos moth flame optimization algorithm for solving the DED problem where plug-in electric vehicles (PEVs) were connected to the grid. Yang et al. [17] proposed an improved grey wolf optimization algorithm to solve the DED problem, where 5-, 10-, and 15-unit test systems were considered. Nagarajan et al. [18] presented an enhanced cheetah optimizer algorithm for the solution of the DED problem incorporating wind and solar energy sources.

The DED problem is still a very complex and constrained optimization problem as it tries to optimize the output power from generators over time to minimize fuel costs while satisfying the constraints. In particular, the level of complexity increases with the inclusion of the operational constraints such as VPLE and POZ. When the studies summarized above were evaluated, various algorithms have been proposed by researchers to solve the DED problem. However, it was observed that the proposed algorithms were insufficient to find the optimal solution because they were not designed in accordance with the structure and constraints of the DED problem. Therefore, in this study, an improved teaching-learning-based artificial bee colony (TLABC) algorithm was proposed for the solution of the DED problem, where the fitness-distance balance based TLABC (FDB-TLABC) [19] and the natural-survivor method based TLABC (NSM-TLABC) [20] algorithms were hybridized. In the NSM-FDB-TLABC algorithm, while the selection of surviving individuals in the teaching-based employed bee stage was carried out using

the NSM method, the guide individual in the learning-based onlooker bee stage was selected using the FDB method. Thus, with the use of NSM and FDB methods in the proposed algorithm, it was aimed to enhance the ability of the TLABC algorithm to imitate nature and to enhance its exploitation and exploration capabilities. To prove the performance of the NSM-FDB-TLABC algorithm, it was applied to solve both DED and benchmark problems.

The contributions of this study were explained as below:
- The NSM-FDB-TLABC algorithm was proposed in the literature as a competitive MHS algorithm.
- The proposed algorithm was implemented for solving both DED and benchmark problems.
- The best optimal solutions were obtained for solving the DED problem by the proposed algorithm.

The outline of the rest of the study is explained as follows: Section 2 presents the formulation of the DED problem. In section 3, the proposed NSM-FDB-TLABC algorithm is introduced. In section 4, the simulation study and results are given. Section 5 presents the conclusion of the study.

II. FORMULATION OF THE DYNAMIC ECONOMIC DISPATCH PROBLEM

In this study, the DED problem is considered. Here, the goal is to minimize the total fuel cost of the system during the dispatch period. Traditionally, the fuel cost of the thermal generating units can be defined as the quadratic cost function. However, in multi-valve stream turbine-based generators, the valve-point loading effect (VPLE) is widely considered. For the DED problem, it is required to model the VPLE on the cost function of the thermal generating units [4]. The cost function including VPLE can be mathematically expressed as in Eq. (1).

$$F_{k,t}\left(P_{k,t}\right) = \delta_k + \beta_k P_{k,t} + \alpha_k P_{k,t}^2 + \left|\mu_k \sin\left(\xi_k\left(P_{k,t}^{\min} - P_{k,t}\right)\right)\right| \quad (1)$$

Here, $F_{k,t}$ and $P_{k,t}$ are the total fuel cost and the output power of the kth thermal generating unit at the time interval t, respectively. $\left\{\delta_k, \beta_k, \alpha_k\right\}$ denote the cost coefficients of the kth thermal generating unit, μ_k and ξ_k are the coefficients of the VPLE. The objective function of the DED problem can be expressed as in Eq. (2) [4]:

$$\text{Minimize } OF = \sum_{t=1}^{T}\sum_{k=1}^{N} F_{k,t}\left(P_{k,t}\right) \quad (2)$$

Here, OF represents the objective function, which is the fuel cost of the system. T and N denote the number of dispatch time periods and the number of generating units, respectively.

A. Constraints

In the DED problem, both equality and inequality constraints are taken into account.

Equality constraints: The power balance equations with transmission losses for each hour are expressed as [4]:

$$P_{D,t} + P_{L,t} = \sum_{k=1}^{N} P_{k,t}, \ t = 1,2,\ldots,T \tag{3}$$

where $P_{D,t}$ is the sum of the power demand at the time interval t and $P_{L,t}$ is the total transmission loss of the system at the time interval t, calculated using the Eq. (4). Here, B_{ji}, B_{0j}, and B_{00} denote the loss coefficients.

$$P_{L,t} = \sum_{j=1}^{N}\sum_{i=1}^{N} P_{j,t}B_{ji}P_{i,t} + \sum_{j=1}^{N} B_{0j}P_{j,t} + B_{00} \tag{4}$$

Inequality constraints:
(*i*) Generator constraints: Each generator's output power is constrained by its upper (P_k^{max}) and lower (P_k^{min}) limits [4], which are determined by:

$$P_k^{min} < P_k < P_k^{max} \tag{5}$$

(*ii*) Ramp-rate limits: In reality, the operating conditions affect the way in which the active output power of each generator is adjusted. It should fall within an acceptable range at each interval and can be modeled by the following ramp rate limits [4]:

$$\begin{cases} P_{k,t} - P_{k,t-1} \leq UR_k \\ P_{k,t-1} - P_{k,t} \leq DR_k \end{cases}, \ t = 1,2,\ldots,T \tag{6}$$

where DR_k and UR_k are the down- and up-rate limits of the kth generating unit.
(*iii*) Prohibited operating zones (POZs): The POZs limits of the thermal generating limits can be described as in Eq. (7). Here, $P_{k,z}^l$ and $P_{k,z}^u$ are the lower and upper limits of the zth POZ, m is the number of the POZs of kth unit [4].

$$P_{k,t} \begin{cases} P_k^{min} \leq P_{k,t} \leq P_{k,1}^l \\ P_{k,z-1}^u \leq P_{k,t} \leq P_{k,z}^l, \ z = 2,3,\ldots,m \\ P_{k,m}^u \leq P_{k,t} \leq P_k^{max} \end{cases} \tag{7}$$

B. Constraint Handling Method

The DED problem consists of equality and inequality constraints. To handle these constraints, the most commonly used constraint handling method, called as the penalty function method, is used. In this method, the constraint violations are multiplied by a penalty coefficient and added to the objective function [21]. All the constraint violation degrees must be determined before using the penalty function approach. In the DED problem considered in this study, three constraint violations must be taken into account. Accordingly, the fitness function (*fitness*) of the DED problem can be expressed as:

$$fitness = OF + \xi_1 \cdot V_{CL} + \xi_2 \cdot V_{RR} + \xi_3 \cdot V_{POZ} \tag{8}$$

where V_{CL} and V_{RR} represent the violation degrees for the capacity limits, the ramp-rate limits of the thermal generating

units, respectively. V_{POZ} is the violation degrees for the POZs. If POZs is not included in the DED problem, it should not be included in the fitness function. ξ_1, ξ_2, and ξ_3 denote the penalty coefficient for the V_{CL}, V_{RR}, and V_{POZ},

III. PROPOSED METHOD: HYBRID NSM AND FDB BASED TLABC (NSM-FDB-TLABC) ALGORITHM

A. Overview of the TLABC algorithm

TLABC is an optimization algorithm that combines the exploration process of the ABC algorithm and the exploitation process of the TLBO algorithm. The teaching-based employed bee stage, the generalized oppositional scout bee stage, and the learning-based looker bee stage are the search phases used in TLABC to find solutions. TLABC begins with the randomly generated *NP* food sources, and then three stages are applied [22].

Teaching-based employed bee stage: Each employed bee looks for a new food source performed using Eq. (9).

$$v_{i,d} = \begin{cases} x_{i,d}^{old} + r_2\left(x_{t,d} - T_F x_{m,d}\right), \text{ if } r_1 < 0.5 \\ x_{n1,d} + F\left(x_{n2,d} - x_{n3,d}\right), \text{ otherwise} \end{cases} \tag{9}$$

In Eq. (9), r_1 and r_2 are the uniformly distributed random numbers within [0,1], $n1$, $n2$, and $n3$ are selected randomly integers within [1, *NP*], where $n1 \neq n2 \neq n3 \neq i$. The scale factor is denoted by F, whose value is between [0, 1].

Learning-based on looker bee stage: Here, an onlooker bee uses the selection probability (p) to determine which food source x_s to seek out. Then, the new food sources are searched by Eq. (10). Here, *rand* is a uniformly distributed random vector within [0, 1], j is the number in the range of [1, *NP*], and $j \neq s$.

$$v_s = \begin{cases} rand\left(x_s - x_j\right) + x_s, \text{ if } f\left(x_s\right) \leq f\left(x_j\right) \\ rand\left(x_j - x_s\right) + x_s, \text{ otherwise} \end{cases} \tag{10}$$

Generalized oppositional scout bee stage: After the learning-based on looker bee stage, the algorithm enters this stage. In this stage, a food source is deemed exhausted and would be abandoned if it could not be improved any further for at least a limited amount of time. A new solution candidate is generated by Eq. (11) and its oppositional solution (x_i^{op}) is generated using Eq. (12). ρ and m are randomly generated numbers between 0 and 1.

$$x_{ij} = \rho\left(x_{max,j} - x_{min,j}\right) + x_{min,j} \tag{11}$$

$$x_{ij}^{op} = m\left(\max\left(x_{ij}\right) + \min\left(x_{ij}\right)\right) - x_{ij} \tag{12}$$

Finally, the better solution of x_i and x_i^{op} are used to replace the old depleted food source according to Eq. (13).

$$x_i = \begin{cases} x_i, & \text{if } f(x_{ij}^{op}) \geq f(x_i) \\ x_{ij}^{op}, & \text{if } f(x_{ij}^{op}) \geq f(x_i) \end{cases} \tag{13}$$

B. Overview of the FDB method

The FDB selection method, presented in the literature by Kahraman et al. in 2020 [23], is a selection method preferred by researchers for the last three years to enhance the search performance of MHS algorithms. The aim of this method is to effectively discover the guiding solution candidate that will contribute the most to the search process in MHS algorithms. In this method, the selection process is performed according to the score value calculated by considering the fitness values of the solution candidates and their distance to the best solution candidate (x_{best}) in the population [23].

In a population (P), the fitness value (fv) of each solution candidate is computed. The vector representing the population and fitness values is given in Eq. (14). Here, m and n represent the number of design variables and solution candidates, respectively.

$$P \equiv \begin{bmatrix} x_{11} & \cdots & x_{1m} \\ \vdots & \ddots & \vdots \\ x_{n1} & \cdots & x_{nm} \end{bmatrix}_{n \times m}, \quad fv \equiv \begin{bmatrix} f_1 \\ \vdots \\ f_n \end{bmatrix}_{n \times 1} \quad (14)$$

The calculation of the FDB score is explained step by step as follows:

(i) The distance value of the ith solution candidate (x_i) from the x_{best} is calculated using Eq. (15). The distance vector can be defined in Eq. (16).

$$\forall_{i=1}^m, P_i \neq P_{best}, D_{P_i} = \sqrt{\left(x_{1[i]} - x_{1[best]}\right)^2 + \ldots + \left(x_{m[i]} - x_{m[best]}\right)^2} \quad (15)$$

$$D_P \equiv \begin{bmatrix} d_1 \\ \vdots \\ d_n \end{bmatrix}_{n \times 1} \quad (16)$$

(ii) The FDB score is calculated with Eq. (17) using the distance values (D_P) given in Eq. (16) and the fitness values (fv) given in Eq. (14), where ς is the weighting factor that is taken value in the range of [0, 1]. In this study, it is set as 0.5. The vector of score vector is expressed as in Eq. (18).

$$\forall_{i=1}^m P_i, S_{P_i} = \varsigma * normfv_i + (1-\varsigma) * normD_{P_i} \quad (17)$$

$$S_P \equiv \begin{bmatrix} s_1 \\ \vdots \\ s_n \end{bmatrix}_{n \times 1} \quad (18)$$

To learn more about the FDB selection process in detail, you can review Ref [23].

C. Overview of the NSM method

The Natural Survivor Method (NSM) is a new method introduced to the literature by Kahraman et al. in 2023 [20], that can be preferred in the update mechanism to identify the survivors in MHS algorithms. It is determined which individuals will survive and which will die by using NSM scores instead of fitness values in the update mechanism in MHS algorithms. In this method, the success of each individual in fulfilling their duties, that is, their NSM score, is calculated

and the individual's survival depends on this score. There are three criteria to determine the NSM score of an individual: (i) the individual's contribution to the mating pool; (ii) the individual's contribution to the population; and (iii) the individual's contribution to its fitness value. The criteria for calculating the NSM score are explained below.

Contribution of the guides: Within the NSM, it is considered that an individual has a better chance of surviving if it makes a greater genetic diversity contribution to the guide solution candidate than its rivals. The distance information was used to determine the similarity between two individuals, and the chances of survival of individuals with different characteristics than the guide solution candidates were increased.

Contribution of the population: In this contribution, the distance information between an individual and others is used, and this information shows the difference between the candidates who will survive in the population and the others. In summary, an individual has a better chance of survival if they contribute more to the population's diversity.

Contribution to the objective function: The most successful people are those who have the highest fitness values for the objective function. The fitness value of the individual is used to represent individual strength.

According to these contributions, the NSM score of x_i is computed by using Eq. (19). Here, $x_{i,NSM_{MPS}}$, $x_{i,NSM_{PS}}$, and $x_{i,NSM_{OFS}}$ correspond to the mating pool source value of x_i, contribution of solution candidate x_i to the P-population, and individual strength of x_i, respectively. w_1, w_2, and w_3 are the weighting coefficients.

$$x_{i,NSM_{score}} = w_1 * x_{i,NSM_{MPS}} + w_2 * x_{i,NSM_{PS}} + w_3 * x_{i,NSM_{OFS}} \quad (19)$$

To obtain more detailed information about the NSM method, you can review [20].

D. Proposed NSM-FDB-TLABC algorithm

In the literature, two powerful versions of the TLABC algorithm were presented. One of these is the FDB-TLABC algorithm [19], while the other is the NSM-TLABC algorithm [20]. In this study, by combining FDB-TLABC and NSM-TLABC, an extremely powerful and competitive hybrid TLABC version was proposed, called as the NSM-FDB-TLABC. In the proposed algorithm, the FDB method was applied to the TLABC algorithm to maximize the ability of the base TLABC algorithm to mimic nature. In other words, the goal was to enhance the TLABC algorithm's exploration, exploitation, and balanced search capabilities [19]. The improvements were made in the learning-based onlooker bee of the TLABC algorithm and the solution candidate given in Eq. (10) chosen by the FDB method was used instead of x_s given in Eq. (20).

$$v_s = \begin{cases} rand\left(x_{FDB} - x_j\right) + x_s, & \text{if } f(x_j) \geq f(x_s) \\ rand\left(x_j - x_{FDB}\right)x_s, & \text{otherwise} \end{cases} \quad (20)$$

In the proposed algorithm, the NSM-based update mechanism was implemented on the teaching-based employed bee stage of the TLABC algorithm. In general, there are three steps common to all MHS algorithms. These include choosing the population's guiding solution candidate, developing a new solution candidate from the selected individual, and figuring out the fitness function values of the newly formed and original individuals. After these three stages are completed, the traditional update mechanism in MHS algorithms is performed, where the fitness function values of the newly created individual and the previous individual are compared, and then the individual with the better fitness function value survives. However, in the NSM-based update mechanism, the NSM score is calculated to determine the surviving individual by using Eq. (17), where the individual with the better score value survives.

The pseudocode of the NSM-FDB-TLABC algorithm is given in Algorithm-1.

Algorithm-1. Pseudocode of the NSM-FDB-TLABC algorithm
1. Initialize the position of individual x_i (i=1,…, NP)
2. Calculate the fitness function value of the population $fv(x_i)$
3. Set *trial*=0 for each individual.
4. **while** $FE < maxFEs$ **do**
//*Teaching-based employed bee stage*//
5.   **for** $i = 1 : NP$
6.   Create a new solution candidate v_i by using Eq. (10)
7.   Compute the fitness function value of each individual $fv(v_i)$
/NSM-based update mechanism/
8.   Calculate the NSM score of x_i and v_i by using Eq. (19)
9.   **if** ($v_i > x_i$) **then** $x_i = v_i$, **else** use x_i;
10.   **if** x_i doesn't improve then *trial(i)* = *trial(i)*+1, **else** *trial(i)*=0;
11.   **end for**
//*Learning-based employed bee stage*//
12.   Compute the probability p
13.   **for** $i = 1 : NP$
14.   Create an individual x_i
/FDB-based selection method/
15.   Calculate the FDB score of the each individual by using Eq. (17)
16.   Select an individual based on the FDB-score of individuals.
17.   Calculate the fitness function value of selected individual v_s
18.   **if** ($v_s > x_i$) **then** $x_i = v_s$, **else** use x_i;
19.   **if** x_i doesn't improve **then** *trial(i)*= *trial(i)*+1, **else** *trial(i)*=0;
20.   **end for**
//*Generalized oppositional bee stage*//
21.   **if** $limit \le \max(trial(i))$ **then**
22.   Create a new solution candidate solution x_i and its oppositional solution x_i^{op}
23.   Specify a better solution candidate between x_i and x_i^{op} by Eq. (12)
24.   **end if**
25.   **end while**

According to Algorithm-1, the NSM-FDB-TLABC algorithm initializes with a randomly generated population in line 1, and then the fitness values of them are calculated in line

2. After that, the search-process lifecycle begins. Between lines 5 and 11, the teaching-based employed bee stage performs. The NSM-based method is applied to the update mechanism of the individual between lines 8 and 10. Then, the learning-based employed bee stage performs from lines 12 to 20. The FDB method is used to select the guide solution candidate between lines 15 and 17, and then the update process is performed. The generalized oppositional bee stage performs in lines 21 to 23. All of these processes continue until the termination requirement is fulfilled, which is specified as the maximum number of fitness function evaluations (maxFEs).

IV. SIMULATION RESULTS AND DISCUSSIONS

In this section, in order to validate the performance of the NSM-FDB-TLABC algorithm, an extensive simulation study was conducted.

- In the first sub-section, the performance of the NSM-FDB-TLABC algorithm on benchmark problems was tested. Accordingly, the CEC2017 [24] and CEC2020 [25] benchmark suites were used. To show the improvement of the proposed algorithm against the its rival algorithms, including FDB-TLABC, NSM-TLABC, FLA [26], EMA [27], and EO [28], their results were analyzed and examined using the statistical analysis methods such as Friedman and Wilcoxon.
- In the second sub-section, the NSM-FDB-TLABC algorithm was implemented to solve the DED problem. To show the superiority of the proposed algorithm in solving the DED problem, their results were compared with the results of the NSM-TLABC, FDB-TLABC, EMA, FLA, and EO algorithms. Moreover, the results of the proposed algorithm were compared with the results reported in the literature.

A. Application of the NSM-FDB-TLABC algorithm on benchmark problems

In this sub-section, the proposed NSM-FDB-TLABC and the 5 MHS algorithms, including FDB-TLABC, NSM-TLABC, FLA, EMA, and EO, were applied to solve the CEC2017 and CEC2020 benchmark problems. All algorithms were run 51 trials and three dimensional search spaces (30, 50, and 100). The maximum number of fitness function evaluations (maxFEs), which was set at 10000*Dimension (D), served as the termination criterion to provide fairness across the methods. Moreover, the parameters of the algorithms were set as given in their original articles. The parameters of the proposed NSM-FDB-TLABC were the same as those of NSM-TLABC and FDB-TLABC algorithms.

To compare the algorithms statistically, Wilcoxon-signed rank and Friedman tests were performed on the results of the benchmark problems for all algorithms. The Friedman test results are presented in Table 1. While performing the Friedman test, the error values of the algorithms for benchmark problems were used. In Table 1, the results of the six experiments were given and the best score value of each experiment was highlighted in bold. According to Table 1, the proposed algorithm yielded the best score value in 5 of 6 experiments. In the experiment conducted in the CEC2017 benchmark suite and 100 dimensional search space, the FLA algorithm ranked first

and the EMA algorithm ranked second, while the proposed algorithm ranked third. On the other hand, when evaluating the mean rank value of all algorithms displayed in the final row of

Table 1, the proposed algorithm achieved the highest ranking of all algorithms, with a score value of 2.2836.
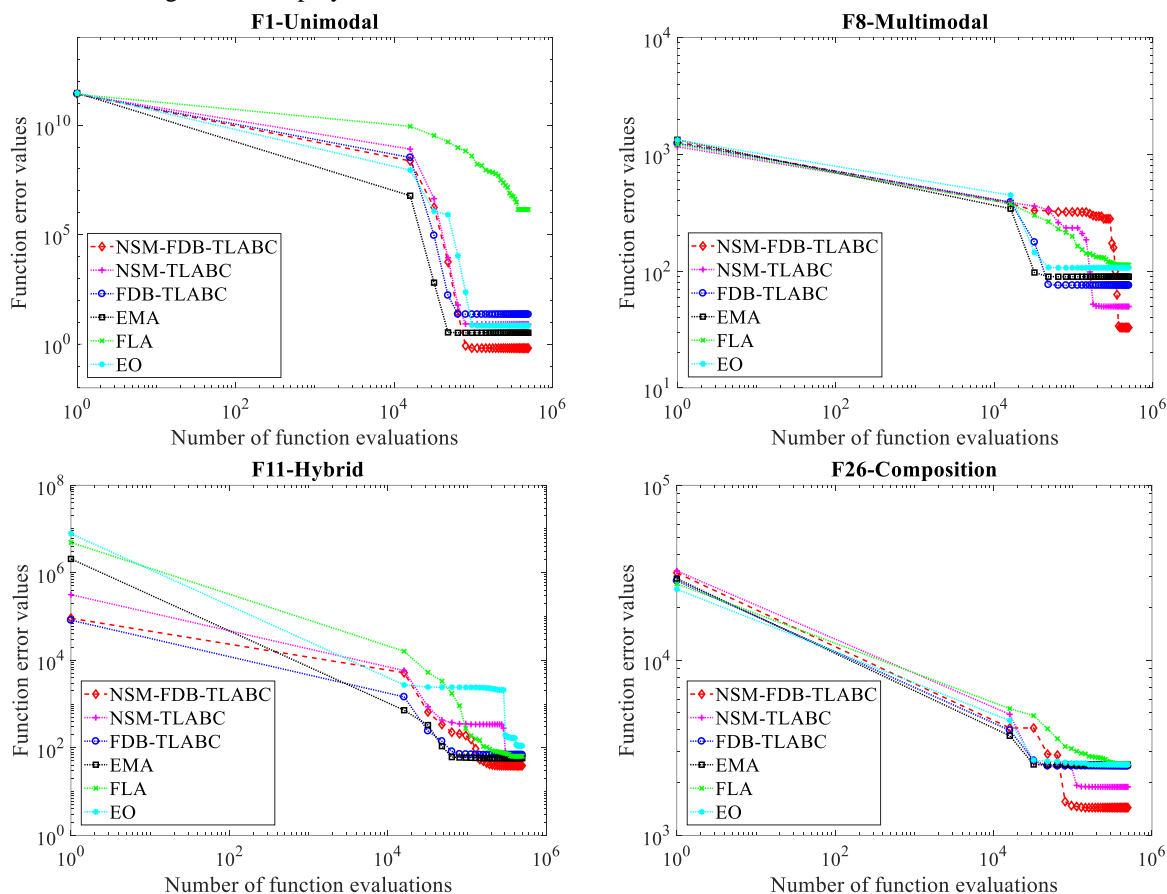

Fig. 1. Convergence graphs of the selected problems for 100-dimensional search space from CEC2017 benchmark suite.

TABLE I
FRIEDMAN TEST RESULTS OF THE ALGORITHMS

	NSM-FDB-TLABC	NSM-TLABC	FDB-TLABC	EMA	FLA	EO
CEC2017 (D=30)	**2.2593**	3.0794	2.5057	4.7417	4.6748	3.7390
CEC2017 (D=50)	**2.0085**	2.9878	2.7028	4.9675	4.4293	3.9040
CEC2017 (D=100)	2.9601	4.0798	3.8661	2.8573	**2.5747**	4.6619
CEC2020 (D=30)	**2.2314**	3.1020	2.5167	4.2814	5.0912	3.7775
CEC2020 (D=50)	**2.0873**	3.1235	2.7137	4.4216	4.7931	3.8608
CEC2020 (D=100)	**2.1549**	2.8608	2.6235	4.8843	4.7725	3.7039
Mean Rank	**2.2836**	3.2056	2.8214	4.3590	4.3893	3.9412

The Wilcoxon test is frequently used to compare MHS algorithms statistically. The NSM-FDB-TLABC and other algorithms were compared using the Wilcoxon test in this study, where the error values obtained from the algorithms were considered. Table 2 presents the results of the Wilcoxon test conducted between the NSM-FDB-TLABC algorithm and its rival algorithms. The number of problems where the NSM-FDB-TLABC won, the number of problems where the NSM-FDB-TLABC and its opponent drew, and the number of

problems where the opponent won are represented by " + ", " = ", and " - " signs. According to Table 2, the proposed algorithm lost only to the EMA and FLA algorithms in the experiment conducted in the CEC2017 benchmark suite and 100 dimensional search space. It outperformed its rivals in all other pairwise comparisons.

Besides the Wilcoxon and Friedman tests, the convergence graphs are used to evaluate the search performance of the NSM-FDB-TLABC algorithm and its competitors. Accordingly, four types of problems, which were F1 (unimodal), F8 (multimodal), F11 (hybrid), and F26 (composition) type problems, were selected from the CEC2017 benchmark problem suite. The convergence curves of these problems were drawn based on the function error values in 100 dimensions. The convergence curves of all algorithms are presented in Fig. 1.

TABLE II
WILCOXON TEST RESULTS OF THE ALGORITHMS

NSM-FDB-TLABC vs. (+/=/-)	NSM-TLABC	FDB-TLABC	EMA	FLA	EO
CEC2017 (D=30)	21/5/3	14/6/9	24/3/2	26/3/0	20/4/5
CEC2017 (D=50)	22/6/1	16/7/6	26/3/0	26/2/1	23/4/2
CEC2017 (D=100)	21/8/0	15/8/6	8/7/14	8/8/13	23/4/2
CEC2020 (D=30)	7/2/1	4/3/3	7/2/1	10/0/0	7/2/1
CEC2020 (D=50)	8/2/0	4/4/2	8/2/0	10/0/0	8/2/0
CEC2020 (D=100)	5/5/0	4/4/2	8/2/0	9/1/0	7/3/0

According to Fig. 1, for the F1-unimodal type problem, only the proposed algorithm converged to an error value of 10^0, while its closest competitor, the EO algorithm, converged to an error value of 10^1. The worst performance was performed by the FLA algorithm, whose error value was over 10^5. For the F8-multimodal type problem, the lowest error value was obtained from the proposed NSM-FDB-TLABC algorithm. Hybrid problems are employed to examine the balance between exploitation and exploration of the algorithms. For the F11-hybrid type problem, the convergence curve of all algorithms demonstrated that the NSM-FDB-TLABC converged to an error value below 10^2. It showed better convergence performance compared than the rivals. Composition type problems, known for their computational complexity, are utilized to assess the search performance of algorithms. For the F26-composition type problem, the proposed algorithm converged with a lower minimum error value than others.

In summary, the evaluation of convergence analysis and statistical analysis results demonstrated the effectiveness of the NSMFDB-TLABC algorithm in solving the CEC2017 and CEC2020 benchmark suites in comparison to its rivals.

B. Solving the DED problem using the NSM-FDB-TLABC algorithm

In this section, to show the performance of the proposed NSM-FDB-TLABC algorithm, it was applied to solve the DED problem. Here, the 5-unit test system was considered. The data for the 5-unit test system and the *B*-coefficients are taken from [4]. Two DED cases on the 5-unit test system are considered, and they are explained as follows:

- Case-1: The 5-unit test system considering transmission losses.
- Case-2: The 5-unit test system considering transmission losses and POZs.

These case studies were solved by the proposed NSM-FDB-TLABC, NSM-TLABC, FDB-TLABC, EMA, EO, and FLA algorithms.

1) Case-1: The 5-unit test system considering transmission losses

In this case, the proposed algorithm was implemented on the 5-unit test system with transmission losses. The optimal solutions obtained from the NSM-FDB-TLABC algorithm are presented in Table 3. The statistical results of the Case-1 including the minimum (min), mean, standard deviation (std), and maximum (max) of the results for NSM-FDB-TLABC, NSM-TLABC, TLABC, EMA, FLA, EO, and the results reported in the literature are presented in Table 4. Accordingly, the proposed algorithm obtained 43044.0111$/h, which was lower 16.6515%, 16.6464%, 15.7955%, 16.3128%, 16.3354%, 0.1694%, 0.2146%, 0.1081%, 0.1886%, and 0.0093% than the NSM-TLABC, FDB-TLABC, EMA, FLA, EO, ICA [1], TVAC-IPSO [2], SOS [3], HIGA [5], and MBF-SSO [6], respectively. However, only the MGDE [9] algorithm achieved 0.0835% better results than the proposed algorithm. On the other hand, according to the mean values of the all algorithms, the proposed algorithm achieved the best mean value among
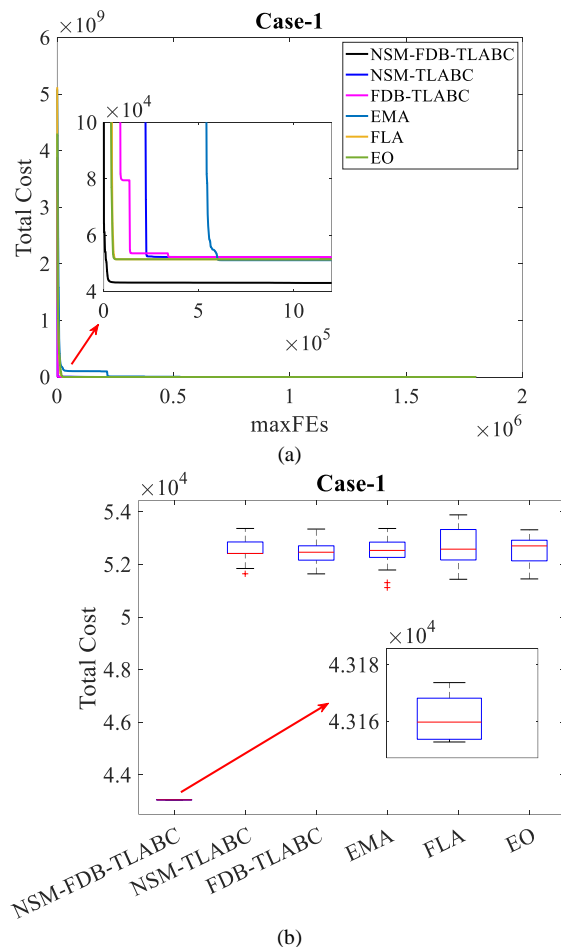
them.

Fig. 2. For Case-1: (a) Convergence curves and (b) box-plots of the algorithms

TABLE III
OPTIMAL SOLUTIONS OF THE CASE-1 OBTAINED FROM NSM-FDB-TLABC ALGORITHM

Hour	P_1 (MW)	P_2 (MW)	P_3 (MW)	P_4 (MW)	P_5 (MW)	Cost ($/h)
1	20.6717	98.5580	30.0000	124.9642	139.6215	1251.2715
2	10.0029	97.6376	66.9647	124.6689	139.8493	1427.1847
3	10.0041	98.9542	106.9202	124.0000	139.9037	1400.2080
4	10.4024	98.8530	112.9200	174.0000	139.8349	1665.7307
5	10.0052	92.6691	112.7733	209.8889	139.4195	1590.4788
6	10.0088	98.7799	112.7703	209.9633	184.4699	1875.0228
7	10.0017	72.3517	112.6499	209.8913	229.5653	1841.8776
8	12.7471	98.3541	112.6477	209.9465	229.5623	1799.7490
9	42.6628	105.3829	112.7129	209.8933	229.5483	2012.7303
10	64.0264	98.3526	112.6859	209.9241	229.5703	1998.7705
11	75.0000	103.7549	112.8779	209.8840	229.5263	2038.1223
12	75.0000	124.5498	112.7418	209.8887	229.5391	2180.5800
13	64.0517	98.2066	112.8542	209.8696	229.5759	2000.2273
14	49.0088	98.7477	112.9922	209.8925	229.5272	1981.2869
15	35.8566	98.7871	112.8989	186.0012	229.5801	2015.8971
16	10.0069	98.5840	112.6975	136.3794	229.5655	1682.8253
17	10.0066	87.6042	112.6405	124.8909	229.5406	1615.6752
18	10.0028	98.5468	112.6697	165.1964	229.5353	1853.6463
19	12.6961	98.3982	112.7147	209.9050	229.5435	1798.9801
20	42.5314	120.0242	112.6369	209.8875	229.5784	2116.7549
21	39.1224	98.5533	112.7461	209.9103	229.5701	1945.7246
22	10.0035	98.4763	112.7261	209.8855	181.8219	1865.0050
23	10.0049	98.8733	112.8114	171.9523	139.2987	1661.9658
24	10.0047	80.3089	112.8588	124.6164	139.6983	1424.2963
					Total Cost ($/h)	**43044.0111**

TABLE IV
THE STATISTICAL RESULTS OF THE CASE STUDIES

	Min.	Mean	Max.	Std.
NSM-FDB-TLABC	43044.0111	**43051.6125**	43060.914	4.6128
NSM-TLABC	51643.4121	52576.7265	53365.3516	401.7314
FDB-TLABC	51640.266	52447.641	53342.9554	396.7994
EMA	51118.4465	52467.1522	53364.3619	503.6893
FLA	51434.3969	52651.9171	53882.4227	651.6330
EO	51448.3000	52573.5138	53314.6128	511.5934
ICA [1]	43117.055	43144.472	43209.533	*NR*
TVAC-IPSO [2]	43136.561	43185.664	43302.233	*NR*
SOS [3]	43090.5925	43103.0828	43162.2146	*NR*
HIGA [5]	43125.365	43162.243	43259.352	*NR*
MBF-SSO [6]	43048	43068	43093	*NR*
MGDE [9]	**43008.1049**	43084.9049	43403.2808	98.5234

NR : Not reported

TABLE V
OPTIMAL SOLUTIONS OF THE CASE-2 OBTAINED FROM NSM-FDB-TLABC ALGORITHM

Hour	P_1 (MW)	P_2 (MW)	P_3 (MW)	P_4 (MW)	P_5 (MW)	Cost ($/h)
1	16.3763	98.5766	30.0003	40.0007	229.1750	1252.5526
2	10.1468	98.7272	30.0005	71.1344	229.5246	1442.7911
3	10.0217	90.1248	30.0006	120.6099	229.5155	1439.2974
4	13.2421	98.5321	70.0003	124.9104	229.5461	1663.5090
5	10.0006	90.2485	110.0000	124.9309	229.5169	1617.8055
6	40.0001	99.9153	112.6257	133.7977	229.5203	1838.3339
7	10.0006	98.5453	112.6350	183.7394	229.5281	1865.7661
8	12.5632	98.6481	112.7112	209.8150	229.5208	1797.4928
9	42.5218	105.5390	112.7582	209.8615	229.5201	2013.2808
10	64.0313	98.5236	112.6322	209.8530	229.5196	1997.1436
11	75.0000	102.4267	114.2132	209.8632	229.5298	2038.7198
12	74.9480	124.7350	112.6653	209.8494	229.5224	2180.5455
13	64.1408	98.4593	112.6663	209.7677	229.5249	1997.1759
14	49.6293	98.5494	112.6301	209.8431	229.5167	1978.1822
15	35.4353	98.5362	112.6669	186.9641	229.5247	2007.7227
16	10.0006	98.0600	112.6616	136.9909	229.5188	1688.4631
17	10.0008	92.5674	107.6671	124.9470	229.5278	1619.5258
18	15.0380	98.5555	112.8514	159.9568	229.5246	1868.8543
19	12.7430	98.5366	112.6403	209.8214	229.5164	1797.6383
20	42.7171	118.0164	114.5427	209.8440	229.5204	2119.3944
21	39.3619	98.5553	112.6340	209.8284	229.5223	1945.0432
22	12.0809	98.5823	112.6513	160.0007	229.5458	1849.2003
23	10.0005	96.0897	72.6795	124.8716	229.5120	1656.6863
24	10.0004	70.8416	32.6953	124.9179	229.5222	1477.6292
					Total Cost ($/h)	**43152.7537**

The convergence curves and the box-plot of all algorithms for Case-1 are presented in Fig. 2. According to Fig. 2 (a), it was clearly seen that the proposed algorithm converged to the best fitness value compared to the rivals. From Fig. 2 (b), the proposed algorithm obtained the best minimum and median values against the others and showed stable search performance among all algorithms.

2) Case-2: The 5-unit test system considering transmission losses and POZs

Here, the proposed algorithm was implemented on the 5-unit test system with transmission losses and POZs of the generating units. The optimal solutions obtained from the NSM-FDB-TLABC algorithm are presented in Table 5. In Table 6, the statistical results of the case studies for all algorithms are

presented. From Table 3, the total cost value obtained from the NSM-FDB-TLABC was 43152.7537$/h, which was lower 17.3067%, 17.1919%, 15.9840%, 15.8453%, 16.7436%, 0.0538%, and 0.0734% than the NSM-TLABC, FDB-TLABC, EMA, FLA, EO, MBF-SSO [6], and MGDE [9] algorithms, respectively. Besides, the proposed algorithm achieved the best mean value among them.

TABLE VI
THE STATISTICAL RESULTS OF THE CASE STUDIES

|	Min.	Mean	Max.	Std.
NSM-FDB-TLABC	**43152.7537**	**43161.3386**	43173.6983	8.1836
NSM-TLABC	52184.1304	52819.029	53688.8109	339.971
FDB-TLABC	52111.7365	52665.5418	53737.1936	436.3525
EMA	51362.5670	52421.6731	53301.1135	531.7966
FLA	51277.8689	52605.8738	53610.1305	606.9064
EO	51831.1520	52710.1195	53545.2565	480.5690
MBF-SSO [6]	43176	*NR*	*NR*	*NR*
MGDE [9]	43184.4654	43280.8562	43461.7934	90.8574

NR : Not reported

(a)

(b)
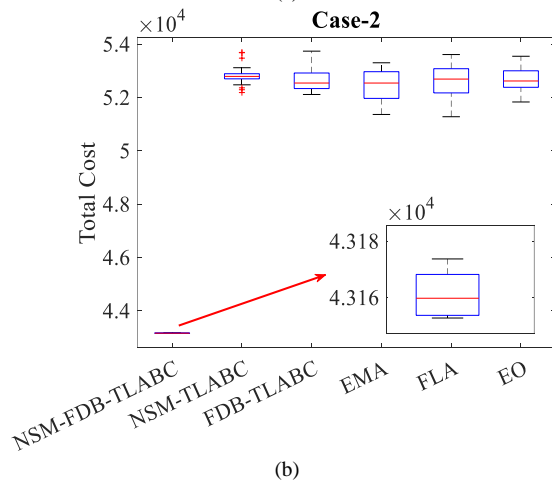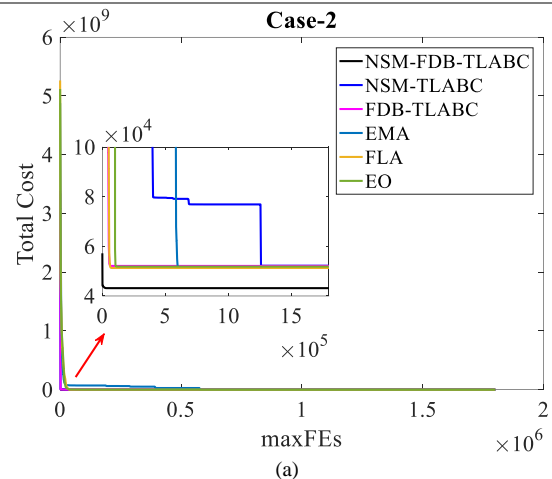
Fig. 3. For Case-2: (a) Convergence curves and (b) box-plots of the algorithms

The convergence curves and the box-plot of all algorithms for Case-2 are presented in Fig. 3. From Fig. 3 (a), it can be seen that the proposed algorithm converged to the best objective function value among all algorithms. On the other hand, when

the box-plots of the algorithms given in Fig. 3 (b) were analyzed, the proposed algorithm achieved a successful search performance against its rivals.

V. CONCLUSION

In this study, the NSM-FDB-TLABC algorithm was presented to the literature as a competitive and powerful algorithm by combining the strengths of the NSM-TLABC and FDB-TLABC algorithms. In the NSM-FDB-TLABC algorithm, the updating mechanism of the teaching-based employed bee stage was redesigned using the NSM-based method as in the NSM-TLABC, and the guide individual in the learning-based employed bee stage was chosen by the FDB-based method as in the FDB-TLABC. One of the most important points of the study was that a comprehensive simulation study was carried out to verify the performance of the NSM-FDB-TLABC algorithm. In the first simulation study, the proposed algorithm and its five rivals were applied to solve the CEC2017 and CEC2020 benchmark problems. The results were analyzed using the Friedman test, Wilcoxon test, and convergence analysis. According to Friedman test results, the proposed algorithm ranked first in terms of mean rank value with 2.2836. In second simulation study, the proposed algorithm and its five rivals were applied to solve two DED case studies. According to their results, the proposed algorithm achieved the best optimal solutions among them. On the other hand, the results of the proposed algorithm were compared with the results reported in the literature. Based on the results of them, the proposed algorithm obtained the best optimal solutions for both case studies. The other important point of the study was that the best optimal solutions for two case studies were presented to the literature. To sum up, the supremacy of the proposed algorithm was proven on both the DED problem and benchmark suites.

In future studies, hybrid uses of the FDB and NSM methods used in this study will be tested on different meta-heuristic algorithms. Additionally, the NSM-FDB-TLABC algorithm presented in the study will be applied to solve different real-world engineering problems.

REFERENCES

[1] B. Mohammadi-Ivatloo, A. Rabiee, A. Soroudi, M. Ehsan. "Imperialist competitive algorithm for solving non-convex dynamic economic power dispatch." Energy, vol. 44. 1, 2012, pp 228-240.

[2] B. Mohammadi-Ivatloo, A. Rabiee, M. Ehsan. "Time-varying acceleration coefficients IPSO for solving dynamic economic dispatch with non-smooth cost function." Energy conversion and management, vol. 56, 2012, pp 175-183.

[3] Y. Sonmez, H. T. Kahraman, M. K. Dosoglu, U. Guvenc, S. Duman. "Symbiotic organisms search algorithm for dynamic economic dispatch with valve-point effects." Journal of Experimental & Theoretical Artificial Intelligence, vol. 29. 3, 2017, pp 495-515.

[4] C. Dai, Z. Hu, Q. Su. "An adaptive hybrid backtracking search optimization algorithm for dynamic economic dispatch with valve-point effects." Energy, vol. 239, 2022, 122461.

[5] B. Mohammadi-Ivatloo, A. Rabiee, A. Soroudi. "Nonconvex dynamic economic power dispatch problems solution using hybrid immune-genetic algorithm." IEEE Systems Journal, vol. 7.4, 2013, pp 777-785.

[6] R. Azizipanah-Abarghooee. "A new hybrid bacterial foraging and simplified swarm optimization algorithm for practical optimal dynamic load dispatch." International Journal of Electrical Power & Energy Systems, vol. 49, 2013, pp 414-429.

[7] Y. Zhang, D. W. Gong, N. Geng, X. Y. Sun."Hybrid bare-bones PSO for dynamic economic dispatch with valve-point effects." Applied Soft Computing, vol. 18, 2014, pp 248-260.

[8] G. Xiong, D. Shi, "Hybrid biogeography-based optimization with brain storm optimization for non-convex dynamic economic dispatch with valve-point effects." Energy, vol. 157, 2018, pp 424-435.

[9] D. Zou, S. Li, X. Kong, H. Ouyang, Z. Li, "Solving the dynamic economic dispatch by a memory-based global differential evolution and a repair technique of constraint handling." Energy, vol. 147, 2018, pp 59-80.

[10] M. Ghasemi, E. Akbari, M. Zand, M. Hadipour, S. Ghavidel, L. Li. "An efficient modified HPSO-TVAC-based dynamic economic dispatch of generating units." Electric Power Components and Systems, vol. 47. 19-20, 2019, pp 1826-1840.

[11] Z. Zheng, J. Li, Y. Han. "An improved invasive weed optimization algorithm for solving dynamic economic dispatch problems with valve-point effects." Journal of Experimental & Theoretical Artificial Intelligence, vol. 32. 5, 2020, pp 805-829.

[12] D. Santra, A. Mukherjee, K. Sarker, S. Mondal, "Dynamic economic dispatch using hybrid metaheuristics." Journal of Electrical Systems and Information Technology, vol. 7, 2020, pp 1-30.

[13] W. Yang, Z. Peng, Z. Yang, Y. Guo, X. Chen, "An enhanced exploratory whale optimization algorithm for dynamic economic dispatch." Energy Reports, vol. 7, 2021, pp 7015-7029.

[14] Z. Hu, C. Dai, Q. Su, "Adaptive backtracking search optimization algorithm with a dual-learning strategy for dynamic economic dispatch with valve-point effects." Energy, vol. 248, 2022, 123558.

[15] S. Basak, B. Bhattacharyya, B. Dey, "Dynamic economic dispatch using hybrid CSAJAYA algorithm considering ramp rates and diverse wind profiles." Intelligent Systems with Applications, vol. 16, 2022, 200116.

[16] W. Yang, X. Zhu, F. Nie, H. Jiao, Q. Xiao, Z. Yang, "Chaos Moth Flame Algorithm for Multi-Objective Dynamic Economic Dispatch Integrating with Plug-In Electric Vehicles." Electronics, vol. 12. 12, 2023, 2742.

[17] W. Yang, Y. Zhang, X. Zhu, K. Li, Z. Yang, "Research on Dynamic Economic Dispatch Optimization Problem Based on Improved Grey Wolf Algorithm." Energies, vol. 17. 6, 2024, 1491.

[18] K. Nagarajan, A. Rajagopalan, M. Bajaj, R. Sitharthan, S. A. Dost Mohammadi, V. Blazek, Optimizing dynamic economic dispatch through an enhanced Cheetah-inspired algorithm for integrated renewable energy and demand-side management. Scientific Reports, vol. 14. 1, 2024, 3091.

[19] S. Duman, H. T. Kahraman, Y. Sonmez, U. Guvenc, M. Kati, S. Aras. "A powerful meta-heuristic search algorithm for solving global optimization and real-world solar photovoltaic parameter estimation problems." Engineering Applications of Artificial Intelligence, vol. 111, 2022, 104763.

[20] H. T. Kahraman, M. Katı, S. Aras, D. A. Taşci. "Development of the Natural Survivor Method (NSM) for designing an updating mechanism in metaheuristic search algorithms." Engineering Applications of Artificial Intelligence, vol. 122, 2023, 106121.

[21] X. Chen, B. Xu, C. Mei, Y. Ding, K. Li. "Teaching–learning–based artificial bee colony for solar photovoltaic parameter estimation." Applied Energy, vol. 212, 2018, pp 1578-1588.

[22] H. T. Kahraman, S. Aras, E. Gedikli. "Fitness-distance balance (FDB): a new selection method for meta-heuristic search algorithms." Knowledge-Based Systems, vol. 190, 2020, 105169.

[23] N. H. Awad, M. Z. Ali, J. J. Liang, B. Y. Qu, P. N. Suganthan."Problem definitions and evaluation criteria for the CEC 2017 special session and competition on single objective bound constrained real-parameter numerical optimization." Technical Report, 2016.

[24] C. T. Yue, K. V. Price, P. N. Suganthan, J. J. Liang, M. Z. Ali, B. Y. Qu,... , P. P. Biswas. "Problem definitions and evaluation criteria for the CEC 2020 special session and competition on single objective bound constrained numerical optimization." Technical Report, 2019.

[25] F. A. Hashim, R. R. Mostafa, A. G. Hussien, S. Mirjalili, K. M. Sallam. "Fick's Law Algorithm: A physical law-based algorithm for numerical optimization." Knowledge-Based Systems, vol. 260, 2023, 110146.

[26] M. H. Sulaiman, Z. Mustaffa, M. M. Saari, H. Daniyal, S. Mirjalili. "Evolutionary mating algorithm. "Neural Computing and Applications, vol. 35. 1, 2023, pp 487-516.

[27] A. Faramarzi, M. Heidarinejad, B. Stephens, S. Mirjalili. "Equilibrium optimizer: A novel optimization algorithm." Knowledge-based systems, vol. 191, 2020, 105190.

BIOGRAPHY

Burçin Özkaya obtained his BSc degree in Electrical and Electronics Engineering from Eskişehir Osmangazi University (ESOGU) in 2014. She received MSc. in Electrical and Electronics Engineering from the Süleyman Demirel University in 2018, and PhD degree in Electrical and Electronics Engineering from Düzce University in 2022. She worked as a Research Assistant with the Department of Electrical and Electronics Engineering at Suleyman Demirel University from 2015 to 2018, and with Department of Electrical and Electronics Engineering at Isparta University of Applied Sciences from 2018 to April 2023. She has been working as an Assistant Professor since April 2023 at Department of Electrical Engineering at Bandırma Onyedi Eylül University. Her research interests include power systems applications, optimization, meta-heuristic algorithms, and artificial intelligence.

Publication Ethics

The journal publishes original papers in the extensive field of Electrical-electronics and Computer engineering. To that end, it is essential that all who participate in producing the journal conduct themselves as authors, reviewers, editors, and publishers in accord with the highest level of professional ethics and standards. Plagiarism or self-plagiarism constitutes unethical scientific behavior and is never acceptable.

By submitting a manuscript to this journal, each author explicitly confirms that the manuscript meets the highest ethical standards for authors and coauthors

The undersigned hereby assign(s) to *Balkan Journal of Electrical & Computer Engineering* (BAJECE) copyright ownership in the above Paper, effective if and when the Paper is accepted for publication by BAJECE and to the extent transferable under applicable national law. This assignment gives BAJECE the right to register copyright to the Paper in its name as claimant and to publish the Paper in any print or electronic medium.

Authors, or their employers in the case of works made for hire, retain the following rights:

1. All proprietary rights other than copyright, including patent rights.
2. The right to make and distribute copies of the Paper for internal purposes.
3. The right to use the material for lecture or classroom purposes.
4. The right to prepare derivative publications based on the Paper, including books or book chapters, journal papers, and magazine articles, provided that publication of a derivative work occurs subsequent to the official date of publication by BAJECE.
5. The right to post an author-prepared version or an of ficial version (preferred version) of the published paper on an i nternal or external server controlled exclusively by t he author/employer, pr ovided that (a) such posting is noncommercial in nature and the paper is made available to users without charge; (b) a copyright notice and full citation appear with the paper, and (c) a link to BAJECE's official online version of the abstract is provided using the DOI (Document Object Identifier) link.

CONTENTS